Fall 2014

Supersonic jet spectroscopy of synthetic foldamers, multichromophores, and their water containing clusters

Evan Gardner Buchanan
Purdue University

Graduate School ETD Form 9
(Revised 12/07)

PURDUE UNIVERSITY
GRADUATE SCHOOL
Thesis/Dissertation Acceptance

This is to certify that the thesis/dissertation prepared

By Evan Gardner Buchanan

Entitled SUPERSONIC JET SPECTROSCOPY OF SYNTHETIC FOLDAMERS, MULTICHROMOPHORES, AND THEIR WATER CONTAINING CLUSTERS

For the degree of Doctor of Philosophy

Is approved by the final examining committee:

Timothy Zwier
Chair

Scott A. McLuckey

Dor Ben-Amotz

Lyudmila Slipchenko

To the best of my knowledge and as understood by the student in the *Research Integrity and Copyright Disclaimer (Graduate School Form 20)*, this thesis/dissertation adheres to the provisions of Purdue University's "Policy on Integrity in Research" and the use of copyrighted material.

Approved by Major Professor(s): Timothy Zwier

Approved by: R. E. Wild 10/09/2014
Head of the Graduate Program Date

SUPERSONIC JET SPECTROSCOPY OF SYNTHETIC FOLDAMERS, MULTICHROMOPHORES, AND THEIR WATER CONTAINING CLUSTERS

A Dissertation

Submitted to the Faculty

of

Purdue University

by

Evan Gardner Buchanan

In partial Fulfillment of the

Requirements of the Degree

of

Doctor of Philosophy

December 2014

Purdue University

West Lafayette, Indiana

For my loving family

ACKNOWLEDGMENTS

I would like to express my sincere gratitude in recognizing everyone who helped contribute to the work contained within this dissertation and helped make my graduate experience enjoyable and meaningful. There are too many people to thank individually, and I hope this acknowledgement sufficiently affirms my sentiment toward everyone not explicitly mentioned. Your contributions are noticed and appreciated. To that end, I would like to specifically thank my family and research advisor. To my family: Robert and Lynn; Colin, Corinne, and Charlie; and John and Lauren; I am blessed to have your unwavering love and support. To my research advisor, Timothy Zwier, you are a tremendous mentor, educator, and friend.

TABLE OF CONTENTS

Page

Page

Page

Page

LIST OF TABLES

Table Page

LIST OF FIGURES

Figure Page

Figure Page

Figure Page

Figure Page

Figure Page

Figure Page

ABSTRACT

Buchanan, Evan Gardner. Ph.D., Purdue University, December 2014. Supersonic Jet Spectroscopy of Synthetic Foldamers, Multichromophores, and Their Water Containing Clusters. Major Professor: Timothy S. Zwier.

A central theme specific to this dissertation concerns the conformation-specific spectroscopy of flexible molecules in an effort to bridge the complexity gap. Generally, molecules in the complexity gap have several flexible coordinates yet conformational isomerization still occurs along a simple reaction coordinate on the potential energy surface. Molecules in this regime benefit greatly from experiments probing the potential energy surfaces and provide a means to develop and test new theories in an effort to explain more complex system. These measurements are possible through the utilization of a supersonic jet expansion to collisionally cool molecules into their vibrational zero-point levels, collapsing the distribution of conformational isomers to the lowest-energy minima on the potential energy surface. This collisional cooling afforded by the expansion allows researchers to study transient species, molecular cluters, radicals and ions in a conformation-specific fashion. Overall, this dissertation contains three sets of molecules in an effort to bridge the complexity gap: synthetic foldamers, multichromophores, and water containing complexes.

For the synthetic foldamers, a set of 21 conformations that represent the full range of H-bonded structures were chosen to characterize the conformational dependence of the

vibrational frequencies and infrared intensities of the local amide I and amide II modes and their amide I/I and amide II/II coupling constants. These amide I/I and amide II/II coupling constants remain similar in size for α-, β-, and γ-peptides despite the increasing number of C-C bonds separating the amide groups. These findings provide a simple, unifying picture for future attempts to base the calculation of both nearest-neighbor and next-nearest-neighbor coupling constants on a joint footing

There are numerous circumstances of fundamental importance in which two or more ultraviolet chromophores are in close proximity, influencing the intrinsic properties of the close lying, vibronically coupled excited states. Whether incorporated in the same molecule or present as separate monomers, the excited state properties depend on the distance, relative orientation, and strength of the electronic coupling between the two chromophores. Our focus here is then the conformational dependent vibronic coupling observed between ultraviolet chromophores, and the effects of adding a single water molecule or network of water molecules on the vibronic coupling.

CHAPTER 1 INTRODUCTION

1.1 Motivation: Bridging the Complexity Gap

With the development and refinement of new methodologies fueled by technology, the field of molecular spectroscopy is well suited to investigate the fundamental properties of neutral[1-3] and ionic compounds[4-5] with increasing size and complexity, including in its ultimate manifestation large macromolecules such as proteins. At the forefront of investigations aimed towards macromolecules, two-dimensional IR[6-8] and electronic spectroscopy[9-10] have made considerable progress in elucidating the dynamics of coupled vibrational modes and electronic states in an effort to correlate biological function and structure. The techniques of two-dimensional spectroscopy mitigates the spectral congestion present in linear spectroscopy by correlating coupled states as off-diagonal elements and is capable of probing the complex, multidimensional free energy surfaces over a wide range of timescales.[6, 11] In terms of proteins, the timescales for interesting conformational transformations range from picoseconds to milliseconds.[12] Generally, two-dimensional spectroscopy employed in the investigation of macromolecules may be regarded as a "top-down" approach, investigating large proteins to determine secondary structural motifs and dynamics. However, to gain structural information, the field of two-dimensional spectroscopy necessarily relies on theoretical models developed to predict experimental spectra,

especially considering the computational cost of fully *ab initio* calculations or density functional theory optimizations and frequency calculations. Furthermore, the experimental spectra contain contributions from numerous conformational isomers further influenced by strong solvent interactions. Although it is desirable to study proteins in their native states, refining the theoretical models requires the ability to decouple solvent interactions from isolated molecules and decompose the experimental spectra into the sum of individual conformations.

At the opposite end of the spectrum, researchers are engaged in fundamental studies of cold, isolated molecules where isomerization occurs along a relatively simple or single reaction coordinate.[13-16] Hindered rotation and *cis/trans* isomerization[17] are prime examples of such elementary reactions. In such cases, one can gain a state-resolved understanding of both the energy flow through the molecule and the timescales to isomerization. Here, the cold environment of a supersonic jet expansion kinetically collapses the room temperature Boltzmann distribution of isomers into a few low-energy minima on the potential energy surface in the vibrational zero-point level, reducing the spectral congestion and allowing for single-conformation studies via double-resonance spectroscopy.[18] Through three body interactions, the collisional cooling begets the formation of weakly bound clusters when solvent molecules are seeded into the expansion.[19-20] Furthermore, the experimental results are readily comparable to *ab initio* and density functional theory calculations, allowing researchers to map out the potential energy surface computationally. Overall, single-conformation spectroscopy on relative small molecules may be regarded as a "bottom-up" approach, generating rules for simple building blocks or analogues and applying them to more complex systems.

Between the two methodologies and size regimes lies an incredible gulf of information termed the "complexity gap".[13, 21] The complexity gap comprises molecules with several competing conformational minima entwined by an increased flexibility or number of degrees of freedom, multiple ultraviolet chromophores either covalently bonded in a single molecule or hydrogen bonded in a cluster, and molecules interacting with a subset of solvent molecules forming the hydration shell. The beauty of a supersonic jet expansion lies in its ability to cool and isolate monomers and clusters, providing new insights about the potential energy surfaces to develop and refine models used by researchers investigating more complex systems. Figure 1.1 serves to pictorialize the complexity gap. The aim of this dissertation is to demonstrate the power of these methods that help bridge the complexity gap. The topics included range from model peptides and synthetic foldamers to multichromophores and water containing clusters. A more complete overview of the topics to be covered is presented in the following sections, with the appropriate chapters highlighted to direct the reader's attention.

.

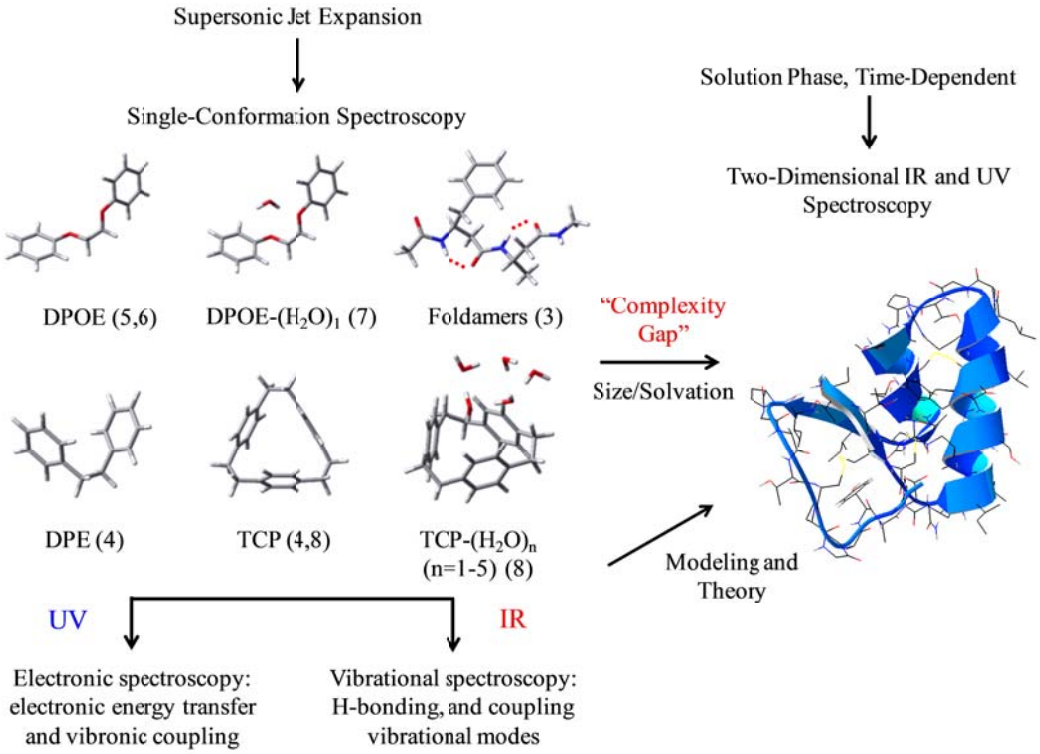

Figure 1.1 Bridging the complexity gap implementing a "bottom-up" approach. Conformation-specific IR and UV spectroscopy provide a detailed structural characterization of the low-energy conformational minima on the potential energy surface. The approach allows researchers to systematically increase the size, flexibility, and solvation of molecules to develop and improve models and theories used to investigate larger systems with more complex free energy surfaces. Chapters concerned with a particular molecule or cluster are provided in parentheses.

1.2 Organization of Thesis

1.2.1 Model Peptides and Synthetic Foldamers

Since the pioneering investigations of the amino acid tryptophan by Levy,[22-23] single-conformation studies of flexible, biologically relevant molecules entrained and cooled in a supersonic jet expansion have focused on the subset of biomolecules and clusters containing at least a single ultraviolet chromophore, including

neurotransmitters,[24-26] sugars,[27] DNA bases and base pairs,[28] naturally occurring amino acids and sequences, and synthetic foldamers incorporating one (β)[29-31] and two (γ)[32-36] additional carbon atoms in the backbone. The difficulty in studying such systems in the gas phase arises due to the relatively low vapor pressures of the molecules, requiring high temperatures for thermal vaporization or laser desorption to obtain a suitable number density to study.[1] Typically, at higher temperatures, biomolecules decompose into smaller subunits, complicating the spectra due to the high internal temperature of the molecules and the presence of decomposition products. A supersonic jet expansion overcomes the spectral complexity by cooling the biomolecules to very low temperatures without condensation.[18] Coupling the supersonic expansion to a time-of-flight mass spectrometer provides mass resolution and helps interpret or eliminates the contribution from decomposition products. From here, single and double-resonance spectroscopy has provided details regarding the low energy conformational preferences or folding propensities of biomolecules. Furthermore, population transfer spectroscopy and stimulated emission pumping population transfer spectroscopy have successfully determined the fractional abundances of conformations and the barrier heights to isomerization.[37-38]

Computational methodology and computer technology has also progressed significantly, allowing the comparison between experimental results and theoretical predictions afforded by calculations of large and complex molecules. There are currently several density functional theory methods incorporating dispersion interactions, forces which are extremely important in determining the lowest energy conformations of flexible molecules.[39] Specific ultraviolet and infrared spectra are assigned to a particular

conformational isomer based on the comparison between theory and experiment. It is therefore fruitful to explore all potential regions of the infrared spectrum diagnostic of conformation. Past experiments have traditionally relied on the NH stretch region of the infrared to establish firm conformational assignments based on the changes in fundamental frequency due to a specific secondary structure.[7-8] Additionally, both the amide I (C=O stretch, ~1700 cm^{-1}) and amide II (NH bend, ~1550 cm^{-1}) regions are sensitive to the local hydrogen bonding environment and therefore diagnostic of secondary structure.[40] Currently, the amide I and amide II regions of the spectrum are exploited by the two-dimensional infrared community, with off-diagonal peaks reporting the coupling between vibrational modes.

In chapter 3, we establish local mode amide I and amide II frequencies based on a Hessian reconstruction method, M05-2X harmonic $^{13}C=^{18}O$ frequencies, and a potential energy distribution analysis to determine nearest and next-nearest neighbor couplings which are characteristic of the hydrogen bonding motif or secondary structure of the amide group.

1.2.2 Multichromophores and Vibronic Coupling

Excitonic interactions remain a particularly interesting and challenging avenue for experiment and theory. Determining the magnitude of coupling alongside competing processes is experimentally challenging and necessarily relies on several spectroscopic techniques relying on both frequency and time-domain measurements. Furthermore, the effect of conformation on the excitonic coupling requires double-resonance spectroscopy. Once found, theory struggles to capture the degree of excitonic splitting, especially when

the excitonic interaction is quenched for physical reasons such as the introduction of vibration mediated coupling despite recent developments in the symmetric and asymmetric Fulton-Gouterman theory for vibronic coupling.[41]

These interactions can arise between identical or different chromophores, either held rigidly together through covalent bonds as part of a single molecule or hydrogen bonded as in the case of clusters. Previous studies include examples from both scenarios including diphenylmethane,[42-43] bis-4-hydroxyphenylmethane,[44], 2-aminopyridine, *o*-cyanophenol, 2-pyridone, and benzoic acid dimers.[45-47] Regardless of the situation, the local excitation occurring on either chromophore may be expressed as

$$\left|A^{*}B\right\rangle \text{ and } \left|AB^{*}\right\rangle \tag{1}$$

where the asterisk indicates the electronic excitation.

When the two chromophores are in identical environments, the symmetry adapted electronic wavefunctions are then composed of a simple sum and difference of the local excited states

$$\Psi = \frac{1}{\sqrt{2}}\left[\left|A^{*}B\right\rangle \pm \left|AB^{*}\right\rangle\right] \tag{2}$$

with the magnitude of the off-diagonal coupling terms determined by

$$H_{12} = \left\langle A^{*}B\left|H\right|AB^{*}\right\rangle \tag{3}$$

Nominally, the coupling is modeled by the long-range columbic coupling interactions of the two chromophores and depends on the distance, orientation, and the relative magnitude of the electronic transition moments.[48]

$$V = \frac{\mu_A \mu_B}{4\pi\varepsilon_0 R^3}\left(2\cos\theta_A \cos\theta_B + \sin\theta_A \sin\theta_B \cos\phi\right) \quad (4)$$

However, at short-distances, as observed in diphenylmethane, orbital overlap and exchange terms become highly important.[42-43] Furthermore, the treatment fails to handle coupled nuclear and electronic motion.[41]

Normally, the Born-Oppenheimer approximation is invoked to separate the electronic motion from the nuclear degrees of freedom. Although the utility of the Born-Oppenheimer approximation in most circumstances is unassailable, the approximation breaks down for numerous polyatomic molecules including photosynthetic proteins due to the number of close-lying excited states and degrees of nuclear freedom. Interestingly, vibration mediated electronic energy transfer has been observed to enhance the efficiency via coupling a vibrational mode with a frequency matching the band gap or when the frequency of a particular mode is critically damped.[49] It is therefore imperative to study model systems where vibronic coupling plays a pivotal role in electronic energy transfer. The Fulton-Gouterman model[50-51] has been used to treat symmetric bichromophores with excited electronic states that can interact to form excitonic states split by an energy, $2V_{AB}$.

As discussed elsewhere in more detail, the symmetry adapted electronic basis wavefunctions for each conformer may be expressed in terms of simple sum and differences of

$$\Psi^{A}{}_{e}(q;Q_0) = \psi^{A}{}^{*}(q^{A};Q^{A}{}_{0})\,\psi^{B}{}_{0}(q^{B};Q^{B}{}_{0}) \tag{5}$$

and

$$\Psi^{B}{}_{e}(q;Q_0) = \psi^{A}(q^{A};Q^{A}{}_{0})\,\psi^{B}{}^{*}(q^{B};Q^{B}{}_{0}) \tag{6}$$

with excitation (*) and likewise for the normal coordinates, $q_{\pm} = (1/2)^{1/2}\,(Q_A \pm Q_B)$. The Hamiltonian in dimensionless elements is given as

$$h = \begin{bmatrix} C + \frac{1}{2}\left(p_+^2 + q_+^2\right) + \frac{1}{2}\left(p_-^2 + q_-^2\right) + bq_- & bq_- \\ bq_- & -C + \frac{1}{2}\left(p_+^2 + q_+^2\right) + \frac{1}{2}\left(p_-^2 + q_-^2\right) + bq_+ \end{bmatrix} \tag{7}$$

where C=V_{AB}/ħω, and b=$(2\hbar\mu\omega^3)^{-1/2}$L with linear displacement LQ_i. The off-diagonal elements, bq_-, mix the lower diagonal block (S^-) with the upper block (S^+) to give the wavefunctions of the S_1 and S_2 states, respectively (the S_1/S_2 state order is reversed with a simple sign change on C). For a vibrational mode pair, $R, \bar{R}$, the eigenfunctions take the following simple forms:

$$\begin{aligned} S_l^{-}(R^m \bar{R}^n) &= \sum_{i=0,\,j=0(even)}^{n} c_{l-,i,j} \left|\Psi_l^{-}, R^i \bar{R}^j\right\rangle + \sum_{i=0,\,j=1(odd)}^{n} c_{l+,i,j} \left|\Psi_l^{+}, R^i \bar{R}^j\right\rangle \\ S_l^{+}(R^m \bar{R}^n) &= \sum_{i=0,\,j=1(odd)}^{n} c_{l-,i,j} \left|\Psi_l^{-}, R^i \bar{R}^j\right\rangle + \sum_{i=0,\,j=0(even)}^{n} c_{l+,i,j} \left|\Psi_l^{+}, R^i \bar{R}^j\right\rangle \end{aligned} \tag{8}$$

The observed excitonic splitting is:

$$\Delta = 2FV_{AB} \tag{9}$$

where F is the Franck-Condon quenching factor associated with the geometry change accompanying electronic excitation of each chromophore. Recently, the theory of vibronic coupling based on the Fulton Gouterman model of vibronic coupling has been extended to asymmetric multichromophores[41] and also reformulated in an adiabatic representation in the weak coupling limit that treats the excitonic splitting as a tunneling splitting.[47]

The spectroscopy of two multichromphores are the subject of this dissertation:: 1,2-diphenoxyethane, and [2,2,2]-paracyclophane. Chapters 5, 6, and 7 are concerned with the spectroscopy and modeling of 1,2-diphenoxyethane, a flexible bichromophore covalently linked by ether groups. Two monomer conformations were observed along with a single DPOE-$(H_2O)_1$ complex. In this manner, the effects of conformation and solvation on vibronic coupling were observed. Chapter 4 deals with the spectroscopy of a trichromophore, [2,2,2]-paracyclophane and a bichormophore analogue, 1,2-diphenylethane. Although the focus of chapter 4 is not necessarily placed on vibronic coupling, firm conformational assignments of the two molecules are provided.

1.2.3 Water Containing Clusters

As nature's solvent, water plays an intimate role in mediating conformational isomerization and reaction dynamics of biomolecule. Through the hydrophobic effect, water is considered to play a pivotal role in protein folding, laying the foundation between the structure and function relationship.[52-53] The solvent shell surrounding the solute is a complex network involving numerous hydrogen bonds, dictating the physical properties of the solute acting as either donor or acceptor. The effect of solvation on the

physical properties of the solute is difficult to untangle from the properties of the isolated solute. It is therefore desirable to devise strategies to simplify the complexity, starting from investigations of the isolated solute molecule and systematically building the solvent shell from the bottom-up, building the network through the addition of a single water molecule.[54] Keeping with this goal, a supersonic jet expansion affords researcher the opportunity to form water clusters in the cold environment through three-body collisions when water is co-expanded with the solute. Typically, the water molecule preferentially binds to the hydrogen bonding sites of the solute, although the cold environment provided by the expansion allows molecules to bind to areas where weaker interactions associated with π-hydrogen bonds and hydrophobic interactions are present. Implementing a time-of-flight mass spectrometer for the separation and detection of ionized clusters provides a size-selective methodology to studying the water clusters. Besides probing the interactions and spectroscopic signatures of the hydrogen bonded network through double-resonance infrared spectroscopy,[21] laser based techniques have been devised to shuttle water molecules between hydrogen bonding sites and dissociate the water molecules from the solute into various product channels on the potential energy surface.[55] Overall, by forming the water clusters in a supersonic jet expansion keen insights are gained into the perturbation and influence of water on the solute. Likewise, spectroscopists are able to study the influence of solute on the hydrogen bonding network of water molecules.

Chapters 7 and 8 deal with the effects of adding water to 1,2-diphenoxyethane (DPOE) (chapter 7) and [2.2.2]paracyclophane (tricyclophane, TCP) (chapter 8). For DPOE, the effect of adding a single water molecule on the vibronic coupling present

between the two ultraviolet chromophores is investigated. For TCP, water clusters (TCP-$(H_2O)_n$, n=1-5) are formed inside the hydrophobic binding pocket, with the water network taking on structures reminiscent of those taken up by benzene-$(H_2O)_n$ clusters.

1.3 References

1. Dean, J. C.; Buchanan, E. G.; Zwier, T. S. Mixed 14/16 Helices in the Gas Phase: Conformation-Specific Spectroscopy of Z-(Gly)(n), n=1, 3, 5. *Journal of the American Chemical Society* **2012,** *134* (41), 17186-17201.

2. Rijs, A. M.; Kabelac, M.; Abo-Riziq, A.; Hobza, P.; de Vries, M. S. Isolated Gramicidin Peptides Probed by IR Spectroscopy. *Chemphyschem* **2011,** *12* (10), 1816-1821.

3. Pirchi, M.; Ziv, G.; Riven, I.; Cohen, S. S.; Zohar, N.; Barak, Y.; Haran, G. Single-molecule fluorescence spectroscopy maps the folding landscape of a large protein. *Nat. Commun.* **2011,** *2*.

4. Rizzo, T. R.; Stearns, J. A.; Boyarkin, O. V. Spectroscopic studies of cold, gas-phase biomolecular ions. *International Reviews in Physical Chemistry* **2009,** *28* (3), 481-515.

5. Nagornova, N. S.; Rizzo, T. R.; Boyarkin, O. V. Highly Resolved Spectra of Gas-Phase Gramicidin S: A Benchmark for Peptide Structure Calculations. *Journal of the American Chemical Society* **2010,** *132* (12), 4040-+.

6. Hochstrasser, R. M. Two-dimensional spectroscopy at infrared and optical frequencies. *Proceedings of the National Academy of Sciences of the United States of America* **2007,** *104*, 14190-14196.

7. Decatur, S. M. Elucidation of residue-level structure and dynamics of polypeptides via isotopp-edited infrared spectroscopy. *Accounts of Chemical Research* **2006,** *39* (3), 169-175.

8. Barth, A.; Zscherp, C. What vibrations tell us about proteins. *Quarterly Reviews of Biophysics* **2002,** *35* (4), 369-430.

9. Engel, G. S.; Calhoun, T. R.; Read, E. L.; Ahn, T.-K.; Mancal, T.; Cheng, Y.-C.; Blankenship, R. E.; Fleming, G. R. Evidence for wavelike energy transfer through quantum coherence in photosynthetic systems. *Nature* **2007,** *446* (7137), 782-786.

10. Read, E. L.; Schlau-Cohen, G. S.; Engel, G. S.; Wen, J. Z.; Blankenship, R. E.; Fleming, G. R. Visualization of excitonic structure in the Fenna-Matthews-Olson photosynthetic complex by polarization-dependent two-dimensional electronic spectroscopy. *Biophysical Journal* **2008,** *95* (2), 847-856.

11. Zanni, M. T.; Hochstrasser, R. M. Two-dimensional infrared spectroscopy: a promising new method for the time resolution of structures. *Current Opinion in Structural Biology* **2001,** *11* (5), 516-522.

12. Buchner, G. S.; Murphy, R. D.; Buchete, N. V.; Kubelka, J. Dynamics of protein folding: Probing the kinetic network of folding-unfolding transitions with experiment and theory. *BBA-Proteins Proteomics* **2011,** *1814* (8), 1001-1020.

13. Zwier, T. S. Laser probes of conformational isomerization in flexible molecules and complexes. *Journal of Physical Chemistry A* **2006,** *110* (12), 4133-4150.

14. Powers, D. E.; Hopkins, J. B.; Smalley, R. E. Vibrational relaxation in jet-cooled phenylalkynes. *J. Chem. Phys.* **1981,** *74* (11), 5971-5976.

15. Hopkins, J. B.; Powers, D. E.; Smalley, R. E. Vibrational relaxation in jet-cooled alkylbenzenes. I. Absorption spectra. *J. Chem. Phys.* **1980,** *72* (9), 5039-5048.

16. Hopkins, J. B.; Powers, D. E.; Mukamel, S.; Smalley, R. E. Vibrational relaxation in jet-cooled alkylbenzenes. II. Fluorescence spectra. *J. Chem. Phys.* **1980,** *72* (9), 5049-5061.

17. Newby, J. J.; Muller, C. W.; Liu, C. P.; Zwier, T. S. Probing EIZ Isomerization on the C10H8 Potential Energy Surface with Ultraviolet Population Transfer Spectroscopy. *Journal of the American Chemical Society* **2010,** *132* (5), 1611-1620.

18. Morse, M. D. Supersonic Beam Sources. *Experimental Methods in the Physical Sciences* **1996,** *29*, 21-47.

19. Goyal, S.; Schutt, D. L.; Scoles, G. Molecular Solvation in Atomic Clusters Studied by Means of Molecular Beam Infrared Spectroscopy. *Acc. Chem. Res.* **1993,** *26*, 123-30.

20. Zwier, T. S. The spectroscopy of solvation in hydrogen-bonded aromatic clusters. *Annual Review of Physical Chemistry* **1996,** *47*, 205-241.

21. Zwier, T. S. Laser spectroscopy of jet-cooled biomolecules and their water-containing clusters: Water bridges and molecular conformation. *Journal of Physical Chemistry A* **2001,** *105* (39), 8827-8839.

22. Rizzo, T. R.; Park, Y. D.; Peteanu, L. A.; Levy, D. H. The electronic spectrum of the amino acid tryptophan in the gas phase. *J. Chem. Phys.* **1986,** *84* (5), 2534-41.

23. Rizzo, T. R.; Park, Y. D.; Levy, D. H. Dispersed fluorescence of jet-cooled tryptophan: Excited state conformers and intramolecular exciplex formation. *J. Chem. Phys.* **1986,** *85* (12), 6945-6951.

24. Brause, R.; Fricke, H.; Gerhards, M.; Weinkauf, R.; Kleinermanns, K. Double resonance spectroscopy of different conformers of the neurotransmitter amphetamine and its clusters with water. *Chemical Physics* **2006,** *327* (1), 43-53.

25. Macleod, N. A.; Simons, J. P. Infrared photodissociation spectroscopy of protonated neurotransmitters in the gas phase. *Mol. Phys.* **2006,** *104* (20-21), 3317-3328.

26. Macleod, N. A.; Simons, J. P. Neurotransmitters in the gas phase: Infrared spectroscopy and structure of protonated ethanolamine. *Physical Chemistry Chemical Physics* **2004,** *6* (10), 2821-2826.

27. Simons, J. P.; Jockusch, R. A.; Carcabal, P.; Hung, I.; Kroemer, R. T.; Macleod, N. A.; Snoek, L. C. Sugars in the gas phase. Spectroscopy, conformation, hydration, co-operativity and selectivity. *International Reviews in Physical Chemistry* **2005,** *24* (3-4), 489-531.

28. de Vries, M. S.; Hobza, P. Gas-phase spectroscopy of biomolecular building blocks. In *Annual Review of Physical Chemistry*, 2007; Vol. 58, pp 585-612.

29. James, W. H.; Baquero, E. E.; Choi, S. H.; Gellman, S. H.; Zwier, T. S. Laser Spectroscopy of Conformationally Constrained alpha/beta-Peptides: Ac-ACPC-Phe-NHMe and Ac-Phe-ACPC-NHMe. *Journal of Physical Chemistry A* **2010,** *114* (3), 1581-1591.

30. James III, W. H.; Baquero, E. E.; Shubert, V. A.; Choi, S. H.; Gellman, S. H.; Zwier, T. S. Single-Conformation and Diastereomer Specific Ultraviolet and Infrared Spectroscopy of Model Synthetic Foldamers: alpha/beta-Peptides. *Journal of the American Chemical Society* **2009,** *131* (18), 6574-6590.

31. Baquero, E. E.; James, W. H., III; Choi, S. H.; Gellman, S. H.; Zwier, T. S. Single-conformation ultraviolet and infrared spectroscopy of model synthetic foldamers: beta-peptides Ac-beta(3)-hPhe-NHMe and Ac-beta(3)-hTyr-NHMe. *Journal of the American Chemical Society* **2008,** *130* (14), 4784-4794.

32. James, W. H., III; Buchanan, E. G.; Mueller, C. W.; Dean, J. C.; Kosenkov, D.; Slipchenko, L. V.; Guo, L.; Reidenbach, A. G.; Gellman, S. H.; Zwier, T. S. Evolution of Amide Stacking in Larger gamma-Peptides: Triamide H-Bonded Cycles. *Journal of Physical Chemistry A* **2011,** *115* (47), 13783-13798.

33. James, W. H., III; Buchanan, E. G.; Guo, L.; Geman, S. H.; Zwier, T. S. Competition between Amide Stacking and Intramolecular H Bonds in gamma-Peptide Derivatives: Controlling Nearest-Neighbor Preferences. *Journal of Physical Chemistry A* **2011,** *115* (43), 11960-11970.

34. Kusaka, R.; Zhang, D.; Walsh, P. S.; Gord, J. R.; Fisher, B. F.; Gellman, S. H.; Zwier, T. S. Role of Ring-Constrained gamma-Amino Acid Residues in alpha/gamma-Peptide Folding: Single-Conformation UV and IR Spectroscopy. *Journal of Physical Chemistry A* **2013,** *117* (42), 10847-10862.

35. Walsh, P. S.; Kusaka, R.; Buchanan, E. G.; James, W. H.; Fisher, B. F.; Gellman, S. H.; Zwier, T. S. Cyclic Constraints on Conformational Flexibility in gamma-Peptides: Conformation Specific IR and UV Spectroscopy. *Journal of Physical Chemistry A* **2013,** *117* (47), 12350-12362.

36. James, W. H.; Muller, C. W.; Buchanan, E. G.; Nix, M. G. D.; Guo, L.; Roskop, L.; Gordon, M. S.; Slipchenko, L. V.; Gellman, S. H.; Zwier, T. S. Intramolecular Amide Stacking and Its Competition with Hydrogen Bonding in a Small Foldamer. *Journal of the American Chemical Society* **2009,** *131* (40), 14243-+.

37. Dian, B. C.; Florio, G. M.; Clarkson, J. R.; Longarte, A.; Zwier, T. S. Infrared-induced conformational isomerization and vibrational relaxation dynamics in melatonin and 5-methoxy-N-acetyl tryptophan methyl amide. *J. Chem. Phys.* **2004,** *120* (19), 9033-9046.

38. Clarkson, J. R.; Dian, B. C.; Moriggi, L.; DeFusco, A.; McCarthy, V.; Jordan, K. D.; Zwier, T. S. Direct measurement of the energy thresholds to conformational isomerization in Tryptamine: Experiment and theory. *J. Chem. Phys.* **2005,** *122* (21).

39. Zhao, Y.; Schultz, N. E.; Truhlar, D. G. Design of density functionals by combining the method of constraint satisfaction with parametrization for thermochemistry, thermochemical kinetics, and noncovalent interactions. *Journal of Chemical Theory and Computation* **2006,** *2* (2), 364-382.

40. Buchanan, E. G.; James, W. H.; Choi, S. H.; Guo, L.; Gellman, S. H.; Muller, C. W.; Zwier, T. S. Single-conformation infrared spectra of model peptides in the amide I and amide II regions: Experiment-based determination of local mode frequencies and inter-mode coupling. *J. Chem. Phys.* **2012,** *137* (9).

41. Nebgen, B.; Emmert, F. L., III; Slipchenko, L. V. Vibronic coupling in asymmetric bichromophores: Theory and application to diphenylmethane. *J. Chem. Phys.* **2012,** *137* (8).

42. Stearns, J. A.; Pillsbury, N. R.; Douglass, K. O.; Mueller, C. W.; Zwier, T. S.; Plusquellic, D. F. Rotationally resolved studies of S-0 and the exciton coupled S-1/S-2 origin regions of diphenylmethane and the d(12) isotopologue. *J. Chem. Phys.* **2008,** *129* (22).

43. Pillsbury, N. R.; Stearns, J. A.; Mueller, C. W.; Plusquellic, D. F.; Zwier, T. S. State-specific studies of internal mixing in a prototypical flexible bichromophore: Diphenylmethane. *J. Chem. Phys.* **2008,** *129* (11).

44. Pillsbury, N. R.; Muller, C. W.; Meerts, W. L.; Plusquellic, D. F.; Zwier, T. S. Conformational Effects on Excitonic Interactions in a Prototypical H-Bonded Bichromophore: Bis(2-hydroxyphenyl)methane. *Journal of Physical Chemistry A* **2009,** *113* (17), 5000-5012.

45. Ottiger, P.; Leutwyler, S.; Koeppel, H. S-1/S-2 excitonic splittings and vibronic coupling in the excited state of the jet-cooled 2-aminopyridine dimer. *J. Chem. Phys.* **2009,** *131* (20).

46. Ottiger, P.; Leutwyler, S. Excitonic splitting and coherent electronic energy transfer in the gas-phase benzoic acid dimer. *J. Chem. Phys.* **2012,** *137* (20).

47. Kopec, S.; Ottiger, P.; Leutwyler, S.; Koeppel, H. Vibrational quenching of excitonic splittings in H-bonded molecular dimers: Adiabatic description and effective mode approximation. *J. Chem. Phys.* **2012,** *137* (18).

48. Scholes, G. D. Long-range resonance energy transfer in molecular systems. *Annual Review of Physical Chemistry* **2003,** *54*, 57-87.

49. Ryu, I. S.; Dong, H.; Fleming, G. R. Role of Electronic-Vibrational Mixing in Enhancing Vibrational Coherences in the Ground Electronic States of Photosynthetic Bacterial Reaction Center. *The Journal of Physical Chemistry B* **2014,** *118* (5), 1381-1388.

50. Fulton, R. L.; Gouterman, M. VIBRONIC COUPLING .2. SPECTRA OF DIMERS. *J. Chem. Phys.* **1964,** *41* (8), 2280-&.

51. Fulton, R. L.; Gouterman, M. VIBRONIC COUPLING OF 2 ELECTRONIC STATES. *Spectrochimica Acta* **1961,** *17* (9-10), 1093-1093.

52. Privalov, P. L.; Makhatadze, G. I. CONTRIBUTION OF HYDRATION TO PROTEIN-FOLDING THERMODYNAMICS .2. THE ENTROPY AND GIBBS ENERGY OF HYDRATION. *Journal of Molecular Biology* **1993,** *232* (2), 660-679.

53. Makhatadze, G. I.; Privalov, P. L. CONTRIBUTION OF HYDRATION TO PROTEIN-FOLDING THERMODYNAMICS .1. THE ENTHALPY OF HYDRATION. *Journal of Molecular Biology* **1993,** *232* (2), 639-659.

54. Pribble, R. N.; Zwier, T. S. SIZE-SPECIFIC INFRARED-SPECTRA OF BENZENE-(H2O)(N) CLUSTERS (N=1 THROUGH 7) - EVIDENCE FOR NONCYCLIC (H2O)(N) STRUCTURES. *Science* **1994,** *265* (5168), 75-79.

55. Clarkson, J. R.; Baquero, E.; Shubert, V. A.; Myshakin, E. M.; Jordan, K. D.; Zwier, T. S. Laser-initiated shuttling of a water molecule between H-bonding sites. *Science* **2005,** *307* (5714), 1443-1446.

CHAPTER 2 METHODS

The techniques and instrumentation described in the following sections have been previously reported in detail.[1-3] Therefore, this chapter serves as a general description of the methodology used to obtain single-conformation spectra of flexible molecules in the complexity gap. Techniques unique to a particular experiment will be addressed further within the appropriate chapter. Likewise, computational details will be outlined in section 2.4 with unique calculations and theoretical models addressed where they have been employed.

2.1 Instrumentation

2.1.1 Supersonic Jet Expansion

A common feature between the experimental techniques discussed in the subsequent sections of this chapter lies in the formation of a supersonic jet expansion to collisionally cool molecules to low temperatures (~ 1 K).[4] The cold environment of a supersonic jet expansion has several distinct advantages, especially as implemented in laser spectroscopy. The technique affords researchers the ability to cool molecules to their vibrational zero-point level, effectively minimizing the spectral congestion due to hot bands and sequence bands, and collapses the total number of conformational minima

at room temperature to the lowest-energy structures with populations largely determined through kinetics as opposed to thermodynamics.[5] The kinetic determination of the final states of a molecule is an artifact of the expansion itself, rapidly cooling the molecules through collisions and isolating the molecules as the expansion proceeds and the density decreases. Without collisions, the molecules are unable to transfer heat, and the final states remain frozen until IR and UV excitation. In turn, single-conformation spectroscopy on isolated molecules is realized, providing a direct comparison to quantum mechanical optimizations and frequency calculations. The low internal temperatures permit researchers to study reactive species, transient complexes, neutrals, and ions from their vibrational zero-point levels.

To form the supersonic jet expansion, samples are typically heated to achieve a sufficient vapor pressure inside a stainless steel reservoir directly behind a pulsed solenoid valve (Parker General Valve, series 9). Molecules are entrained in a buffer gas (He, Ne, or Ar) with a stagnation pressure p_o between 20-40 psi. The mixture is expanded through a circular orifice with a diameter D of approximately 0.5 mm into a vacuum chamber. The total flow is regulated by a pulsed valve driver with a variable high voltage pulse duration and holding voltage. Normal flows are maintained between 2-10 standard cubic centimeters per minute (SCCM) with a fluctuations generally minimized below 10 percent.

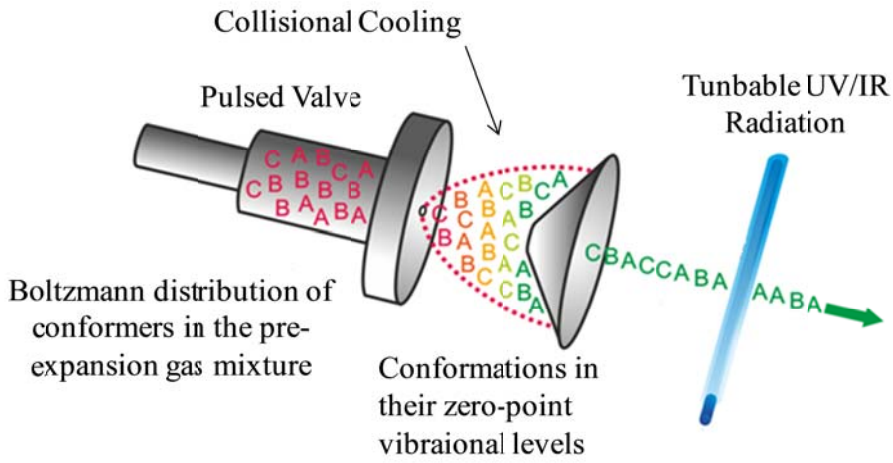

Figure 2.1 A schematic diagram of the pre-expansion mixture, pulsed solenoid valve, and skimmed supersonic jet expansion.

Behind the pulsed valve, a Boltzmann distribution of conformational isomers exists in the pre-expansion mixture. Expanding the mixture into the vacuum chamber creates a directed mass flow, dumping the enthalpy through collisions with the backing gas in the adiabatic isentropic expansion.[4] The expansion is considered supersonic when the local speed of sound is exceeded by the average flow velocity, occurring when the pressure ratio between the pre-expansion and vacuum chamber exceeds a factor of 2.1.[4] The total number of two-body collisions is proportional to p_oD while condensing molecules to form van der Waals complexes, the total number of three-body collisions is proportional to p_o^2D .[4]

Overall, the collision frequency is given by,[6]

$$2^{\frac{1}{2}} n_0 \sigma \upsilon_0 \left[1 + \frac{1}{2}(\gamma - 1) M_{eff}^{\ 2} \right]^{-\frac{1}{2}\left[\frac{(\gamma+1)}{\gamma-1}\right]} \quad (1)$$

Here, M_{eff} contains the information regarding the distance downstream. These collisions drain the internal energy stored within the vibrations and rotations of molecules to a vibrational temperature of ~15 K, a rotational temperature of ~2 K, and a translational temperature of ~1 K. In the idealized continuum model, this excess energy is converted to kinetic energy with the average terminal flow velocity determined by,[4]

$$v = M \sqrt{\frac{\gamma k T_0}{m}} \quad (2)$$

where M is the mach number, γ is the heat capacity ratio of the buffer gas (C_p/C_v= 1.67 for a monatomic), T_0 is the pre-expansion temperature, and m is the mass of the backing gas. A general schematic of the supersonic jet expansion is provided in figure 2.1.

2.1.2 Radiation Sources

Solid state, Q-switched Nd:YAG lasers are employed as a pump laser source to generate tunable infrared and ultraviolet radiation through an infrared parametric oscillator and dye laser respectively. The Q-switch optics, consisting of a quarter-wave plate, polarizer, and a quarter-wave Pockels cell produce nanosecond pulse durations at a repetition rate of 10 or 20 Hz. The Pockels cell modulates the polarization by a quarter-wave rotation upon excitation with approximately 4000 V DC. The voltage required to drive the nonlinear process is generated using a Marx bank consisting of parallel

capacitors isolated connected by solid state switches (IGBT or MOSFET). The bank of capacitors is charged by a 750 V power supply driven by a pulse-width modulated flyback circuit. The capacitors are discharged via an avalanche transistor, triggering the cascade of voltage down the length of the generator. The Pockels cell is triggered approximately 250 μsec after the flashlamp, corresponding to the excited state lifetime of the Nd:YAG doped rod. After the Q-switch opens, light oscillates between the Gaussian output coupler and rear mirror, completing approximately 10 round trips in 33 nsec. This duration is associated with the time required to saturate the gain and is termed the build-up time. The observed pulse width of the laser corresponds to the number of round trips required to remove the gain from the cavity after the build-up time. Pulse durations of approximately 5-7 nanoseconds are common. The laser is configured such that the polarization exiting the laser is horizontally polarized with a fundamental frequency of 9398 cm^{-1} (1064 nm) with a resolution of approximately 3 cm^{-1}. To increase the resolution of the pulsed Nd:YAG laser, a narrow line-width single mode cw source is seeded into the cavity of the host through the polarizer. The seed laser increases the gain efficiency in a particular cavity mode, decreasing the build-up time associated with the mode. Thus, through careful control of the frequency, temperature, and power, the build-up time may be minimized by controlling the cavity length of the host laser using a piezolelectric element attached to the rear mirror. To suppress spatial hole-burning, two additional quarter-wave rotators are placed before and after the Nd:YAG rod. The seed laser may be fiber optically delivered into the host (NP Photonics) or introduced through turning prisms (LightWave). Instructions outlining the procedure to replace the 50 mW 808 nm pump diode in a Lightwave seeder is provided in the appendix. The 532 nm light

may be passed through an etalon viewer to check for proper seeding. Interference fringes should be sharp and the frequency of the seed laser adjusted to maximize the distance between fringes.

A seeded Nd:YAG laser is used to pump an optical parametric converter to obtain tunable infrared radiation. The layout of the LaserVision optical parametric oscillator/amplifier (OPO/OPA) is shown in figure 2.2. To insure the pump pulse is collimated with an appropriate beam waist, the pump pulse passes through a Galilean telescope. After proper collimation, a 70/30 beam splitter directs 30% of the input towards the oscillator stage and 70% towards the amplifier. The pump power directed towards the oscillator and amplifier may be reduced by two separate attenuators. Before entering the oscillator, a KDP type II crystal converts the pump wavelength to 532 nm light through second harmonic generation. The 532 nm photons enter the oscillator through an input coupler, double passing the two KDP type II crystals with an output coupler and grating/tuning mirror assembly forming the cavity. Thus, the grating serves two purposes, both acting as the rear mirror and increasing the resolution of the output infrared radiation from the oscillator. A signal and idler wave are generated through critical phase matching with signal selected by the grating and, by convention, the higher frequency photon. Critical phase matching occurs through angle tuning the crystals in the horizontal plane, requiring the extraordinary photon to be horizontally polarized. The signal and residual 532 nm light are removed before the OPA allowing the idler wave to mix in the OPA stage with 70% of the input radiation. The input idler transforms as the output signal wave through amplification. The parametric process in the OPA stage is

identical to that of the OPO stage, however, no cavity is established. The result is tunable infrared radiation between 1.35 – 5.0 μm.

To extend the tunability of the laser, the output signal and idler are mixed in a $AgGaSe_2$ crystal through difference frequency mixing. Optical beam quality and collimation facilitate the success of mixing in the $AgGaSe_2$ crystal. To achieve the beam quality and collimation, a Dove prism (image inverter) is placed between the OPO and OPA stages. Instructions for installing the Dove prism are presented in figure 2.3. Briefly, the dove prism is rotated to center the 532 nm light on an iris placed before the OPA stage as in figure 2.3. The Dove prism is translated to center the 532 light far field. The process is iterated until the beam is centered at the iris and far field. The image inverter does not change the polarization of laser light from the OPO, but rotates the beam profile through total internal reflection by 90˚. The signal and idler from the OPA stage should be overlapped and propagated approximately 6 feet to expand the beam and smear the power density evenly throughout the beam profil. Unseeding the system will further increase the beam quality, but at the cost of resolution. The beam should create a faint burn on the back of Kodak Linograph paper.

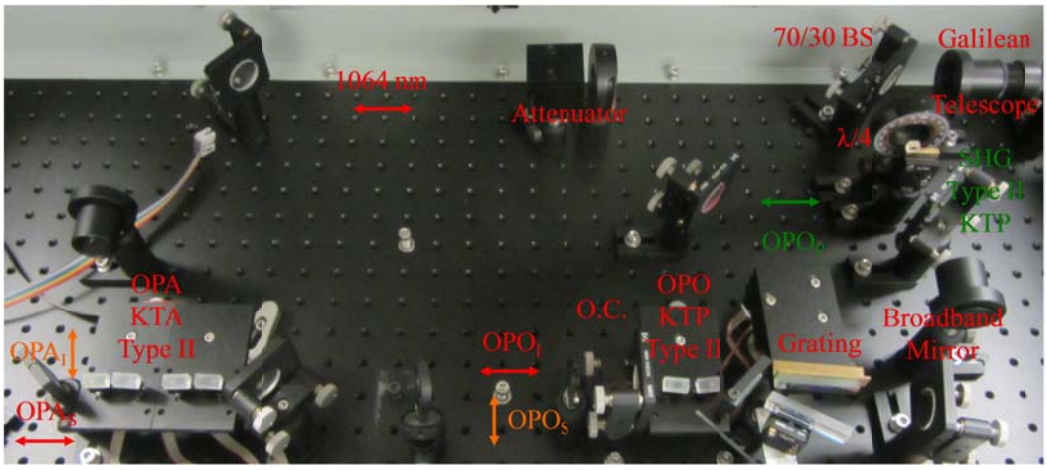

Figure 2.2 Tunable infrared radiation is obtained via an optical parametric oscillator and amplifier. The critical components are labeled and the polarization of light indicated by horizontal or vertical vectors.

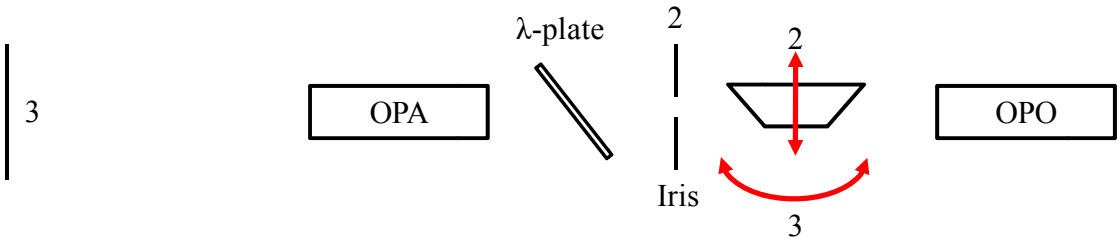

Figure 2.3 Installation of a Dove Prism between the OPO and OPA stage. The Dove prism is rotated and translated to minimize the beam walk.

To obtain tunable ultraviolet radiation, the second harmonic (532 nm) or third harmonic (355 nm) of the Nd:YAG laser is used to pump a dye laser. The dye lasers consist of an oscillator, pre-amplifier, and amplifier to produce visible laser radiation. A 2400 grooves/mm grating serves to select a wavelength from the spontaneous emission from the excited dye molecules with a resolution of 0.06 cm^{-1} at 580 nm. The visible

output is frequency doubled using a BBO crystal. The residual visible radiation is filtered using a Pellin Broca prism.

2.2 Spectroscopic Methods

2.2.1 Single-Resonance Spectroscopy

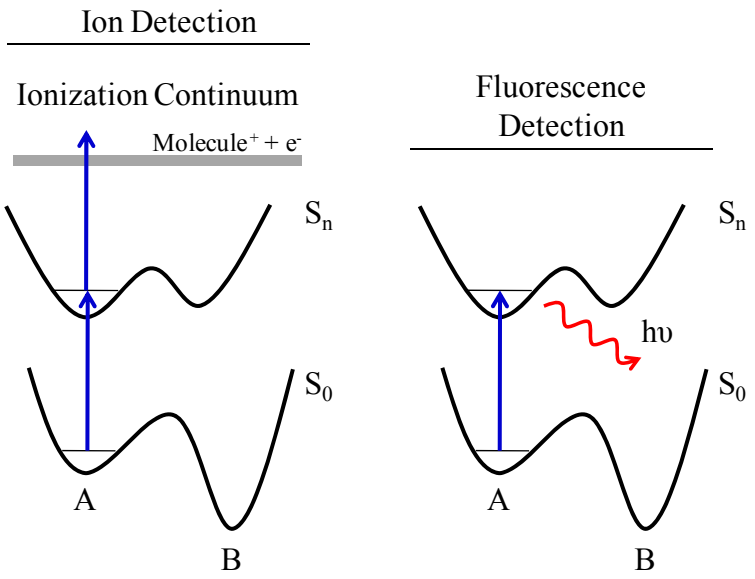

Figure 2.4 Energy level diagrams for resonant two-photon ionization (R2PI) and laser induced fluorescence (LIF), the two methods used to obtain the total electronic spectrum of all conformers present in the expansion.

2.2.1.1 Resonant Two-Photon Ionization

Resonant two-photon ionization (R2PI), coupled with a time-of-flight mass spectrometer (TOF), is a two photon process used to record the total electronic spectrum within a given mass channel. Here, the first photon is resonant with a vibronic transition

to an excited electronic state and the second photon ionizes the sample. The resulting cations are extracted orthogonally using a repeller plate (REP) and accelerated through the draw out grid (DOG). After traveling the one meter long flight tube, the cations impinge on a microchannel plate detector triggering a cascade of electrons to be ejected towards the anode of the detector. A resister converts the current into a voltage which is subsequently amplified by 25. The voltage is integrated using a digital oscilloscope. The source chamber is evacuated by a 1000 l/s turbomolecular pump (Pfeiffer) to a base pressure of approximately 10^{-7}mbar. The TOF tube is differentially pumped using a 200 l/s turbomolecular pump (Pfeiffer) to achieve a base pressure of approximately 10^{-8} mbar. The ion source is based on the Wiley-McLaren geometry (R.M. Jordan).[7] A schematic of the ionization chamber used in this work is show in figure 2.4.

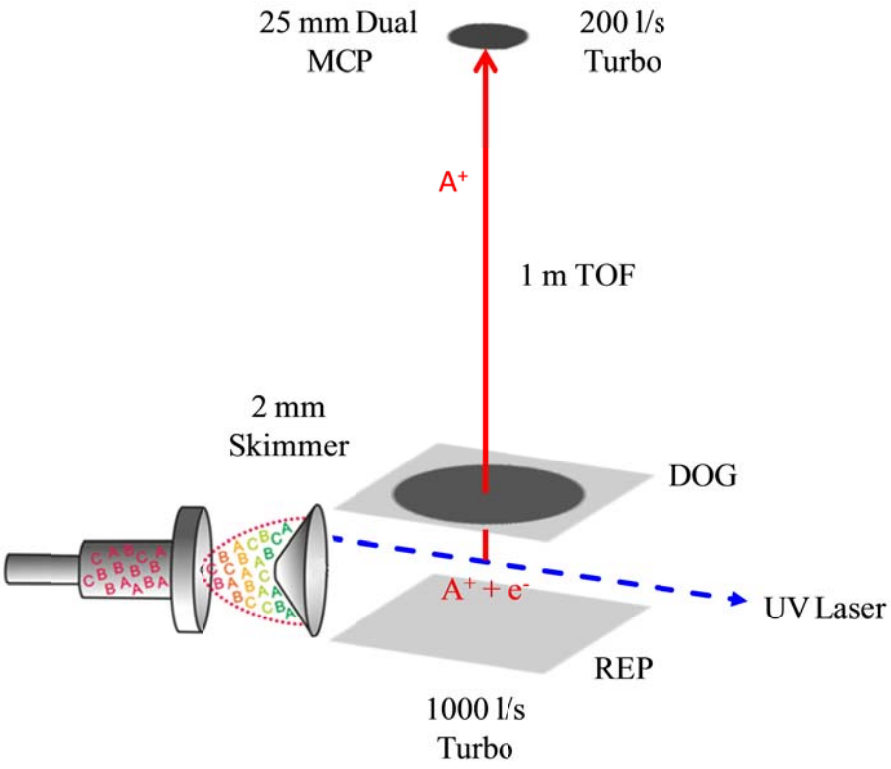

Figure 2.5 A schematic diagram outlining the skimmed, molecular beam, time-of-flight mass spectrometer used to acquire single-conformation spectra with mass resolution.

2.2.1.2 Laser Induced Fluorescence and Dispersed Fluorescence

An alternative approach for recording the total electronic spectrum for all species present in the supersonic jet expansion is laser induced fluorescence (LIF). The disadvantage of LIF comes from the lack of mass resolution. Therefore, it should be noted that the majority of studies pertaining to water clusters and thermally labile molecules have been carried out in ionization. Otherwise, the technique provides the same information with differences arising due to saturation in R2PI, ionization cross sections, and quantum yields. LIF is a single photon process which is resonant with a transition in an excited electronic state. To remove the excess energy, the excited

molecules fluoresce back to the ground state, provided alternative relaxation methods do not compete with the fluorescence process. The fluorescence is collected and imaged onto a photomultiplier tube by two spherical mirrors.[8] Alternative, the emission may be dispersed using a 0.75m monochromator and 2400 groove/mm grating with an adjustable slit width to image the fluorescence wavelength on an ICCD camera. In this manner, dispersed fluorescence provides information about the gound electronic state. The fluorescence chamber used to record LIF and DFL spectra is shown in figure 2.5.

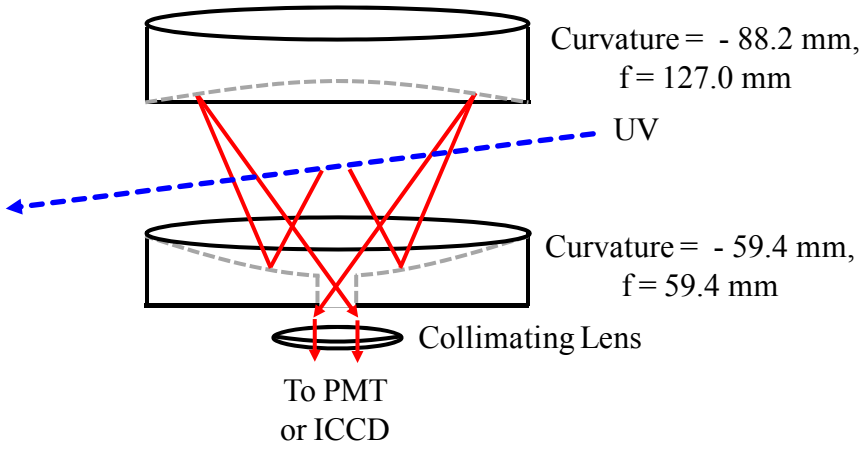

Figure 2.6 Collection optics used to record LIF spectra. The UV light enters the chamber through Brewster angle windows to minimize the amount of scattered light.

2.2.2 Double Resonance Spectroscopy

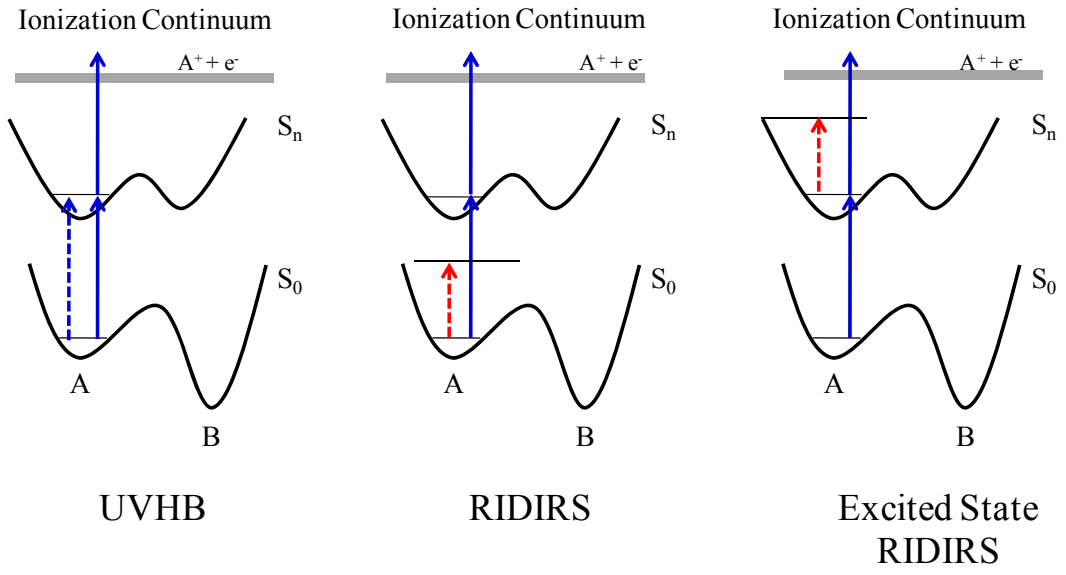

Figure 2.7 Energy level diagrams for conformation –specific, double-resonance experiments. The dotted line denotes the hole-burn laser while the solid arrow depicts the probe

2.2.2.1 Ultraviolet Hole-Burning

Ultraviolet hole-burning (UVHB) was employed to obtain the conformation-specific electronic spectrum. Here, a 10 Hz hole-burn laser is fixed on a transition due to a single conformation while a 20 Hz probe laser is tuned through the region of interest. The two lasers are spatially overlapped with the hole-burn laser preceding the probe by 200 ns. The fluorescence signal from the probe laser is monitored and processed through a gated integrator operated in active baseline subtraction mode. Whenever the probe laser is resonant with a transition which shares the same ground state as the hole-burn

laser, a depletion of the fluorescence or ion signal is observed. The energy level diagram for UVHB is shown in figure 2.6.

2.2.2.2 Infrared Spectroscopy

Fluorescence dip infrared spectroscopy or resonant ion-dip infrared spectroscopy is the analogous method used to obtain the conformation-specific ground state infrared spectrum. Here, a 20 Hz ultraviolet laser is fixed on a transition due to a single conformation and the output of a 10 Hz infrared optical parametric converter (LaserVision) is tuned through the region of interest. The two lasers are spatially overlapped and separated by 200 ns. The integrated signal is processed by a gated integrator operated in active baseline subtraction mode. Depletion in the total fluorescence or ion signal is observed whenever the infrared laser is resonant with a transition which shares the same ground state as the ultraviolet laser.

2.2.2.3 Excited State Infrared Spectroscopy

Infrared spectra in the excited electronic state (excited state RIDIR) were recorded using a two-color resonant two-photon ionization scheme in which the first UV laser is fixed on the UV transition of interest, with the second UV laser (550 nm) used for ionization temporally delayed by 30 ns from the first.[1] This temporal delay depends on the excited state lifetime of the molecule being studied. The 10 Hz IR laser was temporally positioned between the two UV laser pulses. Depletion in the 2-color ion signal was observed when the infrared laser was resonant with a vibrational transition in

the excited electronic state, consistent with reduced ionization efficiency for the vibrationally excited level reached with the IR pulse.

2.2.2.4 Infrared Population Transfer Spectroscopy

Infrared population transfer spectroscopy was used to determine the fractional abundance of conformational isomers in the supersonic jet expansion.[9-11] To do this, IRPT spectra were recorded while monitoring the downstream population of conformer 'i'. After proper normalization, I^i_{IRPT} is recorded as a fractional change in population of conformer 'i' as a function of IR wavenumber $\tilde{\nu}$. Since the total population of all conformers remains constant during the population transfer process, the factional abundance of each conformer 'i', F_i, may be determined from the weighted sum of the IRPT scans that is zero over the entire IRPT wavenumber scan

$$\Delta N_{Tot}(\tilde{\upsilon}) = 0 = \sum_{i=1}^{N} F_i I^i_{IRPT}(\tilde{\upsilon}) \qquad (3)$$

Here I^i_{IRPT} is the IRPT spectrum of conformer 'i', recorded as a fractional population change under identical conditions

IR-population transfer spectroscopy is used here to determine the fractional abundances of the two conformers of DPOE. To make this measurement, the UV laser is fixed on a transition due to a single conformer and positioned to intersect the supersonic free jet at x/D = 6, where x is the distance downstream of the nozzle orifice and D is the nozzle diameter. The infrared laser is positioned at an x/D = 2.5, upstream of the UV probe, and preceding the UV laser pulse by approximately 2 μs. In this manner,

conformers have experienced a sufficient number of collisions with the backing gas to cool to the vibrational zero-point level before infrared excitation; however, IR excitation occurs in a density regime where there are sufficient collisions following IR excitation to re-cool the vibrationally excited and conformationally mixed molecules back to the zero-point level before interrogation with the ultraviolet probe laser. Since IR excitation occurs to levels with energies above the barriers to isomerization, conformational isomerization can occur in competition with vibrational re-cooling. If an infrared transition due to conformer A is excited upstream in the expansion, population will be transferred out of A and into conformer B, leading to a net depletion in the population in A and gain in population in B. If an LIF transition due to A downstream, an IR depletion will be observed, while interrogation of B downstream will yield a gain at this same IR wavelength. IRPT scans are recorded with the IR operating at 10 Hz, and the UV laser at 20 Hz, using the active baseline subtraction mode of a gated integrator to record the difference in LIF signal from the UV laser with or without the IR present. Figure 2.7a represents the energy level diagram for mass-resolved infrared population transfer spectroscopy. A complete prescription for the IRPT experiment may be found elsewhere.[12]

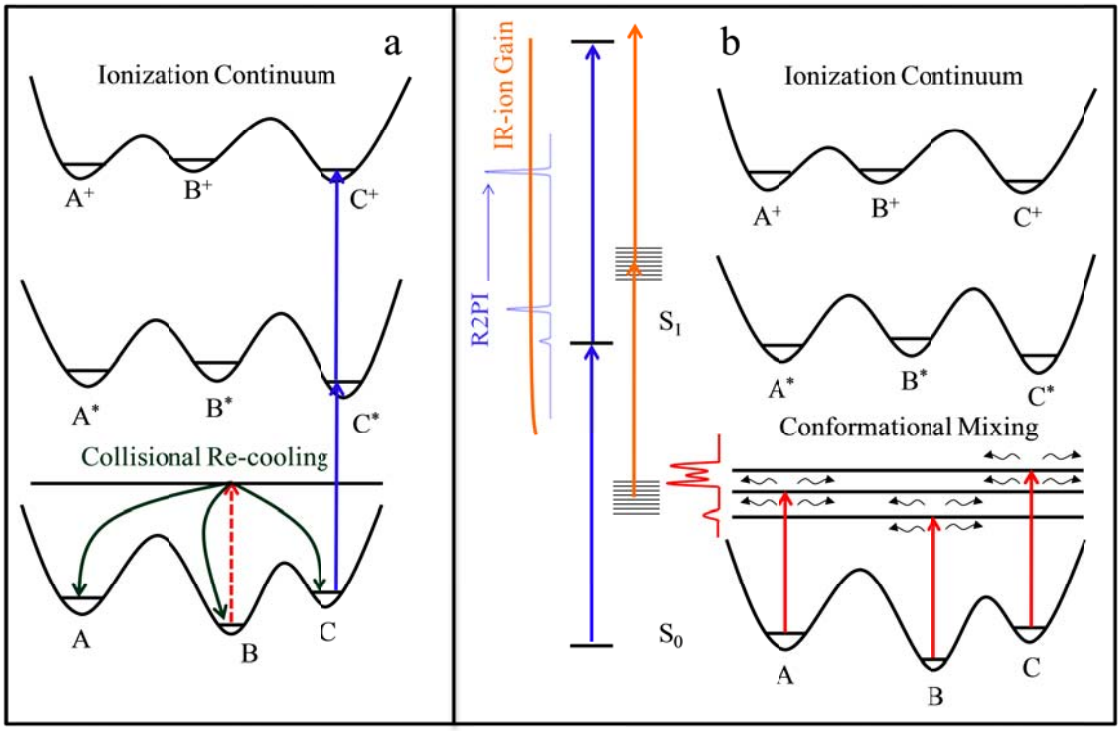

Figure 2.8 (a) The energy level diagrams for infrared population transfer spectroscopy and (b) infrared ion-gain spectroscopy. Under ideal conditions, the populations obtained are equivalent between the two techniques.

2.2.2.5 Infrared Ion-Gain Spectroscopy

A schematic diagram of infrared ion-gain (IRIG) spectroscopy[13] is shown in figure 2.7b. The method differs from RIDIR spectroscopy only in the choice of UV wavelength probed, which is positioned in IRIG spectroscopy at a wavelength to the red of the S_0-S_1 origin of all conformers. Thus, in the absence of the IR laser there is no ion signal in the molecular ion mass channel. The IR laser is tuned through the IR wavelength region of interest. Whenever an IR transition of any of the conformers is encountered, some fraction of the population of that conformer is promoted to a vibrationally excited state, creating a 'hot' conformer with internal energy equal to the

photon energy. Intramolecular vibrational redistribution (IVR) will distribute this energy amongst the vibrational degrees of freedom, which are dominated by low frequency modes, including those that lead to isomerization. If the IR photon is above the barrier(s) to isomerization, conformationally mixed states will be produced, some of which absorb at wavelengths red of the S_0-S_1 origin of the conformers. Tuning the IR produces an IR-induced gain spectrum $I^i_{IRIG}(\tilde{\upsilon})$ against zero background that has contributions from all IR absorbing species contributiong to the gain signal in the mass channel being monitored in the time-of-flight mass spectrum. Under favorable conditions, this gain spectrum is a population-weighted sum of the infrared spectra of all conformers present in the expansion

$$I_{IRIG}(\tilde{\upsilon}) = 0 = c\sum_{i=1}^{N} F_i \gamma_i I^i_{RIDIR}(\tilde{\upsilon}) \qquad (4)$$

where I^i_{RIDIR} is the RIDIR spectrum of conformer '*i*', plotted as a fractional depletion, γ_i is the detection efficiency of conformer '*i*' at the UV wavelength used for detection, and '*c*' is a scaling factor. If the detection efficiencies of the three conformers are equal, they can be subsumed into the scaling factor, and fractional abundances can be extracted from a best-fit of the IRIG scan. As with MRIRPT, the best-fit fractional abundances minimize the difference between the IRIG spectrum and this weighted sum, using RIDIR spectra recorded under identical expansion and laser conditions. Mass analysis minimizes potential contributions to the IR ion gain signal from IR absorptions due to impurities or molecular clusters. In cases where Franck–Condon activity is extensive, it can be difficult to be sure that all conformers of significance have been found. Given the comparative simplicity of the method, IRIG spectroscopy provides another tool that is

useful in part because it is not conformation-specific, and therefore can identify unique infrared absorptions that can signal the presence of other conformers.

The conditions under which γ_i is conformation-independent requires care and should follow three general criteria. First, the cold spectrum must have a relatively sharp onset, so that a probe wavelength can be found not too far to the red of the cold spectrum where IR-excited molecules can be detected against zero background. Second, the R2PI efficiency of all IR-excited conformers must be equal at the probe UV wavelength. If IR excitation is below the barrier(s) to isomerization, IR excitation must produce a ‘‘warm’’ UV spectrum of large breadth compared to the electronic frequency shifts separating the conformers. If there are large electronic frequency shifts between different conformers, one might be concerned that a given probe UV wavelength might favor conformers nearby in wavelength. More typically, as shown in figure 2.7b, IR excitation will exceed the barriers separating the conformers, with IVR producing conformationally mixed states independent of the conformer originally excited, as required. Third, there must be no fast non-radiative processes for the IR-excited molecules in the excited electronic state figure 2.7b, since this would prevent detection of the IR excited ion signal in the UV.

2.2.2.6 Infrared Photodissociation Hole-Filling

The potentially energy surfaces between bare monomer and water containing complexes vary drastically, as the water molecule perturbs the monomer conformations, sometimes stabilizing and destabilizing specific monomer motifs. By dissociating the water cluster with an infrared photon, the possibility of selectively forming a particular

isomer or a new isomer arises. Furthermore, when the binding energy approaches the energy provided by an infrared photon, researchers are afforded the ability to infrared excite above and below the dissociation energy leading to interesting product yields and rates.[14] The photodissociation experiments were performed under hole-filling conditions. Here, a 10 Hz IR laser was fixed on a unique transition of the water complex in the alkyl CH stretch and OH stretching regions. Certainly, the photodissociation experiments are not limited to the two frequency regimes. This allows for an interesting prospect of dissociating the cluster at or near threshold to photodissociation. To perform the experiments, the IR laser was temporally separated from the UV laser by approximately 1.8 μs and spatially positioned to be approximately 2 nozzle diameters downstream of the pulsed valve. This allows for both an initial cooling of the complex to the vibrational zero-point level and a re-cooling after IR excitation. If the energy of a single IR photon exceeds the binding energy of the complex, the water is dissociated, which proceeds to re-cool into the monomer population, or partially re-fills as the water complex. Tuning a 20 Hz laser through the S_0-S_1 region and processing the fluorescence or ion signal via active baseline subtraction produces gains in the monomer conformations and depletions in transition due to the water complex.

2.3 Computational Methods

Searching the potential energy surface for conformational minima requires a systematic exploration especially when the molecular size and complexity begets degrees of freedom and leads to innate differences between chemical intuition and physical reality. To perform this task, a molecular mechanics force field (MMFFs) as

implemented in the MACROMODEL[15] suite of programs searched the conformational landscape given a specific convergence and maximum energy. The gradient was optimized using 10,000 iterations, a convergence of 0.0001, and an energy window of 50.0 kJ/mol to aid in retrieving realistic starting structures. These structures were used as input geometries for quantum mechanical optimization and vibrational frequency calculations performed in Gaussian09.[16] Typically, the Truhlar hybrid meta exchange-correlation functional M052X-6-31+g(d)[17] was employed for optimizations given the necessity to incorporate dispersion interactions for energy stabilization. Harmonic vibrational frequencies were calculated at the same level of theory and used to compare experimental infrared spectra to the calculated structures. Structural isomers were assigned to experimental spectra based on the correspondence to the calculated spectra as well as the relative energy of the conformation.

2.4 References

1. Stearns, J. A. The Fate of Electronically Excited Molecules. **2005**, Dissertation.

2. Clarkson, J. R. Conformational Isomerization Dynamics of Flexible Molecules and Their Water Containing Complexes. **2006**, Dissertation.

3. James, W. H. Single-Conformational Spectroscopy in the Complexity Gap: Synthetic Foldamers. **2009**, Dissertation.

4. Morse, M. D. Supersonic Beam Sources. *Experimental Methods in the Physical Sciences* **1996,** *29*, 21-47.

5. Levy, D. H. Laser Spectroscopy of Cold Gas-Phase Molecules. *Annual Review of Physical Chemistry* **1980,** *31*, 197-225.

6. Lubman, D. M.; Rettner, C. T.; Zare, R. N. How Isolated Are Molecules in a Molecular-Beam. *Journal of Physical Chemistry* **1982,** *86* (7), 1129-1135.

7. Wiley, W. C.; McLaren, I. H. Time-of-Flight Mass Spectrometer with Improved Resolution. *Review of Scientific Instruments* **1955,** *26* (12), 1150-1157.

8. Plusquellic, D. F.; Davis, S. R.; Jahanmir, F. Probing nuclear quadrupole interactions in the rotationally resolved S-1 <- S-0 electronic spectrum of 2-chloronaphthalene. *J. Chem. Phys.* **2001,** *115* (1), 225-235.

9. Dian, B. C.; Longarte, A.; Winter, P. R.; Zwier, T. S. The dynamics of conformational isomerization in flexible biomolecules. I. Hole-filling spectroscopy of N-acetyl tryptophan methyl amide and N-acetyl tryptophan amide. *J. Chem. Phys.* **2004,** *120* (1), 133-147.

10. Dian, B. C.; Florio, G. M.; Clarkson, J. R.; Longarte, A.; Zwier, T. S. Infrared-induced conformational isomerization and vibrational relaxation dynamics in melatonin and 5-methoxy-N-acetyl tryptophan methyl amide. *J. Chem. Phys.* **2004,** *120* (19), 9033-9046.

11. James, W. H.; Muller, C. W.; Buchanan, E. G.; Nix, M. G. D.; Guo, L.; Roskop, L.; Gordon, M. S.; Slipchenko, L. V.; Gellman, S. H.; Zwier, T. S. Intramolecular Amide Stacking and Its Competition with Hydrogen Bonding in a Small Foldamer. *Journal of the American Chemical Society* **2009,** *131* (40), 14243-+.

12. Dian, B. C. The Spectroscopy and Dynamics of Flexible Biomolecules in the Gas Phase. 2003.

13. Buchanan, E. G.; James, W. H., III; Gutberlet, A.; Dean, J. C.; Guo, L.; Gellman, S. H.; Zwier, T. S. Single-conformation spectroscopy and population analysis of model gamma-peptides: New tests of amide stacking. *Faraday Discussions* **2011,** *150*, 209-226.

14. Clarkson, J. R.; Herbert, J. M.; Zwier, T. S. Infrared photodissociation of a water molecule from a flexible molecule-H2O complex: Rates and conformational product yields following XH stretch excitation. *J. Chem. Phys.* **2007,** *126* (13), 134306.

15. Mohamadi, F.; Richards, N. G. J.; Guida, W. C.; Liskamp, R.; Lipton, M.; Caufield, C.; Chang, G.; Hendrickson, T.; Still, W. C. Macromodel - an Integrated Software System for Modeling Organic and Bioorganic Molecules Using Molecular Mechanics. *Journal of Computational Chemistry* **1990,** *11* (4), 440-467.

16. Gaussian 09, R. A., Frisch, M. J.; Trucks, G. W.; Schlegel, H. B.; Scuseria, G. E.; Robb, M. A.; Cheeseman, J. R.; Scalmani, G.; Barone, V.; Mennucci, B.; Petersson, G. A.; Nakatsuji, H.; Caricato, M.; Li, X.; Hratchian, H. P.; Izmaylov, A. F.; Bloino, J.; Zheng, G.; Sonnenberg, J. L.; Hada, M.; Ehara, M.; Toyota, K.; Fukuda, R.; Hasegawa, J.; Ishida, M.; Nakajima, T.; Honda, Y.; Kitao, O.; Nakai, H.; Vreven, T.; Montgomery, Jr., J. A.; Peralta, J. E.; Ogliaro, F.; Bearpark, M.; Heyd, J. J.; Brothers, E.; Kudin, K. N.; Staroverov, V.N.; Kobayashi, R.; Normand, J.; Raghavachari, K.; Rendell, A.; Burant, J. C.; Iyengar, S. S.; Tomasi, J.; Cossi, M.; Rega, N.; Millam, N. J.; Klene, M.; Knox, J. E.; Cross, J. B.; Bakken, V.; Adamo, C.; Jaramillo, J.; Gomperts, R.; Stratmann, R. E.; Yazyev, O.; Austin, A.J.; Cammi, R.; Pomelli, C.; Ochterski, J. W.; Martin, R. L.; Morokuma, K.; Zakrzewski, V. G.; Voth, G. A.; Salvador, P.; Dannenberg, J. J.; Dapprich, S.; Daniels, A. D.; Farkas, Ö.; Foresman, J. B.; Ortiz, J.V.; Cioslowski, J.; Fox, D. J. Gaussian, Inc., Wallingford CT, 2009.

17. Zhao, Y.; Truhlar, D. G. Exploring the Limit of Accuracy of the Global Hybrid Meta Density Functional for Main-Group Thermochemistry, Kinetics, and Noncovalent Interactions. *Journal of Chemical Theory and Computation* **2008,** *4* (11), 1849-1868.

CHAPTER 3 SINGLE-CONFORMATION INFRARED SPECTRA OF MODEL PEPTIDES IN THE AMIDE I AND AMIDE II REGIONS: EXPERIMENT-BASED DETERMINATION OF LOCAL MODE FREQUENCIES AND INTER-MODE COUPLING

3.1 Introduction

Since amide groups are the fundamental linkage in the polypeptide backbone of proteins, IR probes of polypeptide and protein structure have often relied on changes in the amide group's characteristic vibrations to diagnose local and extended secondary structure.[1-3] The amide I region (~1600–1700 cm^{-1}) is especially valuable in this regard, since these modes are quite localized on the amide C=O group, and form a set of vibrations that is largely uncoupled from other vibrational modes. Furthermore, the amide I region is sensitive to the local H-bonding environments of the individual amide groups, whether as amide–amide H-bonds involved in the peptide's secondary structure or as H-bonds between the amide group and its aqueous environment. By comparison, the amide II region has received less attention, in part because the connection between the observed spectral distribution and key secondary structural elements is less clear and less diagnostic, though significant progress is being made.[4]

The recent explosion of interest in 2D IR spectroscopy has been fueled in part by its potential as a probe of polypeptide and protein structure and dynamics.[5-12] The congestion inherent to linear IR spectroscopy is mitigated by the expansion to two

dimensions, with off-diagonal peaks reflecting the coupling between modes, while probing structural changes occurring over a wide range of timescales.

In order to extract structural information from such data, it is necessary to test and refine theoretical models for the dependence of the amide vibrational frequencies and IR intensities on conformation. In large polypeptides, it is necessary to develop robust models which circumvent the need for full *ab initio* or density functional theory (DFT) calculations on the molecule as a whole. To that end, several groups have contributed to the development and refinement of methods for predicting the amide I linear and 2D spectra of simple amides and larger polypeptides.[2, 13-26] A starting point for much of this work is the notion that the amide I and amide II normal modes can be treated as separate sets of coupled local modes on the individual amide groups that are uncoupled from all other vibrations. Under the general framework of the floating oscillator model,[27] a variety of one-exciton and two-exciton Hamiltonian schemes have been developed that make it possible to build vibrational exciton Hamiltonians either separately from local amide I or amide II modes and their corresponding coupling constants, or jointly from both sets of local modes. In this local-to-normal mode approach, diagonalization of the vibrational exciton Hamiltonian yields molecular amide I and/or amide II normal mode frequencies and IR intensities that can be directly compared with experimental spectra. Alternatively, a variety of analytical, normal-to-local mode schemes have been developed that make it possible to extract local mode frequencies and coupling constants from calculated amide I and amide II normal modes and frequencies.[28-30] These methods provide *ab initio* or DFT based local mode frequencies and coupling constants that are a function of peptide conformation and that can either be used directly as predictive

ingredients of local-to-normal mode vibrational exciton Hamiltonian schemes or that can be used indirectly as standards for calibrating parameterized electrostatic models.

To date, essentially all of the experimental tests of these theoretical models have been based on 1D and 2D IR data of amides and polypeptides at room temperature in aqueous solution, with spectra influenced by the contributions from multiple conformations and the strong interactions with water.[9-17] While such conditions correctly meet the final intended goal, there is clearly room for other kinds of tests that more directly probe the fundamental input to the theoretical models. In particular, spectra of isolated peptides in the amide I and amide II regions test the ability of the theoretical models to correctly incorporate the intramolecular effects in the absence of solvent. Since current theoretical models are additive in nature,[13, 15-18, 20-21, 25-26, 31] the spectra of single-conformations of isolated molecules are ideally suited to provide rigorous tests of the intramolecular contributions to the amide I and amide II spectra, both the dominant electrostatic terms, and their future refinement with contributions from covalent, dispersive, and charge transfer interactions.

Motivated by this need for direct, single-conformation spectroscopic tests of electrostatic models, we present here infrared spectra of a series of model methyl-capped di- and tri-amides in the amide I and amide II regions, recorded under jet-cooled conditions in the gas phase, where single-conformation spectroscopy is possible. The structures of the molecules included in the present work are shown in figure 3.1. A total of 34 conformations from 11 molecules are included in the present test set. Nine molecules have been the subjects of previous single-conformation infrared and ultraviolet studies, including α–peptide,[32] β-peptide,[33-34] α/β-peptide,[35-36] and γ-peptide[37-38]

foldamers, while the remaining two are close analogs of α–peptides previously studied by Mons and co-workers.[39-40] Two of the α/β–peptides come in diastereomeric pairs differing in the chirality of a single chiral center. In all cases, the amide NH stretch region served as primary probe of the H-bonding structures formed.

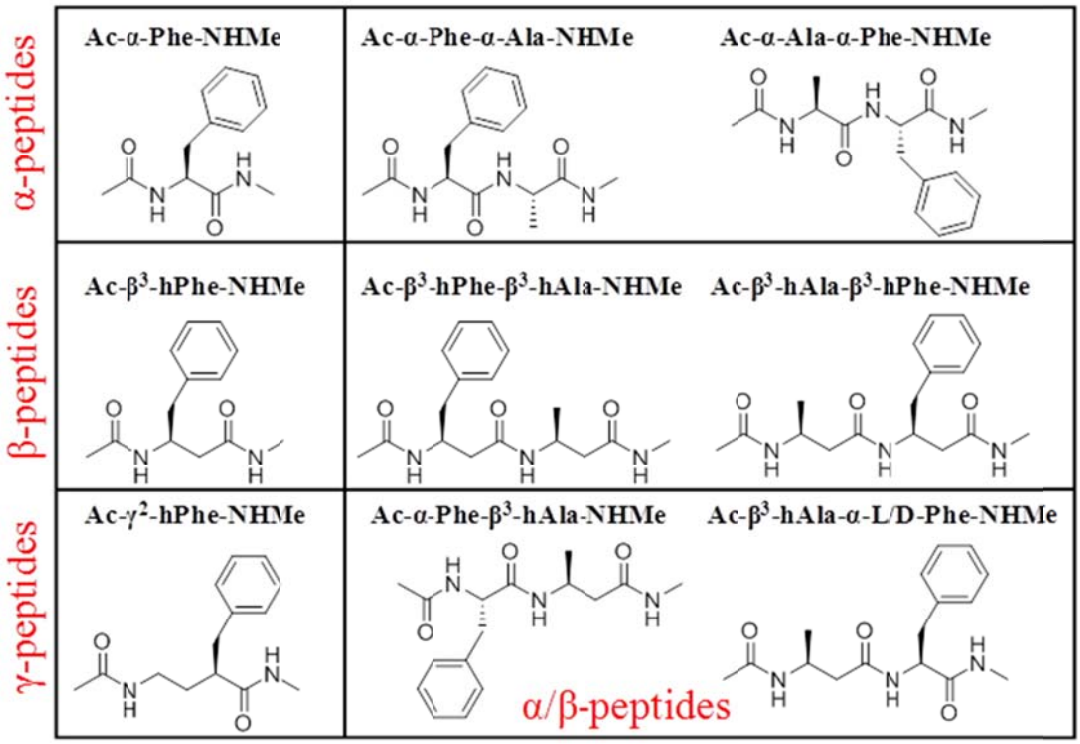

Figure 3.1 Chemical structures of the test set of molecules used in this study. The α/β-peptides include two diastereomers of Ac-β3-hAla-a-Phe-NHMe differing in the chirality of C(a) in the a-peptide subunit. Three constrained α/β-peptides with structures Ac-L-Phe-ACPC-NHMe (αLβACPC), Ac-ACPC-L-Phe-NHMe (βACPCαL) , and Ac-ACPC-D-Phe-NHMe (βACPCαD) are not shown explicitly, since many of the observed conformers have close analogs in the unconstrained α/β-peptides.

Armed with this single-conformation data and assignments based on the amide NH stretch region, we here extend this data on the synthetic foldamers into the amide I

and amide II regions, and supplement it with corresponding spectra on the three model α-peptides. In all cases, the molecules are doubly methyl-capped at both N-terminal and C-terminal ends, as is often done to better mimic local H-bonding preferences present in larger peptides and to remove perturbations in the amide II region caused by the NH_2 group. The three α-peptides were included in the test set because current theoretical models of the amide I and amide II regions focus attention primarily on the α-peptides that make up naturally occurring proteins.

By studying a series of α-, β-, α/β- and γ-peptides, the effects of changing the through-bond distance between the amide groups are probed, as are the accompanying changes brought on by the changed spacing and added flexibility on the relative distance and orientation of H-bonded amide groups. Among the structures probed are single H-bonded rings varying in size from five-membered (C5) to eleven-membered (C11), several sequential double rings (C5/C6, C6/C5, C6/C6, C7/C7, C8/C7), bifurcated double rings (C5/C7, C5/C8), and a unique non H-bonded "amide stacked" γ-peptide structure.

In the present paper we follow a normal-to-local mode approach to determine experimentally based, conformer-specific amide I and amide II local site frequencies, and amide I/I and amide II/II coupling constants, proceeding in four steps.

First, we establish that scaled harmonic vibrational frequency calculations on the optimized structures at the DFT M05-2X/6-31+G(d) level of theory, which faithfully reproduce the NH stretch region, do equally well in the amide I and amide II regions. Second, we apply Cho's Hessian reconstruction (HR) method[13] to our DFT M05-2X harmonic frequency calculations to extract local amide I frequencies and amide I/I

coupling constants. These local amide I frequencies are shown to be in excellent agreement with harmonic, local amide I frequencies obtained from DFT M05-2X/6-31+G(d) calculations on $^{13}C=^{18}O$ substituted isotopologues. This protocol thus places both the uncoupled amide I local mode frequencies and the amide I/I intermode coupling constants on a firm experimental foundation.

Third, potential energy distribution (PED)[41-42] analysis in the amide I region is combined with Hessian reconstruction to check the robustness of the predictions to this alternative means for generating local amide I frequencies and amide I/I coupling constants. We then apply the combined PED/HR scheme to the amide II region, including both NH bend and CN stretch local mode contributions in the PED analysis of the amide II normal modes. Through comparison with local amide II frequencies obtained from DFT M05-2X/6-31+G(d) calculations on N–D substituted isotopologues it is shown that the combined PED/HR scheme provides a reliable way to extract local amide II frequencies and the amide II/II coupling constants from the single-conformation spectral data.

Finally, armed with this experimentally based test set of reduced-dimension Hessian matrices in the amide I and amide II regions, we use these results to probe the physical mechanisms responsible for determining the local site frequencies and nearest- and next-nearest-neighbor couplings, which could in principle have contributions from couplings acting through chemical bonds, H-bonds, or electrostatically through-space. As we shall see, the data set and analysis provide strong evidence that the coupling constants are characteristic of the type of NH···O=C H-bond in which the C=O group (amide I) or NH group (amide II) are involved.

3.2 Methods

3.2.1 Synthetic Methods

Ac-α-Phe-NHMe was purchased from Bachem (E-1170) and used without further purification. Ac-α-Phe-α-Ala-NHMe and Ac-α-Ala-α-Phe-NHMe were synthesized at Purdue University using standard synthetic methods. The synthetic foldamers were synthesized at the University of Wisconsin-Madison using methods previously published.[33-38]

3.2.2 Computational Methods

3.2.2.1 Conformational Assignments and Comparison to DFT Methods

The conformational assignments presented here have been made previously[33-38] through comparison of the experimental NH stretch RIDIR spectra with the predictions of calculations using a well-defined screening process. Specifically, the possible conformational minima of each molecule were identified from an exhaustive search of the potential energy surface using molecular force field conformational searching algorithms (e.g., Amber, MMFFs) contained in the Macromodel suite of programs.[43] An energy filter of 25 kJ/mol was applied to the output of each search and the resultant structures were submitted to DFT B3LYP/6-31+G(d) geometry optimizations[44] and harmonic vibrational frequency calculations. The structures were assigned to various H-bonding conformational families to look for trends in the predicted conformational preferences. Upon completion of calculations at the B3LYP level of theory, another

energy filter, 20 kJ/mol, was applied to the output structures. The structures which survived the energy filter were re-optimized at the DFT M05-2X/6-31+G(d) level, a hybrid meta exchange-correlation functional developed by Truhlar's group for noncovalent interactions that has seen increasing use in cases where dispersion interactions are key to energetic stabilization.[45-46] DFT M05-2X/6-31+G(d) harmonic vibrational frequencies are then calculated, scaled, and compared to the experimental single-conformation IR spectra. An extensive investigation of the accuracy of various levels of theory for the prediction of conformational energies and vibrational frequencies by Rothlisberger and co-workers[47] found DFT M05-2X/6-31+G(d) to be among the best current methods for the purpose, a result confirmed by the present study. This comparison between experiment and theory led to firm conformational assignments of the conformational family type of all conformers, and in the cases used for the primary test set also to specific conformations within a given family type (e.g., with a specific phenylalanine side chain position). All DFT calculations were carried out using the Gaussian software package.[48-49] The DFT M05-2X/6-31+G(d) calculations employed tight scf convergence criteria and an ultrafine grid. Final comparison between experiment and theory were made by obtaining best-fit scale factors for each spectrum that minimized the sum of the squares of the differences between the experimental and calculated wavenumber positions. The average best-fit scale factors were 0.9578±0.0026 for the amide I vibrations, and 0.9538±0.0041 for the amide II vibrations.

3.2.2.2 Hessian Reconstruction and PED Analysis

The program to execute the Hessian reconstruction and PED analysis was developed and implemented by Christian Müller at the Ruhr University Bochum. One of the principal goals of our analysis of the single-conformation infrared spectra in the amide I and amide II regions is extracting from the spectra experimentally tested local site frequencies as well as nearest-neighbor and next-nearest-neighbor coupling constants. Since, after appropriate scaling, the DFT M05-2X/6-31+G(d) calculations match the experimental frequencies and intensities satisfactorily, the calculated amide I and amide II normal modes can be submitted to Hessian reconstruction, a normal-to-local mode scheme that treats the amide I and amide II vibrations as linear combinations of localized vibrations on each of the amide groups.

For the amide I region, we used the original Hessian reconstruction scheme developed by Cho and co-workers.[13] A description of our implementation of this method, which has the advantage of being a generalization of the original scheme to peptides with more than three amide groups, can be found in the appendix.[50]

As a check that the uncoupled frequencies were properly extracted by this procedure, the assigned structures were submitted to a series of isotopic substitutions that completely decoupled the amide I vibration of each of the amide groups in the structure, one at a time. These calculations employed the assigned, optimized structure for a given conformation, but isolated a single carbonyl group by retaining its isotopic composition ($^{12}C=^{16}O$), but substituting $^{13}C=^{18}O$ at each of the other positions in the structure. This completely localized the amide I vibration of the $^{12}C=^{16}O$ group, so that DFT

M05-2X/6-31+G(d) vibrational frequency calculations gave its uncoupled harmonic frequency. The mean absolute error between the local amide I frequencies obtained through Hessian reconstruction and those obtained through isotopic substitution is 0.56 cm^{-1}, while the percentage error relative to the mean of the amide I frequencies obtained by isotopic substitution is 0.03%. This close agreement provides corroborating evidence that the Hessian reconstruction method can yield reliable amide I local mode frequencies. Taking, additionally, the agreement of the DFT M05-2X/6-31+G(d) amide I normal mode frequencies with the experimental amide I frequencies into account, we conclude that Hessian reconstruction can be used to extract not only reliable amide I local mode frequencies, but also reliable, experiment-based amide I/I coupling constants.

As an alternative and straightforward normal-to-local mode method, we developed a modified Hessian reconstruction scheme in which the matrix elements of the **U** matrix are determined from potential energy distribution (PED)[41-42] analysis of the normal modes. The advantage of this combined PED/HR scheme is that it requires, just as the original HR method, only *ab initio* or DFT harmonic frequencies and Cartesian normal mode displacements for the most abundant $^{12}C=^{16}O$ isotopologue of each conformer. PED analysis of the normal modes was carried out with the VEDA4 program developed by Jamróz.[51] Special care was taken that the C=O stretch internal coordinates do not mix with each other or with the NH bend and CN stretch internal coordinates that are the main constituents of the amide II normal modes. The $\mathbf{U}^{PED}$ matrix elements were calculated as the square roots of the corresponding PED percentages, while the signs of each eigenvector element of the $\mathbf{U}^{PED}$ matrix were visually determined from the C=O stretch phases in the corresponding amide I normal mode. The eigenvectors (columns) of

the $\mathbf{U}^{PED}$ matrices were normalized, and, finally, the $\mathbf{U}^{PED}$ matrices were orthonormalized according to the procedure described in the Appendix.[50] The agreement between the original $\mathbf{U}^{PED}$ matrices and their orthonormalized counterparts $\mathbf{U}^{PED(p)}$ is excellent, the mean absolute error between their matrix elements being only $6.3 \cdot 10^{-3}$. More importantly, the agreement with the orthonormal Hessian reconstruction $\mathbf{U}^{(p)}$ matrices is also very good, the mean absolute error between the $\mathbf{U}^{PED(p)}$ and $\mathbf{U}^{(p)}$ matrix elements being only $8.83 \cdot 10^{-3}$, giving rise to mean absolute errors between the local amide I frequencies of $6.7 \cdot 10^{-2}$ cm^{-1} and between the amide I/I coupling constants of 0.33 cm^{-1}. The close agreement between the direct HR and the combined PED/HR schemes as well as their accuracy in reproducing the local amide I frequencies obtained through $^{13}C=^{18}O$ isotopic substitution is a consequence of the high degree of localization of the amide I normal modes on the C=O stretch internal coordinates. PED analysis yields a localization of (79±2)%, i.e. only 21% of the amide I normal mode displacements are distributed over internal coordinates (stretches, bends and torsions) other than the C=O stretch coordinates. This result quantitatively corroborates the fact that amide I normal modes can be accurately described as linear combinations of mainly C=O stretch vibrations. Consequently, it can be concluded that the PED/HR scheme provides a reliable alternative way of determining local amide I frequencies and amide I/I coupling constants.

Encouraged by the results of the combined PED/HR scheme in the amide I region, we extended our analysis into the amide II region. Since, however, our PED results on the localization of the amide II normal modes on a combination of amide NH bend and CN stretch coordinates yield a value of (72±5)%, i.e. a somewhat lower value with a

greater spread than in the amide I region, we do not expect the agreement between **U** matrices, local site frequencies and coupling constants to be of the same quality as in the amide I region. Accordingly, the mean absolute error between the matrix elements $U_{\alpha j}^{PED}$ and $U_{\alpha j}^{PED(p)}$ is $1.16 \cdot 10^{-2}$ in the amide II region, the percentage error relative to the mean of the absolute values $|U_{\alpha j}^{PED(p)}|$ is 2.4%.

As a check that reliable amide II frequencies were extracted by this PED/HR procedure, a series of calculations for each conformer was carried out in which all but one of the amide groups were deuterated (N–D). This lowers the amide II vibrational frequencies of the deuterated amide groups[52] by ~100 cm^{-1}, an amount sufficient to localize the remaining amide II vibration. The agreement between the local amide II frequencies obtained through PED/HR analysis and those obtained via isotopic substitution is very good, yielding a mean absolute error of 1.0 cm^{-1}, approximately twice the error in the amide I region. This agreement, however, can be deemed sufficiently high to render the PED/HR scheme a reliable way for obtaining both experiment-based amide II local mode frequencies and amide II/II coupling constants.

Finally, with the eigenvector matrices $\mathbf{U}^{(p)}$ in the amide I region and $\mathbf{U}^{PED(p)}$ in the amide II region in hand, we calculated amide I and amide II normal mode intensities, which we directly compare to the experimental intensities in figures 3.3–3.**7** (b, in blue). It has to be noted, however, that these intensity calculations have to be considered rather as a joint consistency check of both the eigenvector matrices **U** determined through Hessian reconstruction and the dipole derivatives, $\partial\boldsymbol{\mu}^{(I)}/\partial Q_\alpha$ and $\partial\boldsymbol{\mu}^{(II)}/\partial Q_\alpha$, determined via isotopic substitution. An independent way of determining amide I and amide II

transition dipole moment vectors that obviates calculations on $^{13}C=^{18}O$ and N–D isotopologues is preferable, however unachievable without further assumptions.

3.3 Results and Analysis

The single-conformation data set in the amide I and amide II region includes spectra from seven conformations of three α-peptides: C5(a), C7(a), and C7(g+) of Ac-Phe-NHMe, C5/C7(a) in Ac-Phe-Ala-NHMe, and C7/C7(g−) and two forms of C10(g+), differing in the C10 dihedral angles, in Ac-Ala-Phe-NHMe. We include here R2PI spectra of the three molecules (figure 3.2), with the transitions used as monitor transitions for the RIDIR spectra and conformational assignments labeled on the spectra. The two capped triamides have not been studied previously, but are close analogs of molecules studied by Chin et al.,[39-40] while the capped diamide was the subject of a previous study by Gerhards et al.[32] It is worth noting that the positions of the S_0–S_1 origins in the R2PI spectra of Ac-Ala-Phe-NHMe were sufficiently different from their counterparts in the work of Chin et al.[39-40] on Ac-Ala-Phe-NH_2 that NH stretch spectra were taken to confirm their assignments to the indicated conformations. These S_0–S_1 origin transitions were used as monitor wavelengths to record conformation-specific amide I and amide II spectra. The reader is referred to earlier papers from our group for R2PI spectra and amide NH stretch RIDIR spectra of the β-peptides[33-34] α/β-peptides,[35-36] and γ-peptide[37-38]. A table connecting the letter labels used in this work with the structures in the test set is in included in the appendix.[50]

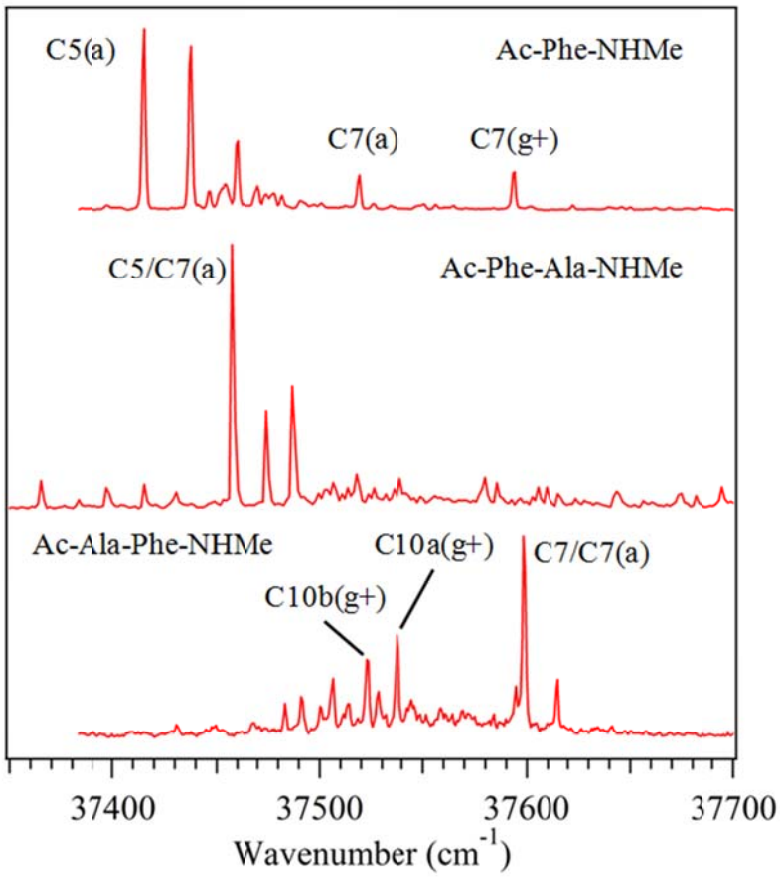

Figure 3.2 Resonant two-photon ionization spectra of the three a-peptides studied in this work: (a) Ac-α-Phe-NHMe, (b) Ac-α-Phe-α-Ala-NHMe, and (c) Ac-α-Ala-α-Phe-NHMe. Transitions assigned to the indicated structures, used as monitor transitions for RIDIR spectra, are labeled in the figure.

Overview RIDIR spectra of the 21 conformers in our primary test set are presented in figures 3.3–3.7, encompassing the amide I and amide II regions (1450–1750 cm^{-1}). These spectra are divided up into conformers containing small single rings (figure 3.3, C5, C6, C7), large single rings (figure 3.4, C9, C10, and C11), sequential double rings (figure 3.5, C5/C6, C6/C6, C6/C5, and C7/C7 and figure 3.6, four unique C8/C7), bifurcated double rings (figure 3.7A,B, C5/C7 and C5/C8), and the amide-

stacked conformer of Ac-γ^2-hPhe-NHMe (figure 3.7C). The stick diagrams below each experimental spectrum give the predictions of DFT M05-2X/6-31+G(d) calculations (a, in black), suitably scaled to best match experiment. Analogous results at the DFT B3LYP/6-31+G(d) level of theory (not shown) in most cases give similarly good predictions for the infrared spectra as M05-2X, with the latter giving better relative conformational energies. The amide II region of Ac-Ala-Phe-NHMe (figure 3.5D) was not recorded for lack of sufficient sample.

The remaining thirteen structures in the full 34 conformation data set are not included explicitly here. For some structural family types, there were several examples of a given conformational family type that differ in the dihedral angles of the H-bonded rings that comprise the peptide backbone. In most circumstances, only one example of each type is included. This is most notably the case in the set of C8/C7 structures in figure 3.6, in which four different types of C8 rings are represented (C8a–d). These rings differ in the dihedral angles along the β-peptide chain, with (ϕ,μ,ψ) angles of (−70,+133,−68) for C8a, (−113,+64,+9) for C8b, (−109,+63,+17) for C8b', (+54,+47,−104) for C8c, and (−59,−44,+101) for C8d. Notice that the C8b and C8b' rings are nearly identical apart from a small change in ψ, while C8c and C8d are close to mirror images of one another.

In other cases, there were additional conformations that were nearly identical to another member of the test set (e.g., comparing spectra of α/β-peptides with and without an ACPC ring in the β-peptide backbone). Their close correspondence with a member of

the test set is a testimony to the reproducibility and characteristic spectral signatures of the various members of the test set.

Of the amide I/II spectra in the figures, only those of the conformers of Ac-Phe-NHMe, Ac-γ^2-hPhe-NHMe (amide I only), and conformer A of Ac-β-ACPC-Phe-NHMe were reported previously.[35]

There are several conformers[33-38] for which the assignment to particular structures is less secure. For this reason, the spectra are not included in the test set. These spectra are good subjects for further investigation both by theory and experiment, since assignments to a given conformational family are sometimes quite firm based on the amide NH stretch region.

Figures 3.3–3.7 also include stick spectra (b, in blue) that show the results of the HR analysis (amide I region) and the PED/HR analysis (amide II region) performed on the assigned structures and combined with local amide I/amide II transition dipole derivatives obtained from the calculations on the $^{13}C=^{18}O$ and N–D isotopologues, respectively. These spectra are in every case essentially identical to the full normal mode calculations from the DFT M05-2X calculations (a, in black). This provides strong evidence that the reduced-dimension HR and PED/HR approaches are able to capture the local amide I/amide II frequencies and coupling constants with quantitative accuracy, and, if combined with local amide I/amide II transition dipole derivatives obtained from the calculations on $^{13}C=^{18}O$ and N–D isotopologues, are able to capture the infrared intensities with sufficient accuracy to reproduce the experimental intensity patterns.

The bottom row stick spectra in figures 3.3-3.7 (c, in red) show the uncoupled local amide I/amide II frequencies and local amide I/amide II infrared intensities obtained from the calculations on the $^{13}C=^{18}O$ and N–D isotopologues, respectively. The comparison between the stick spectra in (b) and (c) gives some sense for the degree to which coupling between the amide I or amide II vibrations shifts the frequencies and changes their intensities. As a result, in the discussion that follows, one can confidently use the reduced-dimension Hessian matrices and resulting normal mode eigenvectors to look for trends in the test data set.

A full listing of the Hessian and eigenvector matrices for the 21-conformer primary test set is given in the appendix.[50] The uncoupled frequencies/intensities report on the dependence of the amide I and amide II modes on their local environment. The off-diagonal terms give quantitative results for the magnitude and sign of the nearest-neighbor and next-nearest-neighbor amide groups couplings. The ability to deconvolve the spectra into the diagonal-term uncoupled local mode frequencies and off-diagonal coupling terms provides a powerful and intuitive framework in which to analyze the data and look for trends in it.

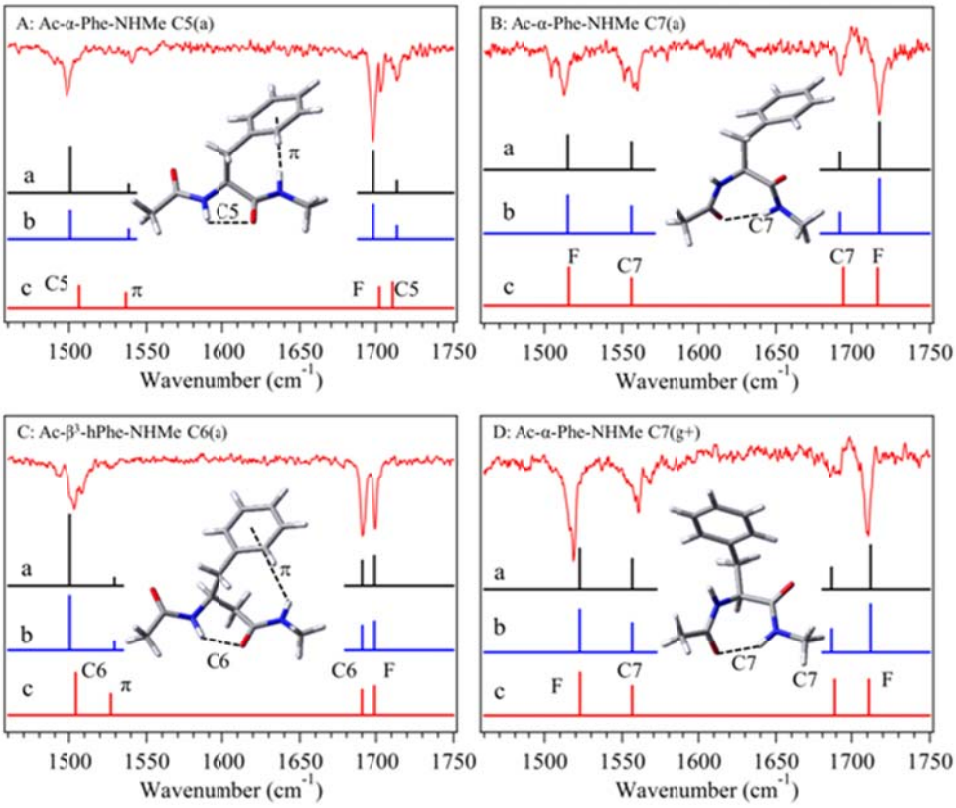

Figure 3.3 Experimental single-conformation IR spectra in the amide I and amide II regions (top trace) of a series of small single-ring H-bonded structures (A) Ac-α-Phe-NHMe C5(a), (B) Ac-α-Phe-NHMe C7(a), (C) Ac-β3-hPhe-NHMe C6(a), and (D) Ac-α-Phe-NHMe C7(g+). The spectra are compared with (a) the predictions of scaled, harmonic frequency calculations at the DFT M05-2X/6-31+G(d) level of theory, (b) Hessian reconstruction (amide I region) and PED analysis (amide II region) of the M05-2X normal modes, and (c) the local mode frequencies and IR intensities from isotopically substituting 13C-18O (amide I region) or N-D (amide II region) into all but one of the amide groups.

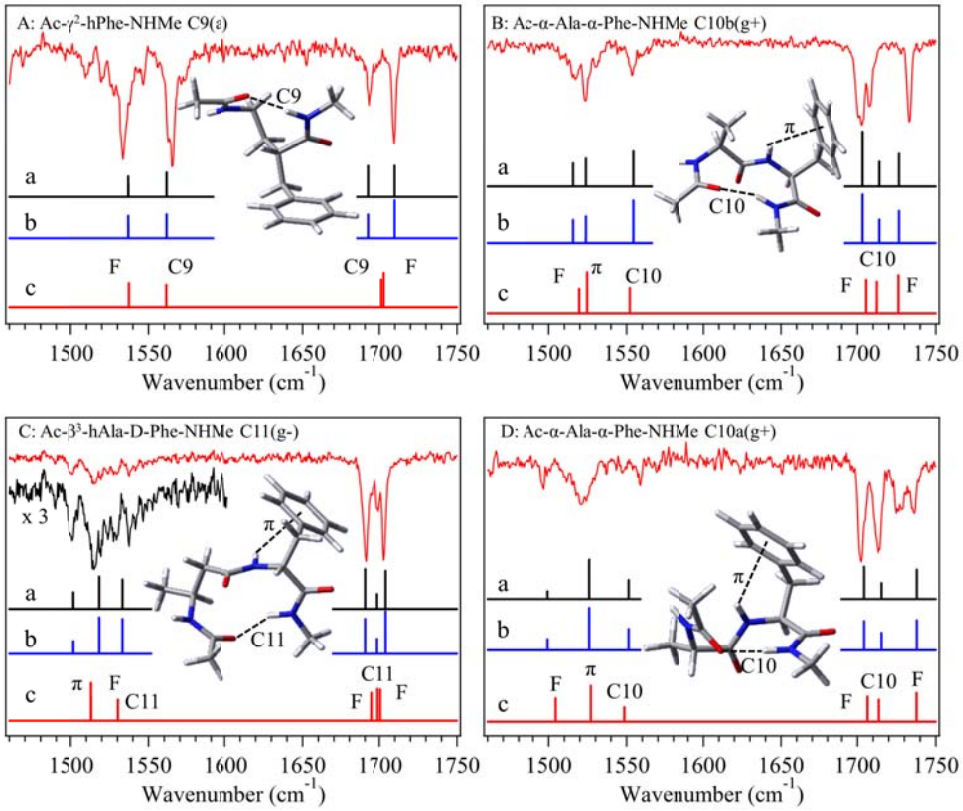

Figure 3.4 Experimental single-conformation IR spectra in the amide I and amide II regions (top traces) of a series of large single-ring H-bonded structures (A) Ac-γ2-Phe-NHMe C9(a), (B) Ac-α-Ala-α-Phe-NHMe C10b(g+), (C) Ac-β3-hAla-D-Phe-NHMe C11(g-), and (D) Ac-α-Ala-α-Phe-NHMe C10b(g+). The spectra are compared with (a) the predictions of scaled, harmonic frequency calculations at the DFT M05-2X/6-31+G(d) level of theory, (b) Hessian reconstruction (amide I region) and PED analysis (amide II region) of the M05-2X normal modes, and (c) the local mode frequencies and IR intensities from isotopically substituting 13C-18O (amide I region) or N-D (amide II region) into all but one of the amide groups.

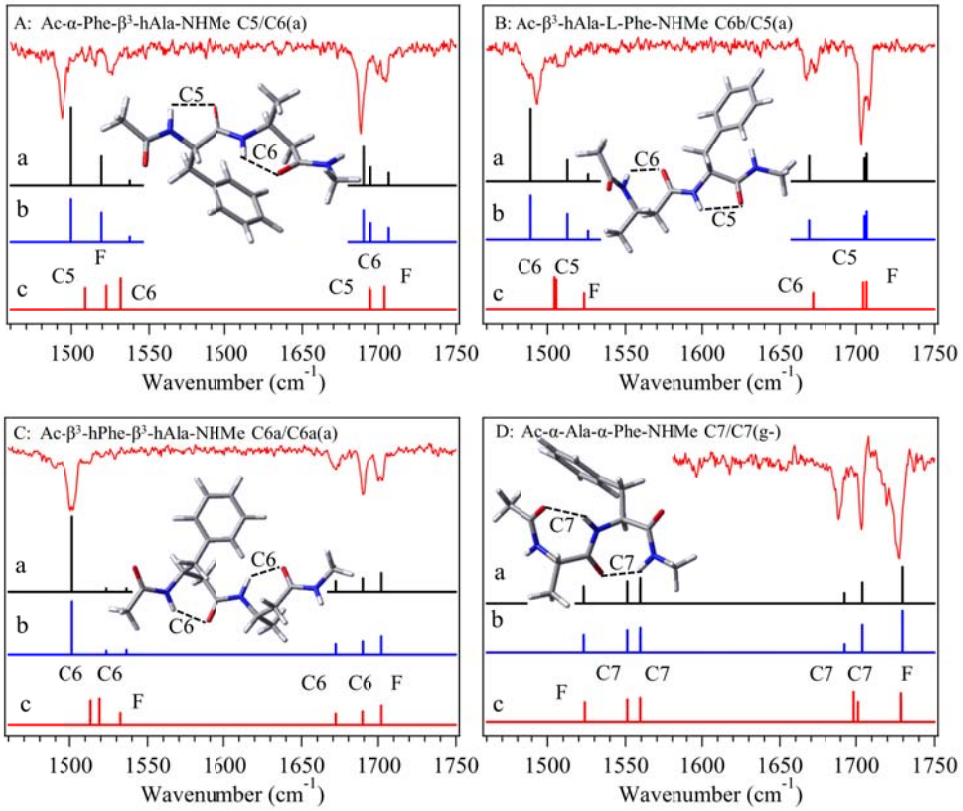

Figure 3.5 Experimental single-conformation IR spectra in the amide I and amide II regions (top traces) of a series of small sequential double-ring H-bonded structures: (A) Ac-α-Phe-β^3-hAla-NHMe C5/C6(a), (B) Ac-β^3-hAla-L-Phe-NHMe C6b/C5(a), (C) Ac-β^3-hPhe-β^3-hAla-NHMe C6a/C6a(a), and (D) Ac-α-Ala-α-Phe-NHMe C7/C7(g-). A second C6a/C6a(a) structure due to Ac-β^3-hAla-β^3-hPhe-NHMe is not included for space reasons, even though it is a part of the test set. The spectra are compared with (a) the predictions of scaled, harmonic frequency calculations at the DFT M05-2X/6-31+G(d) level of theory, (b) Hessian reconstruction (amide I region) and PED analysis (amide II region) of the M05-2X normal modes, and (c) the local mode frequencies and IR intensities from isotopically substituting $^{13}C=^{18}O$ (amide I region) or N-D (amide II region) into all but one of the amide groups.

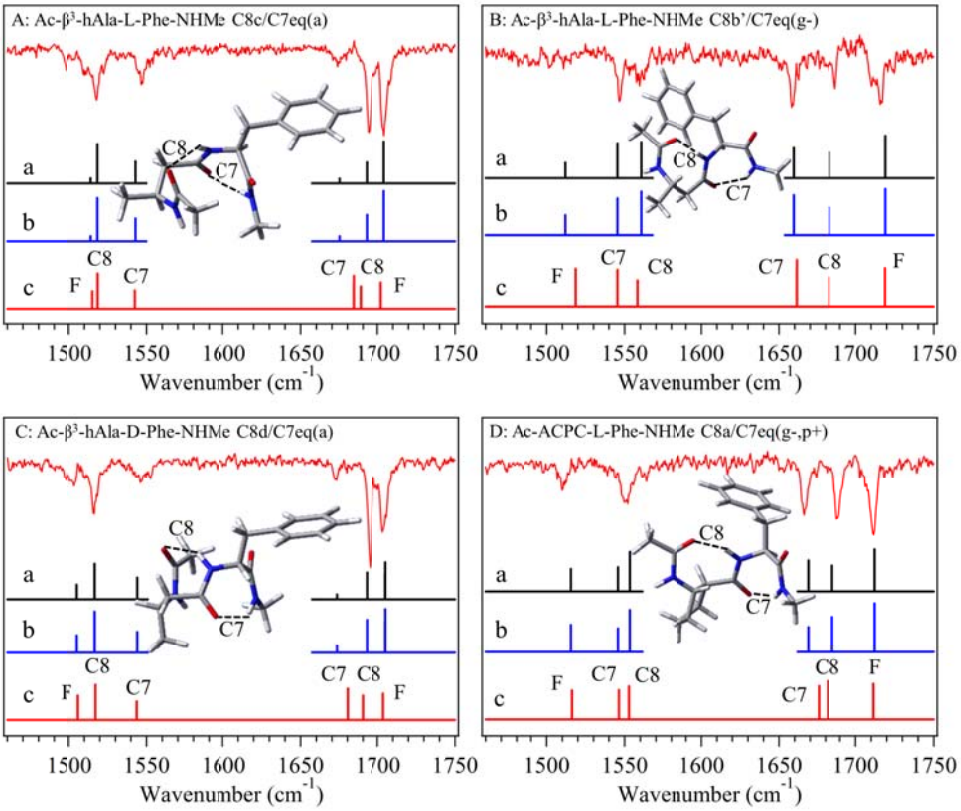

Figure 3.6 Experimental single-conformation IR spectra in the amide I and amide II regions (top traces) of a series of C8/C7eq sequential double-ring H-bonded structures with different C8 rings: (A) Ac-β^3-hAla-L-Phe-NHMe C8c/C7eq(a), (B) Ac-β^3-hAla-L-Phe-NHMe C8b'/C7eq(g-), (C) Ac-β^3-hAla-D-Phe-NHMe C8d/C7eq(a), and (D) Ac-ACPC-L-Phe-NHMe C8a/C7eq(g-,p+). The spectra are compared with (a) the predictions of scaled, harmonic frequency calculations at the DFT M05-2X/6-31+G(d) level of theory, (b) Hessian reconstruction (amide I region) and PED analysis (amide II region) of the M05-2X normal modes, and (c) the local mode frequencies and IR intensities from isotopically substituting $^{13}C=^{18}O$ (amide I region) or N-D (amide II region) into all but one of the amide groups.

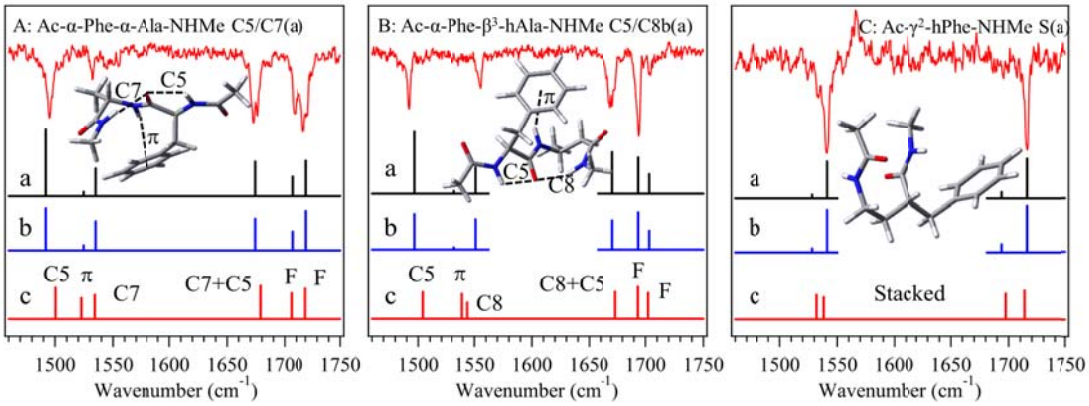

Figure 3.7 Experimental single-conformation IR spectra in the amide I and amide II regions (top trace) of (A) Ac-α-Phe-α-Ala-NHMe C5/C7(a), (B) Ac-α-Phe-β^3-hAla-NHMe C5/C8b(a), and (C) the amide stacked structure S(a) of Ac-γ^2-hPhe-NHMe. The experimental spectra are compared with (a) the predictions of scaled, harmonic frequency calculations at the DFT M05-2X/6-31+G(d) level of theory, (b) Hessian reconstruction (amide I region) and PED analysis (amide II region) of the M05-2X normal modes, and (c) the local mode frequencies and IR intensities from isotopically substituting $^{13}C{=}^{18}O$ (amide I region) or N-D (amide II region) into all but one of the amide groups.

3.4 Discussion

3.4.1 Amide I and Amide II Modes and Their Dependence on Local Environment

3.4.1.1 Local Mode Frequencies

Table 3.1 presents a compilation of the local mode frequencies for the amide I and amide II vibrations in the primary test set of 21 conformations, categorized by the type of H-bonding environment in which each amide group is found. In the amide I region, the notation lists the type of H-bond in which the C=O group is found first, with the NH group environment on that same amide listed second, separated by a slash. For example,

a C7/Free designation for a particular amide I local mode has the C=O group of that amide in a C7 H-bonded ring, and its NH free. This order is reversed for the amide II vibrations, since here it is the NH group that is the main carrier of the normal mode vibration. These results are summarized in pictorial form in figure 3.8 for the amide I region and figure 3.9 for amide II, where the range of frequencies of a given H-bonding environment are shown with double-headed arrows in cases where multiple values are available, and as single points where a single example of a given structural type has been observed. In cases where multiple examples of a given conformational family (e.g., C8a/C7) are observed in the broader set of 34 conformations, IR transitions for members of the set typically fall within a few cm^{-1} of one another.

Table 3.1 Uncoupled vibrational frequency ranges (cm-1) derived from the Hessian reconstruction (amide I) or PED analysis (amide II) as a function of local amide group H-bonding configuration.

	Amide I		Amide II	
	C=O/NH	Freq. Range	NH/C=O	Freq. Range
Free	Free/C5	1702-1711	Free/C6	1522-1532
	Free/C6	1698-1706	Free/C7	1516, 1524
	Free/C7	1702-1728	Free/C8	1506-1519
	Free/C8,C11	1693, 1694	Free/C9	1537, 1542
	Free/C9	1701, 1708	Free/C10	1504, 1520
	Free/C10	1706, 1706	Free/C11	1513
	Free/π (in C10)	1726, 1738	Free/Free, π/Free	1513-1527
	Free/π (in C11)	1701	π/C5, C6, C7	1523-1537
	Stack/stack, stack+π	1714, 1697	Stack, stack+π/stack	1532, 1538
Single Rings	C5/π	1702-1704	C5/Free	1500-1508
	C6/Free, π	1689-1694	C6/Free	1503-1513
	C7/Free	1689-1701	C7/Free	1534-1559
	C8/Free	1682-1690	C8b/Free	1543
	C9, C11/Free	1697-1703	C9/Free	1561, 1562
	C10/Free	1712, 1714	C10/Free	1548, 1550
			C11/Free	1531
Sequential Double Rings	C7/C7	1698	C5/C6b	1504
	C7/C8	1661-1684	C6/C5+p	1531
	C6/C6, C5	1671-1676	C6/C6	1515-1517
	C5/C6+π	1694	C8b', C8a/C7	1553, 1557
			C8c, C8d/C7	1517, 1518
Bifurcated Double Rings	C5+C7/π	1679	π/C5+C7	1522
	C8b+C5/π	1674	π/C8b+C5	1539

The amide I local mode frequencies are spread over 77 cm^{-1}, stretching from 1661 to 1738 cm^{-1}, while amide II modes have frequencies from 1500–1562 cm^{-1}, a range of 62 cm^{-1}. These are isolated molecule frequencies, and hence will undergo further shifts in a room temperature liquid solution. The most natural comparison of the present results is with α-peptides in non-polar solvents such as $CHCl_3$ and CH_2Cl_2. For instance, while the gas phase values for C5 conformers are 1702–1704 cm^{-1} (C5/π) and 1500–1508 cm^{-1} (C5/F) in amide I and amide II, respectively, the corresponding values for fully extended (all C5) structures in $CDCl_3$ solution from Maekawa et al.[10] are 1650 cm^{-1} (amide I) and 1510–1515 cm^{-1} (amide II). This represents a shift of about 50 cm^{-1} in the amide I region, probably due in part to the weak C-H···O=C hydrogen bonds formed by these solvents. By comparison, there is little change in the amide II region.

The amide I local modes generally shift to lower frequency when placed in a H-bond, as is seen most readily in figure 3.8. This relationship is one that has been known for decades.[53] However, the correlation of the amide I frequency shift with the strength of the H-bond − as assessed by the magnitude of the red-shift of the NH stretch fundamental − is not straightforward. For instance, the series of C8/C7 conformers C8c/C7eq(a), C8a/C7eq(g−,p+) and C8b'/C7eq(g−) have C8/F NH stretch fundamentals spread over almost 100 cm^{-1} (3380, 3278, and 3282 cm^{-1}, respectively), with calculated NH···O H-bond distances of 2.20, 1.97, and 1.94 Å, respectively, yet the amide I local mode frequencies differ by only 7 cm^{-1} (1688, 1681, and 1683 cm^{-1}).

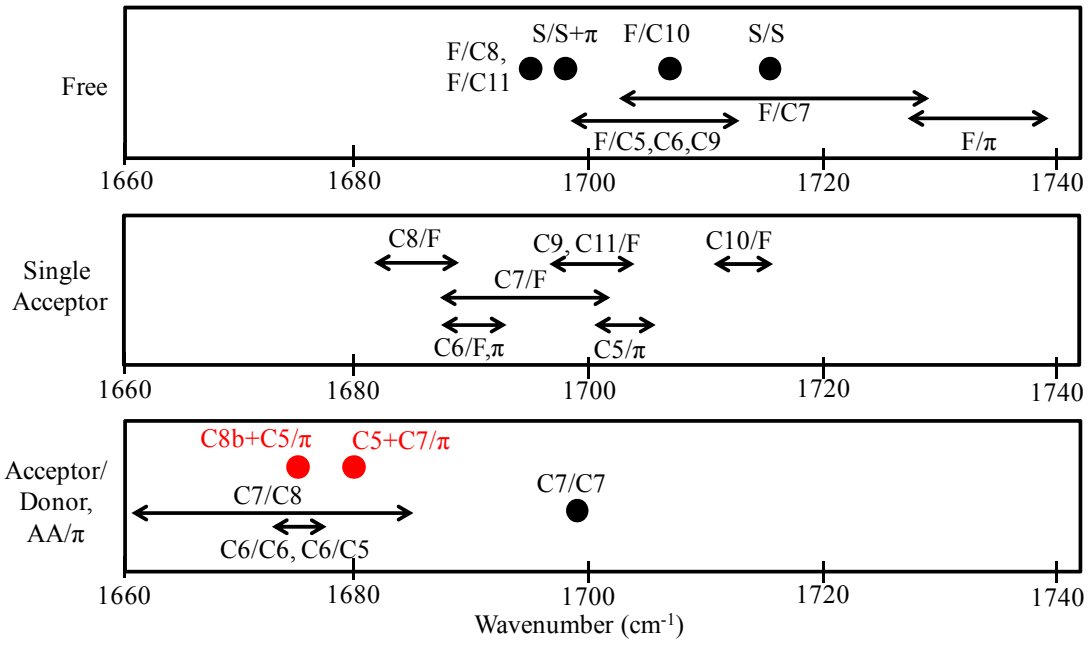

Figure 3.8 Uncoupled, local mode amide I frequencies as a function of local amide group H-bonding environment.

The lowest frequency amide I fundamentals are those involving (i) interior amide groups in which the C=O group acts as acceptor and the NH group as donor, and (ii) interior amides in bifurcated double rings in which the C=O group acts as a double acceptor, with the NH group in a weak π H-bond with the aromatic ring. Thus, there is clearly an effect on the amide I vibration due both to direct H-bonds to the C=O group and indirectly via a "backside" H-bond to the NH group of the same amide.

The diagram in figure 3.8 also makes clear that C=O groups which are not involved in H-bonds with another amide group (and thus are nominally "free", figure 3.8a) have amide I fundamentals spread over a surprisingly large range of 45 cm^{-1}, stretching from 1693 to 1738 cm^{-1}. The set of seven F/C7 amide I fundamentals are especially instructive in this regard, since they are spread over 26 cm^{-1} (1702–

1728 cm^{-1}), despite having the same amide–amide H-bonding environment. Close inspection of the single-conformation structures reveals that the lower frequency members of this set all have a methyl CH···O=C and/or aromatic CH···O=C interactions that act much like NH H-bonds in lowering the amide I frequency. The F/C8 (C5/C8b(a)) and F/C11 (C11(g−)) amide I vibrations are also low in frequency (1693 and 1694 cm^{-1}, respectively) for the same reason, both engaging in aromatic CH···O=C interactions. Thus, the entire local environment of a given C=O group contributes to its frequency, not just the interactions with other amide groups.

Figure 3.9 summarizes the corresponding data for the amide II local mode frequencies. A similar division of the test-set amide groups is made into four sub-categories due to free NH groups (figure 3.9a), single-donor amides in which the NH group is in a H-bond, but its C=O is free (figure 3.9b), and a third category (figure 3.9c) composed of two sub-groups: (i) interior donor/acceptor amide groups in which both NH and C=O are involved in H-bonds, and (ii) interior π/double acceptor amides in which the NH group is involved in a π H-bond and its C=O acts as a double acceptor in bifurcated double rings (π/C5+C7(a) and π/C5+C8b(a)).

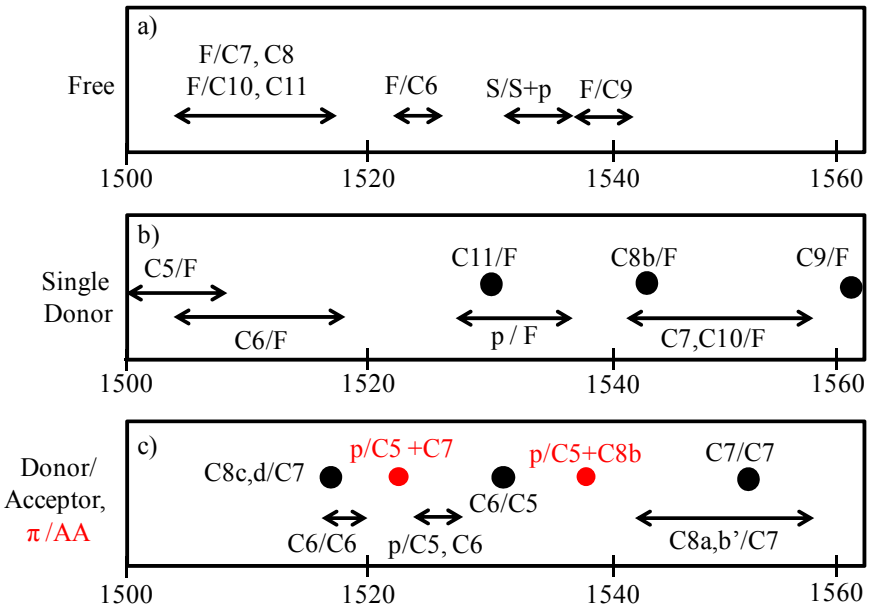

Figure 3.9 Uncoupled, local mode amide II frequencies as a function of local amide group H-bonding environment.

The Cn/F and π/F single donor amide groups (figure 3.9b) span the entire 62 cm^{-1}, with each sized ring taking up a characteristic wavenumber range. The amide II local mode frequencies show a non-monotonic shift with ring size, with those in C5 H-bonds lower in frequency than any of the free NH groups, C6 rings shifting slightly back to higher frequency, with larger rings substantially further shifted, with highest frequencies occurring for C7 and C10 H-bonds in α-peptides, C8b rings in β-peptides, and C9 rings in γ-peptides. The magnitude of this shift correlates with the orientation and strength of the H-bond in which it is involved, with C5 rings in which the NH group is nearly parallel to the C=O acceptor, C6 rings at an oblique angle, and NH groups in C7, C9, and C10 rings pointing directly at the high electron density regions of the C=O group.

The frequency of the amide II fundamentals are quite sensitive to weak interactions, as is evident from the spread in frequency of the (nominally) free NH groups (figure 3.9a), which are spread over the range from 1504–1542 cm^{-1}. This spread is influenced to some degree also by the strength of the H-bond to the C=O group on the same amide. However, interior amides in sequential or bifurcated double rings (figure 3.9c) often show relatively minor shifts from their single-donor values (figure 3.9b), suggesting that once an NH group is involved in a hydrogen bond, its sensitivity to binding at its C=O group is reduced. A closer analysis of the correlation of these frequencies with the full range of amide environments is still needed, and may benefit from exploration of a larger range of peptide structures as the test set of molecules is expanded.

3.4.1.2 Local Mode Intensities and Transition Dipole Moment Directions

Successful modeling of the amide I and amide II regions for the present test set of single-conformation spectra also lends confidence to the local mode intensities predicted by the calculations on isotopically labeled structures, as described in Sec. II.C.2. In the amide I region this is accomplished by carrying out calculations on structures in which one amide is unlabeled ($^{12}C=^{16}O$), while all others are $^{13}C=^{18}O$. It is these intensities that are used as the local mode intensities in the Hessian reconstruction and PED/HR analyses reported in figures 3.3–3.7 and summarized in table 3.1. A full listing of the results of this analysis is included in the Appendix.[50] The calculated intensities in the amide I and amide II regions based on the Hessian reconstruction and PED/HR analyses correctly predict the relative intensities and general spectral patterns observed experimentally.

Since current electrostatic models[13-23] often assume that the local amide I and II intensities are independent of conformation or local H-bonding environment, the present data offer a good test of this approximation.

One might have anticipated that the local mode intensities would be greater in the amide I region than in amide II, but this turns out not to be the case. The range of intensities spanned by the amide I and amide II modes in the test set (178–410 km/mol for amide I, 149–468 km/mol for amide II) is remarkably similar. Furthermore, these intensity ranges are large, spanning more than a factor of two in the amide I modes, and a factor of three in the amide II modes. This would lead one to surmise that models of both regions should include a description of the conformation-specific intensities. [2, 13-24]

The amide I modes with greatest intensities are interior amide groups in C7/C7 or C7/C8b' double rings or a C8a single-ring. The three weakest intensity amide I local modes are all found in C6 rings (e.g., C6b/C5 interior, 178 km/mol). This indicates a mechanism for intensity enhancement or suppression that is related to the local H-bonding environment in which the amide C=O is found. One might anticipate on this basis that the local mode intensity and frequency would be correlated; however, the most intense (C7/C8b') and least intense (C6b/C5) amide I local modes have frequencies of 1661 and 1672 cm^{-1}, within 11 cm^{-1} of one another.

In the present single-conformation data, the local amide II modes are every bit as intense as their amide I counterparts, on average. The structural sensitivity of α-peptides in the amide II region has been recently explored theoretically by Torii[54], who has shown that amide II IR intensities are affected by an oscillating charge flux between the NH

group and the C=O group during the NH bending motion. In the extended C5 configuration, the dipole derivative and charge flux are nearly parallel to one another, working cooperatively to enhance the intensity, while in C7 rings, the charge transfer is nearly perpendicular to the dipole derivative, leading to negligible intensity enhancement.[54] The present data provides a wider range of circumstances in which to test this mechanism.

At the level of theory used to model the present single-conformation IR spectra, the C5 rings do not particularly stand out, with values ranging from 241 to 348 km/mol. Interestingly, the C6 rings in β-peptide sub-units are characteristically even larger (407–468 km/mol), as one might anticipate if the C6 rings, which are structurally similar to C5 rings in α-peptides,[54] also facilitate charge flux in the same direction as the dipole derivative. Equally striking, NH groups in π H-bonds with the phenyl ring of the Phe side chain also have amide II local mode vibrations that are unusually intense (424–440 km/mol), but only when the NH bending motion oscillates towards the π cloud (π/C7 in C7(g+), π/Free in C10 and C11 rings). The π/C5 amide in Ac-Phe-NHMe oscillates parallel to the π cloud, and has intensity among the lowest in the test set (165 km/mol). Thus, Torii's model[54] for intensity enhancement in amide II involving charge flux from the NH to the acceptor group seems a general phenomenon that extends to β- and γ-peptides and to interactions with π clouds.

Furthermore, the coupling between NH bending modes in C5 and C6 sequential double rings leads to a large additional intensity enhancement. As figure 3.5A–C bears out, this coupling leads to an in-phase oscillation in the C6/C6, C5/C6, and C6/C5

sequential double rings that further enhances the lowest frequency amide II transition near 1500 cm^{-1}, making it 2–3 times larger than any other transitions in the amide I and amide II regions. This intense, low-frequency amide II transition is a signature of an extended structure in which adjacent NH groups are in a nearly anti-parallel arrangement, and has been identified in infrared studies of model β-sheet or extended structures in solution.[10, 54]

Finally, also include summaries of the TDM angles for the amide I and II local modes. The amide I mode is primarily a C=O stretch, but includes some C–N stretch character that tips the TDM angle away from the C=O bond axis towards the N atom. Current models of the amide I region typically assume a constant value somewhere in the range 10–20°.[13-23] Somewhat surprisingly, the TDM angles in the present test set span a range from 7–33 degrees relative to the C=O bond. We have searched without success for a clear correlation of these TDM angle changes and properties of the amide group environment in which it is found. While a range this size is not likely to have a dramatic effect on the relative intensities, it is nevertheless a significant change worth recognizing.

3.4.2 Amide I/I and Amide II/II Coupling

We now turn attention to the off-diagonal terms, i.e. the amide I/I and amide II/II coupling constants, in the HR and PED/HR analyses. It is here that the connection with 2D IR studies is perhaps most direct, since such studies reveal couplings between amide groups via off-diagonal peaks in the 2D IR spectrum. The small capped diamides and triamides are ideally suited to test the nearest-neighbor and next-nearest-neighbor

couplings that are key components of the theoretical models used to simulate the 2D IR spectra, and to do so for a series that transcends the typical restrictions in distance and approach angles present in α-peptides by including in the test set β-peptides, γ-peptides, and mixed α/β-peptides. The ability of the HR and PED/HR analyses to reproduce the frequencies, splittings, and intensity patterns provides confidence that the amide I/I and amide II/II coupling constants derived from these analyses are quantitatively accurate.

Careful inspection of the full set of off-diagonal Hessian matrix elements reveals a striking fact: The magnitudes and signs of these coupling constants are characteristic of the C=O···HN H-bonded ring size that connects the two amide groups. Table 3.2 provides a summary of these results, categorized by H-bonded ring size (or other defining structural parameter). Inspection of the table confirms that the amide I/I and amide II/II coupling constants do indeed fall into narrow ranges that are characteristic of a given ring size, with examples in the single-conformation data ranging in size from 5-membered (C5) to 11-membered (C11) rings. The different C8 ring types are differentiated in the table only to the extent that they need to be to account for the ranges in coupling constants observed. In this respect, the C8b rings were unique, showing a much smaller amide I nearest-neighbor coupling, and a much larger amide II coupling than the other C8 ring types (C8a, C8c, C8d). A corollary to the characteristic coupling constants of the H-bonds is that, in most circumstances, non H-bonded groups have characteristically small I/I and II/II couplings, with values so close to zero that they could easily be set to zero with little consequence for the computed spectrum.

The deduction that H-bonds between amide groups dictate their I/I and II/II coupling is arguably the most important result arising from the present work. This deduction should be viewed, not as entirely new or unanticipated, but arising out of an independent test that strengthens and clarifies it. Previous studies of model secondary structures and small peptides in solution have clearly recognized that, of the possible through-bond, through-space, and through H-bond mechanisms for coupling amide vibrations, H-bonds play an important role.[2-3, 55] The results of 2D IR experiments on model secondary structures[4, 10-11, 16] have hinted at the same finding in deducing unique coupling matrix elements between amide groups for each secondary structure type. Nevertheless, the present single-conformation data in the gas phase places this deduction on a broader experimental footing, and proves its generalization beyond α-peptides to the much wider set of H-bonding environments present in β-, γ-, and α/β-peptides.

Thus, the results in table 3.2 provide strong evidence that the principal physical mechanism by which two C=O groups on different amides couple their vibrational motions is through the NH···O=C H-bond that links the two amide groups involved. This is a qualitatively different picture than that provided by the transition dipole coupling (TDC)[17, 56] or transition charge coupling (TCC)[15-16, 21, 25, 57] models that have been the hallmark of most theoretical attempts to model the amide I region.

Table 3.2 Coupling constants (cm-1) as a function of H-bonded ring size or structural type linking the two amide groups.

H-bonded ring	Amide I[a]	Amide II[b]
C5(a)	+6.5 to +6.8	−8.1 to −11.2
C6(b)	−0.3 to −1.5	−8.0 to −11.8
C7(a)	−5.6 to −7.1	0.0 to −3.2
C8a,c,d (b)	−7.3 to −8.2	−1.8 to −2.2
C8b (b)	−1.1 , −2.9	−9.3, −13.2
C9 (g)	−8.2 to −8.9	−1.4 to −2.3
C10(a)	–3.0 to –4.3	−4.4
C11(a/b)	−5.0	−5.0
Non H-bonded	−0.4 to +1.3	−0.9 to +1.2
Stacked(g)	−7.4	−5.8
C11(a,b) turn	−3.4 to +1.9	−4.5 to -10.7

[a]Ranges of coupling constant values from Hessian reconstruction and PED analysis. Cases with only one or two examples are listed as single numbers or separated by a comma.

[b]Nearest-neighbor coupling between N-terminal and interior or interior and C-terminal amide groups in a C10 or C11 ring.

In the TDC model, the oscillating dipoles of the two C=O groups couple electrostatically to one another through-space. In the TCC model, contributions from higher order multipole terms are also included. While it has been recognized for some time[15, 31] that TDC and TCC models do not provide quantitatively accurate descriptions of nearest-neighbor coupling (NNC) in peptides, they are used routinely for next nearest-neighbor couplings (n-NNC) by current models. Furthermore, the scheme invoked by most current models[13-23] for prediction of amide I/I and II/II nearest-neighbor coupling

lacks physical insight, instead relying on coupling maps, i.e. plots of nearest-neighbor coupling constant versus Ramachandran angles, to provide values for the nearest-neighbor coupling constants as a function of conformation.

The present data set provides a new opportunity to quantitatively test the amide I/I coupling constants against the predictions of TDC and TCC models and the coupling maps. This comparison is shown in table 3.3 for nearest-neighbor and next-nearest neighbor coupling constants of the seven α–peptide conformations in our data set. As is evident from the Table, TDC is not even qualitatively correct for nearest-neighbor couplings, even getting the wrong sign in some cases, but reproduces the HR result reasonably well for next-nearest neighbor couplings. The TCC predictions give mixed results for both nearest and next-nearest neighbor couplings, and are not qualitatively better for next-nearest neighbor than TDC. Not unexpectedly, predictions based on the coupling maps are reasonably good, since they were derived from a HR analysis. However, these maps are not available for β- and γ-peptides. At present, these conclusions are based on a limited data set of just seven α-peptide conformations, and therefore must be considered tentative. A more complete analysis will be taken up elsewhere[58] in extending to the full 21-conformer data set and expanding its reach to include larger α-peptides.

Table 3.3 Amide I/I coupling constants obtained from Hessian reconstruction, TDC and TCC models, and a (φ,ψ) Ramachandran angle coupling map. [a]Hessian reconstruction on DFT calculations at the M05-2X/6-31+G(d) level of theory. [b]TDC model of ref. 23. [c]TCC model of ref. 11. [d]Nearest-neighbor (φ,ψ) Ramachandran angle coupling map of ref. 11.

		Amide I/I coupling constants		
Conformer	Method	N-term/Int	Int/C-term	N-/C-term
		J_{12}	J_{23}	J_{13}
Ac-a-Phe-NHMe C5(a)	Hess. Rec.[a]	6.45	-	-
	TDC[b]	-2.45	-	-
	TCC[c]	-2.38	-	-
	Rama. map[d]	5.95	-	-
Ac-a-Phe-NHMe C7(a)	Hess. Rec.[a]	-6.32	-	-
	TDC[b]	-1.60	-	-
	TCC[c]	-6.30	-	-
	Rama. map[d]	-4.12	-	-
Ac-a-Phe-NHMe C7(g+)	Hess. Rec.[a]	-5.76	-	-
	TDC[b]	0.37	-	-
	TCC[c]	-5.81	-	-
	Rama. map[d]	-4.89	-	-
Ac-a-Phe-a-Ala-NHMe C5/C7(a)	Hess. Rec.[a]	6.72	-6.40	1.30
	TDC[b]	-2.61	-0.19	1.35
	TCC[c]	-2.38	-6.52	1.85
	Rama. map[d]	5.98	-5.31	-
Ac-a-Ala-a-Phe-NHMe C10a(g+)	Hess. Rec.[a]	1.68	-0.43	-4.30
	TDC[b]	4.01	5.81	-3.72
	TCC[c]	3.74	2.86	-7.13
	Rama. map[d]	-0.03	-0.14	-
Ac-a-Ala-a-Phe-NHMe C10b(g+)	Hess. Rec.[a]	1.75	-0.81	-4.27
	TDC[b]	-7.73	5.23	-4.84
	TCC[c]	5.53	1.86	-7.74
	Rama. map[d]	2.35	-0.59	-
Ac_a-Ala-a-Phe-NHMe C7/C7(g–)	Hess. Rec.[a]	-5.55	-6.20	1.28
	TDC[b]	-0.40	-0.47	1.08
	TCC[c]	-6.40	-6.43	3.40
	Rama. map[d]	-4.76	-4.43	-

Having established that hydrogen bonds are the primary means by which amide group vibrations couple to one another, table 3.2 shows how the magnitude and sign of the coupling constants depend on the ring size. Several deductions can immediately be drawn from the data set.

- Almost all the coupling constants for both amide I/I and II/II coupling are negative, with the C5 amide I/I coupling a notable exception.
- The magnitudes of the coupling constants span a range from near-zero (C6 I/I or C7 II/II) to as large as –13 cm^{-1}.
- The largest coupling constants are amide II/II rather than I/I, with C5 rings of α-peptides and C6 and C8b rings of β-peptides displaying the largest II/II couplings.

- Importantly, the magnitude of the coupling constants are every bit as large in rings formed by β- and γ-peptide sub-units as they are in α-peptides, indicating that the coupling is not affected significantly by the number of backbone C-atoms separating the amide groups. The C5 and C7 rings are nearest-neighbor configurations in α-peptide sub-units, the C6 and C8 rings in β-peptides, and the C9 rings in γ-peptides. The current test set contains no C7 γ-peptide rings, which are in principle also possible, and have so far only been observed in ring-constrained γ-peptides.[37] The C10 and C11 rings involve next-nearest-neighbor interactions characteristic of an α-peptide or mixed α/β-peptide β-turn, respectively.

- The characteristic ranges of coupling constants hold both when the rings are isolated in a capped diamide, and when they are part of a triamide, where they form one of the rings in a sequential double ring or bifurcated double ring. This fact makes it likely that, in larger peptides, one can construct a coupling matrix simply by inserting characteristic coupling constant values based solely on the H-bonds involved. However, this deduction needs further testing on larger peptides.

- The amide II/II coupling constants cover a range of values similar to those of amide I/I, suggesting that the empirically derived conclusion that II/II coupling is more insensitive than I/I coupling to model secondary structure may need refinement.[4]

Further comment needs to be made regarding circumstances in which the coupling is near zero. As we have already mentioned, the general rule is that amide

groups that are not H-bonded to one another are, with rare exception, near zero (−0.4 to +1.3 cm^{-1} in I/I and −0.9 to +1.2 cm^{-1} in II/II). However, two exceptions to this rule are noted in the last two rows in table 3.2.

First, the amide stacked structure of Ac-γ^2-hPhe-NHMe has amide I/I and II/II coupling constants of −7.4 and −5.8 cm^{-1}, respectively. In this case, the close approach of the two amide groups in an anti-parallel, stacked arrangement produces strong coupling despite the absence of an NH···O=C H-bond. Moreover, in the amide II region, nearest-neighbor coupling in C10 and C11 turns are also larger than other non H-bonded coupling constants. Here, too, although the interior amide is not H-bonded to either the N-terminal or C-terminal nearest neighbors, it is nevertheless acting as the center of a compact turn (C10 is a β-turn in α-peptides) that enhances the N-terminal/interior and C-terminal/interior coupling. Both circumstances involve a close approach of the two amide groups to one another, with electrostatic interactions undoubtedly playing a key role in the coupling mechanism. Such exceptions deserve close scrutiny in future work.

Second, certain sized rings also have coupling constants near zero, suggesting that they give rise to a less favorable NH donor approach angle into the electron density of the C=O acceptor than other sized rings. The C6 rings of β-peptides are near zero for amide I/I coupling (−0.3 to +1.5 cm^{-1}), while the C7 (0.0 to −3.2 cm^{-1}) and C9 (−1.4 to −2.3 cm^{-1}) rings have negligible amide II/II coupling in α- and γ-peptides, respectively. The physical mechanism of this dependence of the coupling constants in both the amide I and amide II regions on the H-bond ring size deserves further investigation, and will be taken up elsewhere.[58]

3.4.3 Comparison with Coupling Constants Derived From Previous Studies

While the coupling constants summarized in table 3.2 are unique results of the single-conformation methods employed here, the C5, C7, and C10 rings of α-peptides provide points of comparison with the values deduced from 1D and 2D IR spectra in solution.[4, 10, 59-61] These are summarized in table 3.4.

Table 3.4 Coupling constants (cm^{-1}) as a function of H-bonded ring size or structural type. [a]This work. [b]Ref. 6. [c]J.-H. Choi, M. Cho, Chem. Phys., 2009, 361, 168. [d]Ref. 4. [e]H. Maekawa, M. De Poli, A. Moretto, C. Toniolo, N.-H. Ge, J. Phys. Chem. B, 2009, 113, 11775. [f]Ref. 47. [g]P. Hamm and M. Zanni, in Concepts and Methods of 2D Infrared Spectroscopy, (Cambridge, 2011), p. 125.

Structure type	(f,y)	Amide I	Amide II
C5 ring	(−155,+160)	+6.5 to +6.8[a]	−8.1 to −11.2[a]
	(±180, ±180)	+4.3[b]	−3.5[b]
b-sheet	(−139,+135)	+6.8[c]	−8.5[d], +0.4[e]
C7 ring	(-84, +55)	−5.6 to −7.1[a]	0.0 to −3.2[a]
C7 ring	(−55,+30)	+8.0±0.5[f]	—
C10a ring	(−70, −13)	+1.7[a]	−9.5[a]
	(−87, +3)	−0.4[a]	−9.2[a]
	i→i+2	−4.3[a]	−4.2[a]
C10b ring	(+52, −135)	+1.9[a]	−4.5[a]
	(−93, +12)	+0.4[a]	−10.7[a]
	i→i+2	−3.0[a]	−4.4[a]
3_{10} helix	(−57, −30)	+3.4[e]	−2.8[e]
	i→i+1	−1.5[c]	−2.4[c]
	(−57, −30)		
3_{10} helix	i→i+2	−5.4[e]	−3.1[e]
a-helix	(−57, −47)	~+8[g], +5.2[c]	−8.7[d], −1.9[e]

For instance, in the amide I region, the C5 rings in the present test set have I/I coupling constants that all fall into a narrow range between +6.5 and +6.8 cm^{-1}. These compare favorably with the values deduced for I/I coupling in fully-extended α-peptide chains composed only of C5 rings. As Maekawa et al.[10] discuss in some detail, the values deduced in previous studies fall in a range from +4.1 to +8.4 cm^{-1}, compared to a value derived from 2D IR spectral fitting of +4.3 cm^{-1}.

The II/II coupling constant derived for fully extended structures (±180°, ±180°) in the work of Maekawa et al.[10] is −3.5 cm^{-1}, only about one-third the value derived in the present study for C5 rings (−8.1 to −11.2 cm^{-1}). However, the C5 rings in the conformations in the present test set have Ramachandran angles (−155°, +160°) somewhat closer to those in anti-parallel β-sheets (−139°, +135°). Tokmakoff[4] has recently deduced an empirical value for the nearest-neighbor amide II'/II' coupling constant in the β-sheet of deuterated poly-L-lysine of −8.5 cm^{-1}, in good agreement with the present result.

Bagchi and Hochstrasser (BH)[62] have recorded 2D IR spectra and modeled them to extract diagonal and off-diagonal Hessian matrix elements for the capped dipeptide N-acetyl-tryptophan methyl amide (NATMA), a molecule whose single-conformation infrared spectroscopy has been studied under jet-cooled conditions in the NH stretch region by our group. BH deduce that NATMA is predominantly in a C7 conformation in CH_2Cl_2, and analyze the 2D IR spectra to obtain the dihedral angles and coupling constants shown in table 3.4, where they are compared with the range of values found for structures containing C7 rings in this work. Interestingly, the dihedral angles differ by

about 30 degrees in CH_2Cl_2 from those in the gas phase, amounts small enough to nominally retain the C7 structure, but modified from that in the gas phase by the non-polar solvent. BH deduce the magnitude of the coupling constant at 8.0±0.5 cm^{-1}, similar in magnitude to that deduced here. It would be worthwhile to obtain single-conformation amide I and amide II spectra of NATMA in the gas phase,[63-64] since to date, there is little data on the same molecules carried out both in the gas phase and in solution.

Ge and co-workers[11-12, 65] have recently studied model peptides designed to form a 3_{10} helix composed entirely of C10 H-bonds, with Ramachandran angles of (-57^o, -30^o). They have developed a coupling map for I/I, I/II, II/I and II/II coupling that has values of +3.4 cm^{-1} for I/I nearest-neighbor coupling, −2.8 cm^{-1} for II/II, and −5.4/−3.1 cm^{-1} values for I/I and II/II coupling across the C10 H-bond (i→i+2). Our test set contains two C10 α-peptide conformations arising from two C10 rings (C10a, C10b), with structures shown in figures 3.10a,b, respectively, differing in the dihedral angles in the C10 ring. Table 3.4 compares these (ϕ,ψ) angles with each other and with those present in an idealized 3_{10} helix (-57^o, -30^o). The Ramachandran angles of the C10a structure are somewhat closer to those of the 3_{10} helix than C10b, particularly in the N-terminal/interior (ϕ,ψ) angle, which re-orients the N-terminal amide so that the C-terminal NH group approaches the C=O oxygen almost head-on.

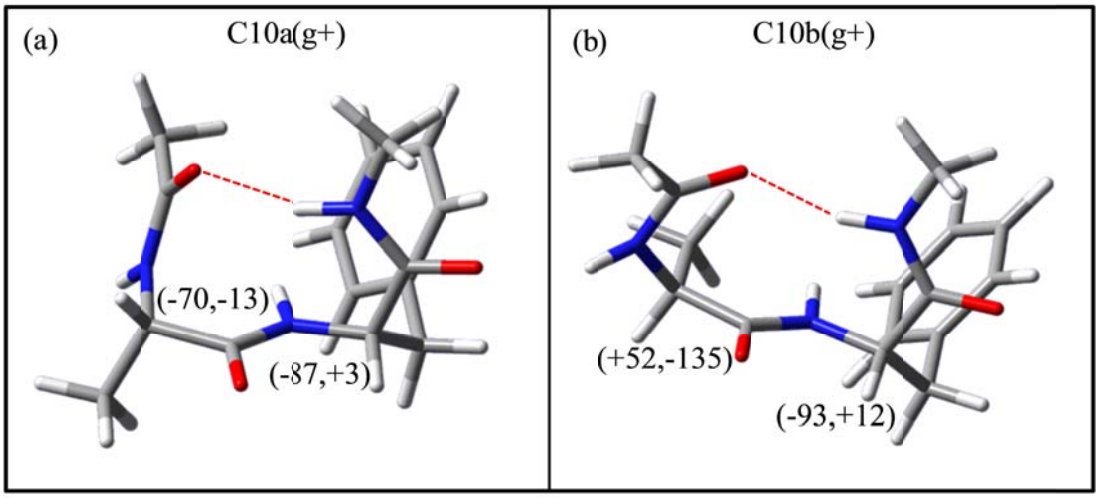

Figure 3.10 The assigned structures for the two C10 conformers of Ac-α-Ala-α-Phe-NHMe. The Ramachandran angles for the Ala and Phe amino acids are given in degrees. The corresponding angles for an idealized 3_{10} helix are (-57, -30).

As already discussed, in the amide I region, both C10 structures have nearest-neighbor couplings that are near zero, and next-nearest-neighbor coupling of $-4.3/-3.0\ cm^{-1}$ for C10a/C10b, consistent with the H-bond connecting these amide groups. The C10 amide II region is the exception to the H-bond rule, with large nearest-neighbor couplings despite the absence of a H-bond linking the central amide group with the N-terminal and C-terminal amides.

3.5 Conclusions

In this paper, we have presented representative examples of single-conformation infrared spectra in the amide I and amide II regions, drawn from a data set of 34 conformations of eleven molecules, recorded for the isolated molecules cooled in a supersonic expansion. These molecules include methyl-capped diamides and triamides

composed of α-peptides, α/β-peptides, β-peptides, and γ-peptides. As such, they represent a diverse set of H-bonded structures, including single-rings, sequential double rings, bifurcated double rings, and amide stacked configurations, with hydrogen bonded rings sizes ranging from 5-membered (C5) to 11-membered (C11) in size.

A subset of 21 of these structures was chosen as representative examples comprising a test set of molecules for more detailed analysis. Using Cho's Hessian reconstruction method[13] in the amide I region and developing a combined potential energy distribution/Hessian reconstruction analysis for the amide II region, we have extracted local mode frequencies, IR intensities and coupling constants for the 21-member test set in both the amide I and amide II region. The local mode frequencies span a range from 1671–1738 cm^{-1} in the amide I region and 1500–1562 cm^{-1} in the amide II region.

While the amide I local mode frequencies are generally shifted down when the C=O group acts as acceptor in an NH···O=C H-bond, the correlation between strength of the H-bond and magnitude of the shift is not very clear, with single rings of different size and H-bond strength sometimes surprisingly close to one another (e.g., C5 and C9 rings, figure 3.8b). Furthermore, the nominally free C=O groups have local mode frequencies spanning a range of 45 cm^{-1}. The lowest frequency amide I vibrations in the test set are those in which the C=O group and NH group are both in H-bonds.

In the amide II region, the local mode frequencies are better correlated with the strength of the H-bond (figure 3.9b), but the shift is non-monotonic, reflecting sensitivity to the orientation of the H-bond in which it is found. When the NH group is in a C5 ring

in which it bends toward its acceptor carbonyl oxygen, the shift is slightly down in frequency. C6 rings are just slightly higher in frequency, with larger rings and even NH···π H-bonds shifted 30–60 cm^{-1} higher in frequency, when the NH group orients itself more directly toward the maximum electron density on the acceptor C=O group, stiffening the bending mode.

A key result of the present study is the experimental evidence it has provided that the magnitudes of the coupling constants between amide groups in both the amide I and amide II regions are, with few exceptions, only large when the two amide groups are linked by a H-bond, and the value obtained is characteristic of the type of H-bond (e.g., the H-bonded ring size) in which it is involved. In the present paper, we have reached this conclusion as an experimental fact. We are currently exploring in more detail the physical mechanism by which the H-bond imparts this coupling, since it is not obvious at first that the two local mode amide I vibrations, which involve motion primarily of the C=O groups, should be coupled to one another by the H-bond formed by the NH group that links the acceptor C=O with the C=O not involved in the H-bond.[58] Similarly, coupling between amide II vibrations is mediated by the H-bond linking the two amide groups, here between the NH group involved in the H-bond and the NH on the amide group containing the C=O acting as H-bond acceptor. These deductions suggest a strategy for future models; namely, to ignore coupling between amide groups not involved in H-bonds with one another, except in rare configurations. It will be important to submit this deduction to further experimental tests. While the test set is an extensive one, it may under-sample certain conformations that are important in proteins. As a first

step, extension of single-conformation spectroscopy to a wider range of γ-peptides, α/γ-peptides, and β/γ-peptides would fill out the array of foldamers structures in the test set more completely. The influence of bound water to the local mode frequencies and coupling constants is especially important, given the vital role played by aqueous solution in most peptide and protein structures of biological relevance. Here, too, there is a role for single-conformation spectroscopy in a supersonic expansion, where molecules in the test set can be complexed with one or more water molecules, which are likely to bind to C=O groups, and may form bridges between amide groups. Finally, it will be important to extend such studies to larger peptides, where secondary structural elements are more fully developed, and the presence of H-bonds reaching further along the peptide chain will become more prevalent.

3.6 References

1. Decatur, S. M. Elucidation of residue-level structure and dynamics of polypeptides via isotope-edited infrared spectroscopy. *Accounts of Chemical Research* **2006,** *39* (3), 169-175.

2. Barth, A.; Zscherp, C. What vibrations tell us about proteins. *Quarterly Reviews of Biophysics* **2002,** *35* (4), 369-430.

3. Krimm, S.; Bandekar, J. VIBRATIONAL SPECTROSCOPY AND CONFORMATION OF PEPTIDES, POLYPEPTIDES, AND PROTEINS. *Advances in Protein Chemistry* **1986,** *38*, 181-364.

4. DeFlores, L. P.; Ganim, Z.; Nicodemus, R. A.; Tokmakoff, A. Amide I '-II ' 2D IR Spectroscopy Provides Enhanced Protein Secondary Structural Sensitivity. *Journal of the American Chemical Society* **2009,** *131* (9), 3385-3391.

5. Ganim, Z.; Chung, H. S.; Smith, A. W.; Deflores, L. P.; Jones, K. C.; Tokmakoff, A. Amide I two-dimensional infrared Spectroscopy of proteins. *Accounts of Chemical Research* **2008,** *41* (3), 432-441.

6. Kim, Y. S.; Hochstrasser, R. M. Applications of 2D IR Spectroscopy to Peptides, Proteins, and Hydrogen-Bond Dynamics. *Journal of Physical Chemistry B* **2009,** *113* (24), 8231-8251.

7. Moran, S. D.; Woys, A. M.; Buchanan, L. E.; Bixby, E.; Decatur, S. M.; Zanni, M. T. Two-dimensional IR spectroscopy and segmental C-13 labeling reveals the domain structure of human gamma D-crystallin amyloid fibrils. *Proceedings of the National Academy of Sciences of the United States of America* **2012,** *109* (9), 3329-3334.

8. Roy, S.; Lessing, J.; Meisl, G.; Ganim, Z.; Tokmakoff, A.; Knoester, J.; Jansen, T. L. C. Solvent and conformation dependence of amide I vibrations in peptides and proteins containing proline. *J. Chem. Phys.* **2011,** *135* (23), 234507.

9. Ghosh, A.; Hochstrasser, R. M. A peptide's perspective of water dynamics. *Chemical Physics* **2011,** *390* (1), 1-13.

10. Maekawa, H.; Ballano, G.; Toniolo, C.; Ge, N. H. Linear and Two-Dimensional Infrared Spectroscopic Study of the Amide I and II Modes in Fully Extended Peptide Chains. *Journal of Physical Chemistry B* **2011,** *115* (18), 5168-5182.

11.Maekawa, H.; De Poli, M.; Toniolo, C.; Ge, N. H. Couplings between Peptide Linkages across a 3(10)-Helical Hydrogen Bond Revealed by Two-Dimensional Infrared Spectroscopy. *Journal of the American Chemical Society* **2009,** *131* (6), 2042-+.

12.Maekawa, H.; Toniolo, C.; Broxterman, Q. B.; Ge, N.-H. Two-dimensional infrared spectral signatures of 3(10)- and alpha-helical peptides. *Journal of Physical Chemistry B* **2007,** *111* (12), 3222-3235.

13.Ham, S.; Cha, S.; Choi, J. H.; Cho, M. Amide I modes of tripeptides: Hessian matrix reconstruction and isotope effects. *J. Chem. Phys.* **2003,** *119* (3), 1451-1461.

14.Ham, S.; Cho, M. Amide I modes in the N-methylacetamide dimer and glycine dipeptide analog: Diagonal force constants. *J. Chem. Phys.* **2003,** *118* (15), 6915-6922.

15.Jansen, T. L.; Dijkstra, A. G.; Watson, T. M.; Hirst, J. D.; Knoester, J. Modeling the amide I bands of small peptides. *J. Chem. Phys.* **2006,** *125* (4), 044312.

16.Maekawa, H.; Ge, N. H. Comparative Study of Electrostatic Models for the Amide-I and -II Modes: Linear and Two-Dimensional Infrared Spectra. *Journal of Physical Chemistry B* **2010,** *114* (3), 1434-1446.

17.Torii, H.; Tasumi, M. MODEL-CALCULATIONS ON THE AMIDE-I INFRARED BANDS OF GLOBULAR-PROTEINS. *J. Chem. Phys.* **1992,** *96* (5), 3379-3387.

18.Wang, L.; Middleton, C. T.; Zanni, M. T.; Skinner, J. L. Development and Validation of Transferable Amide I Vibrational Frequency Maps for Peptides. *Journal of Physical Chemistry B* **2011,** *115* (13), 3713-3724.

19.Woutersen, S.; Pfister, R.; Hamm, P.; Mu, Y. G.; Kosov, D. S.; Stock, G. Peptide conformational heterogeneity revealed from nonlinear vibrational spectroscopy and molecular-dynamics simulations. *J. Chem. Phys.* **2002,** *117* (14), 6833-6840.

20.Hayashi, T.; Zhuang, W.; Mukamel, S. Electrostatic DFT map for the complete vibrational amide band of NMA. *Journal of Physical Chemistry A* **2005,** *109* (43), 9747-9759.

21.Watson, T. M.; Hirst, J. D. Theoretical studies of the amide I vibrational frequencies of Leu -enkephalin. *Mol. Phys.* **2005,** *103* (11-12), 1531-1546.

22.Bour, P.; Keiderling, T. A. Empirical modeling of the peptide amide I band IR intensity in water solution. *J. Chem. Phys.* **2003,** *119* (21), 11253-11262.

23.Ham, S.; Kim, J. H.; Lee, H.; Cho, M. H. Correlation between electronic and molecular structure distortions and vibrational properties. II. Amide I modes of NMA-nD(2)O complexes. *J. Chem. Phys.* **2003,** *118* (8), 3491-3498.

24.Lin, Y. S.; Shorb, J. M.; Mukherjee, P.; Zanni, M. T.; Skinner, J. L. Empirical Amide I Vibrational Frequency Map: Application to 2D-IR Line Shapes for Isotope-Edited Membrane Peptide Bundles. *Journal of Physical Chemistry B* **2009,** *113* (3), 592-602.

25.Gorbunov, R. D.; Kosov, D. S.; Stock, G. Ab initio-based exciton model of amide I vibrations in peptides: Definition, conformational dependence, and transferability. *J. Chem. Phys.* **2005,** *122* (22), 224904.

26.Karjalainen, E.-L.; Ersmark, T.; Barth, A. Optimization of Model Parameters for Describing the Amide I Spectrum of a Large Set of Proteins. *Journal of Physical Chemistry B* **2012,** *116* (16), 4831-4842.

27.Krimm, S.; Abe, Y. INTERMOLECULAR INTERACTION EFFECTS IN AMIDE I VIBRATIONS OF BETA POLYPEPTIDES. *Proceedings of the National Academy of Sciences of the United States of America* **1972,** *69* (10), 2788-2792.

28.Torii, H. Vibrational interactions in the amide I subspace of the oligomers and hydration clusters of N-methylacetamide. *Journal of Physical Chemistry A* **2004,** *108* (35), 7272-7280.

29.Jacob, C. R.; Reiher, M. Localizing normal modes in large molecules. *J. Chem. Phys.* **2009,** *130* (8), 084106.

30.Choi, J. H.; Ham, S. Y.; Cho, M. Local amide I mode frequencies and coupling constants in polypeptides. *Journal of Physical Chemistry B* **2003,** *107* (34), 9132-9138.

31.Hamm, P.; Woutersen, S. Coupling of the amide I modes of the glycine dipeptide. *Bulletin of the Chemical Society of Japan* **2002,** *75* (5), 985-988.

32.Gerhards, M.; Unterberg, C.; Gerlach, A.; Jansen, A. beta-sheet model systems in the gas phase: Structures and vibrations of Ac-Phe-NHMe and its dimer (Ac-Phe-NHMe)(2). *Physical Chemistry Chemical Physics* **2004,** *6* (10), 2682-2690.

33.Baquero, E. E.; James, W. H.; Choi, S. H.; Gellman, S. H.; Zwier, T. S. Single-conformation ultraviolet and infrared spectroscopy of model synthetic foldamers: beta-peptides Ac-beta(3)-hPhe-NHMe and Ac-beta(3)-hTyr-NHMe. *Journal of the American Chemical Society* **2008,** *130* (14), 4784-4794.

34.Baquero, E. E.; James, W. H.; Choi, S. H.; Gellman, S. H.; Zwier, T. S. Single-conformation ultraviolet and infrared spectroscopy of model synthetic foldamers: beta-peptides Ac-beta(3)-hPhe-beta(3)-hAla-NHMe and Ac-beta(3)-hAla-beta(3)-hPhe-NHMe. *Journal of the American Chemical Society* **2008,** *130* (14), 4795-4807.

35.James III, W. H.; Baquero, E. E.; Choi, S. H.; Gellman, S. H.; Zwier, T. S. Laser Spectroscopy of Conformationally Constrained alpha/beta-Peptides: Ac-ACPC-Phe-NHMe and Ac-Phe-ACPC-NHMe. *Journal of Physical Chemistry A* **2010,** *114* (3), 1581-1591.

36.James III, W. H.; Baquero, E. E.; Shubert, V. A.; Choi, S. H.; Gellman, S. H.; Zwier, T. S. Single-Conformation and Diastereomer Specific Ultraviolet and Infrared Spectroscopy of Model Synthetic Foldamers: alpha/beta-Peptides. *Journal of the American Chemical Society* **2009,** *131* (18), 6574-6590.

37.James III, W. H.; Buchanan, E. G.; Guo, L.; Gellman, S. H.; Zwier, T. S. Competition between Amide Stacking and Intramolecular H Bonds in gamma-Peptide Derivatives: Controlling Nearest-Neighbor Preferences. *Journal of Physical Chemistry A* **2011,** *115* (43), 11960-11970.

38.Buchanan, E. G.; James, W. H., III; Gutberlet, A.; Dean, J. C.; Guo, L.; Gellman, S. H.; Zwier, T. S. Single-conformation spectroscopy and population analysis of model gamma-peptides: New tests of amide stacking. *Faraday Discussions* **2011,** *150*, 209-226.

39.Chin, W.; Dognon, J. P.; Canuel, C.; Piuzzi, F.; Dimicoli, I.; Mons, M.; Compagnon, I.; von Helden, G.; Meijer, G. Secondary structures of short peptide chains in the gas phase: Double resonance spectroscopy of protected dipeptides. *J. Chem. Phys.* **2005,** *122* (5), 054317.

40.Chin, W.; Piuzzi, F.; Dognon, J. P.; Dimicoli, I.; Mons, M. Gas-phase models of gamma turns: Effect of side-chain/backbone interactions investigated by IR/UV spectroscopy and quantum chemistry. *J. Chem. Phys.* **2005,** *123* (8), 084301.

41.Keresztu.G; Jalsovsz.G. ALTERNATIVE CALCULATION OF VIBRATIONAL POTENTIAL ENERGY DISTRIBUTION. *Journal of Molecular Structure* **1971,** *10* (2), 304-&.

42.Morino, Y.; Kuchitsu, K. A NOTE ON THE CLASSIFICATION OF NORMAL VIBRATIONS OF MOLECULES. *J. Chem. Phys.* **1952,** *20* (11), 1809-1810.

43. Weiner, P. K.; Kollman, P. A. Amber - Assisted Model-Building with Energy Refinement - a General Program for Modeling Molecules and Their Interactions. *Journal of Computational Chemistry* **1981,** *2* (3), 287-303.

44. Becke, A. D. DENSITY-FUNCTIONAL THERMOCHEMISTRY .3. THE ROLE OF EXACT EXCHANGE. *J. Chem. Phys.* **1993,** *98* (7), 5648-5652.

45. Zhao, Y.; Truhlar, D. G. Density functionals for noncovalent interaction energies of biological importance. *Journal of Chemical Theory and Computation* **2007,** *3* (1), 289-300.

46. Zhao, Y.; Truhlar, D. G. Density functionals with broad applicability in chemistry. *Accounts of Chemical Research* **2008,** *41* (2), 157-167.

47. Doemer, M.; Guglielmi, M.; Athri, P.; Nagornova, N. S.; Rizzo, T. R.; Boyarkin, O. V.; Tavernelli, I.; Rothlisberger, U. Assessing the performance of computational methods for the prediction of the ground state structure of a cyclic decapeptide. *International Journal of Quantum Chemistry* **2012**, DOI: 10.1002/qua.24085.

48. Gaussian 03; Revision C.01, D. F., M. J.; Trucks, G. W.; Schlegel, H. B.; Scuseria, G. E.; Robb, M. A.; Cheeseman, J. R.; Montgomery, Jr., J. A.; Vreven, T.; Kudin, K. N.; Burant, J. C.; Millam, J. M.; Iyengar, S. S.; Tomasi, J.; Barone, V.; Mennucci, B.; Cossi, M.; Scalmani, G.; Rega, N.; Petersson, G. A.; Nakatsuji, H.; Hada, M.; Ehara, M.; Toyota, K.; Fukuda, R.; Hasegawa, J.; Ishida, M.; Nakajima, T.; Honda, Y.; Kitao, O.; Nakai, H.; Klene, M.; Li, X.; Knox, J. E.; Hratchian, H. P.; Cross, J. B.; Bakken, V.; Adamo, C.; Jaramillo, J.; Gomperts, R.; Stratmann, R. E.; Yazyev, O.; Austin, A. J.; Cammi, R.; Pomelli, C.; Ochterski, J. W.; Ayala, P. Y.; Morokuma, K.; Voth, G. A.; Salvador, P.; Dannenberg, J. J.; Zakrzewski, V. G.; Dapprich, S.; Daniels, A. D.; Strain, M. C.; Farkas, O.; Malick, D. K.; Rabuck, A. D.; Raghavachari, K.; Foresman, J. B.; Ortiz, J. V.; Cui, Q.; Baboul, A. G.; Clifford, S.; Cioslowski, J.; Stefanov, B. B.; Liu, G.; Liashenko, A.; Piskorz, P.; Komaromi, I.; Martin, R. L.; Fox, D. J.; Keith, T.; Al-Laham, M. A.; Peng, C. Y.; Nanayakkara, A.; Challacombe, M.; Gill, P. M. W.; Johnson, B.; Chen, W.; Wong, M. W.; Gonzalez, C.; and Pople, J. A.; Gaussian, Inc., Wallingford CT, 2004.

49.Gaussian 09, R. A., Frisch, M. J.; Trucks, G. W.; Schlegel, H. B.; Scuseria, G. E.; Robb, M. A.; Cheeseman, J. R.; Scalmani, G.; Barone, V.; Mennucci, B.; Petersson, G. A.; Nakatsuji, H.; Caricato, M.; Li, X.; Hratchian, H. P.; Izmaylov, A. F.; Bloino, J.; Zheng, G.; Sonnenberg, J. L.; Hada, M.; Ehara, M.; Toyota, K.; Fukuda, R.; Hasegawa, J.; Ishida, M.; Nakajima, T.; Honda, Y.; Kitao, O.; Nakai, H.; Vreven, T.; Montgomery, Jr., J. A.; Peralta, J. E.; Ogliaro, F.; Bearpark, M.; Heyd, J. J.; Brothers, E.; Kudin, K. N.; Staroverov, V.N.; Kobayashi, R.; Normand, J.; Raghavachari, K.; Rendell, A.; Burant, J. C.; Iyengar, S. S.; Tomasi, J.; Cossi, M.; Rega, N.; Millam, N. J.; Klene, M.; Knox, J. E.; Cross, J. B.; Bakken, V.; Adamo, C.; Jaramillo, J.; Gomperts, R.; Stratmann, R. E.; Yazyev, O.; Austin, A.J.; Cammi, R.; Pomelli, C.; Ochterski, J. W.; Martin, R. L.; Morokuma, K.; Zakrzewski, V. G.; Voth, G. A.; Salvador, P.; Dannenberg, J. J.; Dapprich, S.; Daniels, A. D.; Farkas, Ö.; Foresman, J. B.; Ortiz, J.V.; Cioslowski, J.; Fox, D. J. Gaussian, Inc., Wallingford CT, 2009.

50.See the appendix for a summary of the labeling schemes for individual conformations, and the quantitative output for HR and PED analysis of individual conformations in the 21-member test set, including local amide I and II frequencies, amide I/I and amide II/II coupling constants, transition dipole moment characterization, and Hessian reconstruction U matrices.

51.Jamroz, M. H. *Vibrational Energy Distribution Analysis: VEDA 4 program*, Warsaw, 2004.

52.Dijkstra, A. G.; Jansen, T. l. C.; Knoester, J. Modeling the Vibrational Dynamics and Nonlinear Infrared Spectra of Coupled Amide I and II Modes in Peptides. *Journal of Physical Chemistry B* **2011,** *115* (18), 5392-5401.

53.Pimentel, G. C.; McClellan, A. L. *The Hydrogen Bond*. W.H. Freeman: San Francisco, 1960.

54.Torii, H. Mechanism of the Secondary Structure Dependence of the Infrared Intensity of the Amide II Mode of Peptide Chains. *Journal of Physical Chemistry Letters* **2012,** *3* (1), 112-116.

55.Viswanathan, R.; Dannenberg, J. J. A density functional theory study of vibrational coupling in the amide I band of beta-sheet models. *Journal of Physical Chemistry B* **2008,** *112* (16), 5199-5208.

56.Torii, H.; Tasumi, M. Ab initio molecular orbital study of the amide I vibrational interactions between the peptide groups in di- and tripeptides and considerations on the conformation of the extended helix. *Journal of Raman Spectroscopy* **1998,** *29* (1), 81-86.

57.Falvo, C.; Zhuang, W.; Kim, Y. S.; Axelsen, P. H.; Hochstrasser, R. M.; Mukamel, S. Frequency Distribution of the Amide-I Vibration Sorted by Residues in Amyloid Fibrils Revealed by 2D-IR Measurements and Simulations. *Journal of Physical Chemistry B* **2012,** *116* (10), 3322-3330.

58.Müller, C. W.; Zwier, T. S. to be published.

59.Choi, J.-H.; Cho, M. Calculations of intermode coupling constants and simulations of amide I, II, and III vibrational spectra of dipeptides. *Chemical Physics* **2009,** *361* (3), 168-175.

60.Maekawa, H.; De Poli, M.; Moretto, A.; Toniolo, C.; Ge, N. H. Toward Detecting the Formation of a Single Helical Turn by 2D IR Cross Peaks between the Amide-I and -II Modes. *Journal of Physical Chemistry B* **2009,** *113* (34), 11775-11786.

61.Hamm, P.; Zanni, M. *Concepts and Methods of 2D Infrared Spectroscopy*. Cambridge: 2011.

62.Bagchi, S.; Kim, Y. S.; Charnley, A. K.; Smith, A. B.; Hochstrasser, R. M. Two-dimensional infrared investigation of N-acetyl tryptophan methyl amide in solution. *Journal of Physical Chemistry B* **2007,** *111*, 3010-3018.

63.Dian, B. C.; Longarte, A.; Mercier, S.; Evans, D. A.; Wales, D. J.; Zwier, T. S. The infrared and ultraviolet spectra of single conformations of methyl-capped dipeptides: N-acetyl tryptophan amide and N-acetyl tryptophan methyl amide. *J. Chem. Phys.* **2002,** *117* (23), 10688-10702.

64.Dian, B. C.; Longarte, A.; Winter, P. R.; Zwier, T. S. The dynamics of conformational isomerization in flexible biomolecules. I. Hole-filling spectroscopy of N-acetyl tryptophan methyl amide and N-acetyl tryptophan amide. *J. Chem. Phys.* **2004,** *120* (1), 133-147.

65.Maekawa, H.; Formaggio, F.; Toniolo, C.; Ge, N.-H. Onset of 3(10)-helical secondary structure in aib oligopeptides probed by coherent 2D IR spectroscopy. *Journal of the American Chemical Society* **2008,** *130* (20), 6556-6566.

CHAPTER 4 TOWARDS A FIRST-PRINCIPLES MODEL OF FERMI RESONANCE IN THE ALKYL CH STRETCH REGION: APPLICATION TO 1,2 DIPHENYLETHANE AND 2,2,2-PARACYCLOPHANE

4.1 Introduction

The spectroscopy of large, flexible molecules isolated and cooled in a supersonic jet expansion has provided unique insights into the conformational preferences of molecules and molecular clusters, including a growing range of molecules with biological relevance, among them synthetic foldamers,[1-3] peptides,[4-6] carbohydrates,[7] and DNA base pairs.[8] Assigning the observed spectra to specific conformational isomers often involves a systematic search of the potential energy surface using molecular mechanics force fields, further optimization of a subset of the conformers using *ab initio* or density functional theory (DFT) methods, and calculating harmonic vibrational frequencies and infrared intensities of the optimized structures for comparison with experiment. The strength of the structural assignment is based upon the close correspondence between the predictions of the calculations and the experimental spectra, using energetic considerations to constrain the structural search.

In most molecules with biological relevance, intramolecular and/or intermolecular hydrogen bonds dictate the folded structures or cluster geometries formed. Here, the frequencies and intensities characteristically reflect the hydrogen bonding arrangement, reporting, in the case of peptides, on the local environment of the hydrogen bonds in the

amide NH stretch, C=O stretch (amide I), and N−H bending (amide II) regions of the spectrum. Due to the pervasive presence of alkyl groups in most large molecules, the alkyl CH stretch region offers some potential as an additional probe of molecular conformation. Despite the comparatively weak IR intensities of the CH stretch oscillators, the high IR powers available in the 2800−3000 cm^{-1} region often make it possible to obtain high quality single conformation spectra in this region. As a result, the alkyl CH stretch region was used as a basis for assignment of the conformations of the ethylamine side chain of both tryptamine[9] and serotonin,[10] and has provided some constraints on the structures present in isolated and complexed crown ethers.[11-13]

Even in the absence of single conformation data, the CH stretch region is increasingly being used as a probe of molecular structure[14-23] because these modes exhibit a surprising sensitivity to molecular structure.[24-25] Motivated by this sensitivity to geometry, the Strauss group investigated the C−H vibrations of n-alkanes in a series of benchmark studies.[24-25] His group obtained spectra at low temperatures for a range of alkanes with the goal to make definitive assignments of the CH stretching region. Their work highlighted the role of Fermi resonances with the scissor modes in leading to spectral complexity. Recent 2D-IR studies have targeted the CD stretch modes as probes of local conformation in peptides and proteins.[26-28]

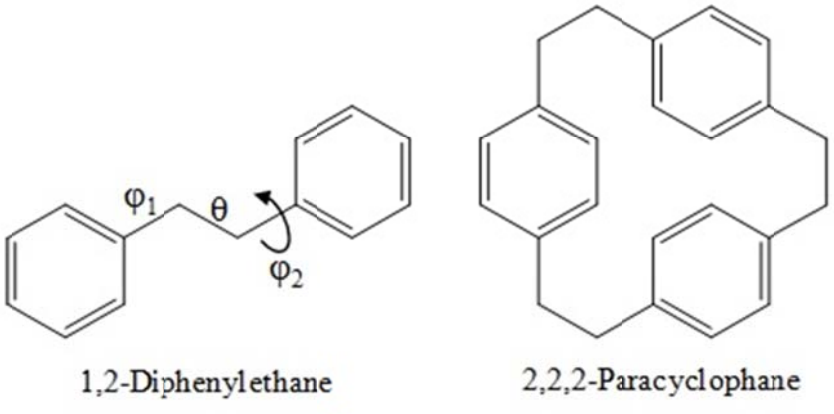

Figure 4.1 Chemical structures of 1,2-diphenylethane (DPE) and 2,2,2-paracyclophane.

However, conformational assignments based on a comparison of the observed alkyl CH stretch spectra with *ab initio* predictions of harmonic frequencies often fail in spectacular fashion due to the presence of extensive bend/stretch Fermi resonance that shifts and splits bands to the point that the comparison with harmonic calculations is fruitless. See for example references 13. While other XH stretch fundamentals are shifted from the overtones of their XH bend fundamentals sufficiently that such 2:1 Fermi resonance is small, the alkyl CH stretch fundamentals (2800−3000 cm^{-1}) engage in strong Fermi resonance mixing with the first overtones of the CH bends, with fundamental frequencies in the 1400−1500 cm^{-1}, producing large anharmonic couplings of 20−30 cm^{-1} or more. Such strong Fermi resonant mixing also extends to other types of CH stretch transitions, with the acetylenic CH stretch fundamentals of ortho, meta, and para-diethynylbenzene serving as a notable recent example.[29]

The present chapter presents single-conformation alkyl CH stretch data for two prototypical hydrocarbons, 1,2-diphenylethane (DPE) and 2,2,2-paracyclophane (TCP).

DPE is a flexible bichromophore with the two phenyl rings linked by a single ethano bridge ($^{-}CH_2CH_2^{-}$), while TCP is a trichromophore macrocycle with three ethano bridges between ultraviolet chromophores. The structures of the two molecules are shown in figure 4.1 with the dihedral angles responsible for the flexibility of the two molecules placed on DPE. As multichromophores, both TCP and DPE produce a set of close-lying electronic excited states with interesting consequences for their conformation-dependent vibronic coupling and electronic energy transfer.[30-32] Furthermore, as an aromatic rich macrocycle, TCP can serve as a binding pocket for various molecules, most notably water.[33] These aspects of the vibronic spectroscopy of DPE and TCP and of water binding to the binding pocket of TCP will be taken up in chapter 8.

The purpose of the present paper is to determine the ground state conformational preferences of DPE and TCP, and then to use these conformations as model systems on which to develop a quantitatively accurate first-principles model of the alkyl CH stretch region. As we shall see, the ground state CH stretch spectrum of TCP is not even approximately accounted for by harmonic vibrational frequency calculations due to the large Fermi resonance contributions. The disconnect between experiment and theory in TCP motivated our study of a simpler analog of the macrocyle, DPE, to gain insight into the Fermi resonance coupling terms present there.

The overall goal, then, is to develop a predictive model of the alkyl CH stretch region of DPE and TCP. We do this in a local mode framework. The local mode picture has emerged as a powerful alternative zero order representation.[34-38] This approach continues to be developed and utilized for the interpretation of a variety of dynamical phenomena[39-46] ranging from the OH stretches of water to the amide stretches of

biological molecules. The great advantage of the local mode approach is the ease of interpretation. This advantage is particularly compelling if one is interested in comparing a series of molecules and trying to sort out which variables, relevant to the interpretation of the spectra, are changing due to changes in environment. For example, when considering how the secondary structure of the protein affects the amide stretch region, Weymuth *et al.*[44] recently found that projecting the normal modes onto a set of localized modes leads to very similar local mode Hamiltonians that can then be analyzed to see how the Hamiltonian coupling parameters change as functions of various torsional angles.

In this Chapter, CH local mode Hamiltonians, that have been dressed via second order Van Vleck perturbation theory, are shown to yield eigenvalues and intensities that are essentially the same as those that are obtained from a full normal mode analysis. Anharmonic couplings between these local modes and vibrational degrees of freedom involving adjacent atoms are calculated in order to include the role of Fermi resonance interactions. We take as a starting point a full-dimensional DFT quadratic Hamiltonian that includes the above mentioned anharmonic terms in order to determine the mode-mixing relevant to spectral prediction. We find that the spectra calculated with this model are essentially identical to those calculated with reduced dimensional Hamiltonians that include just the local mode CH stretch and the scissor degrees of freedom. We then scale the DFT values of select parameters in the reduced dimensional model Hamiltonian in order to fit the experimental spectrum of the C_{2h} symmetry *anti* conformer of DPE. Having determined the scale factors, we apply this Hamiltonian to molecules with considerably more complex spectra, the lower symmetry *gauche*

conformer of DPE and then extending the model to the two lowest energy conformers of TCP, which contain six CH_2 groups. The successes and limitations of this scaling are discussed by comparing our results to the experimental spectra.

4.2 Conformational Assignment

Electronic structure methods are used to identify conformers and their low frequency vibrations. This information is compared to single and double resonance experiments in order record conformation-specific ultraviolet and infrared spectra.[47]

The electronic structure calculations predict the presence of two conformers of DPE and TCP differing in symmetry. Figure 4.2 presents the two optimized structures for the DPE and TCP conformers, respectively. While there are three dihedral angles about which conformational minima may be found in DPE (figure 4.1), the alkylbenzenes display a strong preference for an out-of-plane orientation of $C(\beta)$, with $\varphi_1 = \varphi_2 \sim 90^\circ$.[48] As a result, as in butane, there are two low lying conformational minima in DPE, differing in the central dihedral angle θ, *anti* (~ 180˚), and *gauche* (±60˚). The *anti* conformer has C_{2h} symmetry, while *gauche* has C_2 symmetry. According to the calculations, the *gauche* conformer is the global minimum with the *anti* conformation only 1.8 kJ/mol higher in energy. The TCP conformers are distinguished from one another by the relative positions of the carbon atoms of each of the ethano bridges linking the three benzene rings, as either up (u) or down (d) with respect to the adjacent phenyl ring. Conformer A has C_2 symmetry (ud/du/du), while, as shown in figure 4.2(b), conformer B is C_3 symmetric (du/du/du). According to calculations at the ωB97XD/6-311+g(d,p) level of theory, the C_3 conformer is the global minimum with the C_2

conformation 2.4 kJ/mol higher in energy. The B3LYP/6-311+g(d,p) level of theory yields the same ordering, but with a slightly greater separation of 3.0 kJ/mol.

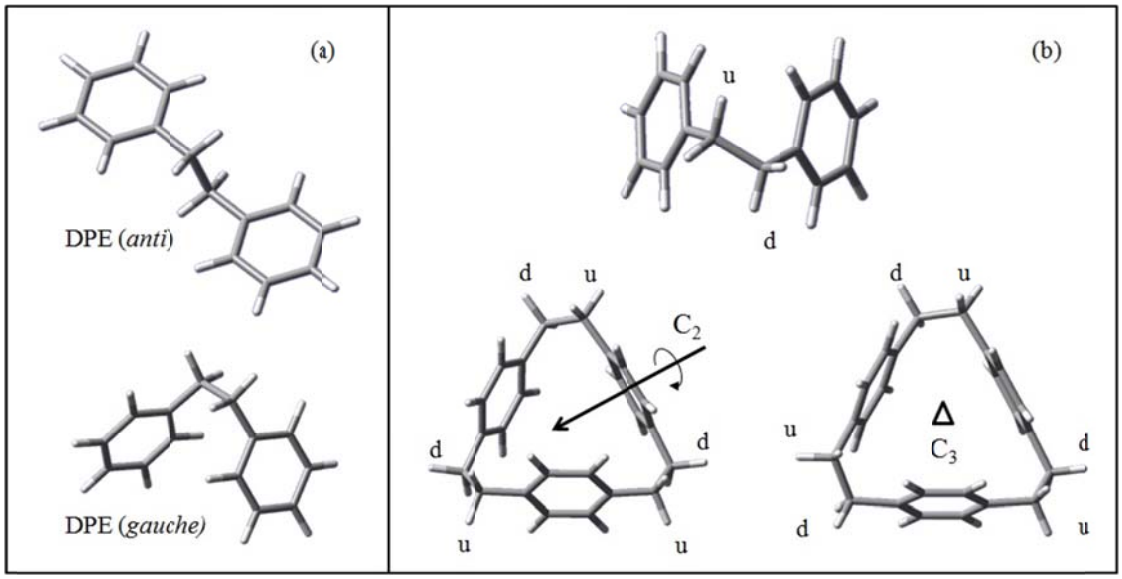

Figure 4.2 (a) Two conformers of DPE optimized at the ωB97Xd level of theory with a 6-311+g(d,p) basis set. The anti conformer has C_{2h} symmetry in which the phenyl groups lie in planes parallel to one another. The gauche conformer has C_2 symmetry. (b) The two conformers of TCP optimized at the same level of theory, differing in the geometry of the ethano bridge. The C_2 conformer is observed experimentally. A side view of the C_2 symmetric conformer is shown omitting one phenyl ring to clarify the up (u)/down (d) designation of the ethano bridge carbons relative to the rings.

Figure 4.3(a) presents the first 200 cm^{-1} of the R2PI spectrum (top trace) and two UVHB spectra (bottom traces) of DPE in the $S_0 - S_1$ origin region. The transitions used as hole-burning transitions are marked with asterisks in the figure. The UVHB spectra reveal the presence of two conformers in the supersonic jet expansion, which together account for all the observed vibronic transitions.

Figures 4.4(a) and 4.4(b) present the dispersed fluorescence (DFL) spectra from the S_1 origins of conformers A and B of DPE, respectively. Table 4.1 presents the calculated vibrational frequencies and symmetries of the low-frequency vibrations and a selected set of the ring-modes of the *gauche* and *anti* conformers of DPE. The close comparison between experiment and theory lead to an assignment of conformer A as the *gauche* conformer, and B as *anti*. First, the low-frequency vibronic structure of conformer A suggests more interaction between the two phenyl rings, consistent with the structure of the *gauche* isomer. Second, the transitions at 27 cm−1 and 47 cm^{-1} in the spectrum of conformer A (figure 4.4(a)) match well with the calculated frequencies of the two lowest frequency totally symmetric fundamentals of the *gauche* conformer (30 and 56 cm^{-1}), but are inconsistent with the *anti* structure, which has no totally symmetric fundamentals below 120 cm−1 (table 4.1). In the spectrum of conformer B, the transition at 120 cm^{-1} is assigned to this fundamental.

Finally, fundamentals due to the ring modes shift in characteristic ways, most notably in the strong bands at 763 cm^{-1} in A, that shifts to 851 cm^{-1} in B (table 4.1). These transitions are assigned to fundamentals of a ring deformationmode equivalent to ν_{12} in benzene, that has a calculated unscaled frequency of 791 cm−1 in A (23^0_1) that shifts to 874 cm^{-1} in B (26^0_1). Taken as a whole, then, the vibronic spectroscopy leads to the assignment of conformer A of DPE as the *gauche* conformer and B as the *anti* conformer (figure 4.2). These assignments are confirmed and strengthened by the successful modeling of the alkyl CH stretch region reported in the results.

Figure 4.3(b) presents the low energy region of the R2PI (top trace) and UVHB spectra (bottom) of 2,2,2-paracyclophane (tricyclophane, TCP) in the $S_0 - S_1$ origin

region. The hole-burning spectrum proves that there is only a single TCP conformer present in the supersonic jet expansion, accounting for all observed transitions. The R2PI spectrum has rather unusual vibronic activity, with Franck-Condon activity involving several low-frequency phenyl torsional modes, and a triad of rather intense transitions starting about 100 cm^{-1} above the origin transition, suggestive of the presence of vibronic coupling involving three close-lying excited electronic states. These aspects of the spectroscopy will be taken up in a future manuscript.

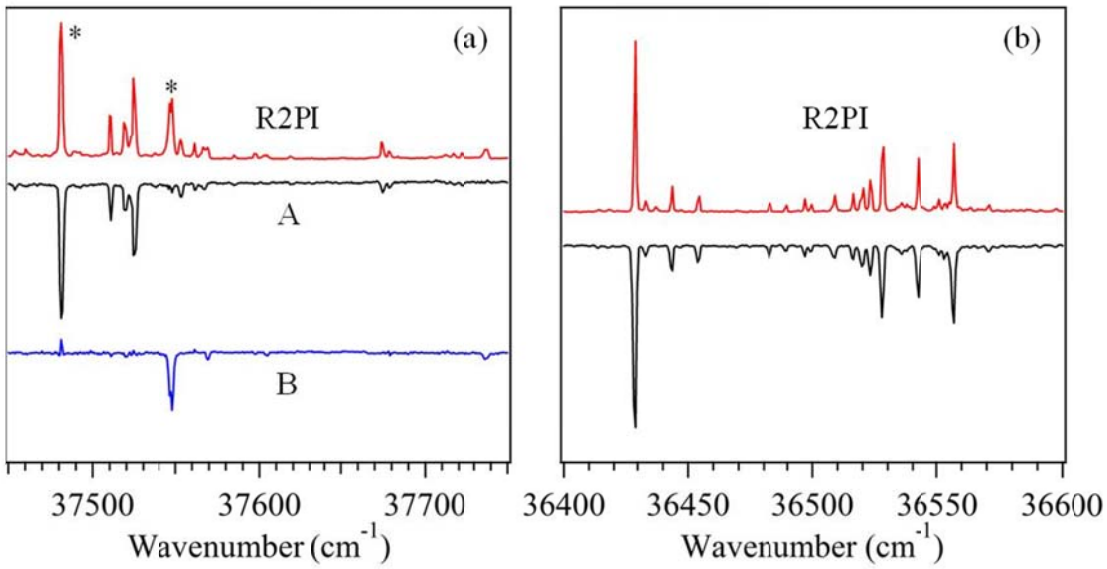

Figure 4.3 Resonant two-photon ionization spectrum of the two conformations present in the supersonic jet expansion of DPE (a) and the single conformation of TCP (b).

Table 4.1 Calculated harmonic frequencies (cm^{-1}) and symmetries for select modes of the two lowest energy conformations of DPE and TCP.

1,2-Diphenylethane (DPE)						2,2,2-Paracyclophane (TCP)					
Anti			*Gauche*			C_2			C_3		
mode #[a]	Frequency (cm^{-1})[b]	Symmetry	mode #[a]	Frequency (cm^{-1})[b]	Symmetry	mode #[a]	Frequency (cm^{-1})[b]	Symmetry	mode #[a]	Frequency (cm^{-1})[b]	Symmetry
1	19	a_u	1	30 (27)	a	1	16 (16)	b	1	36	e
2	37	a_u	2	34	b	2	32 (29)	a	2		
3	48 (49)	b_g	3	56 (47)	a	3	56 (51)	b	3	57	a
4	62	b_u	4	120	a	4	73	a	4	75	e
5	120 (120)	a_g	5	124	b	5	95	b	5		
6	240	a_g	6	239	a	6	108	a	6	138	a
15 (6b)	631 (620)	a_g	16 (6b)	639 (619)	a						
26 (12)	874 (853)	a_g	23 (12)	791 (763)	b						

[a]Varsanyi notation is given in parentheses for certain ring modes.

[b]Experimental frequencies are given in parentheses for modes referred to in the text. Calculated frequencies are not scaled.

Figure 4.4(c) shows the dispersed fluorescence spectrum from the S_1 origin of the single observed conformer of TCP. Low-frequency transitions at 16, 29, and 51 cm^{-1} are readily apparent in the spectrum. These transitions correlate well with the three lowest frequency vibrations of the C_2 conformer, with calculated frequencies of 16, 32, and 56 cm^{-1}. The assignment of the 16 cm^{-1} transition to the "b" symmetry fundamental requires vibronic coupling, and likely arises because the "A" symmetry excited state has its origin in close proximity to the B-state origin, with the "b" fundamental built off the weak A origin. As in DPE, the alkyl CH stretch region provides strong additional evidence for the assignment of the observed conformer of TCP as the C_2 symmetry conformer, but this only after developing the theoretical model that is the primary subject of this chapter.

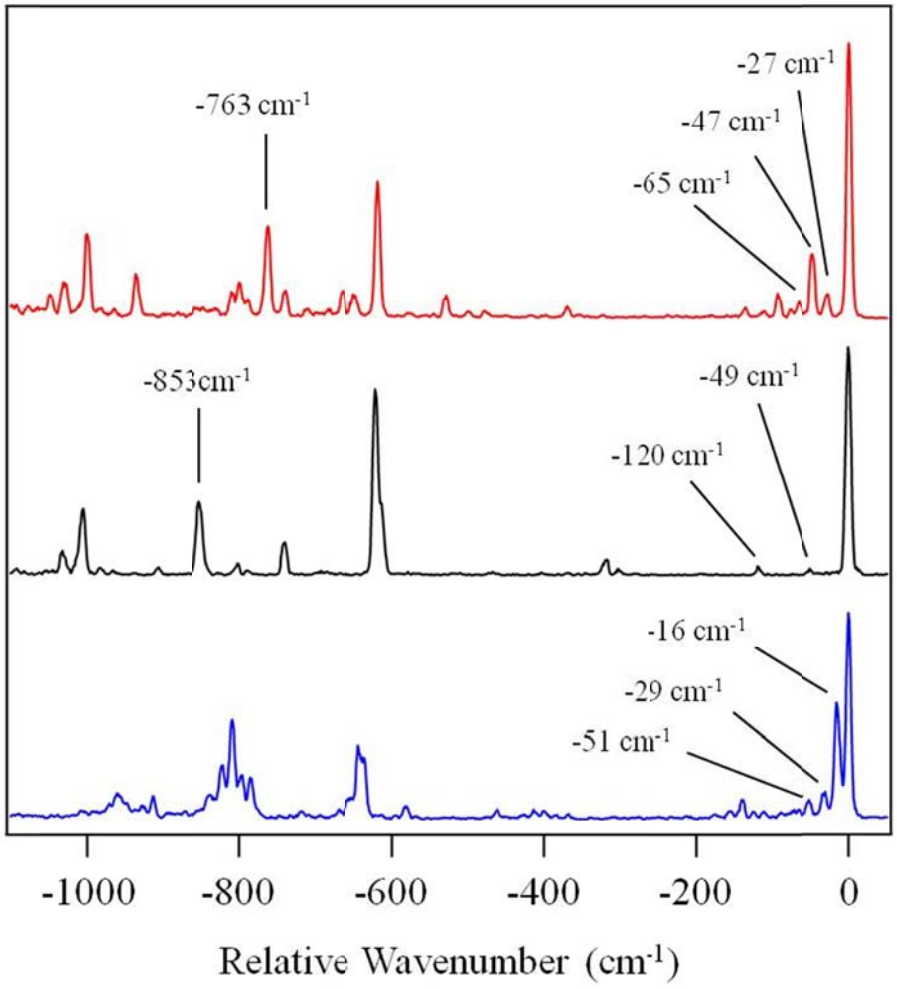

Figure 4.4 Dispersed Fluorescence spectra of the S1 origins of the gauche (a) and anti (b) isomers of DPE, and (c) the C2 symmetry conformer of TCP. The low frequency and ring mode transitions used to assign the conformations are labeled.

Table 4.2 Coordinate definitions for the stretches R_{ij} , bends θ_{ijk}, and dihedral angles ϕ_{ijkl} based on the numbering scheme presented in figure 4.5.

i	*j*	R_{ij}	*k*	θ_{ijk}	*l*	ϕ_{ijkl}
2	1	S_{13}				
3	2	S_{14}	1	S_{15}		
4	3	S_{16}	2	S_{17}	1	S_{18}
5	2	S_1	3	S_5	4	S_6
6	2	S_2	3	S_7	4	S_8
7	3	S_3	2	S_9	1	S_{10}
8	3	S_4	2	S_{11}	1	S_{12}

4.3 Theoretical Model

In this section, we model the CH spectral region using as a starting point a quadratic local mode alkyl CH stretch Hamiltonian that yields eigenvalues and transition intensities that are essentially the same as those of the full normal mode Hamiltonian. We then determine the anharmonic couplings to the states that are likely to be in resonance.

4.3.1 Harmonic Analysis

There are two approaches to calculating normal modes. In the simplest approach, for an N particle system one calculates the $3N\times3N$ Hessian $Vij = \partial^2 V/\partial qi\partial qj$, where $\mathbf{q}$ are the mass weighted Cartesian coordinates and V ($\mathbf{q}$) is the potential. Diagonalization of this matrix, $\mathbf{U}\mathbf{V}\mathbf{U}^T$ provides a direct route to the normal modes via $\mathbf{Q} = \mathbf{U}\mathbf{q}$.

The alternative approach, referred to as the Wilson FG matrix approach,[49] involves choosing a set of internal coordinates **S** and expressing the vibrational Hamiltonian in terms of them and their conjugate momenta. Since we are using GAUSSIAN09[50] for our electronic structure calculations, our internal coordinates are chosen to coincide with the **Z**-matrix shown in Table 4.2 where the numbering scheme corresponds to the structure in Figure 4.5. With these definitions, the CH stretch coordinates are $\{S_1, S_2, S_3, S_4\} = \{R_{52}, R_{62}, R_{73}, R_{83}\}$. Having defined the coordinates, one determines the transformation matrix between internal coordinates and mass weighted Cartesian coordinates **S** = **Bq**. This **B**-matrix can be constructed analytically using geometrical considerations.[49] If one includes the center of mass coordinates and rotational constraints such as those of Eckart,[49] along with the true internal coordinates, the **B**-matrix can be inverted. The harmonic contribution to the internal coordinate Hamiltonian is

$$H^{HO} = \frac{1}{2}\left[\sum_{i=1}^{3N-6}\sum_{j=1}^{3N-6} P_i G_{ij} P_j + S_i F_{ij} S_j\right] \tag{1}$$

where

$$G = B^T B \tag{2}$$

and

$$F = \left[B^{-1}\right]^T V B^{-1} \tag{3}$$

The elements of the **G**-matrix are obtained from geometrical considerations,[49] and the Hessian **V** is obtained with electronic structure programs.

We partition *HHO* into three parts

$$H^{HO} = H_{LM} + H_{NM} + W \tag{4}$$

The first contribution describes the L = 4 CH stretches {S_1,S_2, S_3, S_4. The second contribution H_{NM} is composed of the $M = (3N - 6) - L$ modes that describe the remaining vibrations. These modes are transformed to the normal coordinates and conjugate momenta {**Q**, **p**} to yield

$$H_{NM} = \frac{1}{2}\sum_{i=1}^{M}\left[P_i^2 + \omega_i^2 Q_i^2\right] \tag{5}$$

The coupling contribution takes the form

$$W = \sum_{i=1}^{L}\sum_{i'=1}^{M}\left[P_i g_{ii'} p_{i'} + S_i f_{ii'} Q_{i'}\right] \tag{6}$$

The normal mode transformation is necessary, due to the large couplings between these modes.

The simplest local mode approach is to ignore the coupling W, transform the H_{LM} to raising and lowering operators and ignore the stretch-stretch coupling terms of the form [$a_i^\dagger a_j^\dagger$ + *h.c.*]. With this approximation, the fundamentals can be described using a local mode basis $\left|\upsilon_1,\upsilon_2,\upsilon_3,\cdots\upsilon_L\right\rangle$, that consist of L basis functions with

$$N_L = \sum_{i}^{L}\upsilon_i = 1 \tag{7}$$

These are good approximations due the frequency mismatch between the CH stretches and the remaining degrees of freedom and the weak coupling between CH stretches. An alternative approach is to develop a CH stretch Hamiltonian that has incorporated into it the effects of the coupling to the remaining *M* degrees of freedom. Canonical Van Vleck perturbation theory (CVPT)[51-52] can be used to obtain such a representation.

Transforming *HHO* to raising and lowering operators, CVPT is used to transform away the bilinear terms that couple local modes to normal modes as well as localmode couplings $[a_i^{\dagger}a_j^{\dagger} + h.c.]$. . We refer to this Hamiltonianas a "dressed" H^{dr}_{LM} Hamiltonian since, at second order, it has the same form as the original, but its coefficients have changed to account for the coupling to the remaining degrees of freedom.[53]

The intensities of the transitions are also affected by the coupling between the high and low frequency modes. For this reason, we also "dress" the dipole derivatives using Van Vleck perturbation theory.[54-56]

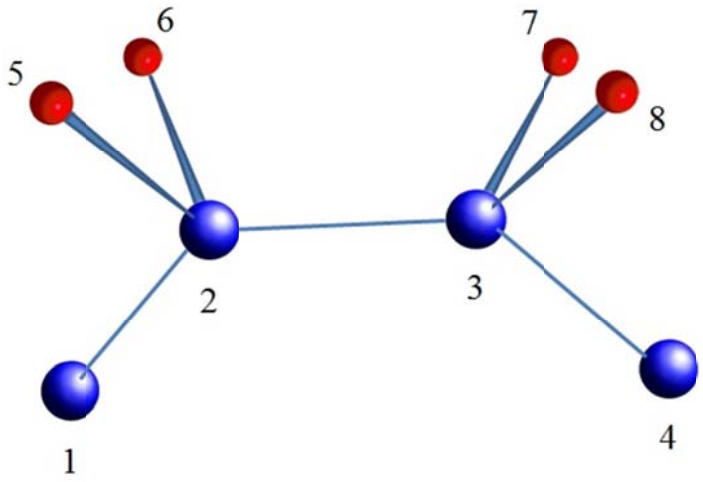

Figure 4.5 Bend and Stretch coordinates included in the anharmonic calculations.

We compare the local mode treatments in Table 4.3 for the difluoroethane molecule in the gauche configuration. This molecule belongs to the C_2 point group. The two lower energy transitions correspond to symmetric CH_2 excitation, and the two higher transitions correspond to asymmetric CH_2 modes. These results were obtained with

GAUSSIAN09[50] using a hessian calculated with DFT using the B3LYP functional and the 6-311+G(d,p) basis. We have found similar results for all the molecules included in this investigation. One can see that while the local mode Hamiltonian is good, except for some of the intensities, the dressed local mode is in quantitative agreement with the normal mode Hamiltonian. This representation provides the interpretive advantages of the localized representation, yet retains all of the information included in the full normal mode analysis.

Table 4.3 Comparison of eigenvalues (cm^{-1}) and intensities (KM/mol) of 1,2-difluoroethane in the gauche configuration for the local mode Hamiltonian, the dressed local mode Hamiltonian, and normal mode Hamiltonian HHO obtained using the GAUSSIAN09 package.[52]

Sym.	E_{LM}	I_{LM}	E_{LM}^{dr}	I_{LM}^{dr}	E_{HO}	I_{HO}
b	3048.8	6.0	3037.3	8.2	3037.1	8.2
a	3057.0	31.2	3047.7	38.8	3047.8	39.0
a	3105.1	7.4	3093.0	13.1	3092.8	13.1
b	3111.3	30.4	3106.3	35.0	3106.1	35.0

4.3.2 Fermi Coupling

We have calculated the cubic coupling contributions to the Fermi interactions in both rectilinear and curvilinear representations. We show an example comparison in the Appendix. The magnitudes of the couplings to nearly degenerate states tend to be similar in both representations.

However, for lower frequency modes, we find that the curvilinear coordinates lead to smaller couplings, hence this representation is used throughout.

The cubic potential is expressed as

$$V = \sum_{i=1}^{4}\sum_{j=5}^{12}\sum_{k=5}^{12} F_{ijk} S_i S_j S_k \qquad (8)$$

The coordinates include those associated with the motions of the H-atoms of the ethano-bridge described in that last four lines of Table 4.2. Only those terms that are linear in the alkyl CH stretches and bilinear in the bend and dihedral angles are calculated. The force constants, which are calculated using finite difference methods, are projected onto the modes mixed local-normal coordinates of Eq. 3. In order to calculate a spectrum associated with the CH stretches anharmonically coupled to the normal mode degrees of freedom, we set up and diagonalize a vibrational Hamiltonian that contains the CH stretch fundamental and all combination states and overtones with a total of two quanta of excitation and whose energies are within an energy window centered at the energy of the fundamental. The size of the window is increased until the spectrum is converged.

4.4 Results

The above described procedure was applied to the two conformers of DPE and TCP shown in figures 2(a) and 2(b), respectively. In this section, we describe the results of these calculations, beginning with several simplifications.

The normal modes of DPE and TCP that are predominantly localized on the ethano bridge vibrational degrees of freedom typically have small admixtures of ring

modes. These mixings lead to additional lines in the eigenstate resolved spectra. However, at lower resolution, there is minimal difference between model calculations that include the ring modes and those that do not. The ring modes can be decoupled by doubling both the carbon and hydrogen masses of the atoms in the phenyl rings. A simple example serves to illustrate the consequences of this doubling. The unscaled Gaussian B3LYP calculation of *anti*-DPE yields two modes that are predominantly ring modes at 1481.8 and 1482.6 cm^{-1} as well as two modes that are predominantly the in-phase and out-of-phase scissor modes at 1486.1 and 1503.5 cm^{-1}, respectively. Doubling the phenyl carbon and hydrogen masses leads to scissor modes with frequencies 1485.4 and 1502.7 cm^{-1}, respectively. This shift upon mass doubling is a measure of the coupling between the scissor modes and the modes of the two phenyl rings. Since the alkyl CH stretches have smaller couplings and larger energy mismatches between alkyl and phenyl CH stretches, this step has negligible consequences.

The four CH stretches are anharmonically coupled to normal modes that are linear combinations of the ethano bridge bending and dihedral angles. The relevant normal modes are those involving HCH bending and twisting, the highest frequency of which are the scissor modes [e.g., mode 5 of Figure 4.9]. By comparing calculations with and without the lower frequency modes, we find that only the scissor modes are relevant in the calculation of the spectra. With this approximation, the dressed Hamiltonian for the *anti*-DPE conformer is

$$H_a^{dr} = \begin{pmatrix} 3048 & & & & & & \\ -19 & 3048 & & & & & \\ 3 & -8 & 3048 & & & & \\ -8 & 3 & -19 & 3048 & & & \\ -1 & -1 & 32 & 32 & 2988 & & \\ 0 & 0 & 0 & 0 & -12 & 2988 & \\ 32 & 32 & -1 & -1 & 0 & -12 & 2988 \end{pmatrix} \tag{9}$$

The Hamiltonian subscript serves to identify the conformer, the *anti* and *gauche* conformers labeled *a* and *g*, respectively. This 7 × 7 matrix includes the four CH stretch local modes and overtones and a combination band of the scissor modes. We begin with a discussion of the stretches. For the *anti* conformer all the CH stretches have the same environment, hence the first four diagonal elements are the same. Hydrogen atoms 1 and 2 form one CH_2 group, and hydrogen atoms 3 and 4 form the other. As expected the most significant coupling between the CH stretches is for those that share a carbon atom. The next most important coupling, which is −8 cm^{-1}, is between CH stretches that are *trans* to one other.

The nature of the coupling to the scissor modes is most apparent in a fully local representation, so we have taken plus/minus linear combinations of the in- and out-of-phase scissor normal modes to obtain scissor modes that correspond to motion on the individual CH_2 groups. If $|n_{s1}, n_{s2}\rangle$ represent the localized scissor mode kets, then the three scissor states of relevance are $|5\rangle = |0,2\rangle, |6\rangle = |1,1\rangle$ and $|7\rangle = |2,0\rangle$. Now the only significant Fermi coupling, which is 32 cm^{-1}, occurs between the stretches and scissor overtones of the individual CH_2 groups. Transforming to the local scissor mode representation leads to a 12 cm^{-1} bilinear coupling between these modes.

Similar Hamiltonians, to be discussed below, are obtained for the other conformer of DPE and those of TCP. In order for these Hamiltonians to have predictive spectroscopic accuracy, some of their parameters need to be scaled. We carry out this scaling using the above described *anti* conformer, fitting its calculated spectrum to the experimental one. This conformer is chosen since its spectrum is the easiest to assign and interpret. Having determined the fit parameters, the remaining Hamiltonians can be scaled in order to make predictions that are then compared to experiment.

We first scale all the internal force constants by 0.984, this being a scaling factor that yields good scissor fundamental frequencies for 1,2-difluoroethane[57] for calculations carried out with the B3LYP/6-311+G(d,p) method. We then include four additional scaling factors: the CH force constants are scaled by α_{CH}; the cubic Fermi coupling terms are scaled by α_{FC}; the matrix elements of CH stretch Hamiltonian H_{LM} are scaled as $H_{ij} = \beta H_{ij} + (1-\beta)\overline{E}\delta_{ij}$ is the average of the CH stretch zero-order frequencies. This choice leaves $\overline{E}$ unaffected by the β scaling. Finally, we include a diagonal anharmonicity (E_{anh}) of the local scissor modes, so that the overtones are not resonant with the combination band. These parameters are determined by adjusting the constants to fit the experimental spectrum of a single conformer. In the absence of the Fermi resonance, adjusting α_{CH} and β would allow one to fit exactly the two observed CH stretch transition frequencies. In the presence of the scissors mode, there is Fermi coupling. In order to get both the relative intensity sharing and the separation of the two Fermi coupled states, we adjust the position of the scissor modes with E_{anh} and the strength of the Fermi coupling using α_{FC}. We obtain $\{\alpha_{CH}, \alpha_{FC}, \beta, E_{anh}\}$={0.9595, 0.68,

0.85, -47cm^{-1}}. The 0.68 scaling factor for the Fermi coupling is, at first glance, surprising. However, the discrepancy between matrix elements calculated directly from cubic coupling terms and those obtained from effective Hamiltonians, by fitting parameters to spectral data, has been noted previously. For example, McCoy and Sibert[58] using curvilinear normal coordinates showed that the magnitude of the symmetric stretch fundamental to bend overtone matrix element in H_2O decreased from 54.9 to 36.8 cm^{-1} in going from second to eighth order perturbation theory. The decrease from the former value, obtained directly from the cubic coupling terms, is a result of indirect cubic coupling terms whose contributions enter at higher order perturbation theory. The latter value agrees well with the 37.6 cm^{-1} value obtained from a parameter fit of an effective Hamiltonian.[59] The anharmonicity is also relatively large. We note that our results are sensitive to the position of the overtone, which depends on both the harmonic frequency and anharmonicity. We have used a frequency scaling for the scissor modes based on 1,2-difluoroethane. If our scaled scissor frequencies are too high, this would explain the larger than expected anharmonicity value.

After scaling the Hamiltonian takes the form below

$$H_a^{dr} = \begin{pmatrix} 2925 & & & & & & \\ -15 & 2925 & & & & & \\ 3 & -7 & 2925 & & & & \\ -7 & 3 & -15 & 2925 & & & \\ -1 & -1 & 21 & 21 & 2993 & & \\ 0 & 0 & 0 & 0 & -12 & 2940 & \\ 21 & 21 & -1 & -1 & 0 & -12 & 2993 \end{pmatrix} \qquad (10)$$

The corresponding Hamiltonian for the *gauche* conformer has the form

$$H_a^{dr} = \begin{pmatrix} 2927 & & & & & & \\ -15 & 2917 & & & & & \\ -8 & 3 & 2927 & & & & \\ 3 & 4 & -15 & 2917 & & & \\ 21 & 21 & 0 & 1 & 2886 & & \\ 0 & 0 & 0 & 0 & -2 & 2933 & \\ 0 & 1 & 21 & 21 & 0 & -2 & 2886 \end{pmatrix} \tag{11}$$

Comparing the Hamiltonians of these two conformers there are several points worth noting. In contrast to the *anti* conformer, the CH stretches of the *gauche* do not have equivalent environments. The strength of the Fermi coupling is the same for both conformers. There is substantially less coupling between the localized scissor modes for the *gauche* conformer.

In order to understand how these changes lead to spectra changes, we transform the stretch basis as follows:

$$\begin{aligned} |\Psi_1\rangle &= [(|1\rangle + |2\rangle) + (|3\rangle + |4\rangle)] \\ |\Psi_2\rangle &= [(|1\rangle + |2\rangle) - (|3\rangle + |4\rangle)] \\ |\Psi_3\rangle &= [(|1\rangle - |2\rangle) - (|3\rangle - |4\rangle)] \\ |\Psi_4\rangle &= [(|1\rangle - |2\rangle) + (|3\rangle - |4\rangle)] \end{aligned} \tag{12}$$

For the C_{2h} conformer, these states have a_g, b_u, b_g, and a_u symmetry, respectively. For the C_2 conformer they have a, b, b, and a symmetry, respectively. The scissor basis are also symmetrized as

$$\begin{aligned} |\Psi_5\rangle &= |2,0\rangle^+ = [|2,0\rangle + |0,2\rangle]/\sqrt{2} \\ |\Psi_6\rangle &= |1,1\rangle \\ |\Psi_5\rangle &= |2,0\rangle^- = [|2,0\rangle - |0,2\rangle]/\sqrt{2} \end{aligned} \tag{13}$$

where the first two states have a_g and a symmetry for the C_{2h} and C_2 conformers, respectively, while ψ_7 has b_u and b symmetry. For the *anti* conformer, the stretch contribution of the Hamiltonian becomes diagonal since the four states of Eq. 10 transform according to distinct irreducible representations of this C_{2h} molecule. Moreover, a little analysis shows that the 2 infrared active states correspond to the stretches $|\Psi_2\rangle$ and $|\Psi_4\rangle$. In the absence of Fermi coupling, the energies and intensities are shown graphically in Figure 4.6. The oscillator strengths of the symmetrized CH stretch states fundamentals of Eq. 10 are indicated by the vertical width of the boxes centered at their corresponding transition energies.

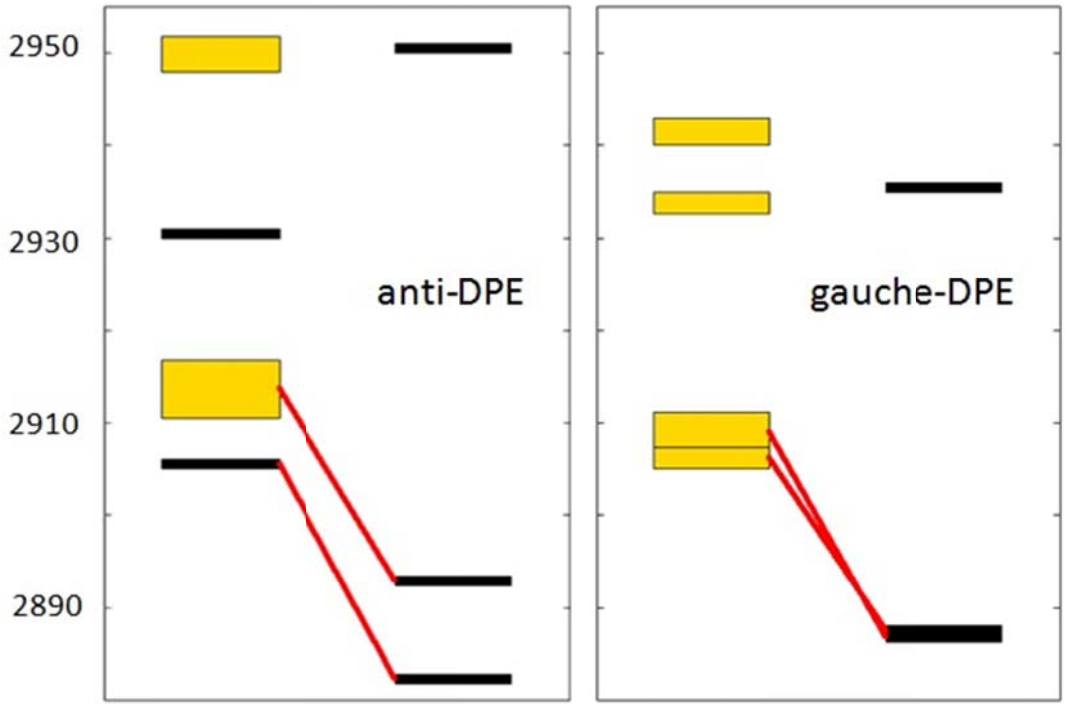

Figure 4.6 Comparison of stretch/scissor energetics and couplings for *anti*-DPE and *gauche*-DPE. The width of the CH stretch states is proportional to the oscillator strength, and the vertical center of the box corresponds to the transition energies associated with the states of Eq. (10). For the *gauche* conformer, these energies are 2909, 2906, 2942, and 2934 cm-1. The width of the lines connecting CH stretches to scissor overtones and combinations is proportional to the associated couplings.

The Hamiltonian matrix $H^{dr}{}_{g}$ in the symmetrized basis of Eqs. 10−11 is

$$H_g^{dr} = \begin{pmatrix} 2908 & & & & & & \\ 0 & 2905 & & & & & \\ 0 & 11 & 2941 & & & & \\ 0 & 0 & 0 & 2933 & & & \\ 30 & 0 & 0 & -2 & 2886 & & \\ 0 & 0 & 0 & -1 & -3 & 2933 & \\ 0 & 29 & 1 & 0 & 0 & 0 & 2886 \end{pmatrix} \qquad (14)$$

For the *gauche* conformer the only appreciable coupling between the CH stretches is the 11 cm^{-1} coupling between the *b* symmetry states at 2905 and 2941 cm^{-1}. The coupling between that *a* symmetry states $|\Psi_1\rangle$ and $|\Psi_4\rangle$ is only −0.2 cm^{-1}. As a result, the symmetrized states are close approximations to the eigenstates of the dressed Hamiltonian, with the result that the left side of the panels in Figure 4.6 contain the same information as is given in the dressed local mode spectra. These in turn are what one would obtain in the normal mode limit with scaling.

We now return to the role of the Fermi resonance interactions. The right side of each panel includes the scissor states obtained by diagonalizing the scissor Hamiltonian. This Hamiltonian corresponds to the last three rows and columns of the above Hamiltonian matrices. The significantly larger quadratic coupling (12 versus 2 cm^{-1}) between the scissor states for *anti*-DPE compared to *gauche*-DPE is the reason for the different splitting between the two lowest scissor states.

The spectra that result from the coupling schemes depicted in Figure 4.6 are shown in Figures 4.7(a) and 4.7(b). Also shown are the corresponding experimental spectra. The agreement in (a) is expected, since the spectrum has been fit using the parameters described above and whose best fit values are given in the figure caption. The left side panel of Figure 4.6 indicates that one expects the *anti* conformer spectrum to consist of three lines. The highest frequency corresponds to $|\Psi_4\rangle$. The next two lines are part of a Fermi dyad, being admixtures of $|\Psi_2\rangle$ and $|\Psi_7\rangle$. The relative intensities of the two highest peaks are similar to those found experimentally. The differences are ameasure of the quality of the DFT calculated dipole derivatives, as none of the dipole

derivatives have been adjusted in this study. For the *gauche* conformer, one expects six lines, two at low frequencies, and 4 at high frequencies, and this is what is calculated. The lowest energy line is composed of two unresolved lines.

We now turn to the TCP molecule. An inspection of the structures in Figure 4.2 shows that the three ethano bridges have similar *gauche* configurations, hence we expect that distinguishing between the two TCP conformers should be substantially more challenging than distinguishing between those of DPE. To highlight this similarity, we show the spectral results for the harmonic Hamiltonian model in Figure 4.8 along with the experimental result. We find that at this level of theory the alkly CH spectra are so similar that they do not serve to distinguish between the two conformers of TCP. The role of the Fermi coupling must be considered. This same conclusion is reached from a normal mode analysis, since with the neglect of Fermi coupling our results are indistinguishable from the normal mode results with scaled CH stretch frequencies.

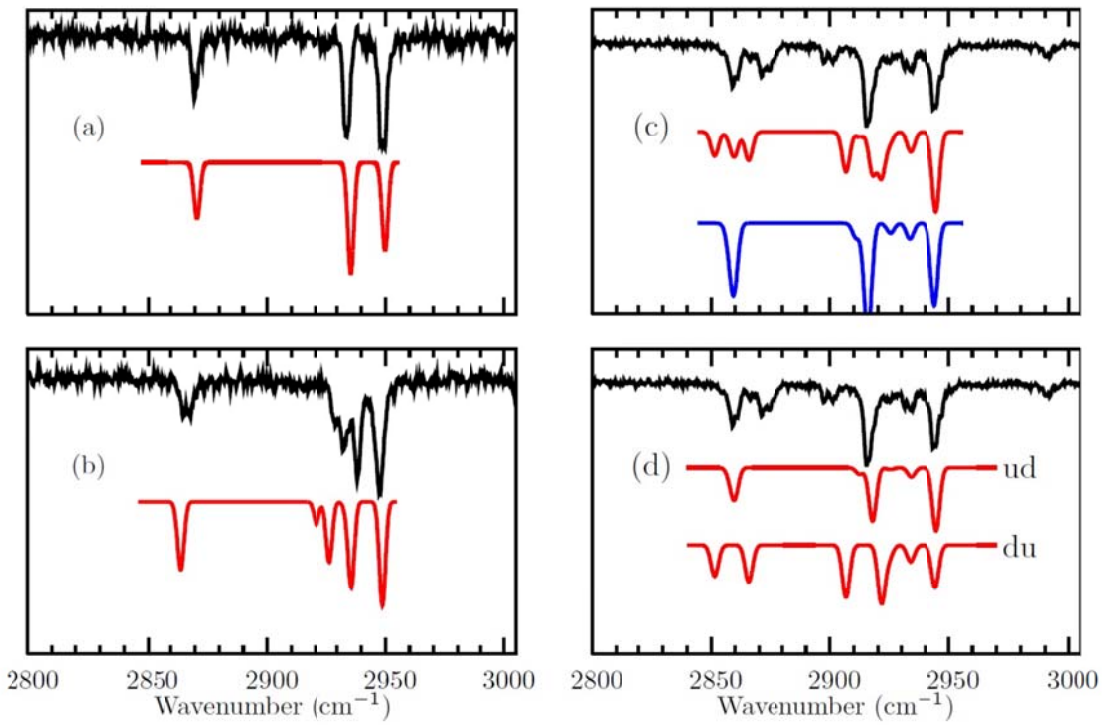

Figure 4.7 Comparison of the experimental (upper line) and theoretical spectra for (a) anti-DPE, (b) gauche-DPE, and (c) TCP. In each panel, the top curve is experimental result. In (c) the C2 symmetry TCP conformer result is shown in red, while that for the C3 conformer is shown in blue. (d) shows the ud (middle) and du (lower) contributions to the TCP C2 conformer spectrum. Note the close similarity between the ud result and the spectrum obtained for conformer C3. Scaling factors for the B3LYP/6-311+(d,p) calculations areαCH = 0.9595, αFC = 0.68, β = 0.85, and Eanh = −47 cm^{-1}. The theoretical spectra are calculated assuming Gaussian lineshapes, where the width is chosen to match approximately the widths of the experimental lines.

Given the usefulness of the local mode representation for interpreting the DPE spectra, we wish to continue employing it for the analysis of TCP. Due to the presence of multiple ethano bridges, there is an additional step required to achieve localization. The normal modes with scissor character are not localized on individual ethano bridges; thus, one must determine the appropriate linear combinations of scissor normal modes that provides localization. There are many ways of doing this. We achieve the desired

localization by adding $n\varepsilon$ to each of the diagonal G-matrix elements. Here, n takes a different value (0, 1, or 2) depending on the $-CH_2CH_2-$ bridge with which the internal coordinate is associated, and the value of ε is large enough to localized the resulting normal modes. This procedure determines the transformation between normal and local modes of the altered Hamiltonian. When applied to the $\varepsilon = 0$ Hamiltonian one obtains the same modes but with slightly different diagonal frequencies and the inclusion of small couplings between the modes of differing ethano bridges. For a wide range of ε values, these couplings, are insensitiveto the value of ε. Moreover, all these couplings are all less than a wavenumber, hence they can be ignored in the analysis. This localization step does not visibly change the displayed spectra, but does greatly simplify the analysis.

Inspection of Figure 4.2(b) shows that one of the ethano bridges rotates into the other under C_2 rotation, whereas the third ethano bridge rotates into itself. We will refer to the former as the du ethano bridges and the latter as the ud ethano bridge. There are two scaled stretch-scissor Fermi coupled ethano bridge Hamiltonians for TCP, one for the ud bridge

$$H_{ud}^{dr} = \begin{pmatrix} 2902 & & & & & & \\ -13 & 2902 & & & & & \\ 4 & -6 & 2926 & & & & \\ 3 & 4 & -12 & 2902 & & & \\ 21 & 21 & 21 & 21 & 2884 & & \\ 0 & 0 & 0 & 0 & 6 & 2930 & \\ 1 & 0 & 0 & 1 & 0 & 6 & 2884 \end{pmatrix} \qquad (15)$$

and the other for the two du bridges

$$H_{du}^{dr} = \begin{pmatrix} 2909 & & & & & & \\ -13 & 2926 & & & & & \\ 4 & -6 & 2923 & & & & \\ 3 & 4 & -12 & 2895 & & & \\ 1 & 0 & 21 & 21 & 2874 & & \\ 0 & 0 & 0 & 0 & 6 & 2930 & \\ 21 & 22 & 0 & 1 & 0 & 6 & 2892 \end{pmatrix} \qquad (16)$$

Comparing these Hamiltonians to the *gauche* conformer of DPE, there are several similar features. The cubic couplings are almost identical. Apparently, these couplings, whose determination is the most time consuming part of the calculation, are transferable from one system to another for this class of molecules. A second similarity is that the H^{dr}_{ud} Hamiltonian has the same structure as *gauche*-DPE, this being expected by symmetry. There are also some differences. The two local CH environments lead to a greater frequency difference between CH stretches in TCP than in *gauche*-DPE. We consistently find that the CHs that are closer to parallel to the plane of the benzene ring have higher frequencies.

Combining the above ud and du Hamiltonian resultsgives the middle spectrum in Figure 4.7(c). Although the agreement is not as good as that found for the *gauche* conformer of DPE shown in (b), one can clearly correlate the peaks in the theoretical spectrum with those of the experiment. The individual contributions to the C_2 TCP spectrum are given in the lower two lines of Figure 4.7(d), with the middle line corresponding to H^{dr}_{ud} and the bottom line corresponding to H^{dr}_{du}. Interestingly, the ud contribution is nearly identical to the C^3 TCP conformer result displayed on the bottom line of figure 4.7(c). In this higher symmetry conformer, all three ethano bridge Hamiltonians are found to be essentially the same, and they are all similar to the ud

Hamiltonian of Eq. 13. This leads to a predicted C_3 conformer spectrum with fewer lines than observed in the experimental spectrum. The calculated spectra strongly suggest that the conformer observed experimentally is the C_2 conformer, a result that is consistent with the conformational assignments described in Sec. II. It is worth considering why the Fermi resonances enable us to distinguish between conformers. In the absence of Fermi coupling (figure 4.8), the C_2 and C_3 conformers are very similar, with the peaks of the C_2 conformer being slightly broader, since the lines of the ud and du ethano bridges are separated by about 4 cm^{-1}. This result could have been anticipated by comparing the CH stretch contribution of the Hamiltonian matrices of Eqs. 13 and 14. The latter has two CH stretch diagonal elements at 2895 and 2909 cm^{-1}, while the former has the corresponding elements both at 2902 cm^{-1}. This difference, however, is reduced by the presence of the 3 cm^{-1} coupling between the CH stretch states, leading to a spectrum with just three readily resolved peaks. As an aside there is also a very weak set of transitions corresponding to the excitation of the asymmetric stretch $|\Psi_4\rangle$. The more significant difference between the ud and du ethano bridges is found for the scissor overtones that are degenerate for the former and separated by 18 cm^{-1} for the latter. It is this large difference in combination with Fermi coupling that enables one to distinguish the conformers of TCP.

4.5 Conclusions

This paper presents a theoretical model of the alkyl CH stretch vibrations for use as a probe for distinguishing between conformers of relatively complex molecular

systems. The conformers of the relatively complex molecules 1,2-diphenylethane and 2,2,2-paracyclophane were used to illustrate the accuracy and limitations of the model. The model is based on a local mode representation in which CH oscillators couple to themselves and to nearly resonant states. We find that single-conformation spectra reported here are insensitive to the rings modes and that simple model Hamiltonians, which include CH stretches Fermi coupled to nearby scissor modes, are adequate for describing the distinguishing spectral features. The parameters of the Hamiltonian, which are initially calculated using density functional theory methods, serve as a starting point for our analysis. Select parameters are then scaled to fit the spectrum of one the conformers of 1,2-diphenylethane. Assuming the scaling factors are transferable, allows us to generate spectra for the remaining conformer of DPE, the single observed conformer of TCP, and provides predictions for the C_3 conformer of TCP, which was not observed experimentally. The simple, physically intuitive picture provided by this model shows promise for its application to a wider range of flexible molecules. Among the targets for future work are the crown ethers,[12-13, 60] short peptides,[61-62] and model lignin compounds[63] for which single-conformation data are becoming available.

4.6 References

1. Baquero, E. E.; James, W. H., III; Choi, S. H.; Gellman, S. H.; Zwier, T. S. Single-conformation ultraviolet and infrared spectroscopy of model synthetic foldamers: beta-peptides Ac-beta(3)-hPhe-NHMe and Ac-beta(3)-hTyr-NHMe. *Journal of the American Chemical Society* **2008,** *130* (14), 4784-4794.

2. James, W. H., III; Baquero, E. E.; Shubert, V. A.; Choi, S. H.; Gellman, S. H.; Zwier, T. S. Single-Conformation and Diastereomer Specific Ultraviolet and Infrared Spectroscopy of Model Synthetic Foldamers: alpha/beta-Peptides. *Journal of the American Chemical Society* **2009,** *131* (18), 6574-6590.

3. James, W. H., III; Buchanan, E. G.; Guo, L.; Geman, S. H.; Zwier, T. S. Competition between Amide Stacking and Intramolecular H Bonds in gamma-Peptide Derivatives: Controlling Nearest-Neighbor Preferences. *J. Phys. Chem. A* **2011,** *115* (43), 11960-11970.

4. Chin, W.; Piuzzi, F.; Dimicoli, I.; Mons, M. Probing the competition between secondary structures and local preferences in gas phase isolated peptide backbones. *Phys. Chem. Chem. Phys.* **2006,** *8* (9), 1033-1048.

5. Fricke, H.; Funk, A.; Schrader, T.; Gerhards, M. Investigation of secondary structure elements by IR/UV double resonance spectroscopy: Analysis of an isolated beta-sheet model system. *Journal of the American Chemical Society* **2008,** *130* (14), 4692-4698.

6. Rijs, A. M.; Kabelac, M.; Abo-Riziq, A.; Hobza, P.; de Vries, M. S. Isolated Gramicidin Peptides Probed by IR Spectroscopy. *ChemPhysChem* **2011,** *12* (10), 1816-1821.

7. Simons, J. P.; Davis, B. G.; Cocinero, E. J.; Gamblin, D. P.; Stanca-Kaposta, E. C. Conformational change and selectivity in explicitly hydrated carbohydrates. *Tetrahedron-Asymmetry* **2009,** *20* (6-8), 718-722.

8. Crews, B. O.; Abo-Riziq, A.; Pluhackova, K.; Thompson, P.; Hill, G.; Hobza, P.; de Vries, M. S. Guanine-aspartic acid interactions probed with IR-UV resonance spectroscopy. *Phys. Chem. Chem. Phys.* **2010,** *12* (14), 3597-3605.

9. Carney, J. R.; Zwier, T. S. Conformational flexibility in small biomolecules: tryptamine and 3-indole-propionic acid. *Chem. Phys. Lett.* **2001,** *341* (1-2), 77-85.

10. LeGreve, T. A.; Baquero, E. E.; Zwier, T. S. Infrared and ultraviolet spectral signatures and conformational preferences of jet-cooled serotonin. *Journal of the American Chemical Society* **2007,** *129* (13), 4028-4038.

11. Kusaka, R.; Inokuchi, Y.; Ebata, T. Laser spectroscopic study on the conformations and the hydrated structures of benzo-18-crown-6-ether and dibenzo-18-crown-6-ether in supersonic jets. *Phys. Chem. Chem. Phys.* **2007,** *9* (32), 4452-4459.

12. Kusaka, R.; Inokuchi, Y.; Ebata, T. Structure of hydrated clusters of dibenzo-18-crown-6-ether in a supersonic jet-encapsulation of water molecules in the crown cavity. *Phys. Chem. Chem. Phys.* **2008,** *10* (41), 6238-6244.

13. Shubert, V. A.; James, W. H., III; Zwier, T. S. Jet-Cooled Electronic and Vibrational Spectroscopy of Crown Ethers: Benzo-15-Crown-5 Ether and 4 '-Amino-Benzo-15-Crown-5 Ether. *J. Phys. Chem. A* **2009,** *113* (28), 8055-8066.

14. Benitez, J. J.; San-Miguel, M. A.; Dominguez-Meister, S.; Heredia-Guerrero, J. A.; Salmeron, M. Structure and Chemical State of Octadecylamine Self-Assembled Monolayers on Mica. *Journal of Physical Chemistry C* **2011,** *115* (40), 19716-19723.

15. Brindza, M. R.; Ding, F.; Fourkas, J. T.; Walker, R. A. n-alkane adsorption to polar silica surfaces. *Journal of Chemical Physics* **2010,** *132* (11).

16. Carney, J. R.; Zwier, T. S. The infrared and ultraviolet spectra of individual conformational isomers of biomolecules: Tryptamine. *J. Phys. Chem. A* **2000,** *104* (38), 8677-8688.

17. Gruenloh, C. J.; Florio, G. M.; Carney, J. R.; Hagemeister, F. C.; Zwier, T. S. C-H stretch modes as a probe of H-bonding in methanol-containing clusters. *J. Phys. Chem. A* **1999,** *103* (4), 496-502.

18. Ji, N.; Ostroverkhov, V.; Chen, C.-Y.; Shen, Y.-R. Phase-sensitive sum-frequency vibrational spectroscopy and its application to studies of interfacial alkyl chains. *Journal of the American Chemical Society* **2007,** *129* (33), 10056.

19. Lu, R.; Gan, W.; Wu, B. H.; Zhang, Z.; Guo, Y.; Wang, H. F. C-H stretching vibrations of methyl, methylene and methine groups at the vapor/alcohol (n=1-8) interfaces. *Journal of Physical Chemistry B* **2005,** *109* (29), 14118-14129.

20. Mathew, N. A.; Rickard, M. A.; Kornau, K. M.; Pakoulev, A. V.; Block, S. B.; Yurs, L. A.; Wright, J. C. Coherent Multidimensional Vibrational Spectroscopy of Representative N-Alkanes. *J. Phys. Chem. A* **2009,** *113* (36), 9792-9803.

21. Nobre, T. M.; de Sousa e Silva, H.; Furriel, R. P. M.; Leone, F. A.; Miranda, P. B.; Zaniquelli, M. E. D. Molecular View of the Interaction between iota-Carrageenan and a Phospholipid Film and Its Role in Enzyme Immobilization. *Journal of Physical Chemistry B* **2009,** *113* (21), 7491-7497.

22. Santos, C. S.; Baldelli, S. Alkyl Chain Interaction at the Surface of Room Temperature Ionic Liquids: Systematic Variation of Alkyl Chain Length (R = C-1-C-4, C-8) in both Cation and Anion of RMIM R-OSO3 by Sum Frequency Generation and Surface Tension. *Journal of Physical Chemistry B* **2009,** *113* (4), 923-933.

23. Walker, R. A.; Conboy, J. C.; Richmond, G. L. Molecular structure and ordering of phospholipids at a liquid-liquid interface. *Langmuir* **1997,** *13* (12), 3070-3073.

24. Macphail, R. A.; Strauss, H. L.; Snyder, R. G.; Elliger, C. A. C-H STRETCHING MODES AND THE STRUCTURE OF NORMAL-ALKYL CHAINS .2. LONG, ALL-TRANS CHAINS. *Journal of Physical Chemistry* **1984,** *88* (3), 334-341.

25. Snyder, R. G.; Aljibury, A. L.; Strauss, H. L.; Casal, H. L.; Gough, K. M.; Murphy, W. F. ISOLATED C-H STRETCHING VIBRATIONS OF N-ALKANES - ASSIGNMENTS AND RELATION TO STRUCTURE. *Journal of Chemical Physics* **1984,** *81* (12), 5352-5361.

26. Miller, C. S.; Ploetz, E. A.; Cremeens, M. E.; Corcelli, S. A. Carbon-deuterium vibrational probes of peptide conformation: Alanine dipeptide and glycine dipeptide. *Journal of Chemical Physics* **2009,** *130* (12).

27. Naraharisetty, S. R. G.; Kasyanenko, V. M.; Zimmermann, J.; Thielges, M. C.; Romesberg, F. E.; Rubtsov, I. V. C-D Modes of Deuterated Side Chain of Leucine as Structural Reporters via Dual-frequency Two-dimensional Infrared Spectroscopy. *Journal of Physical Chemistry B* **2009,** *113* (14), 4940-4946.

28. Zimmermann, J.; Gundogdu, K.; Cremeens, M. E.; Bandaria, J. N.; Hwang, G. T.; Thielges, M. C.; Cheatum, C. M.; Romesberg, F. E. Efforts toward Developing Probes of Protein Dynamics: Vibrational Dephasing and Relaxation of Carbon-Deuterium Stretching Modes in Deuterated Leucine. *Journal of Physical Chemistry B* **2009,** *113* (23), 7991-7994.

29. Stearns, J. A.; Zwier, T. S. Infrared and ultraviolet spectroscopy of jet-cooled ortho-, meta-, and para-diethynylbenzene. *J. Phys. Chem. A* **2003,** *107* (49), 10717-10724.

30. Ottiger, P.; Leutwyler, S. Excitonic Splittings in Jet-Cooled Molecular Dimers. *Chimia* **2011,** *65* (4), 228-230.

31. Pillsbury, N. R.; Stearns, J. A.; Muller, C. W.; Plusquellic, D. F.; Zwier, T. S. State-specific studies of internal mixing in a prototypical flexible bichromophore: Diphenylmethane. *Journal of Chemical Physics* **2008,** *129* (11), 114301.

32. Rodrigo, C. P.; Mueller, C. W.; Pillsbury, N. R.; James, W. H., III; Plusquellic, D. F.; Zwier, T. S. Conformer-specific vibronic spectroscopy and vibronic coupling in a flexible bichromophore: Bis-(4-hydroxyphenyl)methane. *Journal of Chemical Physics* **2011,** *134* (16).

33. Zwier, E. G. B. a. T. S. Chapter 8 **2014**.

34. Halonen, L. Local mode vibrations in polyatomic molecules. *Advances in Chemical Physics, Vol 104* **1998,** *104*, 41-179.

35. Henry, B. R.; Tarr, A. W.; Mortensen, O. S.; Murphy, W. F.; Compton, D. A. C. RAMAN AND INFRARED EXCITATION OF LOCAL MODE STATES IN NEOPENTANE. *Journal of Chemical Physics* **1983,** *79* (6), 2583-2589.

36. Lawton, R. T.; Child, M. S. LOCAL MODE VIBRATIONS OF WATER. *Molecular Physics* **1979,** *37* (6), 1799-1807.

37. Mortensen, O. S.; Henry, B. R.; Mohammadi, M. A. THE EFFECTS OF SYMMETRY WITHIN THE LOCAL MODE PICTURE - A REANALYSIS OF THE OVERTONE SPECTRA OF THE DIHALOMETHANES. *Journal of Chemical Physics* **1981,** *75* (10), 4800-4808.

38. Sibert, E. L.; Reinhardt, W. P.; Hynes, J. T. INTRAMOLECULAR VIBRATIONAL-RELAXATION AND SPECTRA OF CH AND CD OVERTONES IN BENZENE AND PERDEUTEROBENZENE. *Journal of Chemical Physics* **1984,** *81* (3), 1115-1134.

39. Baiz, C. R.; Kubarych, K. J.; Geva, E.; Sibert, E. L., III. Local-Mode Approach to Modeling Multidimensional Infrared Spectra of Metal Carbonyls. *J. Phys. Chem. A* **2011,** *115* (21), 5354-5363.

40. Garden, A. L.; Halonen, L.; Kjaergaard, H. G. Widening of the hydrogen bonded OH-streching bands due to the wagging and OO-stretching modes in H2O center dot H2O. *Chem. Phys. Lett.* **2011,** *513* (4-6), 167-172.

41. Hazra, M. K.; Sinha, A. Spectra and Integrated Band Intensities of the Low Order OH Stretching Overtones in Peroxyformic Acid: An Atmospheric Molecule with Prototypical Intramolecular Hydrogen Bonding. *J. Phys. Chem. A* **2011,** *115* (21), 5294-5306.

42. Mathew, N. A.; Yurs, L. A.; Block, S. B.; Pakoulev, A. V.; Kornau, K. M.; Sibert, E. L., III; Wright, J. C. Fully and Partially Coherent Pathways in Multiply Enhanced Odd-Order Wave-Mixing Spectroscopy. *J. Phys. Chem. A* **2010,** *114* (2), 817-832.

43. Peng, C. S.; Jones, K. C.; Tokmakoff, A. Anharmonic Vibrational Modes of Nucleic Acid Bases Revealed by 2D IR Spectroscopy. *Journal of the American Chemical Society* **2011,** *133* (39), 15650-15660.

44. Weymuth, T.; Jacob, C. R.; Reiher, M. A Local-Mode Model for Understanding the Dependence of the Extended Amide III Vibrations on Protein Secondary Structure. *Journal of Physical Chemistry B* **2010,** *114* (32), 10649-10660.

45. Yang, K. S.; Hudson, B. Computation of Deuterium Isotope Perturbation of C-13 NMR Chemical Shifts of Alkanes: A Local Mode Zero-Point Level Approach. *J. Phys. Chem. A* **2010,** *114* (46), 12283-12290.

46. Zhao, J.; Wang, J. Amide Vibrations and Their Conformational Dependences in beta-Peptide. *Journal of Physical Chemistry B* **2010,** *114* (48), 16011-16019.

47. Zwier, T. S. Laser probes of conformational isomerization in flexible molecules and complexes. *J. Phys. Chem. A* **2006,** *110* (12), 4133-4150.

48. Hopkins, J. B.; Powers, D. E.; Smalley, R. E. VIBRATIONAL-RELAXATION IN JET-COOLED ALKYLBENZENES .1. ABSORPTION-SPECTRA. *Journal of Chemical Physics* **1980,** *72* (9), 5039-5048.

49. E. B. Wilson, J. C. D., and P. C. Cross. Molecular Vibrations.

50. Gaussian 09, R. A., Frisch, M. J.; Trucks, G. W.; Schlegel, H. B.; Scuseria, G. E.; Robb, M. A.; Cheeseman, J. R.; Scalmani, G.; Barone, V.; Mennucci, B.; Petersson, G. A.; Nakatsuji, H.; Caricato, M.; Li, X.; Hratchian, H. P.; Izmaylov, A. F.; Bloino, J.; Zheng, G.; Sonnenberg, J. L.; Hada, M.; Ehara, M.; Toyota, K.; Fukuda, R.; Hasegawa, J.; Ishida, M.; Nakajima, T.; Honda, Y.; Kitao, O.; Nakai, H.; Vreven, T.; Montgomery, Jr., J. A.; Peralta, J. E.; Ogliaro, F.; Bearpark, M.; Heyd, J. J.; Brothers, E.; Kudin, K. N.; Staroverov, V.N.; Kobayashi, R.; Normand, J.; Raghavachari, K.; Rendell, A.; Burant, J. C.; Iyengar, S. S.; Tomasi, J.; Cossi, M.; Rega, N.; Millam, N. J.; Klene, M.; Knox, J. E.; Cross, J. B.; Bakken, V.; Adamo, C.; Jaramillo, J.; Gomperts, R.; Stratmann, R. E.; Yazyev, O.; Austin, A.J.; Cammi, R.; Pomelli, C.; Ochterski, J. W.; Martin, R. L.; Morokuma, K.; Zakrzewski, V. G.; Voth, G. A.; Salvador, P.; Dannenberg, J. J.; Dapprich, S.; Daniels, A. D.; Farkas, Ö.; Foresman, J. B.; Ortiz, J.V.; Cioslowski, J.; Fox, D. J. Gaussian, Inc., Wallingford CT, 2009.

51. Ramesh, S. G.; Sibert, E. L. Combined perturbative-variational investigation of the vibrations of CHBr3 and CDBr3. *Journal of Chemical Physics* **2004,** *120* (23), 11011-11025.

52. Sibert, E. L. THEORETICAL-STUDIES OF VIBRATIONALLY EXCITED POLYATOMIC-MOLECULES USING CANONICAL VANVLECK PERTURBATION-THEORY. *Journal of Chemical Physics* **1988,** *88* (7), 4378-4390.

53. Sibert, E. L. Dressed local mode Hamiltonians for CH stretch vibrations. *Molecular Physics* **2013,** *111* (14-15), 2093-2099.

54. Abbate, S.; Gangemi, R.; Longhi, G. Dipole and rotational strengths for overtone transitions of a C(2)-symmetry HCCH molecular fragment using Van Vleck perturbation theory. *Journal of Chemical Physics* **2002,** *117* (16), 7575-7586.

55. McCoy, A. B.; Sibert, E. L. CALCULATION OF INFRARED INTENSITIES OF HIGHLY EXCITED VIBRATIONAL-STATES OF HCN USING VANVLECK PERTURBATION-THEORY. *Journal of Chemical Physics* **1991,** *95* (5), 3488-3493.

56. McCoy, A. B.; Sibert, E. L. AN ALGEBRAIC APPROACH TO CALCULATING ROTATION VIBRATION-SPECTRA OF POLYATOMIC-MOLECULES. *Molecular Physics* **1992,** *77* (4), 697-708.

57. Durig, J. R.; Liu, J.; Little, T. S.; Kalasinsky, V. F. CONFORMATIONAL-ANALYSIS, BARRIERS TO INTERNAL-ROTATION, VIBRATIONAL ASSIGNMENT, AND ABINITIO CALCULATIONS OF 1,2-DIFLUOROETHANE. *Journal of Physical Chemistry* **1992,** *96* (21), 8224-8233.

58. McCoy, A. B.; Silbert, E. L. PERTURBATIVE APPROACHES TO HIGHLY EXCITED MOLECULAR VIBRATIONS OF H2O, D2O, AND HDO. *Journal of Chemical Physics* **1990,** *92* (3), 1893-1901.

59. Baggott, J. E. NORMAL-MODES AND LOCAL MODES IN H2X - BEYOND THE CHL, K RELATIONS. *Molecular Physics* **1988,** *65* (3), 739-749.

60. Kusaka, R.; Inokuchi, Y.; Ebata, T. Water-mediated conformer optimization in benzo-18-crown-6-ether/water system. *Phys. Chem. Chem. Phys.* **2009,** *11* (40), 9132-9140.

61. Buchanan, E. G.; James, W. H., III; Choi, S. H.; Guo, L.; Gellman, S. H.; Mueller, C. W.; Zwier, T. S. Single-conformation infrared spectra of model peptides in the amide I and amide II regions: Experiment-based determination of local mode frequencies and inter-mode coupling. *Journal of Chemical Physics* **2012,** *137* (9).

62. Dean, J. C.; Buchanan, E. G.; Zwier, T. S. Mixed 14/16 Helices in the Gas Phase: Conformation-Specific Spectroscopy of Z-(Gly)(n), n=1, 3, 5. *Journal of the American Chemical Society* **2012,** *134* (41), 17186-17201.

63. Dean, J. C.; Buchanan, E. G.; James, W. H., III; Gutberlet, A.; Biswas, B.; Ramachandran, P. V.; Zwier, T. S. Conformation-Specific Spectroscopy and Populations of Diastereomers of a Model Monolignol Derivative: Chiral Effects in a Triol Chain. *J. Phys. Chem. A* **2011,** *115* (30), 8464-8478.

CHAPTER 5 GROUND STATE CONFORMATIONAL PREFERENCES AND CH STRETCH-BEND COUPLING IN A MODEL ALKOXY CHAIN: 1,2-DIPHENOXYETHANE

5.1 Introduction

1,2-diphenoxyethane (DPOE) is a model flexible bichromophore in which two phenyl rings cap the two ends of an O-CH_2-CH_2-O linkage that is the fundamental repeating unit of polyethylene glycol (PEG) or poly(ethylene oxide) (PEO) polymers. Those developing force fields for PEG and PEO have used 1,2-dimethoxyethane (CH_3-O-CH_2-CH_2-O-CH_3, DMOE) as a model, mapping out the torsional potential energy surface via *ab initio* methods, and fitting the results to simple torsional potential energy functions that account for the energy dependence of the minima on the local and nearest-neighbor dihedral angles along the chain.[1-6] The conformations of DMOE are characterized by three dihedral angles θ_1, τ, and θ_2 shown schematically below involving the C-O-C-C (θ_1), O-C-C-O (τ), and C-C-O-C (θ_2) groups. These are characterized as *trans*, *gauche(+)*, or *gauche(-)*, with the tgt conformer having the greatest population in most circumstances, but *ttt* dominant in an Ar matrix.[7] In DPOE, the orientation of the phenyl rings creates two additional dihedral angles (ϕ_1 and ϕ_2).

Experimental tests of these potentials in DMOE are provided by an array of bulk-phase properties of DMOE,[1-4, 6] by infrared studies in the gas phase[8] and by temperature-

dependent Raman studies[9] of DMOE as a pure liquid and in its miscible solutions with H_2O that provide populations of the conformations as a function of temperature.

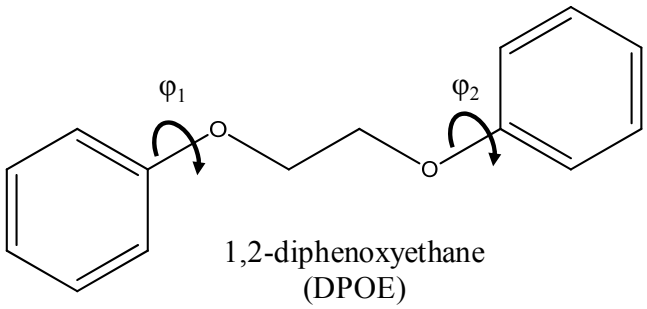

1,2-diphenoxyethane
(DPOE)

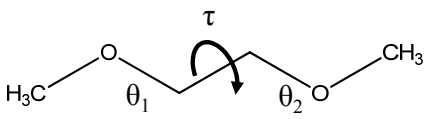

1,2-dimethoxyethane
(DMOE)

Studies of the conformations of flexible molecules in the gas phase are complementary to those in solution, providing benchmark tests for calculations on conformational preferences in the absence of solvent effects. When a supersonic expansion is used to cool the molecules, the most stable conformations can be studied in exquisite detail in the absence of isomerization. When an aromatic moiety is incorporated into the molecule, IR-UV and UV-UV double resonance methods can be used to obtain spectroscopic signatures of individual conformations free from interference from one another.[10-21] Furthermore, population transfer methods have been devised that determine the fractional abundances of the conformers, and measure the barriers to conformational isomerization.[11, 15, 22-24]

The present work describes the results of single-conformation UV and IR spectroscopy and infrared population transfer spectroscopy on 1,2-diphenoxyethane. By phenyl capping both ends of the O-CH_2-CH_2-O chain, a model flexible bichromophore is obtained, with interesting consequences for the UV spectroscopy, which now contains excited states that come in closely-spaced pairs. In this respect, DPOE is a natural

extension of other studies that have focused on vibronic coupling (sometimes termed 'internal mixing') between the near-degenerate S_1 and S_2 states.[25-31] To that end, experimental investigations of flexible bichromophores and molecular homodimers have fueled theoretical developments to explain the vibronic coupling present in bichromophores. This includes extending the diabatic Fulton-Gouterman model to multiple dimensions[32] and to account for asymmetric bichromophores.[33] Recently, Luetwyler and co-workers developed an adiabatic approach for bichromophores in the weak coupling limit, reproducing the diabatic results for 2-aminopyridine, *o*-cyanophenol, and 2-pyridone dimers.[34-35]

While the excited states of DPOE are fascinating subjects, their proper interpretation rests on a foundation of firm conformational assignments of the conformers in the ground electronic state. Furthermore, as its name implies, DPOE can be viewed as a disubstituted ethane, with a central CH_2-CH_2 group that will report on its local conformation via its alkyl CH stretch absorptions in the 2800-3000 cm^{-1} region. This region is notoriously challenging to assign due to extensive stretch-bend Fermi resonance, which often make assignments based on simple normal mode analysis via calculated harmonic vibrational frequencies difficult or impossible.[36-37]

In Chapter 4, a reduced-dimension model that was able to account for the Fermi resonance in 1,2-diphenylethane and its macrocycle extension, 2.2.2-paracyclophane was developed. Here, we describe the extension of this model to DPOE. As we shall see, the alkyl CH stretch spectra have Fermi resonances that differ markedly from their counterparts in DPE and TCP. Mid-IR spectra in the CH bend region help to pin down the wavenumber positions of their overtones, providing important input to the model.

While the UV spectroscopy plays a necessary role in making these conformational assignments, a more detailed characterization of the excited states themselves will be taken up elsewhere.[38]

Having made the ground state assignments, we will return to the calculated ground state torsional potential energy surface to see how the conformational preferences compare to those in DMOE, and how the phenyl capping groups modify them. We also compare our results with previous studies of other flexible bichromophores in which the two aromatic moieties are separated by a single covalently-linked chain of varying complexity, including diphenylmethane,[25-26] bis-(2-hydroxyphenyl)methane,[39-40] bis-(4-hydroxyphenyl)methane,[32] 3-(4-Hydroxyphenyl)-N-benzylpropionamide,[41] diphenoxymethane,[28] and Ac-Phe-Phe-NH_2.[42] The present work also provides a foundation for on-going work on the single-conformation spectroscopy of benzo and dibenzocrown ethers,[36, 43-46] forming one of the initial motivations for the study of DPOE, which constitutes a segment of dibenzo-15-crown-5.[47]

5.2 Infrared Population Transfer Spectroscopy

Infrared population transfer spectroscopy (IRPT) was used to determine the fractional abundance of each conformer present in the supersonic jet expansion.[12, 23, 48] To do this, IRPT spectra were recorded while monitoring the downstream population of conformer 'i'. After proper normalization, I^{i}_{IRPT} is recorded as a fractional change in population of conformer 'i' as a function of IR wavenumber $\tilde{\nu}$. Since the total population of all conformers remains constant during the population transfer process, the fractional

abundance of each conformer 'i', F_i, may be determined from the weighted sum of the IRPT scans that is zero over the entire IRPT wavenumber scan:

$$\Delta N_{tot}(\tilde{\nu}) = 0 = \sum_i F_i \times I^i_{IRPT}(\tilde{\nu}) \quad (1)$$

Here I^i_{IRPT} is the IRPT spectrum of conformer 'i', recorded as a fractional population change under identical conditions. A more detailed description of the conditions used for these scans is included in the Supplementary Material.

5.3 Computational Methods

In order to assign the observed spectra to particular conformers, the experimental data must be compared to calculated spectra for the possible conformational isomers of the molecule. In a molecule the size of DPOE, an exhaustive search of the potential energy surface can be carried out in order to identify all possible conformational minima, initially using a molecular mechanics force field (MMFFs) as implemented in the MacroModel suite of programs.[49] These structures were used as input geometries for DFT optimization, using the dispersion parameterized density functional M05-2X with a 6-31+G(d) basis set.[50-51] Harmonic vibrational frequencies were calculated at the same level of theory in order to compare the experimental frequencies to the optimized structures. Using the force field minima as starting structures for geometry optimization, DFT M05-2X/6-31+G(d) optimizations produced 26 minima. These structures are characterized by the five dihedral angles (ϕ_1, θ_1, τ, θ_2, ϕ_2) linking the two phenyl groups. The middle three dihedral angles (C(ph)OCC, OCCO, and CCOC(ph)) are labeled as

trans, *gauche(+),* or *gauche*(-), while the phenyl ring orientations (C(ph2)C(ph1)OC) are labeled as in-plane or out-of-plane, using a cut-off of 20 degrees to distinguish the two.

Relaxed potential energy scans for motion along each of the three unique dihedrals (e.g., (ϕ_1/ϕ_2, θ_1/θ_2, τ) were calculated and transition states determined using the QST3 method as implemented in Gaussian *09*.[52] For each of the points on the potential energy scan, the dihedral angle of interest was set at a fixed angle while full geometry optimizations were carried out on all other coordinates. The results of these scans and their consequences for the ground state conformational preferences of DPOE will be taken up in the Discussion section.

5.4 Calculated Structure and Their Energies

Table 5.1 lists the full set of conformational isomers for DPOE predicted by calculations at the DFT M05-2X/6-31+G(d) level of theory, arranged from lowest energy to highest energy. There are a total of 26 minima, with two conformers (conformers 1 and 18) that have inversion symmetry, while the other 24 are composed of 12 "chiral" pairs that are non-superimposable mirror images of one another. The 14 unique structures are spread over 15 kJ/mol, with the C_{2h} symmetry i/*ttt*/i structure the global minimum, and its C_2 symmetry i/*tg*$\pm$*t*/i counterpart 2.67 kJ/mol higher in energy. Figure 5.1 shows the structures of these two lowest energy conformers, which differ primarily in the central OCCO dihedral (τ), whether *trans* or *gauche*.

Table 5.1 Dihedral angle labels and relative energies (kJ/mol) for the conformational isomers of DPOE, calculated at the DFT M05-2X/6-31+G(d) level of theory.

Conformer (Degeneracy)	φ_1	θ_1	τ	θ_2	φ_2	Relative Energy
i/ttt/i (1)	180.0	-180.0	-180.0	-180.0	0.0	0.000
i/tg+t/i (2)	-1.8	-177.9	71.6	-177.9	-1.8	2.670
i/ttg-/i (2)	-179.4	178.1	178.9	-81.2	179.5	5.558
o+/g-g+t/i- (2)	25.0	-106.7	72.0	-175.3	-5.6	6.761
o+/g+g-g+/o- (2)	154.7	104.8	-75.8	104.8	-27.3	8.013
i/tg-g-/i- (2)	-177.6	177.6	-69.9	-77.1	-5.5	8.606
o+/g+g+t/i (2)	73.6	61.8	60.7	-174.9	-4.2	8.908
i/g-g-g+/i- (2)	-2.4	-79.4	-71.8	100.2	-11.8	10.615
o+/g-g+g+/o+ (2)	132.5	-86.8	60.8	66.9	21.7	11.103
i/g+tg-/i (1)	-178.4	80.4	-180.0	-80.4	178.4	11.573
o+/g+tg+/i (2)	47.8	73.7	-176.9	79.7	-175.4	11.762
i/g-g-g-/i (2)	176.4	-77.1	-70.2	-77.1	-4.4	14.165
o-/g-g-g-/o+ (2)	-76.0	-65.5	-53.7	-65.5	105.9	15.013
i-/g+g+g+/o- (2)	-172.5	75.1	58.4	65.5	-112.2	15.183

*Angles ranging between $-5° \leq \varphi_1/\varphi_2 \leq 5°$ are designated "i", $-5° > \varphi_1/\varphi_2 \geq -20°$ as "i-", $5° < \varphi_1/\varphi_2 \leq 20°$ as "i+", $\varphi_1/\varphi_2 > 20°$ as "o+", and $\varphi_1/\varphi_2 < -20°$ as "o-".

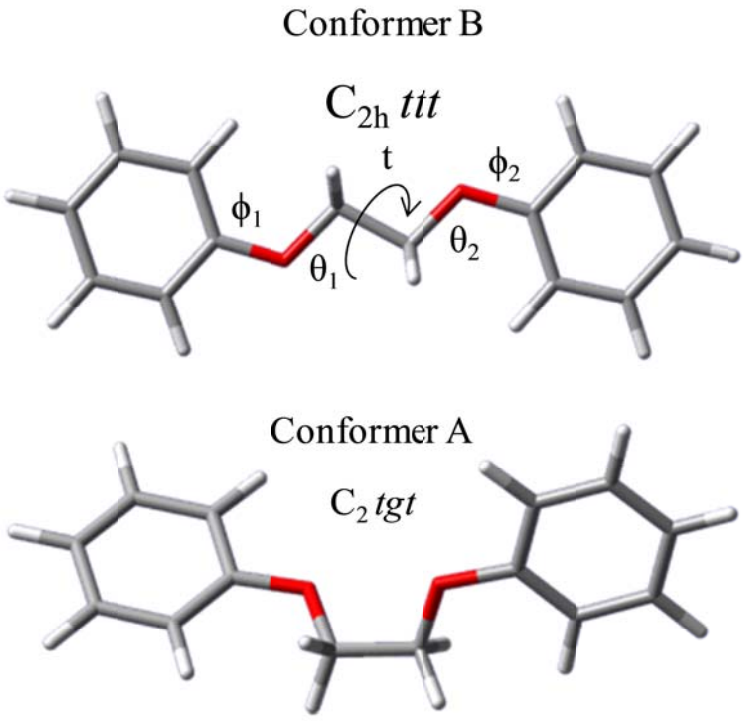

Figure 5.1 Structures and dihedral angles of the two lowest-energy conformers of DPOE. The C_{2h} symmetry structure is the global minimum, while the C_2 symmetry *gauche* structure is 2.67 kJ/mol higher in energy at the DFT M05-2X/6-31+G(d) level of theory.

5.5 Experimental Results

Figure 5.2 presents the LIF excitation spectrum (top, red) and ultraviolet hole-burning spectra (middle traces, black) for the two monomer conformations of DPOE. The bottom trace (blue) is a third UVHB spectrum assigned to a DPOE-$(H_2O)_1$ complex. Due to the hygroscopic nature of the DPOE solid, the DPOE-H_2O complex is present in the expansion even without the addition of water vapor to the expansion. The assignment of these transitions to the DPOE-H_2O complex was made on the basis of its OH stretch

IR spectrum. The vibronic and infrared spectroscopy of DPOE-H_2O will be taken up in chapter 7, and are not considered further here.

The UVHB spectra shown in figure 5.2 account for all the transitions observed in the LIF spectrum. Previous studies of alkoxy-benzene derivatives, such as 1,2-diethoxybenzene,[36] indicate a strong preference for an in-plane geometry for the first alkyl carbon relative to the plane of the phenoxy group, associated with dihedrals ϕ_1 and ϕ_2 . The preference for in-plane structures near the phenyl ring was also observed in the benzo-crown ethers,[36, 43-46] although in that case the potential for out-of-plane structures is enhanced by the constraints of the macrocycle. Based on that work, it was possible to correlate unique S_0-S_1 frequency shifts associated with the degree of planarity of the C(α) and C(β) atoms relative to the phenoxy plane.[36] In DPOE, the S_0-S_1 origin transitions of its two observed conformers occur at frequencies (36432 and 36519 cm^{-1}), consistent with geometries for the phe-O-C(α)-C(β) that are in plane for both phenyl rings in the two observed conformers of DPOE.

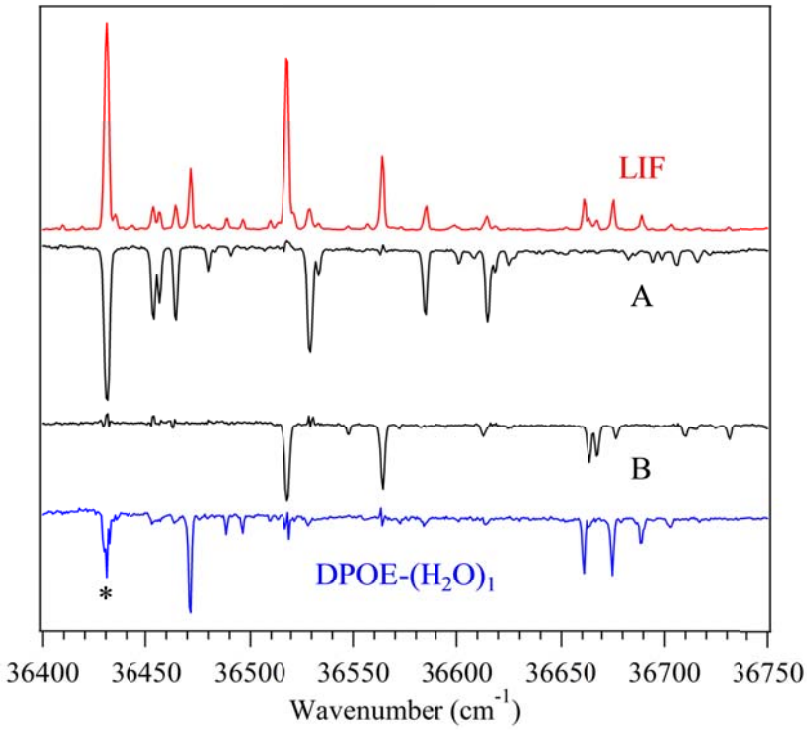

Figure 5.2 LIF (top trace) and UVHB (bottom traces) spectra of the two monomer conformations and the water containing cluster are presented. The band marked with an asterisk is an artifact arising from incomplete subtraction.

It is noteworthy that conformer A has significantly more vibronic activity than conformer B. This is consistent with a reduction in symmetry and more interaction between the two phenyl rings in conformer A than in conformer B, suggesting that A is the *tgt* isomer (a shortened label we will use to refer to the i/tgt/i structure), while B is *ttt* (short for i/*ttt*/i). The prominent vibronic structure in the UVHB spectrum of conformer A appears +24, +35, +99, +155, and +185 cm^{-1} above the electronic origin. This is to be compared with the calculated totally symmetric low frequency modes for the ground state of the C_2 *gauche* conformer, with frequencies of 25, 36, 103, 158, and 193 cm^{-1}. If these low frequency vibrations are not changed much by electronic excitation, they strongly support

the assignment of conformer A to the *gauche* structure (figure 5.1). By contrast, the lowest frequency totally symmetric mode (a_g symmetry) in the C_{2h} *ttt* conformer is at 149 cm^{-1}, in reasonable agreement with the transitions at +146/149 in the UVHB spectrum of B. The band at +46 cm^{-1} is assigned to a vibronically induced transition involving a b_u symmetry fundamental with calculated ground state frequency of 51 cm^{-1}. Further consideration of the excited state spectroscopy will be taken up elsewhere.[38]

In order to test these proposed assignments further, we recorded resonant ion-dip infrared spectra of the two conformers in the alkyl CH stretch and mid-infrared regions. These are shown in figure 5.3, where they are compared with the predictions of calculations for the *ttt* and *tgt* conformers. The stick spectra are scaled, harmonic vibrational frequencies and infrared intensities from the M05-2X6-31+G(d) calculations for the two conformers.

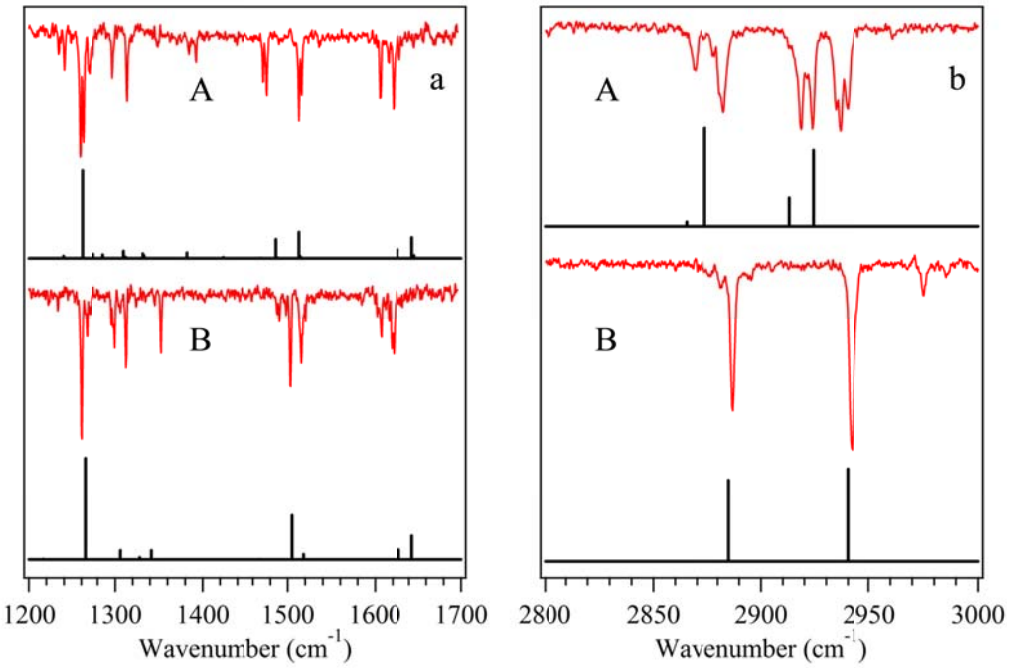

Figure 5.3 Fluorescence-dip infrared spectrum of (a) conformer A (top) and conformer B(lower) in the 1200-1700 cm-1 region that encompasses the C-O stretch (1200-1300 cm-1) and CH bend (1450-1550 cm-1) fundamentals. (b) Corresponding spectrum in the alkyl CH stretch region (2800-3000 cm-1). Calculated vibrational frequencies are shown in black below the individual isomers. Stick spectra were scaled by 0.962 in the mid infrared and 0.928 in the CH stretch region.

The alkyl CH stretch spectrum of conformer B (figure 5.3b, bottom) is particularly striking for its simplicity, showing only two transitions despite the presence of 4 CH groups. The stick spectrum for the *ttt* conformer reproduces this simple spectrum. In the lower-frequency symmetric stretch region, there are two states corresponding to +/- linear combinations of the two CH_2 symmetric stretches. The in-phase combination has a_g symmetry and is therefore dipole forbidden, while the out-of-phase combination has b_u symmetry and is dipole-allowed. The higher-frequency asymmetric stretch region also contains two states, here corresponding to the +/- linear

combinations of the CH_2 asymmetric stretch. The linear combination with b_g symmetry is dipole forbidden, while the combination with a_u symmetry is dipole-allowed.

Note that in conformer B, there is little evidence of Fermi resonance mixing with the CH bend overtones, enabling a clear match-up of the experimental transitions with calculation. The scale factor used to match experiment with calculation in the alkyl CH stretch region was chosen based on this comparison in conformer B, leading to a best-fit scale factor of 0.928.

The corresponding spectrum of conformer A (figure 5.3b, top) shows a total of six resolved transitions, suggesting that Fermi resonances with the CH bend overtones likely play a larger role here. Nevertheless, the calculated results from the harmonic calculations faithfully reproduce the over-all pattern of transitions, confirming and strengthening the assignment of conformer A to the C_2 symmetry *tgt* structure (figure 5.1). The lower symmetry of the *tgt* structure produces four allowed fundamentals that show a pattern similar to that in the experimental spectrum, with additional smaller splittings that motivate application of the model we have developed to quantitatively account for stretch/bend coupling in alkyl groups.[53] To that end, it is useful to have infrared spectra that extend into the CH bend region in order to fix their fundamental frequencies. More generally, the CH bend (1400-1550 cm^{-1}) and C-O stretch (1200-1300 cm^{-1}) regions should be sensitive to the conformation, providing additional evidence for the assignments made. An overview of the mid-infrared spectra of conformers A and B are shown in figure 5.3a, where they are compared with harmonic vibrational frequency calculations. Here the scale factor was chosen to align the stick spectra best with the CO stretch, occurring experimentally at 1265 cm^{-1}.

In the CO stretch region, the spectrum of conformer B is dominated by this transition at 1265 cm^{-1}. This transition is assigned as the out-of-phase combination of the two C-O stretch vibrations that stretches one C-O bond while the other contracts. The in-phase combination is IR forbidden, but calculated to appear 10 cm^{-1} higher in frequency. In the CH bend region, the experimental spectrum is dominated by two transitions at 1503 and 1516 cm^{-1}. The calculations show two transitions in this region, which are complicated mixtures of both alkyl and aromatic CH bends.

The corresponding spectrum of conformer A (figure 5.3a, top) has two rather intense transitions at 1476 and 1513 cm^{-1}. The calculations reproduce this pattern. Analysis of the normal modes of the *tgt* conformer shows that the lower frequency of the two is a nearly pure CH_2 bend, while the higher frequency mode with large IR intensity is a mixed alkyl/aromatic CH bend. Further details of these modes and their influence on the CH stretch region will be taken up in the next section.

As a final aspect of the characterization of the conformations of DPOE, we have carried out infrared population transfer measurements (IRPT) on DPOE in the alkyl CH stretch region with the goal of determining the fractional abundances of the two conformers. The individual IRPT spectra are shown in the middle (conformer A, black) and bottom (conformer B, red) traces, clearly displaying a kind of reflection symmetry that is anticipated for a case where only two conformers are present, with IR excitation leading to population transfer between them, leading to a depletion in the conformer undergoing IR excitation and gain in the signal from the conformational product. The weighted sum shown in blue above the two IRPT spectra was obtained by recursively calculating the variance from zero and permuting the individual IRPT spectra of

conformers A and B. The small residual deviation from zero is attributed to the presence of a minor amount of the DPOE-H_2O complex also present in the expansion, which produces only gains in the IRPT spectra. Despite this complication, fractional abundances were extracted from the scans, with best-fit values of $F_{ttt} = 0.53 \pm 0.01$ and $F_{tgt} = 0.47 \pm 0.01$. Thus, the *ttt* and *tgt* conformers of DPOE have nearly equal populations in the supersonic expansion.

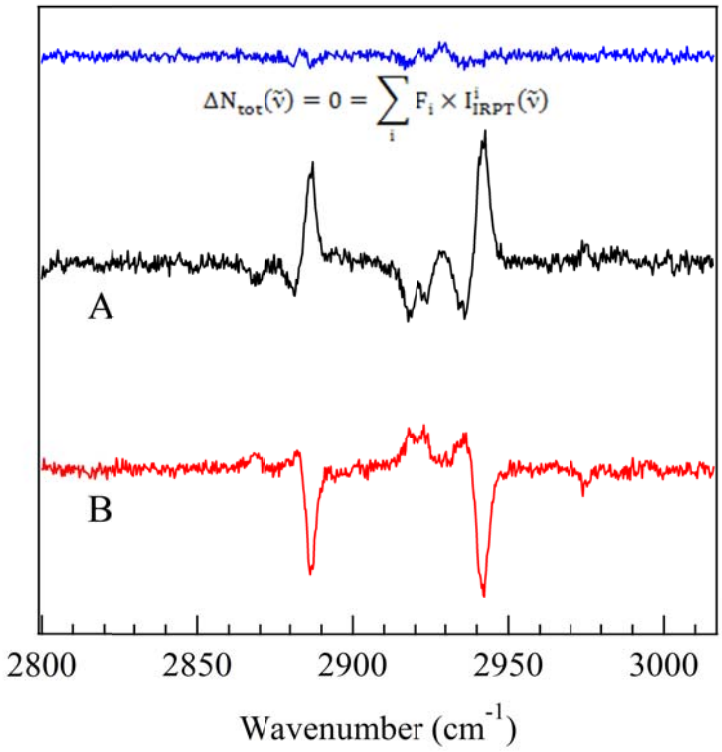

Figure 5.4 Infrared population transfer spectra for the two monomer conformations. The sum of the two lower trace weighted by the relative populations produces the top. The top spectrum deviates slightly from zero due to the presence of the DPOE-H2O complex in minor abundance.

5.6 Modeling the Alkyl CH Stretch Spectrum of DPOE Conformers

Figure 5.5 presents stick diagrams of the scaled vibrational frequencies and IR intensities of the seven lowest energy conformers of DPOE in the three wavenumber ranges of most consequence for conformational assignments: the C-O stretch (1200-1350 cm^{-1}), CH bend (1450-1550 cm^{-1}), and alkyl CH stretch (2800-3000 cm^{-1}) regions. The experimental single-conformation IR spectra of the *ttt* and *tgt* conformers are included for comparison. This broader comparison strengthens the conformational assignments by showing the unique fit provided by the *ttt* structure to the spectrum of conformer B and *tgt* to that of conformer A. The excellent fit to the spectra of the observed conformers also makes it possible to surmise the spectroscopic signatures of the other conformers with some confidence.

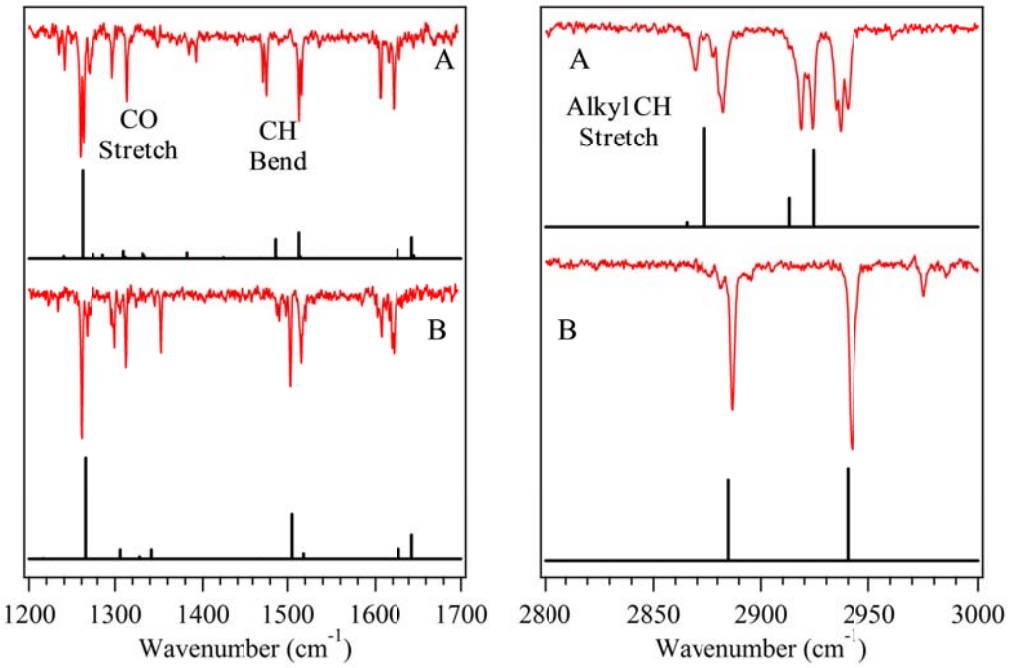

Figure 5.5 Fluorescence-dip infrared spectra in the CO stretch, CH bend, and alkyl CH stretch regions, compared to stick spectra of structures in the first 10 kJ/mol, showing the sensitivity of these regions to the DPOE conformation. See text for further discussion.

The alkyl CH stretch region is modeled by a local-normal mode Hamiltonian that includes Fermi couplings. The details of this Hamiltonian have been published elsewhere where it was applied first to 1,2-diphenylethane (DPE) and tricyclophane (TCP).[53] As a result, our discussion of the model is brief and presented mostly in the context of DPOE, bringing in results from diphenylethane DPE in order to set certain scaling parameters based on a conformer of that molecule. We first describe the harmonic contribution and then the inclusion of the cubic terms in order to treat the Fermi interactions. Spectra are obtained via a variational calculation that includes CH stretch fundamentals as well as overtones and combination bands of modes whose energies lie within a specified energy range of the CH stretches.

The vibrations are described using curvilinear coordinates with a Hamiltonian whose harmonic contribution H^{HO} is comprised of the sum of three parts: (i) a local mode Hamiltonian H^{LO} describing the CH alkyl stretches and the couplings between them, (ii) a normal mode contribution H^{NM} describing the remaining degrees of freedom in a normal mode representation, and (iii) a coupling contribution W that includes bilinear couplings between the local and normal modes. Second order Van Vleck perturbation theory is carried out to obtain a dressed Hamiltonian that has the same form as H^{HO} but now without the coupling term W. This dressed Hamiltonian, when combined with a dressed dipole moment function, predicts spectra that are in agreement with the full normal mode Hamiltonian.

The Fermi resonance interactions are modeled by calculating the cubic couplings between the local mode CH stretches and the normal modes. The couplings are calculated in the internal coordinates and only those stretches, bends, and dihedral angles that involve motion of the CH bond are included. The bend and dihedral angle degrees of freedom are rewritten in terms of the normal coordinates of H^{NM}.

A central step in the analysis is to recognize that the above approach can be simplified. The pioneering studies of the Strauss group,[54-55] highlighted the pivotal role of the HCH scissor modes for describing the spectra of alkanes. In the DPE study, it was found that the phenyl modes only weakly coupled to the scissor modes and hence had little role in the alkyl region of the CH spectrum.[53] The mid-IR results reported in figure 5.3a enable a more in-depth investigation of this coupling between scissor modes and ring modes and provide the appropriate scaling frequency scaling factors that need to be applied to the DFT results. The following discussion focuses on the spectral lines in the

vicinity of the scissor mode transitions near 1500 cm^{-1} observed for the *tgt* conformer A. We choose this conformer, since the normal mode picture adequately describes the observed spectra. Four peaks are observed, consistent with the DFT B3LYP/6-311+(d,p) predictions shown in table 5.2. These frequencies are reported as dressed HO results, but agree with the frequencies predicted by full normal mode harmonic calculations to within 0.1 cm^{-1}. We also report frequency scaled results, where the scaling was chosen to improve overall agreement with experiment for these four modes.

Table 5.2 Comparison of experimental and calculated dressed harmonic oscillator vibrational frequencies (in cm-1) and intensities (KM/mole) for the CH2 scissors modes of the C2 symmetry tgt DPOE conformer A.

Sym.	Exp.	Unscaled		Scaled (.989)		Decoupled	
		Freq.	IR Int.	Freq.	IR Int.	Freq.	IR Int.
a	1471	1496.97	4.50	1480.5	4.5	1482.02	1.4
b	1475	1497.86	112.3	1481.4	112.2	1484.30	31.2
b	1514	1525.54	157.2	1508.8	157.3	1505.59	241.0
a	1517	1527.06	11.9	1510.3	11.9	1508.54	14.9

The experimental and dressed H^{HO} results of table 5.2 contain two doublets separated by about 40 cm^{-1} and 28 cm^{-1}, respectively. The two higher frequency peaks mainly correspond to CH ring bends, while the two lower energy peaks correspond mainly to the scissor modes. The relative intensities (figure 5.3a) are quite well matched

by the theoretical prediction with the exception that the DFT results predict too little intensity in the states of 'a' symmetry compared to those of 'b' symmetry.

In order to better understand the nature of this mixing we vary the masses on various atoms, artificially tuning the states in and out of resonance. A normal mode calculation with the masses on the phenyl rings doubled leads to the decoupled scissor frequencies of table 5.2. Increasing the ethano bridge hydrogen mass by 1.2 leads to the decoupled phenyl mode frequencies reported in the table. Regardless of the precise values of the masses, we find that there is a 2-3 cm^{-1} shift in frequency upon decoupling. A simple perturbative analysis of the shift upon decoupling indicates a coupling of 7-9 cm^{-1} between the localized motions of the scissors and the ring modes. This coupling is consistent with the substantial intensity sharing between modes of the same symmetry.

We shall see below that the overtones of the scissor modes have sizeable anharmonicities. As a result, the scissor overtones will shift out of resonance with these ring modes. Comparing calculations that include ring modes with those that do not, we find additional lines in the stick spectra of the former calculation compared to the latter. When we artificially broaden the theoretical transitions as we have in figure 5.6, these differences are no longer discernible. Moreover, the complicated eigenstate description of the full dimensional problem obscures the simpler underlying coupling structures that determine the observed spectral features. This relatively simplicity is essential for it helps provide the necessary insights into how model parameters obtained via electronic structure calculations should be scaled to obtain spectroscopic accuracy.[53] For this reason the results below are obtained using Hamiltonians that do include the ring modes.

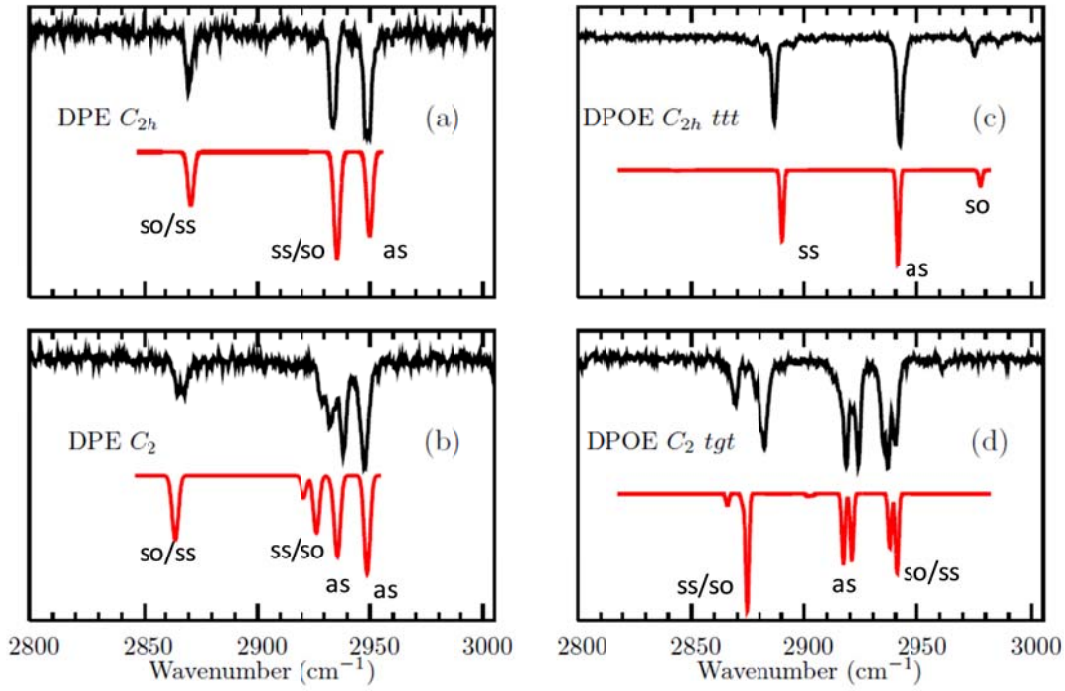

Figure 5.6 Comparison of experimental and theoretical infrared spectra for the CH alkyl stretch region of the C_{2h} and C_2 symmetry conformers of (a,b) 1,2-diphenylethane (DPE) and (c,d) DPOE, respectively. The transitions are labeled as excitation to symmetric stretches (ss), asymmetric stretches (*as*), or scissor overtones (*so*). The *os/ss* and *ss/os* designation indicates Fermi mixing between *os* and *ss* states where the major component is listed first. In (d) although the highest energy peak is labeled (*ss/so*) it contains significant asymmetric stretch character.

Armed with this insight based on the mid-IR data, we return now to the CH alkyl stretch region of DPOE. Fitting the parameters of the model Hamiltonian requires scaling in a more rigorous way than is typically done when comparing harmonic DFT calculations with experiment. Our model developed for 1,2-diphenylethane (DPE) included four scale factors in order to fit the alkyl CH stretch spectrum of the *C_{2h} trans* conformer of DPE.[53] These results are reproduced in figure 5.6a. The four factors correspond to fitting the positions of the three peaks as well as the relative intensities of

the two Fermi coupled states; that is, those corresponding to the two lower energy states. More specifically, the CH force constants are scaled by α_{CH}, the cubic Fermi coupling terms are scaled by α_{FC}; the matrix elements of CH stretch Hamiltonian H^{LM} are scaled as

$$H_{ij} = \beta H_{ij} + (1- \beta)E_{avg}\, \delta_{ij} \qquad (2)$$

where E_{avg} is the average of the CH stretch zero-order frequencies. This choice leaves E_{avg} unaffected by the β scaling. Finally we include a diagonal anharmonicity E_{anh} of the local scissor modes, so that the overtones are not resonant with the combination band. We obtained [α_{CH}, α_{FC}, β, E_{anh}]=[0.9595, 0.68, 0.85, -47 cm^{-1}]. The only difference between the DPOE and DPE model parameters is an overall scaling of all vibrational force constants, other than the alkyl CH stretches. For DPOE we have used the scaling obtained by fitting the fundamental scissor modes of DPOE (table 5.2), while for DPE the scale factor was obtained by fitting the scissor modes of 1,2-difluoroethane. This scaled Hamiltonian was then used to predict spectra for the C_2 *tgt* conformer of DPOE (figure 5.6d). Further comparison of the scaling factors in DPE and DPOE is given in supplementary material.

The agreement between the theoretical and experimental spectra in figure 5.6d for the C_2 *tgt* conformer of DPOE is excellent. The results clearly allow one to distinguish the *ttt* and *tgt* conformers of DPOE. It is very encouraging that the model developed for DPE serves so well here with only a minor adjustment of the scissor overtone energy. There are two notable features of these spectra. First, for both DPE and DPOE, the C_2 conformers possess twice the number of allowed IR transitions as the C_{2h} conformers. In these higher symmetry conformers half the states have *g* symmetry and are therefore not

IR active. Second, there are profound differences between the spectra of the DPE and DPOE conformers of the same symmetry. These differences arise from the higher frequency of the scissor modes in DPOE, as can be seen from the state designations provided in figure 5.6; states with little mixing are labeled symmetric stretch (ss), asymmetric stretch (*as*), or scissor overtone (ss). The Fermi mixed states are labeled as (*ss/so*) or (*so/ss*) with the leading designation being the larger component. Clearly the highest energy transitions in DPOE have leading *so* character while in DPE the lowest energy states have *so* character. These features are discussed in more detail below in section 5.7.2.

5.7 Discussion

5.7.1 Conformational Preferences of DPOE

The experimental data presented in this work have determined the presence of only two conformers of gas phase DPOE, *ttt* and *tgt*, following thermal equilibration at a pre-expansion temperature of 363 K and cooling in a supersonic expansion. The IRPT measurements have also provided a quantitative measure of the relative populations of these two conformers, with a 53±1%:47±1% *ttt*:*tgt* population ratio observed.

By comparison, calculations carried out at the DFT M05-02X/6-31+G(d) level of theory predict the *ttt* conformer as the global minimum, with the *tgt* counterpart second in energy, some 2.7 kJ/mol higher in energy. In seeking to understand these experimental results, we note that the M05-2X/6-31+G(d) calculations give torsional mode frequencies

that are remarkably close to experiment (5.5 Results). Furthermore, the barriers to conformational isomerization are sufficiently high (see below) that free energy calculations which treat the vibrations as harmonic should provide good predictions of the relative populations of the conformations.

Table 5.3 summarizes the DFT M05-2X/6-31+G(d) predictions for the fractional abundances of DPOE and DMOE at room temperature, and the DPOE abundances at 363 K, the pre-expansion temperature of the DPOE sample. The measured fractional abundances of the *ttt* and *tgt* conformers (0.53:0.47) match well with the calculated relative abundances at 363 K. However, since the experiment failed to detect any other higher-lying conformers, it seems likely that population initially present in the higher-energy conformers undergoes isomerization to the lower-lying minima during the collisional cooling process, ending up either in the *ttt* or *tgt* minima. In order to better understand the pathways for collisional cooling between minima, transition states connecting the low-lying conformational minima of DPOE were calculated at the same level of theory. These are gathered into a pictorial summary in figure 5.7.

Based on the heights of the barriers shown in figure 5.7, it seems plausible that the major pathways for collisional cooling are ones that retain the *trans* or *gauche* conformation about the central dihedral angle τ. Thus, the *ttg*+ → *ttt* barrier is only 6.17 kJ/mol, while that for *g*-*g*+*t* → *tgt* is even smaller (4.09 kJ/mol), funneling population within the *trans* or *gauche* sub-populations. It is worth noting that the average internal energy of the conformers of DPOE at 363 K is ~40 kJ/mol (3400 cm^{-1}), so that quenching of isomerization occurs at energies well below the initial internal energies of the conformers. In the limit that all Boltzmann population in the central *trans* and *gauche*

dihedral structures is funneled into the *ttt* and *tgt* minima, one predicts a *ttt*:*tgt* population ratio of 45:55, reasonably close to the 53:47 ratio observed experimentally.

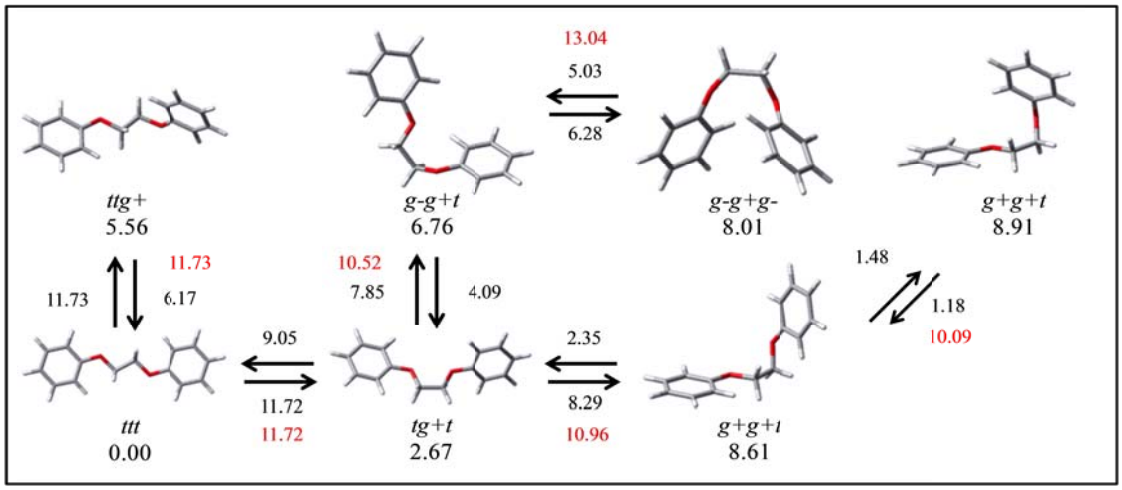

Figure 5.7 Calculated relative energies of the minima in the first 10 kJ/mol, and the transition states connecting them, at the M05-2X/6-31+G(d) level of theory. Numbers in red are the energies of the transition state relative to the ttt global minimum, while the numbers in black next to the arrows give the barrier heights in kJ/mol relative to the minimum on the reactant side of the arrow.

Table 5.3 Comparison of the calculated relative energies and fractional abundances of DPOE and DMOE at the DFT M05-2X/6-31+G(d) level of theory.

DPOE					DMOE		
Structure	Rel. Energy (kJ/mol)	Fractional Abundance 298 K	363 K	Exp.	Structure	Rel. Energy (kJ/mol)	Fractional Abundance 298 K
i/ttt/i	0	0.43	0.34	0.53±.01	ttt	0	0.38
i/tg+t/i	2.67	0.29	0.28	0.47±.01	tg-g+	2.586	0.27
i/ttg-/i	5.558	0.09	0.11		tg+t	3.067	0.22
o/g-g+t/i	6.761	0.06	0.07		ttg+	6.073	0.07
o/g+g-g+/o	8.013	0.03	0.05		g-g-g+	8.696	0.02
i/tg-g-/i	8.606	0.03	0.04		g-g-g-	9.386	0.02
g+/g+g+t/i	8.908	0.02	0.04		tg+g+	9.431	0.02
i/g-g-g+/i	10.612	0.01	0.02		g-/g+g-	9.987	0.01
o/g-g+g+/o	11.103	0.01	0.02		g-tg+	11.678	0
i/g+tg-/i	11.573	0	0.01		g-tg-	12.938	0

It is also worth comparing the present results with the conformational populations predicted for 1,2-dimethoxyethane (DMOE). Its status as a model for PEG/PEO has made it the subject of a large number of investigations, both experimental[8-9, 56-58] and theoretical.[1-4, 6] One of the notable aspects of this work is the conclusion that there is an oxygen *gauche* effect[4] in which adjacent O atoms in the O-CH_2-CH_2-O are lower in energy relative to *trans* than their purely alkyl counterparts. This preference for *gauche* conformations about the C-C bonds is thought to be due to the absence of steric constraints involving the O atoms. This is based on fractional abundances from electron diffraction[57] and NMR[56, 58] on gas phase DMOE,[1] and from Raman measurements in solution.[9] We see here that, despite this added stability of the *gauche* configuration for

the central τ dihedral, the *ttt* conformer is still the lowest energy structure calculated for both DPOE and DMOE, as most of the recent theoretical treatments have surmised.[1-4, 6]

The comparison shown in table 5.3 between the relative energies of the conformers in DPOE and DMOE shows a modest effect of the two capping phenyl rings on the conformational preferences of the OCCO chain. In the lowest energy conformations, the phenyl rings seem to adapt their conformation to accommodate the preferences of the OCCO chain linking them. More highly folded structures such as *tgg* and *ggg* conformers, tend to be lower in energy in DMOE than DPOE due to steric constraints imposed by the phenyl rings with these highly folded chains. It would be useful for those developing force fields for PEG/PEO polymer to test those force fields against the data on DPOE provided here.

5.7.2 Stretch-Bend Coupling in DPOE

One of the most striking results of the present study is the comparison afforded by figure 5.6 between the alkyl CH stretch spectra of the C_{2h} and C_2 symmetry conformers of DPE and DPOE. Spectra from the same-symmetry conformers of DPE and DPOE are remarkably different, despite the close similarity between the two structures themselves. The reason all four spectra are so different can be accounted for by examining the model ingredients from which the spectra were generated. The symmetry of the CH stretch modes is illustrated in figure 5.8 for an ethano bridge linkage for both C_2 and C_{2h} geometries. The symmetrized local mode bases are obtained by taking +/- linear combinations of the individual CH stretch states where the sign of the term is depicted by

the arrows in the figure, with the resulting vibrational symmetries labeled. These four CH stretch states are coupled to three eigenstates of the scissor Hamiltonian. To a very good approximation, two of these states are the +/- linear combinations of the local mode scissor states corresponding to having 2 quanta of excitation in one scissor, and zero in the other. These +/- combinations have a_g/ b_u symmetry, respectively, for the C_{2h} conformer and *a/b* symmetry for the C_2 conformer. The remaining state corresponds to a state with one quantum of excitation in each scissor mode. This state is not important for understanding the spectra other than to break the degeneracy of the +/- overtones for reasons to be discussed below.

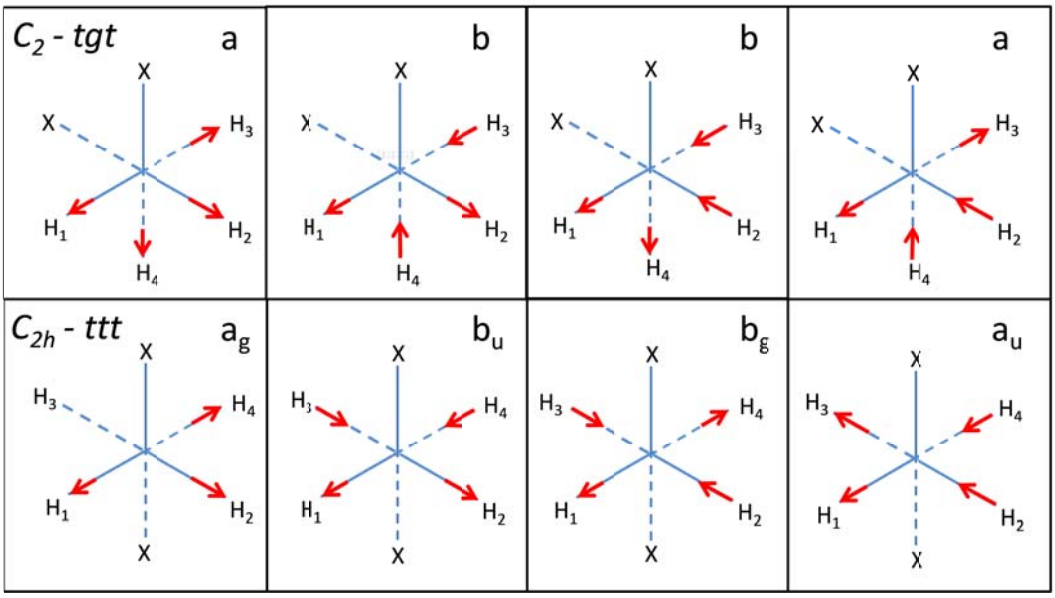

Figure 5.8 Symmetrized local mode states are obtained by taking +/- linear combinations, as indicated by the red arrows, of local mode stretch states. H1 and H2 belong to the same CH2 group while H3 and H4 belong to the second CH2 in the ethano bridge. Columns 1 and 2 correspond to symmetric CH stretches of individual CH2 groups; columns 3 and 4 correspond to asymmetric CH stretches .

Having examined the symmetry we are now in a position to consider the mixing of the states, the central components of which are depicted in figure 5.9. This figure shows on the vertical axis the energies of the CH stretch states of figure 5.8 on the left side, with their symmetry labels, and the scissor overtones and combination bands on the right side. The width of the boxes shows the DFT predicted infrared transition intensities from the zero-point levels of each conformer. For the C_{2h} conformer only those states with *u* symmetry are IR active, whereas for the C_2 conformer states of both *a* and *b* symmetries are IR active.

The lines in figure 5.9 connecting the CH stretch states to the scissor overtones indicate that in all cases it is only the symmetric stretch states that are Fermi coupled to the scissor overtones. For the C_{2h} conformer this result directly follows from the scissor overtone states having either a_g or b_u symmetry, symmetries that correspond to the in- and out-of-phase symmetric stretch, respectively. This lack of coupling to the asymmetric stretch modes, however, extends to the states of lower symmetry, so there must be a more general argument, which we now consider.

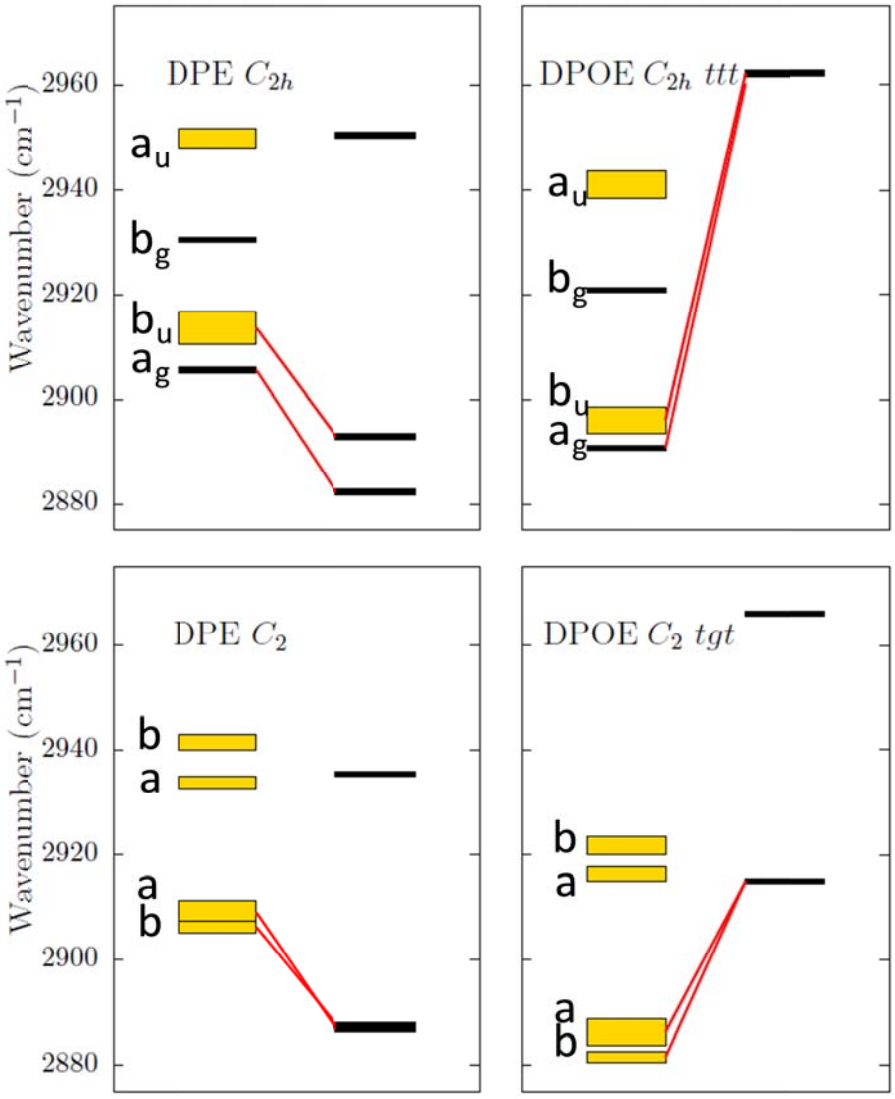

Figure 5.9 Comparison of CH stretch (left) /scissor overtone (right) energies and couplings for the (a) C2h and (b) C2 symmetry conformers of DPE, and the (c) ttt C2h and (d) tgt C2 conformers of DPOE. The width of the CH stretch states is proportional to the infrared oscillator strength from the conformer's zero-point level, and the vertical center of the boxes corresponds to the transition energies associated with the scaled Hamiltonian in the absence of Fermi couplings. The width of the lines connecting CH stretches to scissor overtones and combinations is proportional to the magnitude of the associated couplings.

The nature of the Fermi coupling can be understood most readily in a fully local mode perspective. We have found that the only significant Fermi coupling occurs within a single CH_2 moiety and is linear in the CH stretch and bilinear in the scissor mode. The corresponding coupling matrix elements between the local CH stretch and contiguous scissor overtone have very similar magnitudes, lying between 21 and 22 cm^{-1} for all conformers of DPOE and DPE. The localized nature of the Fermi coupling to a single CH_2 group explains why the scissor combination mode, corresponding to one quantum of excitation in each scissor of different CH_2 moieties, is only weakly coupled to the stretches. The similar magnitude of the coupling is the reason the asymmetric stretches are not coupled to the scissor modes, since this coupling scales as the difference between local mode couplings.

Given that the asymmetric stretches are decoupled from the scissor modes, the only coupling between the asymmetric stretch and the scissor modes is the indirect coupling through the symmetric CH stretches, which occurs only in the C_2 conformers. In DPOE, the coupling between the symmetric and asymmetric CH stretch states of figure 5.8 is -5 cm^{-1}/ -15 cm^{-1} for the *a*/*b* symmetry states, while in DPE, the corresponding couplings are 0 cm^{-1}/ -11 cm^{-1}. The magnitude of this coupling is small, since it results from the interactions between the two CH_2 groups of the ethano bridge. It should be noted that we have not shown this coupling in figure 5.9. The only instance where this coupling has any consequence is for the higher energy transition of the *tgt* C_2 conformer of DPOE, which gives this state some asymmetric stretch character. Consequently, for a qualitative understanding, we can treat the asymmetric stretches as being decoupled from the remaining degrees of freedom.

Given the coupling pathways in figure 5.9, we expect six transitions to appear in the infrared spectra of the C_2 conformers and three transitions for the C_{2h} conformers. Moreover, based on figure 5.9d, the six transitions for the C_2 conformer of DPOE are expected to appear as three *a/b* symmetry doublets. The middle doublet corresponds to transitions to asymmetric stretch states. The highest and lowest frequency doublets correspond to transitions involving the Fermi coupled states whose principal character are described in the spectra of figure 5.6.

The coupling between the basis states for DPE and DPOE are similar, however, the spectra are very different. The principle reason for this difference lies in the frequencies of the scissor modes. For DPE, the spectral complexity for the C_2 conformer (Figure 9b) is due to the overtone of the scissor modes pushing the symmetric CH stretches up to the asymmetric CH stretches, leading to intermixing of these four states. In this case, the lowest energy features consist of two transitions corresponding to the overtones of the scissors. In DPOE, the scissor overtones are significantly higher in energy than the symmetric stretch states with which they are coupled. Furthermore, their energy varies significantly between the two conformers, with frequencies almost 50 cm^{-1} higher in the C_{2h} *ttt* conformer than in C_2 *tgt*. As a result, in the C_2 conformer (figure 5.9d), the scissors overtones are pushed by mixing above the asymmetric stretch fundamentals (C_2 conformer), while in the C_{2h} conformer they appear at so high a frequency (figure 5.9c) that they hardly engage in mixing with the CH stretch states. Thus, the position and effect of the stretch-bend Fermi resonances in DPOE and DPE are qualitatively different, arguing for caution in assigning features to Fermi resonance bands in molecules where other information is lacking.

5.8 Conclusions

The ground state conformational properties and spectroscopy of 1,2-diphenoxyethane (DPOE) have been studied on a conformation-specific basis under jet-cooled conditions in the gas phase. Two conformers, of C_{2h} and C_2 symmetry, corresponding to *ttt* and *tgt* conformers, were observed and determined to be present with nearly equal populations in the expansion. Calculations carried out at the DFT M05-2X/6-31+G(d) level of theory account for the relative energies and conformational properties, and shed light on the torsional potential energy surface on which conformational isomerization occurs. The results for DPOE were contrasted with those for 1,2-dimethoxyethane, which has played a role as model for polyethylene glycol (PEG) polymers. The phenyl rings only shift the conformational energies of the main conformers by modest amounts, with lowest energy conformers predicted for both DPOE and DMOE to be due to the *trans* conformers about the central C-C bond.

DPOE has been an excellent model system in which to further develop a stretch-bend coupling model for the alkyl CH stretch region. The frequencies of the CH stretch fundamentals and CH bend (scissors) overtones change dramatically in DPOE relative to DPE, leading to wholesale changes in the appearance, and relative energy ordering of the Fermi resonance split levels. The prospects for extending this model from DPOE to DMOE, and on to PEG/PEO polymers and crown ethers, is excellent.

There are several important extensions of this work remaining to be carried out. First, SEP-population transfer experiments[24, 59-62] could be used to measure the barriers to isomerization in DPOE and DPE. If successful, such measurements could also provide bounds on the relative energies of the *ttt* and *tgt* conformational minima. Second, it

would be interesting to extend single-conformation studies of this type to longer chain analogs such as diphenoxybutane, in which the alkyl chain is sufficiently long to fold back on itself and facilitate interaction between the aromatic rings. Third, DPOE is a model flexible bichromophore, with close-lying excited states whose spectroscopy and vibronic coupling can be studied in exquisite detail. Finally, the spectroscopic signatures of the DPOE-H_2O complex, whose presence so far has been viewed primarily as an annoyance arising from the hygroscopic nature of the sample (figure 5.2), can shed light on the way in which a single bound H_2O molecule can affect the ground state conformational preferences and vibronic coupling in the excited states.

5.9 References

1. Anderson, P. M.; Wilson, M. R. Developing a force field for simulation of poly(ethylene oxide) based upon ab initio calculations of 1,2-dimethoxyethane. *Mol. Phys.* **2005,** *103* (1), 89-97.

2. Borodin, O.; Smith, G. D. Development of quantum chemistry-based force fields for poly(ethylene oxide) with many-body polarization interactions. *Journal of Physical Chemistry B* **2003,** *107* (28), 6801-6812.

3. Lee, H.; Venable, R. M.; MacKerell, A. D., Jr.; Pastor, R. W. Molecular dynamics studies of polyethylene oxide and polyethylene glycol: Hydrodynamic radius and shape anisotropy. *Biophysical Journal* **2008,** *95* (4), 1590-1599.

4. Sasanuma, Y.; Sugita, K. The attractive gauche effect of ethylene oxides. *Polymer Journal* **2006,** *38* (9), 983-988.

5. Velinova, M.; Tsoneva, Y.; Shushkov, P.; Ivanova, A.; Tadjer, A. Systematic Derivation and Testing of AMBER Force Field Parameters for Fatty Ethers from Quantum Mechanical Calculations. In *Advances in the Theory of Quantum Systems in Chemistry and Physics*, Hoggan, P. E. E.; Brandas, E. J. J.; Maruani, J.; Piecuch, P.; DelgadoBarrio, G., Eds. 2012; Vol. 22, pp 461-480.

6. Vorobyov, I.; Anisimov, V. M.; Greene, S.; Venable, R. M.; Moser, A.; Pastor, R. W.; MacKerell, A. D., Jr. Additive and classical drude polarizable force fields for linear and cyclic ethers. *Journal of Chemical Theory and Computation* **2007,** *3* (3), 1120-1133.

7. Yoshida, H.; Kaneko, I.; Matsuura, H.; Ogawa, Y.; Tasumi, M. IMPORTANCE OF AN INTRAMOLECULAR 1,5-CH...O INTERACTION AND INTERMOLECULAR INTERACTIONS AS FACTORS DETERMINING CONFORMATIONAL EQUILIBRIA IN 1,2-DIMETHOXYETHANE - A MATRIX-ISOLATION INFRARED SPECTROSCOPIC STUDY. *Chemical Physics Letters* **1992,** *196* (6), 601-606.

8. Yoshida, H.; Tanaka, T.; Matsuura, H. Conformational stability of 1,2-dimethoxyethane in the gas phase studied by infrared spectroscopy: Importance of an intramolecular 1,5-CH center dot center dot center dot O interaction. *Chemistry Letters* **1996,** (8), 637-638.

9. Goutev, N.; Ohno, K.; Matsuura, H. Raman spectroscopic study on the conformation of 1,2-dimethoxyethane in the liquid phase and in aqueous solutions. *Journal of Physical Chemistry A* **2000,** *104* (40), 9226-9232.

10. Abo-Riziq, A.; Grace, L.; Crews, B.; Callahan, M. P.; van Mourik, T.; de Vries, M. S. Conformational Structure of Tyrosine, Tyrosyl-glycine, and Tyrosyl-glycyl-glycine by Double Resonance Spectroscopy. *Journal of Physical Chemistry A* **2011,** *115* (23), 6077-6087.

11. Buchanan, E. G.; James, W. H., III; Choi, S. H.; Guo, L.; Gellman, S. H.; Mueller, C. W.; Zwier, T. S. Single-conformation infrared spectra of model peptides in the amide I and amide II regions: Experiment-based determination of local mode frequencies and inter-mode coupling. *J. Chem. Phys.* **2012,** *137* (9).

12. Buchanan, E. G.; James, W. H., III; Gutberlet, A.; Dean, J. C.; Guo, L.; Gellman, S. H.; Zwier, T. S. Single-conformation spectroscopy and population analysis of model gamma-peptides: New tests of amide stacking. *Faraday Discussions* **2011,** *150*, 209-226.

13. Chin, W.; Piuzzi, F.; Dimicoli, I.; Mons, M. Probing the competition between secondary structures and local preferences in gas phase isolated peptide backbones. *Physical Chemistry Chemical Physics* **2006,** *8* (9), 1033-1048.

14. de Vries, M. S.; Hobza, P. Gas-phase spectroscopy of biomolecular building blocks. In *Annual Review of Physical Chemistry*, 2007; Vol. 58, pp 585-612.

15. Dean, J. C.; Buchanan, E. G.; James, W. H., III; Gutberlet, A.; Biswas, B.; Ramachandran, P. V.; Zwier, T. S. Conformation-Specific Spectroscopy and Populations of Diastereomers of a Model Monolignol Derivative: Chiral Effects in a Triol Chain. *Journal of Physical Chemistry A* **2011,** *115* (30), 8464-8478.

16. Dean, J. C.; Buchanan, E. G.; Zwier, T. S. Mixed 14/16 Helices in the Gas Phase: Conformation-Specific Spectroscopy of Z-(Gly)(n), n=1, 3, 5. *Journal of the American Chemical Society* **2012,** *134* (41), 17186-17201.

17. Robertson, E. G.; Simons, J. P. Getting into shape: Conformational and supramolecular landscapes in small biomolecules and their hydrated clusters. *Physical Chemistry Chemical Physics* **2001,** *3* (1), 1-18.

18. Schwing, K.; Fricke, H.; Bartl, K.; Polkowska, J.; Schrader, T.; Gerhards, M. Isolated ss-Turn Model Systems Investigated by Combined IR/UV Spectroscopy. *Chemphyschem* **2012,** *13* (6), 1576-1582.

19. Simons, J. P. Bio-active molecules in the gas phase. *Physical Chemistry Chemical Physics* **2004,** *6* (10), E7-E7.

20. Simons, J. P. Good vibrations: probing biomolecular structure and interactions through spectroscopy in the gas phase. *Mol. Phys.* **2009,** *107* (23-24), 2435-2458.

21. Zwier, T. S. Laser probes of conformational isomerization in flexible molecules and complexes. *Journal of Physical Chemistry A* **2006,** *110* (12), 4133-4150.

22. Clarkson, J. R.; Dian, B. C.; Moriggi, L.; DeFusco, A.; McCarthy, V.; Jordan, K. D.; Zwier, T. S. Direct measurement of the energy thresholds to conformational isomerization in Tryptamine: Experiment and theory. *J. Chem. Phys.* **2005,** *122* (21).

23. Dian, B. C.; Florio, G. M.; Clarkson, J. R.; Longarte, A.; Zwier, T. S. Infrared-induced conformational isomerization and vibrational relaxation dynamics in melatonin and 5-methoxy-N-acetyl tryptophan methyl amide. *J. Chem. Phys.* **2004,** *120* (19), 9033-9046.

24. LeGreve, T. A.; Clarkson, J. R.; Zwier, T. S. Experimental determination of conformational isomerization energy thresholds in serotonin. *Journal of Physical Chemistry A* **2008,** *112* (17), 3911-3920.

25. Pillsbury, N. R.; Stearns, J. A.; Mueller, C. W.; Plusquellic, D. F.; Zwier, T. S. State-specific studies of internal mixing in a prototypical flexible bichromophore: Diphenylmethane. *J. Chem. Phys.* **2008,** *129* (11).

26. Stearns, J. A.; Pillsbury, N. R.; Douglass, K. O.; Mueller, C. W.; Zwier, T. S.; Plusquellic, D. F. Rotationally resolved studies of S-0 and the exciton coupled S-1/S-2 origin regions of diphenylmethane and the d(12) isotopologue. *J. Chem. Phys.* **2008,** *129* (22).

27. Chou, S. G.; Rodrigo, C. P.; Mueller, C. W.; Douglass, K. O.; Zwier, T. S.; Plusquellic, D. F. Rotationally Resolved C-2 Symmetric Conformers of Bis-(4-hydroxyphenyl)methane: Prototypical Examples of Excitonic Coupling in the S-1 and S-2 Electronic States. *Journal of Physical Chemistry A* **2011,** *115* (34), 9643-9652.

28. Zehnacker, A.; Lahmani, F.; Breheret, E.; Desvergne, J. P.; BouasLaurent, H.; Germain, A.; Brenner, V.; Millie, P. Laser induced fluorescence of jet-cooled non-conjugated bichromophores: Bis-phenoxymethane and bis-2,6-dimethylphenoxymethane. *Chemical Physics* **1996,** *208* (2), 243-257.

29. Zehnacker, A.; Lahmani, F.; Desvergne, J. P.; Bouas-Laurent, H. Conformation-dependent intramolecular exciplex formation in jet-cooled bichromophores. *Chemical Physics Letters* **1998,** *293* (5-6), 357-365.

30. Wang, X.; Levy, D. H.; Rubin, M. B.; Speiser, S. Supersonic jet spectroscopy and intramolecular electronic energy transfer in naphthalene-(CH2)(n)-anthracene bichromophoric molecules. *Journal of Physical Chemistry A* **2000,** *104* (28), 6558-6565.

31. Zehnacker, A.; Lahmani, F.; van Walree, C. A.; Jenneskens, L. W. Intramolecular donor-acceptor interactions in jet-cooled bichromophoric molecules: Comparison between SiMe2 and CMe2 spacers. *Journal of Physical Chemistry A* **2000,** *104* (7), 1377-1387.

32. Rodrigo, C. P.; Mueller, C. W.; Pillsbury, N. R.; James, W. H., III; Plusquellic, D. F.; Zwier, T. S. Conformer-specific vibronic spectroscopy and vibronic coupling in a flexible bichromophore: Bis-(4-hydroxyphenyl)methane. *J. Chem. Phys.* **2011,** *134* (16).

33. Nebgen, B.; Emmert, F. L., III; Slipchenko, L. V. Vibronic coupling in asymmetric bichromophores: Theory and application to diphenylmethane. *J. Chem. Phys.* **2012,** *137* (8).

34. Ottiger, P.; Leutwyler, S.; Koeppel, H. Vibrational quenching of excitonic splittings in H-bonded molecular dimers: The electronic Davydov splittings cannot match experiment. *J. Chem. Phys.* **2012,** *136* (17).

35. Ottiger, P.; Leutwyler, S. Excitonic Splittings in Jet-Cooled Molecular Dimers. *Chimia* **2011,** *65* (4), 228-230.

36. Shubert, V. A.; James, W. H.; Zwier, T. S. Jet-Cooled Electronic and Vibrational Spectroscopy of Crown Ethers: Benzo-15-Crown-5 Ether and 4 '-Amino-Benzo-15-Crown-5 Ether. *Journal of Physical Chemistry A* **2009,** *113* (28), 8055-8066.

37. Carney, J. R.; Zwier, T. S. The infrared and ultraviolet spectra of individual conformational isomers of biomolecules: Tryptamine. *Journal of Physical Chemistry A* **2000,** *104* (38), 8677-8688.

38. Buchanan, E. G.; Plusquellic, D. F.; Zwier, T. S. Excitonic splitting and vibronic coupling in 1,2-diphenoxyethane: Conformation-specific effects in the weak coupling limit**in preparation**.

39. Pillsbury, N. R.; Mueller, C. W.; Zwier, T. S. Conformational Isomerization and Collisional Cooling Dynamics of Bis(2-hydroxyphenyl)methane. *Journal of Physical Chemistry A* **2009,** *113* (17), 5013-5021.

40. Pillsbury, N. R.; Muller, C. W.; Meerts, W. L.; Plusquellic, D. F.; Zwier, T. S. Conformational Effects on Excitonic Interactions in a Prototypical H-Bonded Bichromophore: Bis(2-hydroxyphenyl)methane. *Journal of Physical Chemistry A* **2009,** *113* (17), 5000-5012.

41. Baquero, E. E.; James, W. H., III; Choi, T. H.; Jordan, K. D.; Zwier, T. S. Single Conformation Spectroscopy of a Flexible Bichromophore: 3-(4-Hydroxyphenyl)-N-benzylpropionamide. *Journal of Physical Chemistry A* **2008,** *112* (44), 11115-11123.

42. Gloaguen, E.; Valdes, H.; Pagliarulo, F.; Pollet, R.; Tardivel, B.; Hobza, P.; Piuzzi, F.; Mons, M. Experimental and Theoretical Investigation of the Aromatic-Aromatic Interaction in Isolated Capped Dipeptides. *Journal of Physical Chemistry A* **2010,** *114* (9), 2973-2982.

43. Kusaka, R.; Inokuchi, Y.; Ebata, T. Laser spectroscopic study on the conformations and the hydrated structures of benzo-18-crown-6-ether and dibenzo-18-crown-6-ether in supersonic jets. *Physical Chemistry Chemical Physics* **2007,** *9* (32), 4452-4459.

44. Kusaka, R.; Inokuchi, Y.; Ebata, T. Structure of hydrated clusters of dibenzo-18-crown-6-ether in a supersonic jet-encapsulation of water molecules in the crown cavity. *Physical Chemistry Chemical Physics* **2008,** *10* (41), 6238-6244.

45. Kusaka, R.; Inokuchi, Y.; Ebata, T. Water-mediated conformer optimization in benzo-18-crown-6-ether/water system. *Physical Chemistry Chemical Physics* **2009,** *11* (40), 9132-9140.

46. Kusaka, R.; Inokuchi, Y.; Xantheas, S. S.; Ebata, T. Structures and Encapsulation Motifs of Functional Molecules Probed by Laser Spectroscopic and Theoretical Methods. *Sensors* **2010,** *10* (4), 3519-3548.

47. Buchanan, E. G.; Gutberlet, A.; Rodrigo, C. P.; Zwier, T. S. Electronic coupling and macrocycle-H_2O interactions in dibenzo-15-crown-5 ether and its water-containing complexes**manuscript in preparation**.

48. Dian, B. C.; Longarte, A.; Winter, P. R.; Zwier, T. S. The dynamics of conformational isomerization in flexible biomolecules. I. Hole-filling spectroscopy of N-acetyl tryptophan methyl amide and N-acetyl tryptophan amide. *J. Chem. Phys.* **2004,** *120* (1), 133-147.

49. Mohamadi, F.; Richards, N. G. J.; Guida, W. C.; Liskamp, R.; Lipton, M.; Caufield, C.; Chang, G.; Hendrickson, T.; Still, W. C. MACROMODEL - AN INTEGRATED SOFTWARE SYSTEM FOR MODELING ORGANIC AND BIOORGANIC MOLECULES USING MOLECULAR MECHANICS. *Journal of Computational Chemistry* **1990,** *11* (4), 440-467.

50. Zhao, Y.; Truhlar, D. G. Density functionals for noncovalent interaction energies of biological importance. *Journal of Chemical Theory and Computation* **2007,** *3* (1), 289-300.

51. Zhao, Y.; Truhlar, D. G. Density functionals with broad applicability in chemistry. *Accounts of Chemical Research* **2008,** *41* (2), 157-167.

52. Gaussian 09, R. A., Frisch, M. J.; Trucks, G. W.; Schlegel, H. B.; Scuseria, G. E.; Robb, M. A.; Cheeseman, J. R.; Scalmani, G.; Barone, V.; Mennucci, B.; Petersson, G. A.; Nakatsuji, H.; Caricato, M.; Li, X.; Hratchian, H. P.; Izmaylov, A. F.; Bloino, J.; Zheng, G.; Sonnenberg, J. L.; Hada, M.; Ehara, M.; Toyota, K.; Fukuda, R.; Hasegawa, J.; Ishida, M.; Nakajima, T.; Honda, Y.; Kitao, O.; Nakai, H.; Vreven, T.; Montgomery, Jr., J. A.; Peralta, J. E.; Ogliaro, F.; Bearpark, M.; Heyd, J. J.; Brothers, E.; Kudin, K. N.; Staroverov, V.N.; Kobayashi, R.; Normand, J.; Raghavachari, K.; Rendell, A.; Burant, J. C.; Iyengar, S. S.; Tomasi, J.; Cossi, M.; Rega, N.; Millam, N. J.; Klene, M.; Knox, J. E.; Cross, J. B.; Bakken, V.; Adamo, C.; Jaramillo, J.; Gomperts, R.; Stratmann, R. E.; Yazyev, O.; Austin, A.J.; Cammi, R.; Pomelli, C.; Ochterski, J. W.; Martin, R. L.; Morokuma, K.; Zakrzewski, V. G.; Voth, G. A.; Salvador, P.; Dannenberg, J. J.; Dapprich, S.; Daniels, A. D.; Farkas, Ö.; Foresman, J. B.; Ortiz, J.V.; Cioslowski, J.; Fox, D. J. Gaussian, Inc., Wallingford CT, 2009.

53. Buchanan, E. G.; Kidwell, N. M.; Zwier, T. S.; Sibert III, E. L. Towards a first-principles model of Fermi resonance in the alkyl CH stretch region: Application to 1,2-diphenylethane and [2.2.2]paracyclophane. *J. Chem. Phys.* **2013,** *138*, 064308.

54. Macphail, R. A.; Strauss, H. L.; Snyder, R. G.; Elliger, C. A. C-H stretching modes and the structure of normal alkyl chains. 2. Long, all-trans chains. *J. Phys. Chem.* **1984,** *88* (3), 334-341.

55. Snyder, R. G.; Aljibury, A. L.; Strauss, H. L.; Casal, H. L.; Gough, K. M.; Murphy, W. F. Isolated C-H stretch vibrations of n-alkanes --Assignments and relation to structure. *J. Chem. Phys.* **1984,** *81* (12), 5352-5361.

56. Abe, A.; Inomata, K. GAS-PHASE NMR OF 1,2-DIMETHOXYETHANE. *Journal of Molecular Structure* **1991,** *245* (3-4), 399-402.

57. Astrup, E. E. Investigation of the molecular structure and conformation of 1,2-dimethoxyethane, CH3-O-CH2-CH2-O-CH3, in the gas phase. *Acta Chemica Scandinavica Series a-Physical and Inorganic Chemistry* **1979,** *33* (9), 655-664.

58. Inomata, K.; Abe, A. Conformation of 1,2-dimethoxyethane in the gas phase --A rotational isomeric state simulation of NMR vicinal coupling constants. *J. Phys. Chem.* **1992,** *96* (20), 7934-7937.

59. Clarkson, J. R.; Dian, B. C.; Moriggi, L.; DeFusco, A.; McCarthy, V.; Jordan, K. D.; Zwier, T. S. Direct measurement of the energy thresholds to conformational isomerization in Tryptamine: Experiment and theory. *J. Chem. Phys.* **2005,** *122* (21), 214311.

60. Pillsbury, N. R.; Muller, C. W.; Zwier, T. S. Conformational Isomerization and Collisional Cooling Dynamics of Bis(2-hydroxyphenyl)methane. *Journal of Physical Chemistry A* **2009,** *113* (17), 5013-5021.

61. Pillsbury, N. R.; Zwier, T. S. Conformational Isomerization of 5-Phenyl-1-pentene Probed by SEP-Population Transfer Spectroscopy. *Journal of Physical Chemistry A* **2009,** *113* (1), 126-134.

62. Selby, T. M.; Zwier, T. S. Flexing the muscles of m-divinylbenzene: Direct measurement of the barriers to conformational isomerization. *Journal of Physical Chemistry A* **2007,** *111* (19), 3710-3718.

CHAPTER 6 EXCITONIC SPLITTING AND VIBRONIC COUPLING IN 1,2-DIPHENOXYETHANE: CONFORMATION-SPECIFIC EFFECTS IN THE WEAK COUPLING LIMIT

6.1 Introduction

Excitonic and vibronic coupling between electronic chromophores plays an essential role in the absorption/emission properties and excited state dynamics of molecular samples with important applications, including light-harvesting complexes,[1-4] chromophore arrays (e.g., J- and H-aggregates),[5-6] conjugated polymers,[7-9] and fluorescence resonance energy transfer (FRET).[10] This interest is fueled in part by new experimental methods such as 2D-electronic spectroscopy,[11-12] which are providing new insight to the femtosecond dynamics of electronic energy transfer. Among the issues under active investigation is the possible role played by electronic coherence in directing electronic energy transfer through an array of chromophores, and the extent to which vibrational motions are involved.[13-14]

Regardless of the circumstance, the structural and dynamical consequences of electronic near-degeneracy provide a particular challenge to modern theories seeking to understand them. While many of these applications involve multiple chromophores in a complex environment at room temperature, one useful strategy is to seek to control or remove many of the complicating factors in order to focus attention on the fundamental aspects of interchromophore coupling. To that end, laser spectroscopy of the gas-phase

bichromophore cooled in a supersonic jet provides exquisite details of the vibronic coupling on a single-vibronic level basis free from the interference from solvent.[15-22] When the two chromophores are incorporated into separate molecules, the supersonic expansion serves as a means for synthesizing the molecular dimer and collapsing its population entirely into the ground state vibrational zero-point level.[15-23]

The other circumstance in which multiple chromophores exist in close proximity is when they are incorporated as part of the same molecule. Model bichromophores can either be held rigidly in a framework which defines the interchromophore separation and orientation,[24-25] or as part of a flexible linker along which the interchromophore distance and orientation may vary.[26-38] Flexible linkages offer the tantalizing prospect of studying interchromophore vibronic coupling on a conformation-specific basis under jet-cooled conditions in which population is collisionally cooled into more than one conformational zero-point level. The uncoupled excited state energies and inter-chromophore electronic coupling will be modulated from one conformer to the next by changes in the distance and relative orientation of the chromophores, and the nature of the vibrational motions involved.

Model flexible bichromophores can either incorporate two identical monomers,[28-35] or consist of chemically distinct donor and acceptor sub-units.[39-40] In a few cases, conformation-specific data have shed light on the way in which the ground state conformation of the molecule dictates the excited state spectroscopy and dynamics, producing conformation-selective broadening in the excitation spectrum, red-shifted emission, or differing energy thresholds to exciplex formation.[29-30, 39]

Recent experiments and theory are shedding qualitative new light on the spectroscopic consequences of interchromophore coupling.[16, 18-19, 41] Much of this work compares experiment with the predictions of a diabatic model of the vibronic coupling based on Förster theory,[42] as developed by Fulton and Gouterman[43-44] for the specific case of a bichromophore coupled by a single vibrational mode. Extension of this model to multiple vibrational modes[34, 41] and to asymmetric bichromophores[41] have contributed to the growing ability to quantitatively account for the observed vibronic coupling patterns.

Recently, Leutwyler, Köppel, and co-workers have developed an adiabatic vibronic coupling model and used it to obtain a quantitatively accurate account of the observed excitonic splitting in 2-aminopyridine, *o*-cyanophenol, 2-pyridone, and benzoic acid dimers, all of which are in the weak coupling limit.[16, 45] The theory reproduces the experimental excitonic splitting determined by the diabatic model, but provides a more intuitive picture of the excitonic splitting in the weak coupling limit. Here, the electronic energy transfer occurs through a barrier on the adiabatic surface, with the excitonic splitting modeled as a tunneling splitting in which both nuclear distortions and interchromophore electronic energy transfer contribute to the tunneling rate.

In experiments to date on jet-cooled bichromophores, there are relatively few examples in which both the S_0-S_1 and S_0-S_2 transitions have been spectroscopically characterized. When the two chromophores are sufficiently different, fast electronic energy transfer between the two chromophores inhibits the identification of the life-time broadened S_2 state. Furthermore, in cases where the two chromophores are identical and conformational symmetry exists, only one of the S_0-S_1 or S_0-S_2 transitions is often dipole-allowed.[17] In several aromatic dimers, Leutwyler and co-workers have cleverly

addressed this by breaking the symmetry through recording the spectrum of the singly ^{13}C substituted isotopomer in natural abundance using resonant two-photon ionization (R2PI) coupled with time-of-flight mass analysis.[18-19, 46]

Previous work from our group has focused attention on a series of prototypical flexible bichromophores that possess a single conformational isomer for diphenylmethane (DPM)[33, 35], and two isomers of both bis-(2-hydroxyphenyl)methane (2HDPM)[32] and bis-(4-hydroxyphenyl)methane (b4HPM).[34] In these molecules, the spectroscopic consequences of internal mixing between the two excited electronic states has been characterized in some detail. In DPM, the excitonic splitting was determined to be 123 cm^{-1}, leading to a dual emission from the (nominal) S_2 origin that reported on its mixing with nearby vibrational levels built off the S_1 origin. This has stimulated theoretical developments that employ a multi-mode asymmetric vibronic coupling model as an extension of the theoretical framework developed by Fulton and Gouterman[43, 47] for symmetric bichromophores.[41]

Chapter 5 reported on the ground state conformational preferences of 1,2-diphenoxyethane (C_6H_5-O-CH_2-CH_2-O-C_6H_5, DPOE) and provides the foundation for the current chapter, which we briefly summarize here. A conformational search of the torsional potential energy surface for DPOE located 26 conformational minima. Two of the conformational isomers possessed an inversion center, while the remaining twelve structures are composed of pairs of non-superimposable mirror images with dihedral angles of opposite sign but identical magnitude. Experimentally, two conformational isomers were observed in the supersonic jet expansion and assigned based on infrared and vibronic data to the two lowest energy conformers of DPOE, with C_2 (*tgt*) and C_{2h}

(*ttt*) symmetry, as shown in figure 6.1. Here the central three dihedral angles are labeled as *trans* (*t*) or *gauche* (*g*). To establish the conformational assignments, calculated harmonic vibrational frequency were compared to the experimental alkyl CH stretch, CH bend, and CO stretch spectra. Using a reduced-dimension model, the Fermi resonances present in the alkyl CH stretch infrared spectrum were successfully modeled, confirming and strengthening the assignments based on the vibronic spectroscopy.

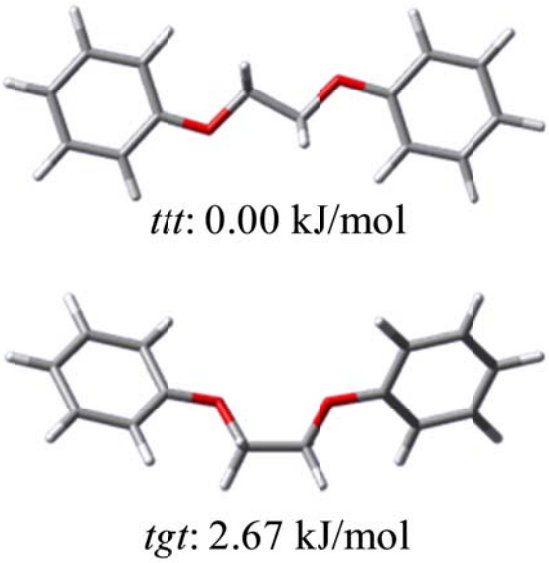

Figure 6.1 Optimized structures for the two observed conformers of DPOE, with their relative energies calculated at the DFT M05-2X/6-31+G(d) level of theory.

In the current chapter, we provide a detailed spectroscopic characterization of the vibronic and rovibronic spectroscopy of DPOE in the region of the close-lying S_1 and S_2 state origins. High resolution ultraviolet spectra prove that the two dipole-allowed S_0-S_1 and S_0-S_2 origins of the *tgt* isomer are separated by 1.02 cm^{-1}. Although the S_0-S_1 origin of the *ttt* conformer is dipole-forbidden, 2C-R2PI spectra of the M+1 mass channel for

monomers possessing a single ^{13}C atom show a spectrum for the *ttt* conformer that possesses two dipole-allowed origins arising from near-complete localization of the electronic excitation in one or the other ring, with splitting of ~4 cm^{-1}. Thus, despite the seeming close proximity of the two chromophores, interchromophore coupling in DPOE is in the extreme limit of weak coupling. The results for DPOE thus provide a window on the spectroscopic consequences of vibronic coupling in this weak coupling limit in which the two electronic states are no more than a few cm^{-1} from one another over much of the torsional potential energy surface, with electronic excitation localized or delocalized by minute asymmetries in the local environment.

6.2 Computational Methods

Excited state structural optimizations and vibrational frequency calculations for the *ttt* and *tgt* conformers of DPOE were performed using time-dependent density functional theory (TDDFT) at the M05-2X/6-31+G(d) level of theory. Rotationally resolved spectra were fit to an asymmetric rotor Hamiltonian using the genetic algorithm as implemented in the *JB95* spectral fitting program.[48] The two optimized structures, *ttt* and *tgt*, were used as input for fitting the rotational spectra.

To better understand the excitonic splitting, the transition dipole coupling model (TDM) and the Fulton Gouterman (FG) model have been employed.[43, 47] The transition dipole coupling model (TDM) is a simple electrostatic model in which the excitonic splitting is approximated utilizing the columbic interaction between the two electronic transition moments on the individual phenyl rings A and B. The interchromophore coupling is given by

$$V_{AB} = \frac{\mu_A \mu_B}{4\pi\varepsilon R^3}(2\cos\theta_A \cos\theta_B - \sin\theta_A \sin\theta_B \cos\varphi) \quad (1)$$

where μ is the magnitude of the electronic transition moment, R is the distance between the two transition moment vectors, θ is the angle between the two transition moment vectors along R, and φ is the dihedral between the two vectors.

The FG model for vibronic coupling uses a diabatic approach to model the vibronic structure observed in absorption and dispersed fluorescence.[18,19] In earlier work, we implemented a version of this model to explain the multi-mode vibronic coupling observed in bis-(4-hydroxyphenyl)methane.[34] We use this same program to compare the model predictions with experiment in DPOE. Details of the model are given elsewhere.[34, 41]

6.3 Results

6.3.1 R2PI and Dispersed Fluorescence

Figure 6.2 shows the 2C-R2PI spectrum (top trace) and the ultraviolet hole-burning spectra (bottom traces) of the two monomer conformations present in the supersonic jet expansion. 2C-R2PI was employed to avoid saturating the excitation spectrum. The small excursion from zero marked with an asterisk in the figure is present due to incomplete subtraction through the gated integrator when tuning through the *tgt* S_0-S_1 origin. As discussed in the previous study reporting on the ground state preferences of DPOE,[49] the two isomers adopt geometries with C_2 and C_{2h} symmetry, differing exclusively by the central OCCO dihedral angle, *gauche* or *trans*. For this reason, the C_2 symmetric conformer has been labeled *tgt* and the C_{2h} isomer as *ttt* representing the *gauche* and *trans* isomers respectively. The *tgt* origin occurs at 36423 cm^{-1} and the *ttt* origin at 36509 cm^{-1}. The calculations predict an in-plane geometry of both Ph-O-C groups in both conformers, as is observed in alkoxy-benzenes such as 1,2-diethoxybenzene.[50]

Given the C_2 symmetry of the *tgt* conformer A, calculations predict that transitions from S_0 to both the S_1(A) and S_2(B) electronic excited states will be dipole-allowed. The UVHB spectrum of the *tgt* conformer has several low-frequency vibronic transitions, including transitions +24, +26, +35, +99, +155, and +185 cm^{-1} from the origin (figure 6.2). Of these, the transitions at +24, +35, +99, and +155 cm^{-1} are totally symmetric fundamentals with frequencies virtually unchanged from their values in the ground electronic state, as summarized in table 6.1. As an example, the DFL spectrum of

the +24 cm^{-1} band is shown in figure 6.3a. The spectrum is dominated by a false origin at -25 cm^{-1}, with vibronic structure built off this false origin closely similar to that of the electronic origin. The DFL spectra from the other totally symmetric fundamentals are similar, with false origins associated with X^1_1 transitions dominating the spectrum. These spectra are included in the appendix. The two remaining transitions at +26 cm^{-1} and +185 cm^{-1} are b symmetry fundamentals. Their DFL spectra are shown in figure 6.3a. These bands also display strong false origins in emission that confirm their assignments to 'b' fundamentals with ground state frequencies of 30 and 186 cm^{-1}. Table 6.1 compares the observed ground and excited state frequencies of the *tgt* conformer with those predicted by calculation. The close correspondence confirms the assignments given. The 'b' symmetry fundamentals appear in excitation as a result of vibronic coupling between the S_1 and S_2 states. It is striking that all vibronic transitions are assigned to vibronic bands built off the single observed origin at 36423 cm^{-1}. Thus, the location of the strong dipole-allowed S_0-S_2 origin requires further investigation in what follows.

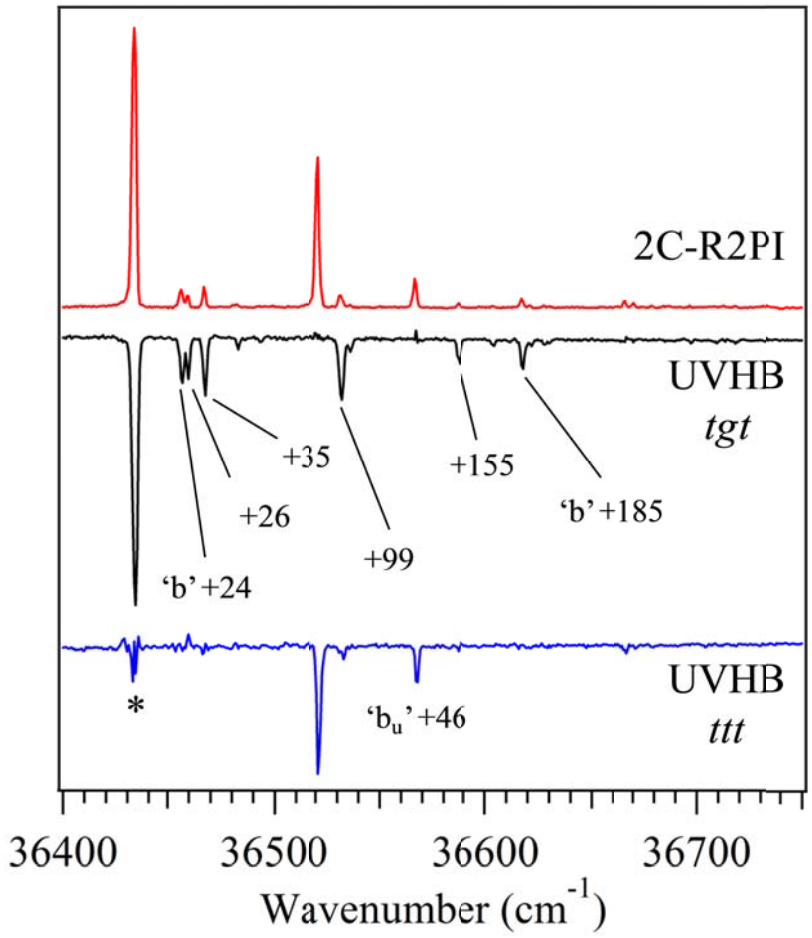

Figure 6.2 2C-R2PI and UVHB spectra of the two isomers present in the supersonic expansion. The asterisk marks an artifact due to incomplete subtraction through the gated integrator. Both UVHB spectra show vibronically induced fundamentals.

The C_{2h} symmetry *ttt* conformation has $S_1(A_g)$ and $S_2(B_u)$ electronic excited states with transitions from the ground electronic state $S_0(A_g)$ that are dipole forbidden and dipole-allowed, respectively. The UVHB spectrum of the *ttt* conformer is shown in the bottom trace of figure 6.2. According to the calculations, the lowest frequency totally symmetric mode ($\nu_{28}(a_g)$, labeled R) in the C_{2h} *ttt* conformer is at 149 cm^{-1}, in reasonable agreement with the weak transition at +146 cm^{-1} in the UVHB spectrum of the *ttt* isomer.

The band 46 cm^{-1} above the B_u origin is assigned to a vibronically induced transition involving the lowest frequency b_u symmetry fundamental (ν_{84}, labeled $\bar{R}$ here) with calculated ground state frequency of 46 cm^{-1} (table 6.1). Figure 6.4 presents the form of the R and $\bar{R}$ vibrational modes, which involve symmetric and asymmetric in-plane bends of the two phenyl rings. It would appear built off the dipole-forbidden A_g symmetry excited state ($A_gX\ b_u$), gaining its oscillator strength completely through vibronic coupling. Its frequency position (+46 cm^{-1}) suggests that the dipole-forbidden origin must be near to the allowed A_g-B_u origin at 36509 cm^{-1}.

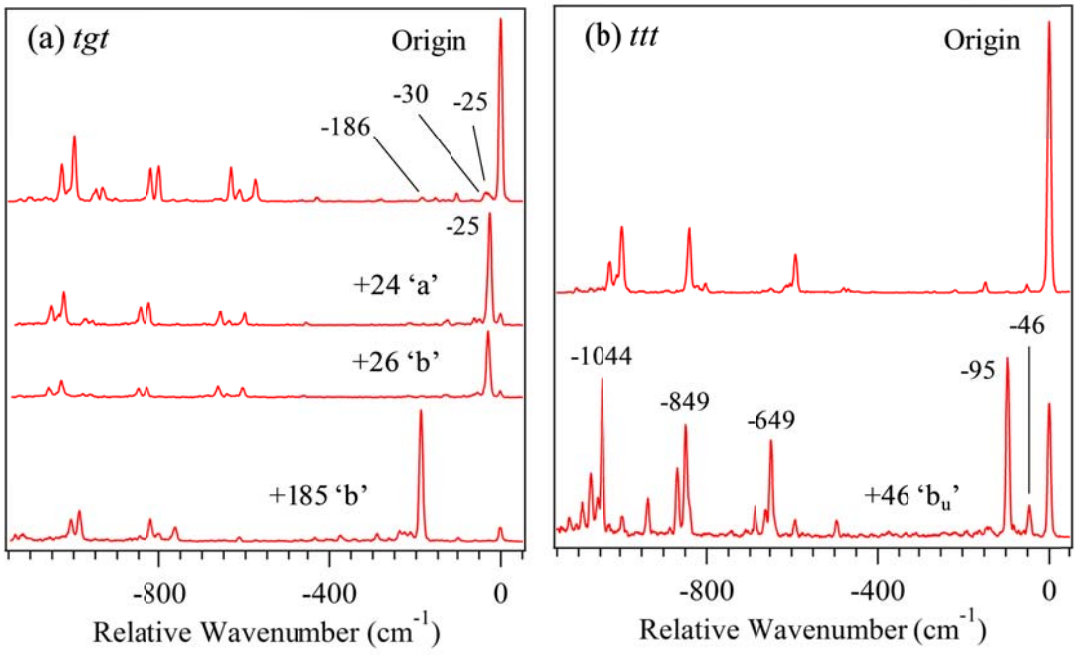

Figure 6.3 Dispersed fluorescence spectra of the origin and key vibronic bands of (a) the *tgt* conformer and (b) the *ttt* conformer of DPOE.

Table 6.1 A comparison of the calculated ground state vibrational frequencies to the experimental ground and excited state vibrational frequencies (in cm^{-1}) is presented. The Mulliken labeling scheme has been used for the normal modes.

C_2 (*tgt*)					C_{2h} (*ttt*)				
Mode #	Calc. Frequency	Exp. S_0 Freq	Exp. S_1 Freq	Symmetry (mode)	Mode #	Calc. Frequency	Exp. S_0 Freq	Exp. S_1 Freq	Symmetry (mode)
40	158	157	154	a	28 (R)	149	147	146	a_g
41	104	103	98	a	41	166			b_g
42	36	36	34	a	55	141			a_u
43	25	25	24	a	56	38			a_u
82	194	186	185	b	57	22			a_u
84	30	30	26	b	84 ($\bar{R}$)	51	46	46	b_u

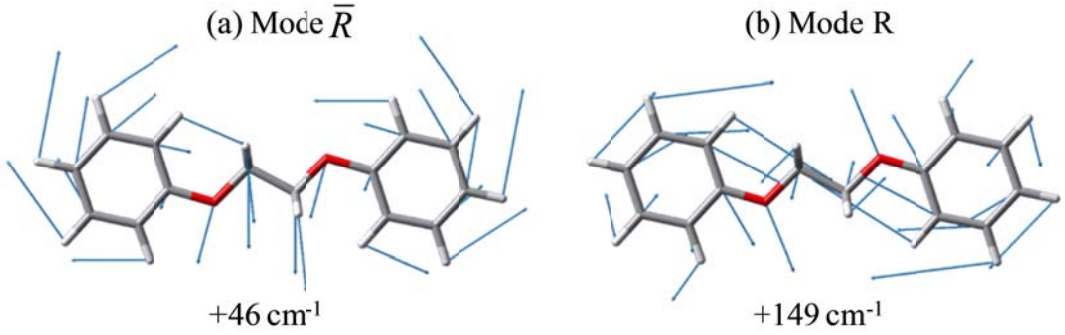

Figure 6.4 Form of the normal modes of the ttt conformer of DPOE for the (a) bu symmetry $\bar{R}$ vibration (46 cm-1) and (b) its ag counterpart R (149 cm-1).

The DFL spectra of the B_u electronic origin and $A_g(\bar{R}^1{}_0)$ transitions are presented for the *ttt* conformer in figure 6.3b. The origin emission spectrum has contributions only from a_g fundamentals, consistent with originating from a B_u excited electronic state. The $A_g(\bar{R}^1{}_0)$ band, however, has unusual vibronic activity, most notably in the triad of peaks observed at 0, -46, and -95 cm^{-1}. The 0 and -95 cm^{-1} transitions are attributed to vibronic coupling, producing $\Delta v_{84} = \pm 1$ Herzberg-Teller selection rules. What is puzzling is the

band at -46 cm^{-1}, which should only appear from an A_g symmetry vibronic level ($B_u x b_u$) in the excited state, since its ground state vibronic symmetry is $A_g x b_u = B_u$. Its DFL spectrum also shows increased intensity in several ring modes relative to the B_u 0^0_0 spectrum above it. The enhancement of ring mode intensity in emission was previously observed in the spectrum of the S_2 origin of bis-(4-hydroxyphenyl)methane[34] and attributed to vibronic coupling effects. In that case, the Fulton-Gouterman (FG) model was able to give a quantitative account of these intensity changes. We will present further analysis of this band using the FG model in the Discussion section.

6.3.2 High Resolution UV Spectra

One intriguing possibility for the location of the S_0-S_2 origin in the *tgt* conformer is that the electronic splitting is so small that it is unresolved from the S_0-S_1 origin. Motivated by this notion, we recorded a high resolution UV spectrum (~21 MHz resolution) of the band at 36423 cm^{-1} assigned to the S_0-S_1 origin. The resulting spectrum is presented in figure 6.5(a) with the experimental spectrum as the top trace and the best fit produced by genetic algorithms as implemented in the *JB95* spectral fitting program.[48] As hypothesized, the band is indeed composed of two transitions with band centers separated by 1.02 cm^{-1}. The two transitions are assigned to the S_0-S_1 (36422.91 cm^{-1}) and S_0-S_2 (36423.93) origins. The ground and excited state rotational constants and transition dipole moment (TDM) directions are summarized in table 6.2. Note that the S_0-S_1 transition is a 23:77 a:c-type band while the S_0-S_2 origin is a pure b- type transition, with TDM directions that are perpendicular to one another. Furthermore, the excited state rotational constants of the two overlapped origin bands are remarkably similar to

one another. Both these facts point to the electronic excitation being delocalized over the two rings, leading to geometry changes upon electronic excitation that are shared between the two rings, consistent with the C_2 geometry for the *tgt* conformer.

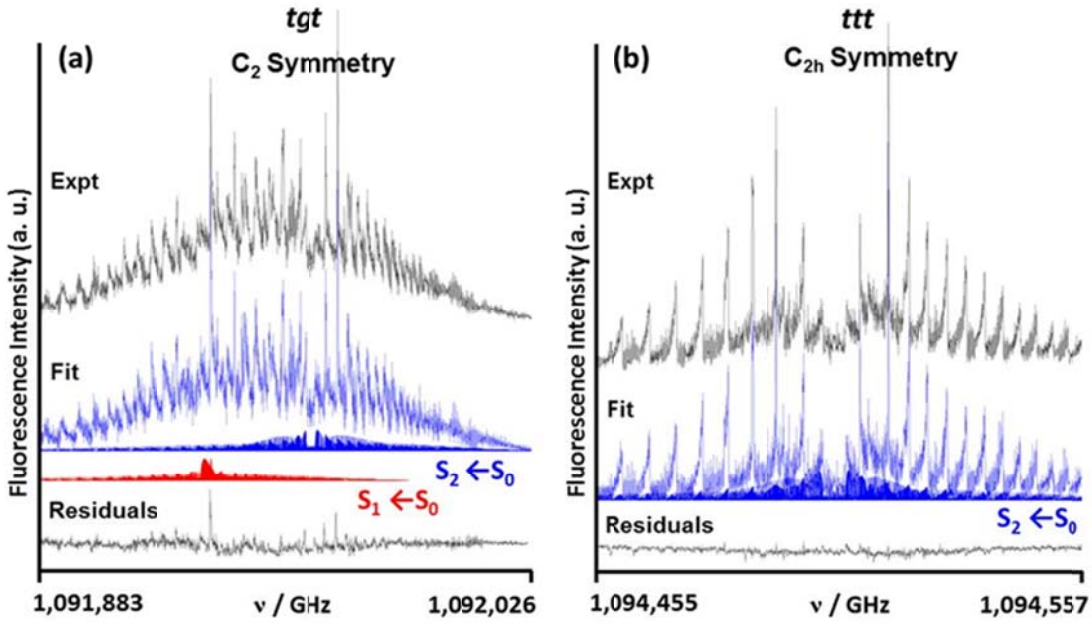

Figure 6.5 High resolution LIF excitation spectrum of the electronic origin bands associated with the (a) *tgt* conformer and (b) *ttt* conformers. The fit to the experimental spectrum is shown in the bottom trace alongside the residuals to the fit.

Figure 6.5(b) presents the high resolution spectrum of the S_0-S_1 origin of the *ttt* conformer. Once again, the fit is shown below for comparison, with best fit parameters shown in table 6.2. In this case, a single band is able to account for all observed rovibronic structure. The band is a b-type band, consistent with its assignment to the A_g-B_u transition of the C_{2h} *ttt* conformer. A high resolution scan of the +46 cm^{-1} transition of the *ttt* conformer is included in the appendix. This transition is also of b-type, as

anticipated based on the assignment of this transition to the b_u symmetry $\bar{R}$ fundamental built off the A_g excited state. Given the close proximity of two electronic origins in the *tgt* conformer, and the position of the +46 cm^{-1} transition relative to its calculated frequency, it seems likely that the splitting between the A_g and B_u excited states should also be small. Proof for this conjecture comes in the next section.

Table 6.2 The rotational constants for the two isomers of DPOE. The S0-S1 origin of the ttt conformer is dipole-forbidden and therefore not observed. Rotational constants have been rounded for clarity (see Table S1 of the appendix for a complete listing of fitted parameters including uncertainties).

C_2 (*tgt*)				
	S_0 State (MHz)		S_1 State (MHz)	S_2 State (MHz)
A	1873.8	ΔA	-66.4	-66.2
B	177.9	ΔB	0.9	0.8
C	171.1	ΔC	0.6	0.6
			24:76% a:c-type	100% b-type
C_{2h} (*ttt*)				
A	2508.9	ΔA	-	-61.0
B	157.9	ΔB	-	-0.3
C	148.9	ΔC	-	-0.5
				100% b-type

6.3.3 ^{13}C-Substitution R2PI Spectroscopy

Following the lead of Leutwyler and co-workers,[18-19, 46] we recorded R2PI spectra of DPOE while monitoring the M+1 mass channel associated with incorporation of a single ^{13}C atom in the molecule, which contains 14 carbon atoms. Since 12 of the 14 carbons are in the two aromatic rings that typically give rise to similar electronic frequency shifts, the M+1 R2PI spectrum reflects primarily the effects of symmetry

breaking on the electronic spectroscopy. These effects are anticipated to be particularly striking in the *ttt* conformer, since breaking the symmetry of the two rings can turn on intensity in the dipole-forbidden A_g-A_g electronic transition.

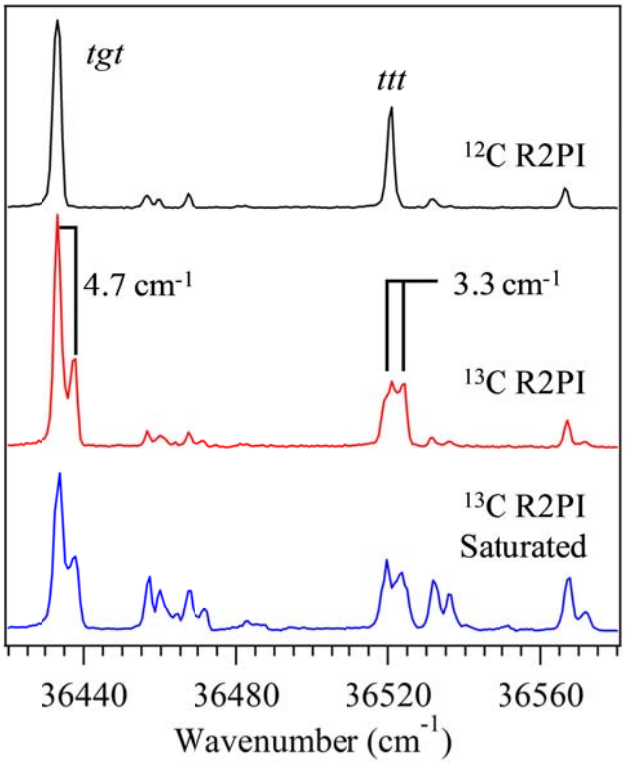

Figure 6.6 R2PI spectra in the S0-S1/S2 origin regions of the tgt and ttt conformers of DPOE monitoring (a) the all 12C parent mass channel, (b) the M+1 mass channel associated with incorporation of one 13C into the molecule under (b) unsaturated and (c) partially saturated conditions. The observed splittings of 4.7 cm-1 and 3.3 cm-1 for the tgt and ttt conformations place upper bounds on the excitonic splittings of the two conformers. See text for further discussion.

Figure 6.6 compares R2PI spectra recorded in the *m/z* 214 mass channel (all ^{12}C DPOE, top trace) to that in the M+1 mass channel, recorded under unsaturated (red, middle) and partially saturated (blue, bottom) conditions. The ^{13}C substitution in the ring

produces a doublet at the *tgt* origin, split by 4.7 cm^{-1}, which is now resolved even under low resolution. The magnitude of this splitting is more than four times the excitonic splitting (1.02 cm^{-1}), indicating that most of the splitting in the ^{13}C spectrum is site splitting due to the fact that one ring contains a ^{13}C atom, while the other does not. On that basis, we surmise that the observed doublet should be interpreted as arising from electronic excitation largely localized on the all ^{12}C or singly ^{13}C substituted rings of DPOE.

Similar arguments hold for the R2PI spectrum of the ^{13}C *ttt* conformer. Here, we see a partially resolved and somewhat broadened doublet with a splitting of 3.3 cm^{-1}. Strikingly, the two transitions are nearly equal in intensity, as would occur if electronic excitation were completely localized on one or the other ring. This is consistent with a splitting of 3.3 cm^{-1}, which is 30% less than the splitting in the *tgt* conformer. We surmise on this basis that the splitting of the electronic origins in the all ^{12}C isotopomer is significantly smaller than 1 cm^{-1} for the *ttt* conformer. The partially saturated spectra show that the band splittings present at the origins carry forward to other vibronic bands in the spectrum.

6.3.4 Collisional Studies

One important benefit of the ^{13}C R2PI spectrum is that it provides the electronic frequency positions of these transitions relative to the all-^{12}C spectrum. In particular, the +46 cm^{-1} transition of the *ttt* conformer is directly overlapped with the main band of the ^{12}C spectrum, and would therefore be excited simultaneously under conditions for dispersed fluorescence. This raises the possibility that the -46 cm^{-1} transition in the *ttt*

+46 cm^{-1} DFL spectrum (figure 6.6.3b) could arise from the ^{13}C isotopomer, which would have an allowed transition with $\Delta v=0$ Franck-Condon factors to the b_u fundamental in the ground electronic state. Indeed, its intensity relative to the $\Delta v = \pm 1$ transitions on either side of it, are approximately correct for ascribing the -46 cm^{-1} transition to ^{13}C DPOE.

It is noteworthy that the +46 cm^{-1} DFL spectrum shown in figure 6.3b was recorded at x/D=38, far downstream relative to conditions often used for recording DFL spectra. Under most circumstances, the effects of collisions on DFL spectra are minimal, since the collision frequency in the jet is typically slow relative to the excited state fluorescence lifetime (~30 ns in this case). However, the emission from the +46 cm^{-1} transition of *ttt* DPOE is a notable exception.

Figure 6.7a and figure 6.7b present a series of DFL spectra from the +46 cm^{-1} transition of *ttt* taken as a function of distances from the nozzle orifice (with diameter D), ranging from x/D=5.5 to 38. A close-up of two regions of the DFL spectra are shown that highlight bands at -46 cm^{-1} and -889 cm^{-1} whose intensity is sensitive to the x/D position. Clearly, both bands grow in intensity by more than a factor of five as excitation occurs closer to the nozzle where collisions with buffer gas are more frequent.

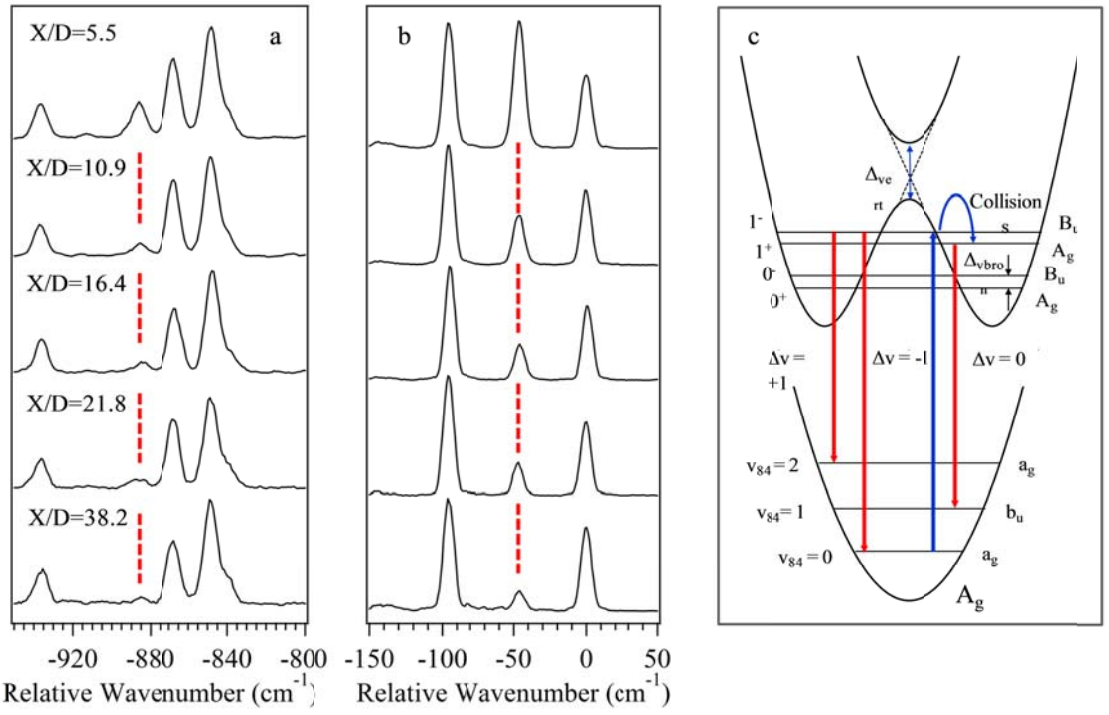

Figure 6.7 Close-up views of the (a) -800 to -950 cm-1 and (b) +50 to -150 cm-1 regions of the ttt +46 cm-1 DFL spectrum taken with laser excitation occurring at different distances (x/D, D=nozzle diameter) from the nozzle in the expansion. Transitions marked with a dotted line grow in intensity at small x/D due to collisions with the backing gas. (c) Energy level diagram depicting the excitation, emission, and collisional energy transfer processes responsible for the collision free ("0", -95 cm-1) and collision-induced (-46 cm-1) emission.

Figure 6.7c displays an energy level diagram that summarizes the collisional mechanism responsible for the growth in this -46 cm^{-1} emission. The two excited states are drawn in an adiabatic representation in which the geometry changes accompanying electronic excitation of one or the other ring lead to displacements producing two equivalent, displaced wells in the excited state. The 1.02 cm^{-1} splitting between S_0-S_1 and S_0-S_2 origins is, in this adiabatic picture, a tunneling splitting associated with a process in which both electronic excitation and nuclear change accompany the tunneling.

The +46 cm^{-1} transition in the excitation spectrum is to a B_u vibronic state that is (nominally) the b_u in-plane bending fundamental ($\bar{R}$) built off the A_g electronic origin ($A_g(\bar{R}^1{}_0)$). This state gains its oscillator strength by vibronic coupling with the B_u electronic state, and produces $\Delta v(\bar{R})=\pm 1$ Herzberg-Teller selection rules in emission to produce transitions at "0" (resonance fluorescence) and -95 cm^{-1} (ending in v=2 in the ground state). There is no dipole-allowed or vibronically induced method of producing the $\Delta v=0$ emission from this level to the corresponding v=1 level (at -46 cm^{-1}) in the ground state. However, if collisions with buffer gas occur during the excited state lifetime (figure 6.7c), they can produce the other member of the v=1 tunneling doublet, which is less than 1 cm^{-1} away. This level is of $B_u x b_u = A_g$ vibronic symmetry, and has a dipole-allowed transition to the v=1 level in the ground state, with emission frequency -46 cm^{-1} from resonance fluorescence, as observed.

Interestingly, even at x/D = 38, some intensity remains in the -46 and -896 cm^{-1} bands. Although the remaining intensity could be attributed to collisions with an extremely large cross section for the collisional energy transfer process, it seemed more likely to us that this residual intensity arises from overlap with the ^{13}C 0^0_0+46 cm^{-1} transition (Sec. III.C). As a final test of this conjecture, we recorded SEP ion-dip spectra from the *ttt* +46 cm^{-1} intermediate state while monitoring the ^{13}C and all ^{12}C mass channels. The results are shown in figure 6.8.

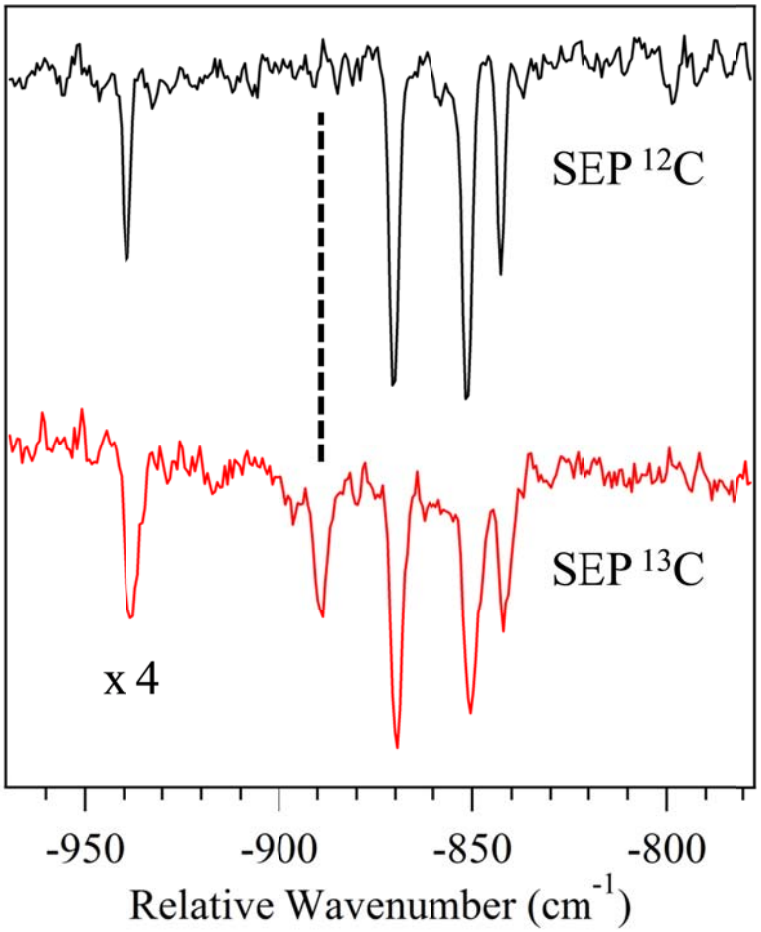

Figure 6.8 The 12C and 13C stimulated emission pumping spectra indicating the 889 cm-1 transition is due to the 13C spectrum.

Ufortunately, since the SEP "dump" laser frequency at -46 cm^{-1} was near resonances in absorption for the *tgt* conformer, the SEP ion-dip spectrum could not be recorded in the region of figure 6.7b where the -46 cm^{-1} transition occurs. Instead, the corresponding collision-induced band at -889 cm^{-1} (figure 6.7a) was free from such interference. As figure 6.8 shows, the transition at -889 cm^{-1} is clearly observed in the ^{13}C spectrum, but is completely absent in the ^{12}C spectrum, confirming that the ^{13}C

isotopomer is the likely source of the remaining -46 cm^{-1} intensity in figure 6.6.3b/7b. This transition is dipole-allowed in the ^{13}C spectrum due to localization of the electronic excitation induced by one ring possessing a ^{13}C atom.

6.4 Discussion

6.4.1 The Weak Vibronic Coupling Limit

The primary goal of the present study has been to map out in some detail the conformational dependence of the excited state surfaces present in the model flexible bichromophore 1,2-diphenoxyethane (DPOE). In earlier work, LIF excitation, UV-hole burning, and resonant ion-dip infrared spectra were used to observe and assign transitions due to two conformations, the *ttt* conformer of C_{2h} symmetry, and the *tgt* conformer, with C_2 symmetry. In this paper, we have determined the magnitude of the excitonic splitting between the S_1 and S_2 states for both conformers, and determined and analyzed the spectroscopic signatures of vibronic coupling between the S_1 and S_2 states in the two conformations.

Perhaps the most striking result of this work is the extraordinarily small excitonic splittings present in the two conformers, with the *tgt* conformer possessing a splitting of 1.02 cm^{-1}, and its *ttt* counterpart even smaller based on the spectrum of its isotopomer containing a single ^{13}C atom in one of the rings. This is to be compared with an electronic transition from S_0 of more than 34,000 cm^{-1}. Thus, DPOE is in the extreme

limit of weak vibronic coupling, with an excitonic splitting similar in size to the recently-studied benzoic acid dimer (0.94 cm^{-1}).[45]

The splittings of the exciton coupled S_1 and S_2 origins reported in previous jet-cooled studies of the C_2 symmetric bichromophores, bis-(4-hydroxyphenyl)methane[34] and diphenylmethane[33] were in excess of 100 cm^{-1} because of the close proximity of the two chromophores. In these cases, both exciton states are orbitally allowed and the vibronic spectra built off of each origin are readily resolved. The close proximity of the two rings rotates the direction of each ring's TDM and induced an out-of-ring-plane TDM component, significantly increasing the excitonic coupling relative to a monomer point-dipole model.[35] In contrast, the chromophores of DPOE are more weakly coupled because of the larger inter-ring separations that minimize direct interactions between the rings.

The weak coupling in DPOE is evident from predictions for the exciton splitting based on the transition dipole coupling of Förster theory,[10] and from vertical splittings calculated at the TDDFT M05-2X/6-31+G(d) level of theory. These are summarized in table 6.3 for DPOE. The TDDFT vertical splittings (9 cm^{-1} for *tgt*, 25 cm^{-1} for *ttt*) and transition dipole coupling estimates (17 cm^{-1} for *tgt*, 43 cm^{-1} for *ttt*) are generally consistent with one another, and are quite small compared to those in DPM and b4HPM. For the *ttt* isomer of DPOE, the distance between the center-of-masses of the two aromatic rings is 8.6 Å, while in *tgt* this distance is 8.0 Å. Yet, these estimates are still more than 10-fold too large compared to the experimental splittings between the S_0-S_1 and S_0-S_2 origins (1 cm^{-1} or less).

Within the diabatic model typically used for analysis of excitonic splitting, the vertical splitting (Δ_{elec}) is vibrationally "quenched" by a Franck-Condon factor that accounts for the shift in excited state geometry relative to the ground state minimum.[16] This leads in the weak vibronic coupling limit to a "quenched" vibronic splitting Δ_{vibron} that is more than 10-fold smaller, with experimental splittings of 1.02 cm^{-1} (*tgt*) or less (*ttt*).

Table 6.3 Calculated vertical frequencies, S_1/S_2 splittings and oscillator strengths at the TDDFT M05-2X/6-31+G(d) level of theory. Comparison with experimental splittings and the excitonic splittings predicted with the transition dipole coupling model (TDM).

Conformer: *tgt*				
	Vertical Splitting (cm^{-1})	Scaled Vertical Splitting (cm^{-1})	Exp. Freq (cm^{-1})	Calc. Osc. Strength
S_0-S_1	43617	36422.91	36422.91	0.0277
S_0-S_2	43628	36432.09	36423.93	0.0440
	TDDFT Splitting	9 cm^{-1}	Exp. Splitting	
	TDM Splitting	17 cm^{-1}	1.02 cm^{-1}	
Conformer: *ttt*				
	Vertical Splitting (cm^{-1})	Scaled Vertical Splitting (cm^{-1})	Exp. Freq (cm^{-1})	Calc. Osc. Strength
S_0-S_1	43737	36523.12	-	0.0000
S_0-S_2	43767	36548.17	36508.77	0.0683
	TDDFT Splitting	25 cm^{-1}	Exp. Splitting	
	TDM Splitting	43 cm^{-1}	~ 1.0 cm^{-1}	

In this circumstance, the observed splitting is understood most intuitively in an adiabatic model in which the observed splitting is considered as a nonadiabatic tunneling

splitting on the lower double-minimum potential energy surface. This is shown schematically for the two conformers of DPOE in figure 6.9. As Kopec *et al.* have laid out in some detail,[46] this tunneling splitting cannot be calculated from the shape of the lower double minimum surface alone, since the tunneling is influenced by nonadiabatic interactions with the upper electronic state.

At the same time, the rotational constants and TDM orientations extracted from the rotationally resolved spectra provide unequivocal evidence that the electronic excitation is completely delocalized over the two aromatic rings, with TDM directions consistent with excited states which are equal contributions from local excitations of anisole ($C_6H_5OCH_3$). In the end, this is a requirement of the symmetric configurations for the two conformers, in which the two aromatic chromophores are placed in equivalent configurations.

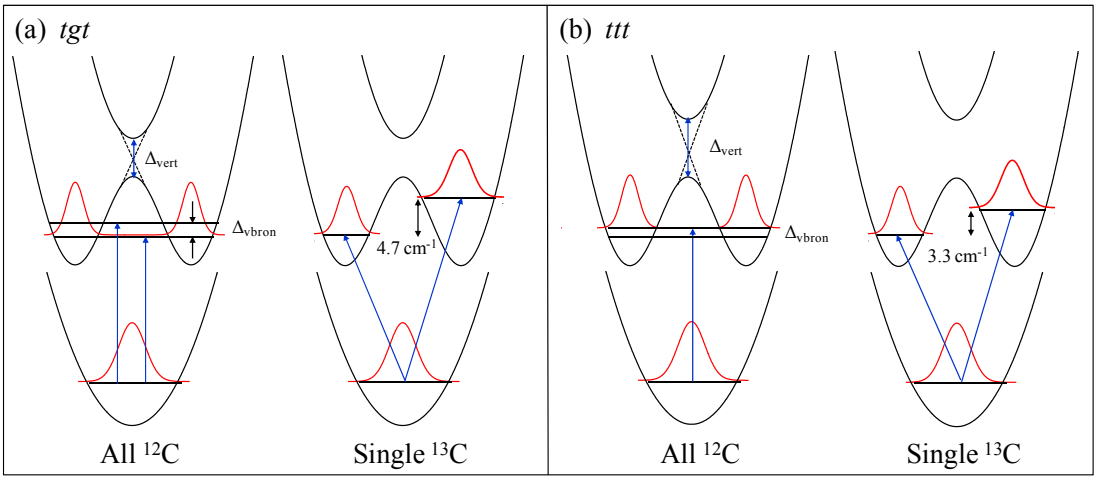

Figure 6.9 Schematic adiabatic potential energy curves for the (a) tgt and (b) ttt conformers of DPOE showing (left) electronic delocalization of the symmetric all 12C structures with tunneling splittings of Δvibron=1.02 and ~1 cm-1, respectively, and (right) the electronic localization associated with incorporation of a single 13C atom into one of the rings, with S1/S2 splittings of 4.7 and 3.3 cm-1, respectively.

On this basis, one would anticipate that most other geometries that are away from these highly symmetric points on the excited state potential energy surfaces will be characterized by nearly localized electronic excitation of the two rings with even modest shifts of a few cm^{-1} in the site frequencies sufficient to cause electronic localization, since the nonadiabatic tunneling splittings at C_2 and C_{2h} geometries are 1 cm^{-1} or less. This fact was brought home in dramatic fashion by the R2PI spectra of the singly ^{13}C-substituted isotopomer of DPOE, where shifts in the zero-point energies of the two excited states of 3-4 cm^{-1} led to substantial localization of the electronic excitation, as figure 6.9 illustrates. In the *ttt* conformer, this turned a pair of electronic transitions in which one is dipole-allowed and the other dipole-forbidden into a pair of transitions that have nearly equal oscillator strengths, with excitation localized either on the ^{13}C-substituted ring or the non-substituted one, with a splitting of 3.3 cm^{-1}. One could imagine that, in the condensed phase, small asymmetries or fluctuations in the solvent surroundings will be sufficient to localize electronic excitation there too. The effects of asymmetric solvation are seen already in the DPOE-H_2O complex involving the asymmetry induced by a single H_2O molecule.[51]

6.4.2 Spectroscopic Signatures of Vibronic Coupling Involving Near-Degenerate Excited States

We have just proven that in both the *tgt* and *ttt* conformers of DPOE, the first two levels on the adiabatic double-minimum potential energy surface, associated with electronic character

$$\psi_1 = \frac{1}{\sqrt{2}}\left(|A^*B> + |AB^*>\right)$$
$$\psi_2 = \frac{1}{\sqrt{2}}\left(|A^*B> - |AB^*>\right) \qquad (2)$$

are separated in energy by no more than 1 cm^{-1} at the C_2 and C_{2h} geometries associated with the *tgt* and *ttt* conformers, respectively. This splitting is small compared to all vibrational frequencies in the *tgt* and *ttt* conformers. As a result, each vibrational level is split by nonadiabatic effects into a pair of levels. We focus in this section on the spectroscopic signatures of this near-degeneracy in the vibronic spectroscopy of the two conformers.

In the C_2 *tgt* conformer, both members of the tunneling doublet associated with each vibronic level carry oscillator strength from S_0. As a result, every vibronic transition in the *tgt* spectrum in figure 6.2 is in fact an unresolved doublet, as was shown in figure 6.5 to be the case at the electronic origin by high resolution spectroscopy. Furthermore, the strong intensities observed in the non-totally symmetric fundamentals result from vibronic coupling between the two states, with the S_1 state borrowing intensity from S_2 and vice versa. Since the emission from both members of the pair is dipole-allowed, a strong $\Delta v=0$ false origin appears in the DFL spectra of both totally symmetric and non-totally symmetric fundamentals (figure 6.3a).

By contrast, the C_{2h} *ttt* conformer has only one dipole-allowed electronic transition (A_g-B_u), but ^{13}C R2PI spectra located the dipole-forbidden A_g-A_g origin split by only 3.3 cm^{-1}. Based on a comparison with the *tgt*, where a 4.7 cm^{-1} ^{13}C splitting arose from a 1.02 cm^{-1} non-adiabatic tunneling splitting, the two states are placed within 1 cm^{-1} of one another. As a result, once again, each vibronic band is split into a pair of transitions, but in this case only one member of each pair carries intensity. Vibronic coupling nevertheless plays an important role in the spectrum, with the band 46 cm^{-1} above the A_g-B_u origin assigned to b_u symmetry $\bar{R}$ fundamental built off the A_g electronic state, gaining its intensity purely through vibronic coupling.

It is worth noting that the smaller splitting ascribed to the *ttt* conformer is opposite to the ordering of the splittings predicted by TDM model or TDDFT calculations (Table 6.3). One possible reason for this smaller splitting would be that the *ttt* conformer has a larger Franck-Condon quenching than *tgt*. However, comparison of the DFL spectra of the S_1 origins of *ttt* (Figure 6.6.3b) and *tgt* conformers (Figure 6.6.3a) show little difference between the two in the intensities of the ring modes that dominate this quenching factor. In the end, the only experimentally measured quantity we report here for the *ttt* conformer is the 3.3 cm^{-1} splitting in the ^{13}C R2PI spectrum, which is the composite of the quenched excitonic and zero-point energy effects that include contributions from the different sets of inter-ring modes for each conformer given in table 6.1. A direct measure of the splitting in the ^{12}C isotopomer would require comparison of the one-photon and two-photon allowed transitions, a task left for future work.

The adiabatic model developed by Kopec *et al.*[16] projects non-adiabatic coupling onto a single effective vibrational coordinate, leading to accurate predictions for the

nonadiabatic tunneling splitting at the electronic origin in model homodimers. By contrast, a multi-mode version of the diabatic Fulton-Gouterman model has recently been developed, providing a means for modeling the observed vibronic intensities in DPOE. The *tgt* conformer was not modeled due to the unresolved overlap of contributions from the two excited states in the excitation and dispersed fluorescence spectra. In the *ttt* conformer, the model is able to account for the vibronic intensities in the R/$\bar{R}$ pair of interchromophore bends both in excitation and in dispersed fluorescence from the dipole-allowed B_u origin. Similar modeling of the intensities in the origin emission into the ring mode pairs 6a, 1, and 12 (in Varsanyi notation)[52] at -590/-610, -802/-840, and -996/-1005 cm^{-1} are similarly successful (figures 6.10-614). Similar modeling of the $A_g(\bar{R}^1)$ emission (the +46 cm^{-1} band) accounts for the vibronically induced emission to v"=0,2. However, the strong emission bands from the $A_g(\bar{R}^1)$ level to transitions at -649, -849, and -1044 cm^{-1} are not accounted for in the FG model, pointing to the need for further refinement of intermode coupling in the theory.

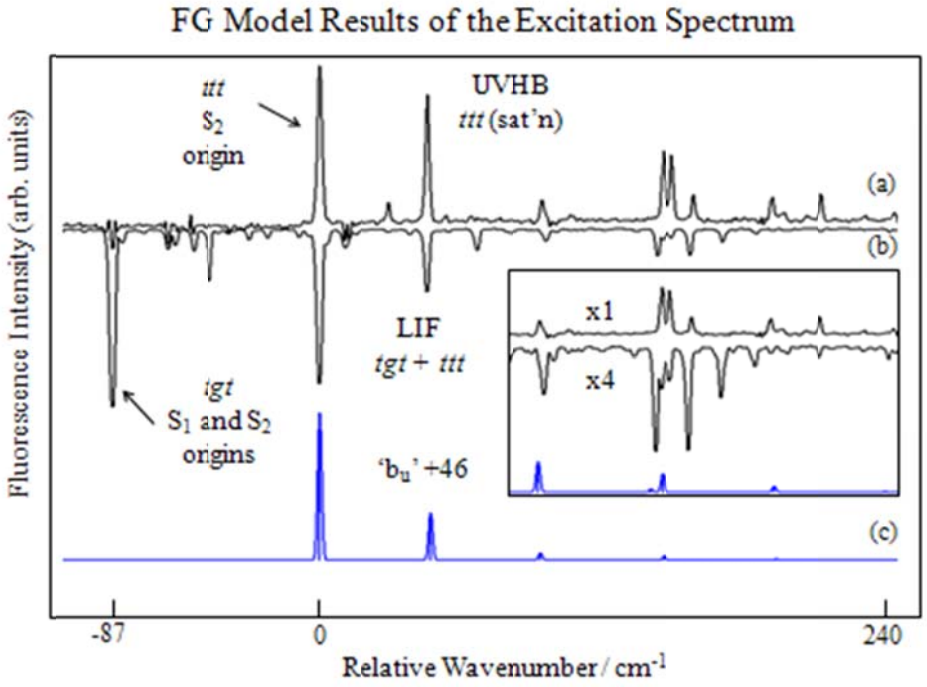

Figure 6.10 UV-HB (a) and LIF (b) spectra of DPOE and the FG[1-3] model predictions (c) of the R / $\bar{R}$ mode pair (46/149 cm^{-1}) of the *ttt* conformer using the parameters given in Figure S2. It is noted that both observed spectra are saturated in order to facilitate better comparison with model predictions. The relative intensities from the model are in good agreement with the unsaturated UVHB spectrum of Figure 6.2.

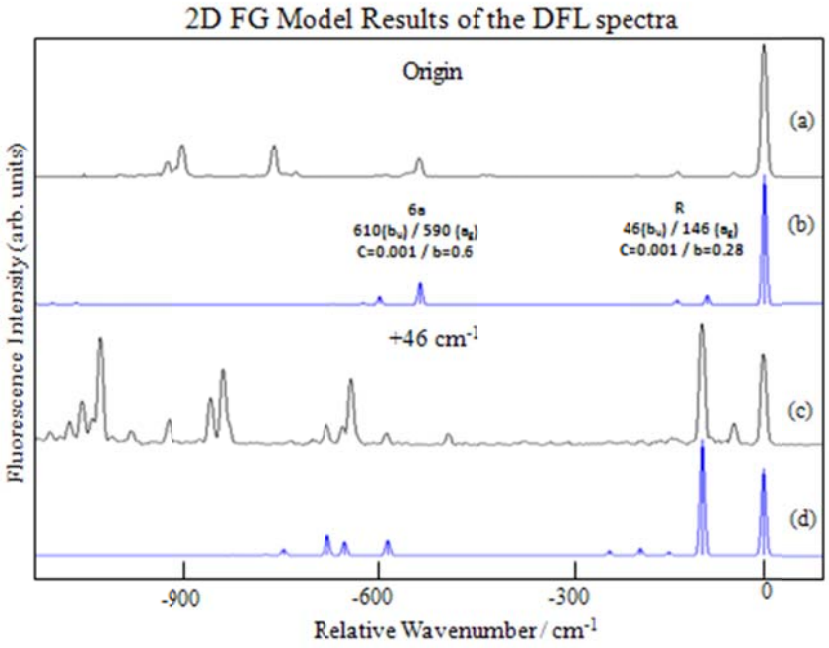

Figure 6.11 Observed DFL spectra of the (a) origin and (c) +46 cm-1 bands of DPOE. Shown below each band in (b) and (d) are the predictions from the FG model for the inter-ring mode pair R/ $\overline{R}$ and ring mode pair 6a/ $\overline{6}a$

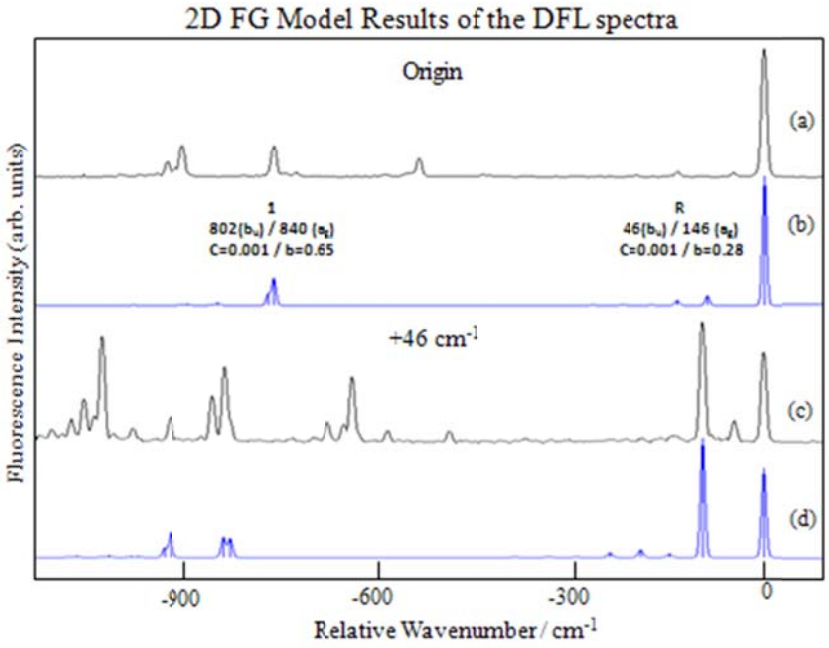

Figure 6.12 Observed DFL spectra of the (a) origin and (c) +46 cm-1 bands of DPOE. Shown below each band in (b) and (d) are the predictions from the FG model for the inter-ring mode pair R/ $\overline{R}$ and ring mode pair $1/\overline{1}$.

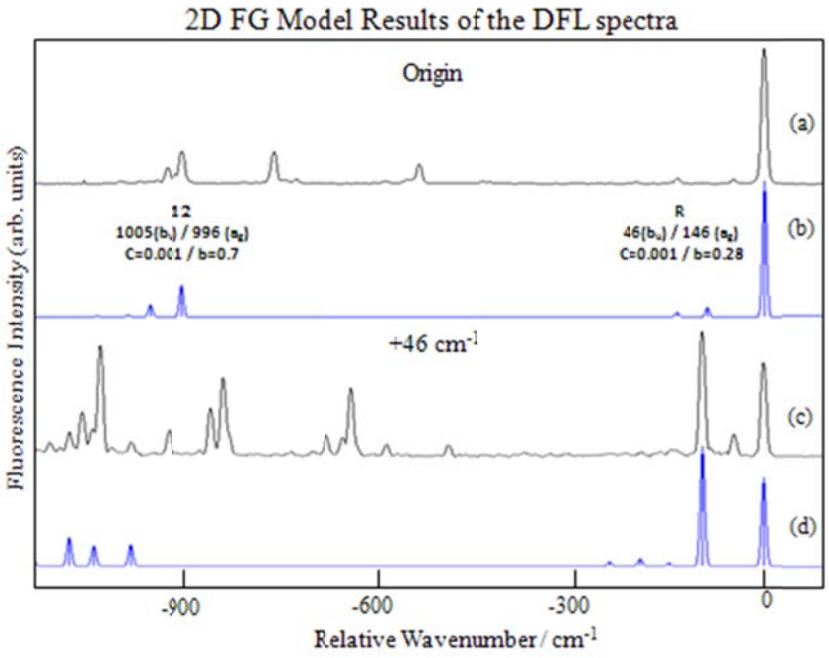

Figure 6.13 Observed DFL spectra of the (a) origin and (c) +46 cm-1 bands of DPOE. Shown below each band in (b) and (d) are the predictions from the FG model for the inter-ring mode pair $R / \overline{R}$ and ring mode pair $12 / \overline{12}$.

6.4.3 Collision Induced Electronic Energy Transfer

One of the more striking results of the present study is the unusual sensitivity of the DFL spectrum of the *ttt* +46 cm^{-1} band to collisions, as shown in figure 6.7a/b. As discussed in some detail in 6.3.4 and shown pictorially in figure 6.7c, we have shown that the bands that grow in can be ascribed to the lower member of the non-adiabatic tunneling doublet associated with the R^1_0 fundamental. This state is dipole forbidden from the S_0 zero-point level, but its close proximity (within 1 cm^{-1}) to the other member of the tunneling doublet initially populated by the laser provides a pathway for collisional energy transfer that is extremely facile, and competes with fluorescence even under conditions under which one would typically have thought were collision-free.

Table 6.4 presents estimates of the number of collisions experienced by DPOE during the lifetime of the excited state (30 nsec), assuming a gas-kinetic cross section for transfer between members of the tunneling doublet (σ_{coll} = 75 Å^2). Under conditions closest to the nozzle, there are multiple collisions during the excited state lifetime, suggesting that the two tunneling states could have their populations equilibrated. On the other hand, at x/D=38, where only 1% of the excited state molecules undergo a gas-kinetic collision, the remaining intensity is likely to be mostly or entirely due to the ^{13}C isotopomer. Invoking these assumptions, the intensity ratio on the right of the table is the collision-induced intensity in the -46 cm^{-1} band relative to the sum of the "0" and -95 cm^{-1} transitions. This ratio falls off at a rate in keeping with the fall off in number of collisions. While this data is not sufficient to quantify the magnitude of the collision cross section as a function of position in the expansion, it seems likely to us that very large cross sections for electronic energy transfer across this small tunneling doublet are at play, with glancing collisions with cross sections significantly exceeding gas kinetic are possible.

Table 6.4 Fractional collision-induced intensity in the $\Delta v_{84}=0$ transition of the *ttt* conformer of DPOE relative to that in the $\Delta v_{84}=\pm 1$ transitions as a function of distance from the nozzle in nozzle diameters, x/D. The number of gas-kinetic collisions experienced by DPOE in its excited state lifetime is given for comparison.

x/D	# of Collisions[a]	Fractional Collision Induced Intensity
5	2.15	0.56
11	0.32	0.17
16	0.11	0.08
22	0.05	0.05
38	0.01	0.00[b]

It is interesting to consider how these studies under jet-cooled conditions in the gas phase transfer into condensed phase environments in which collisions are likely to provide an efficient means of interchromophore electronic energy transfer in chromophore arrays, multichromophore polymers, and the like.

6.5 Conclusions

We have presented detailed spectroscopic data on the close-lying S_1/S_2 states of DPOE that prove that the molecule is in the extreme limit of weak vibronic coupling. At the C_2 and C_{2h} geometries, the electronic excitation is delocalized over the two rings (by symmetry), but the splitting between the two states is 1 cm^{-1} or less. Given this weak coupling, it is likely that the two potential energy surfaces lie within a few cm^{-1} of one another over large regions of the torsional potential energy surface. In this weak vibronic coupling limit, the excitonic splitting is best thought of as a nonadiabatic tunneling splitting on the lower double-minimum potential energy surfaces associated with

electronic excitation on one or the other aromatic ring. This splitting is more than a factor of 10 smaller than vertical splittings calculated via standard methods. In light of this weak vibronic coupling, the smallest of perturbations to one of the rings is sufficient to localize the electronic excitation on one or the other ring. This was illustrated in dramatic fashion in the spectra recorded for the ^{13}C isotopomer that contains a single ^{13}C atom somewhere in one or the two aromatic rings. This zero-point asymmetry was enough to split the electronic origins by 4.7 cm^{-1} (*tgt*) and 3.3 cm^{-1} (*ttt*), and nearly completely localize the electronic excitation. One would anticipate similar effects by asymmetric solvation in the condensed phase. We will show elsewhere the interesting effects associated with binding a single H_2O molecule to DPOE.[51]

6.6 References

1. Panitchayangkoon, G.; Voronine, D. V.; Abramavicius, D.; Caram, J. R.; Lewis, N. H. C.; Mukamel, S.; Engel, G. S. Direct evidence of quantum transport in photosynthetic light-harvesting complexes. *Proc. Natl. Acad. Sci. U. S. A.* **2011,** *108* (52), 20908-20912.

2. Pelzer, K. M.; Griffin, G. B.; Gray, S. K.; Engel, G. S. Inhomogeneous dephasing masks coherence lifetimes in ensemble measurements. *J. Chem. Phys.* **2012,** *136* (16).

3. Engel, G. S.; Calhoun, T. R.; Read, E. L.; Ahn, T. K.; Mancal, T.; Cheng, Y. C.; Blankenship, R. E.; Fleming, G. R. Evidence for wavelike energy transfer through quantum coherence in photosynthetic systems. *Nature* **2007,** *446* (7137), 782-786.

4. Lee, H.; Cheng, Y. C.; Fleming, G. R. Coherence dynamics in photosynthesis: Protein protection of excitonic coherence. *Science* **2007,** *316* (5830), 1462-1465.

5. Polyutov, S.; Kuhn, O.; Pullerits, T. Exciton-vibrational coupling in molecular aggregates: Electronic versus vibronic dimer. *Chem. Phys.* **2012,** *394* (1), 21-28.

6. Tempelaar, R.; Stradomska, A.; Knoester, J.; Spano, F. C. Anatomy of an Exciton: Vibrational Distortion and Exciton Coherence in H- and J-Aggregates. *J. Phys. Chem. B* **2013,** *117* (1), 457-466.

7. Habuchi, S.; Fujita, H.; Michinobu, T.; Vacha, M. Twist Angle Plays an Important Role in Photophysical Properties of a Donor-Acceptor-Type Conjugated Polymer: A Combined Ensemble and Single-Molecule Study. *J. Phys. Chem. B* **2011,** *115* (49), 14404-14415.

8. Tozer, O. R.; Barford, W. Exciton Dynamics in Disordered Poly(p-phenylenevinylene). 1. Ultrafast Interconversion and Dynamical Localization. *J. Phys. Chem. A* **2012,** *116* (42), 10310-10318.

9. Maus, M.; De, R.; Lor, M.; Weil, T.; Mitra, S.; Wiesler, U. M.; Herrmann, A.; Hofkens, J.; Vosch, T.; Mullen, K.; De Schryver, F. C. Intramolecular energy hopping and energy trapping in polyphenylene dendrimers with multiple peryleneimide donor chromophores and a terryleneimide acceptor trap chromophore. *Journal of the American Chemical Society* **2001,** *123* (31), 7668-7676.

10. Scholes, G. D. Long-range resonance energy transfer in molecular systems. *Annual Review of Physical Chemistry* **2003,** *54*, 57-87.

11. Hybl, J. D.; Ferro, A. A.; Jonas, D. M. Two-dimensional Fourier transform electronic spectroscopy. *J. Chem. Phys.* **2001,** *115* (14), 6606-6622.

12. Jonas, D. M. Two-dimensional femtosecond spectroscopy. *Annual Review of Physical Chemistry* **2003,** *54*, 425-463.

13. Fassioli, F.; Olaya-Castro, A.; Scholes, G. D. Coherent Energy Transfer under Incoherent Light Conditions. *J. Phys. Chem. Lett.* **2012,** *3* (21), 3136-3142.

14. Hossein-Nejad, H.; Olaya-Castro, A.; Scholes, G. D. Phonon-mediated path-interference in electronic energy transfer. *J. Chem. Phys.* **2012,** *136* (2).

15. Borst, D. R.; Roscioli, J. R.; Pratt, D. W.; Florio, G. M.; Zwier, T. S.; Muller, A.; Leutwyler, S. Hydrogen bonding and tunneling in the 2-pyridone center dot 2-hydroxypyridine dimer. Effect of electronic excitation. *Chem. Phys.* **2002,** *283* (1-2), 341-354.

16. Kopec, S.; Ottiger, P.; Leutwyler, S.; Koppel, H. Vibrational quenching of excitonic splittings in H-bonded molecular dimers: Adiabatic description and effective mode approximation. *J. Chem. Phys.* **2012,** *137* (18).

17. Muller, A.; Talbot, F.; Leutwyler, S. S-1/S-2 exciton splitting in the (2-pyridone)(2) dimer. *J. Chem. Phys.* **2002,** *116* (7), 2836-2847.

18. Ottiger, P.; Leutwyler, S.; Koppel, H. S-1/S-2 excitonic splittings and vibronic coupling in the excited state of the jet-cooled 2-aminopyridine dimer. *J. Chem. Phys.* **2009,** *131* (20), 204308.

19. Ottiger, P.; Leutwyler, S.; Koppel, H. Vibrational quenching of excitonic splittings in H-bonded molecular dimers: The electronic Davydov splittings cannot match experiment. *J. Chem. Phys.* **2012,** *136* (17).

20. Le Barbu-Debus, K.; Broquier, M.; Lahmani, F.; Zehnacker-Rentien, A. Localization of electronic and vibrational energy in the jet-cooled m-cyanophenol/o-cyanophenol dimer: laser induced fluorescence and fluorescence-dip IR spectra. *Molecular Physics* **2005,** *103* (11-12), 1655-1662.

21. Seurre, N.; Le Barbu-Debus, K.; Lahmani, F.; Zehnacker-Rentien, A.; Sepiol, J. Electronic and vibrational spectroscopy of jet-cooled m-cyanophenol and its dimer: laser-induced fluorescence and fluorescence-dip IR spectra in the S-0 and S-1 states. *Chem. Phys.* **2003,** *295* (1), 21-33.

22. Southern, C. A.; Levy, D. H.; Stearns, J. A.; Florio, G. M.; Longarte, A.; Zwier, T. S. Spectroscopic consequences of localized electronic excitation in anthranilic acid dimer. *J. Phys. Chem. A* **2004,** *108* (21), 4599-4609.

23. Heid, C. G.; Ottiger, P.; Leist, R.; Leutwyler, S. The S(1)/S(2) exciton interaction in 2-pyridone center dot 6-methyl-2-pyridone: Davydov splitting, vibronic coupling, and vibronic quenching. *J. Chem. Phys.* **2011,** *135* (15).

24. Chattoraj, M.; Paulson, B.; Shi, Y.; Closs, G. L.; Levy, D. H. Electronic Energy Transfer--Density of States. *Journal of Physical Chemistry* **1993,** *97* (50), 13046-13051.

25. Yip, W. T.; Levy, D. H.; Kobetic, R.; Piotrowiak, P. Energy transfer in bichromophoric molecules: The effect of symmetry and donor/acceptor energy gap. *Journal of PHysical Chemistry A* **1999,** *103* (1), 10-20.

26. Vandantzig, N. A.; Levy, D. H.; Vigo, C.; Piotrowiak, P. Vibronic coupling and energy-transfer in bichromophoric molecules -- The effect of symmetry. *J. Chem. Phys.* **1995,** *103* (12), 4894-4906.

27. Wang, X.; Levy, D. H.; Rubin, M. B.; Speiser, S. Supersonic jet spectroscopy and intramolecular electronic energy transfer in naphthalene-(CH2)(n)-anthracene bichromophoric molecules. *Journal of Physical Chemistry A* **2000,** *104* (28), 6558-6565.

28. Zehnacker, A.; Lahmani, F.; Breheret, E.; Desvergne, J. P.; BouasLaurent, H.; Germain, A.; Brenner, V.; Millie, P. Laser induced fluorescence of jet-cooled non-conjugated bichromophores: Bis-phenoxymethane and bis-2,6-dimethylphenoxymethane. *Chem. Phys.* **1996,** *208* (2), 243-257.

29. Zehnacker, A.; Lahmani, F.; Desvergne, J. P.; Bouas-Laurent, H. Conformation-dependent intramolecular exciplex formation in jet-cooled bichromophores. *Chemical Physics Letters* **1998,** *293* (5-6), 357-365.

30. East, A. L. L.; Cid-Aguero, P.; Liu, H. S.; Judge, R. H.; Lim, E. C. Conformational geometries and conformation-dependent photophysics of jet-cooled 1,3-diphenylpropane. *J. Phys. Chem. A* **2000,** *104* (7), 1456-1460.

31. Lee, J. K.; Judge, R. H.; Boo, B. H.; Lim, E. C. Conformation-selective photoionization of covalently-linked diaryl compounds: Excimer-mediated one-color two-photon ionization in seeded beams of 1,3-diphenylpropane. *J. Chem. Phys.* **2002,** *116* (20), 8809-8816.

32. Pillsbury, N. R.; Muller, C. W.; Meerts, W. L.; Plusquellic, D. F.; Zwier, T. S. Conformational Effects on Excitonic Interactions in a Prototypical H-Bonded Bichromophore: Bis(2-hydroxyphenyl)methane. *Journal of Physical Chemistry A* **2009,** *113* (17), 5000-5012.

33. Pillsbury, N. R.; Stearns, J. A.; Muller, C. W.; Plusquellic, D. F.; Zwier, T. S. State-specific studies of internal mixing in a prototypical flexible bichromophore: Diphenylmethane. *J. Chem. Phys.* **2008,** *129* (11), 114301.

34. Rodrigo, C. P.; Mueller, C. W.; Pillsbury, N. R.; James, W. H., III; Plusquellic, D. F.; Zwier, T. S. Conformer-specific vibronic spectroscopy and vibronic coupling in a flexible bichromophore: Bis-(4-hydroxyphenyl)methane. *J. Chem. Phys.* **2011,** *134* (16), 164312.

35. Stearns, J. A.; Pillsbury, N. R.; Douglass, K. O.; Muller, C. W.; Zwier, T. S.; Plusquellic, D. F. Rotationally resolved studies of S-0 and the exciton coupled S-1/S-2 origin regions of diphenylmethane and the d(12) isotopologue. *J. Chem. Phys.* **2008,** *129* (22), 224305.

36. Inokuchi, Y.; Boyarkin, O. V.; Kusaka, R.; Haino, T.; Ebata, T.; Rizzo, T. R. UV and IR Spectroscopic Studies of Cold Alkali Metal Ion-Crown Ether Complexes in the Gas Phase. *J. Am. Chem. Soc.* **2011,** *133* (31), 12256-12263.

37. Kokubu, S.; Kusaka, R.; Inokuchi, Y.; Haino, T.; Ebata, T. Laser spectroscopic study on (dibenzo-24-crown-8-ether)-water and -methanol complexes in supersonic jets. *Physical Chemistry Chemical Physics* **2010,** *12* (14), 3559-3565.

38. Kusaka, R.; Inokuchi, Y.; Ebata, T. Structure of hydrated clusters of dibenzo-18-crown-6-ether in a supersonic jet-encapsulation of water molecules in the crown cavity. *Physical Chemistry Chemical Physics* **2008,** *10* (41), 6238-6244.

39. Vandantzig, N. A.; Shou, H. S.; Alfano, J. C.; Yang, N. C. C.; Levy, D. H. Photoinduced charge-transfer in bichromophoric molecules in the gas-phase. *J. Chem. Phys.* **1994,** *100* (10), 7068-7078.

40. Baquero, E. E.; James, W. H., III; Choi, T. H.; Jordan, K. D.; Zwier, T. S. Single Conformation Spectroscopy of a Flexible Bichromophore: 3-(4-Hydroxyphenyl)-N-benzylpropionamide. *J. Phys. Chem. A* **2008,** *112* (44), 11115-11123.

41. Nebgen, B.; Emmert, F. L.; Slipchenko, L. V. Vibronic coupling in asymmetric bichromophores: Theory and application to diphenylmethane. *J. Chem. Phys.* **2012,** *137* (8).

42. Forster, T. Delocalized excitation and excitation transfer. In *Modern Quantum Chemistry*, Sinanoglu, O., Ed. Academic: New York, 1965; p 93.

43. Fulton, R. L.; Gouterman, M. VIBRONIC COUPLING .1. MATHEMATICAL TREATMENT FOR 2 ELECTRONIC STATES. *J. Chem. Phys.* **1961,** *35* (3), 1059-&.

44. Fulton, R. L.; Gouterman, M. VIBRONIC COUPLING .2. SPECTRA OF DIMERS. *J. Chem. Phys.* **1964,** *41* (8), 2280-&.

45. Ottiger, P.; Leutwyler, S. Excitonic splitting and coherent electronic energy transfer in the gas-phase benzoic acid dimer. *J. Chem. Phys.* **2012,** *137* (20).

46. Kopec, S.; Ottiger, P.; Leutwyler, S.; Koppel, H. Vibrational quenching of excitonic splittings in H-bonded molecular dimers: Adiabatic description and effective mode approximation. *Journal of Chemical Physics* **2012,** *137* (18), 184312.

47. Fulton, R. L.; Gouterman, M. VIBRONIC COUPLING OF 2 ELECTRONIC STATES. *Spectrochimica Acta* **1961,** *17* (9-10), 1093-1093.

48. Plusquellic, D. F. *National Institute of Standards and Technology* **v2.07.08,** *http://www.nist.gov/pml/div686/sources_detectors/jb95.cfm*.

49. Buchanan, E. S., EL; Zwier, TS. Ground State Conformational Preferences of a

Model flexible Bichromophore: 1,2-Diphenoxyethane. *J. Phys. Chem. A* **2013,** *117* (13), 2800-2811.

50. Shubert, V. A.; James, W. H.; Zwier, T. S. Jet-Cooled Electronic and Vibrational Spectroscopy of Crown Ethers: Benzo-15-Crown-5 Ether and 4 '-Amino-Benzo-15-Crown-5 Ether. *Journal of Physical Chemistry A* **2009,** *113* (28), 8055-8066.

51. Buchanan, E. G.; Gord, J. R.; Zwier, T. S. Solvent Effects on Vibronic Coupling in a Flexible Bichromophore: Electronic Localization and Energy Transfer induced by a Single Water Molecule. *J. Phys. Chem. Lett.* **2013,** *4*, 1644-1648.

52. Varsanyi, G. *Assignments for Vibrational Spectra of 700 Benzene Derivatives*. Wiley: New York, 1974.

CHAPTER 7 SOLVENT EFFECTS ON VIBRONIC COUPLING IN A FLEXIBLE BICHROMOPHORE: ELECTRONIC LOCALIZATION AND ENERGY TRANSFER INDUCED BY A SINGLE WATER MOLECULE

7.1 Introduction

Multichromophore arrays play an integral role in nature as antenna for the absorption of light and as a conduit for directing the electronic excitation to specific sites from which charge separation can occur. At the heart of such processes are the excited state local site energies and inter-chromophore excitonic couplings in the array, which depend critically on the relative spatial positions, orientations, and local environments of the chromophores.[1-2] One important component of the local environment is the exposure to and interaction with the solvent, which in most natural environments is water. In the condensed phase, solvent effects are but one aspect of the local environment, and its influence can be difficult to separate from other effects.

As a result, there is a role for studies that isolate particular aspects of the problem in model systems that can be studied in detail. Investigations of isolated flexible bichromophores through single-conformation spectroscopy have provided unique insights to the intrinsic properties of close lying, vibronically coupled electronic states as a function of the conformation of the molecule.[3-5] These have complemented elegant work on the close-lying excited states present in homomolecular dimers.[6-7] By isolating the molecule in the gas phase, and cooling the molecule to its conformational zero-point

levels in a supersonic expansion, interrogation via single- and double-resonance laser spectroscopy and dispersed fluorescence (DFL) probes in exquisite detail the vibronic spectroscopy of each conformation and inter-chromophore coupling.[3]

Here, we build on a recent study of vibronic coupling in 1,2-diphenoxyethane (DPOE)[8-9] by forming the DPOE-$(H_2O)_1$ complex in a supersonic expansion and studying its single conformation infrared and ultraviolet spectroscopy. The bound water molecule plays a dual function, perturbing the local environments of the two chromophores and reporting on the perturbation via its OH stretch infrared spectrum. To understand these effects, we must briefly review what is known about the DPOE monomer. In the absence of H_2O, DPOE spreads its population over two conformations, one of C_2 symmetry (*tgt*) and the other of C_{2h} symmetry (*ttt*). The laser-induced fluorescence excitation spectrum and UV hole-burning spectra of the two conformers of DPOE are reproduced in figures 7.1a)-c). The structures responsible for each are shown in figure 7.1e). The two close-lying excited singlet states of DPOE (S_1 and S_2) have been proven to be delocalized over the two aromatic chromophores, but are extraordinarily weakly coupled to one another, with excitonic splittings of one cm^{-1} or less.[8] While symmetry prevents seeing both electronic origins of the *ttt* isomer, for *tgt*, the S_0-S_1 and S_0-S_2 origin transitions are unresolved in the low-resolution spectrum in figure 7.1b), but have been rotationally resolved at high resolution, with a splitting of only 1.02 cm^{-1}.[8] In such circumstances, the effect of even a single water molecule bound to the bichromophore can substantially change the nature of the electronic excited states and their solvent-mediated coupling due to the different environments of the two electronic chromophores.[8]

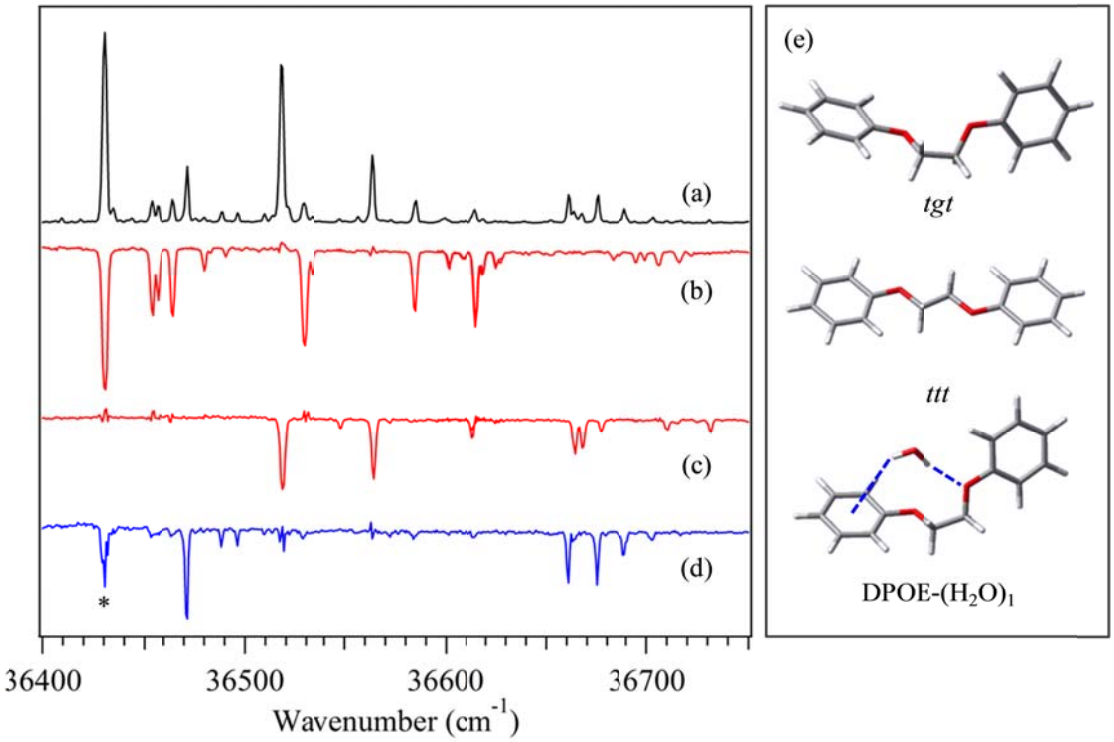

Figure 7.1 (a) LIF excitation spectrum of jet-cooled DPOE in the presence of trace amounts of H2O in the expansion. (b-d) UV hole-burning spectra of the (b,c) two DPOE conformers, and of the (d) DPOE-$(H2O)_1$ complex. The transition marked with an asterisk is an artifact of incomplete subtraction by the gated integrator of the intense signal present at the tgt origin. (e) Structures of the DPOE conformers and DPOE-$(H2O)_1$.

7.2 Results and Discussion

The LIF excitation spectrum shown in figure 7.1a) was recorded with trace H_2O present in the expansion. Figure 7.1d) presents the UV hole-burning (UVHB) spectrum of the set of transitions that increase in the presence of H_2O, identifying the S_0-S_1 origin transition of DPOE-$(H_2O)_1$ at 36471 cm^{-1}, just 40 cm^{-1} to the blue of that in the *tgt* isomer. These transitions are also observed in the resonant two-photon (R2PI) spectrum

appearing in the DPOE monomer mass channel due to efficient fragmentation following photoionization, much as occurs in benzene-$(H_2O)_n$ clusters.[10-11] Figure 7.2 shows a portion of the R2PI spectra without (a) and with (b, c) water present in the expansion, when monitoring the DPOE monomer (a, b) and the $[DPOE\text{-}H_2O]^+$ mass channels (c). The transitions assigned to the DPOE-$(H_2O)_1$ complex appear most clearly among the transitions of the DPOE monomer in the monomer mass channel, with the complex undergoing fragmentation following photoionization with high efficiency. This is analogous to the efficient fragmentation that occurred in benzene-$(H_2O)_n$ clusters, in which the preferred geometries of the ionized clusters are very different than their neutral counterpart, leading to poor Franck-Condon factors to energies below the dissociation threshold for the complex.[10, 12] The transitions in the $[DPOE\text{-}H_2O]^+$ mass channel are assigned to the DPOE-$(H_2O)_2$ cluster, which also fragments with near unit efficiency by loss of a single H_2O molecule, in this case appearing in $[DPOE\text{-}H_2O]^+$ mass channel, with no significant interference in the $DPOE^+$ monomer mass channel where we detect the DPOE-$(H_2O)_1$ complex. As a result, the RIDIR spectra recorded for the DPOE-H_2O complex in S_0, S_1, and S_2 states have no interference from DPOE-$(H_2O)_2$.

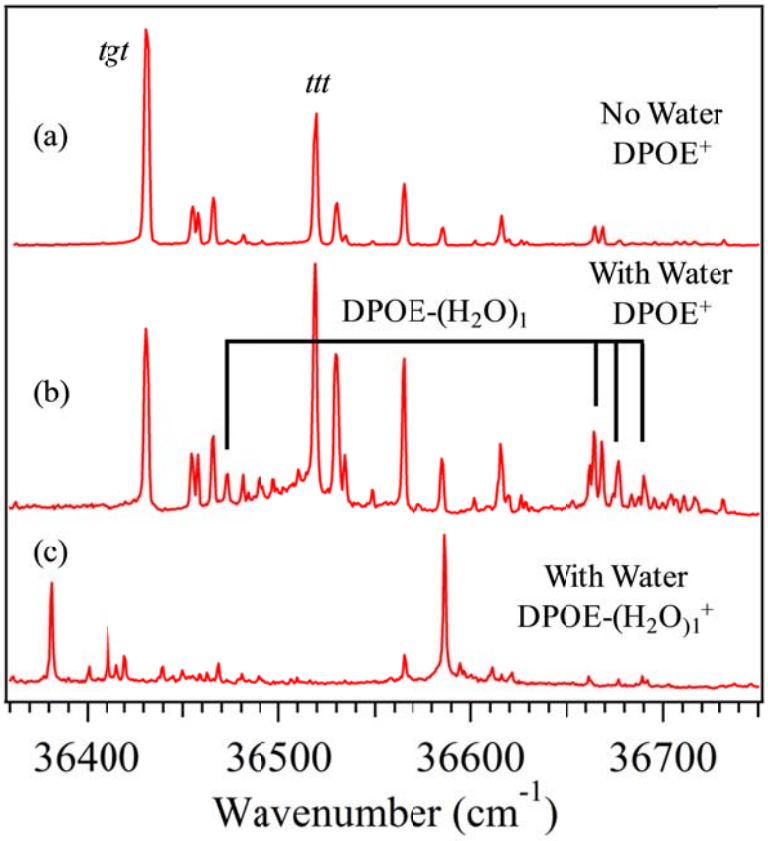

Figure 7.2 The resonant two-photon ionization spectrum (a) the $DPOE^+$ mass channel without water (b) the $DPOE^+$ mass channel with water and (c) the $DPOE\text{-}(H_2O)_1^+$ mass channel. The tie lines in (b) mark the S_1 0^0_0 and S_2 0^0_0, 93^1_0, and 93^2_0 transitions. The experimental spectrum recorded in the $DPOE\text{-}(H_2O)_1^+$ mass channel was obtained by Patrick S. Walsh.

This is most relevant to the S_2-state RIDIR spectrum, in proving that the four OH stretch fundamentals observed in that spectrum (Figure 7.7c) are exclusively from the $DPOE\text{-}(H_2O)_1$ complex. It is worth noting that an IR-induced fragmentation of the 1:2 cluster into the DPOE monomer mass channel would appear as a gain rather than as a depletion, while we observe only depletion. The spectroscopy of the larger $DPOE\text{-}(H_2O)_n$ clusters with n=1-4 will be taken up elsewhere.[13]

Spectroscopic evidence points clearly to a structure for DPOE-$(H_2O)_1$ that retains the *tgt* structure for DPOE. First, the DFL spectrum of the DPOE-$(H_2O)_1$ S_1 origin (figure 7.3b) is nearly identical to that of the *tgt* isomer (figure 7.3a), with Franck-Condon activity in ring modes that reflect the reduced symmetry of the *tgt* structure (C_2 symmetry) relative to the *ttt* conformer (C_{2h}). Second, resonant ion-dip infrared (RIDIR) spectra[14] in the alkyl CH stretch (figure 7.4a) and mid-infrared regions (figure 7.4b) are nearly identical to those of the *tgt* monomer, and quite distinct from those in the *ttt* isomer.[9] Although the symmetry of the *ttt* conformer would be reduced upon binding the water molecule, such structures built from the *ttt* scaffold are more than 7.0 kJ/mol higher in energy. The alkyl CH stretch region is particularly clear in reflecting the *tgt* structure of the ethyl group, including Fermi resonance coupling with CH bend overtones.[9]

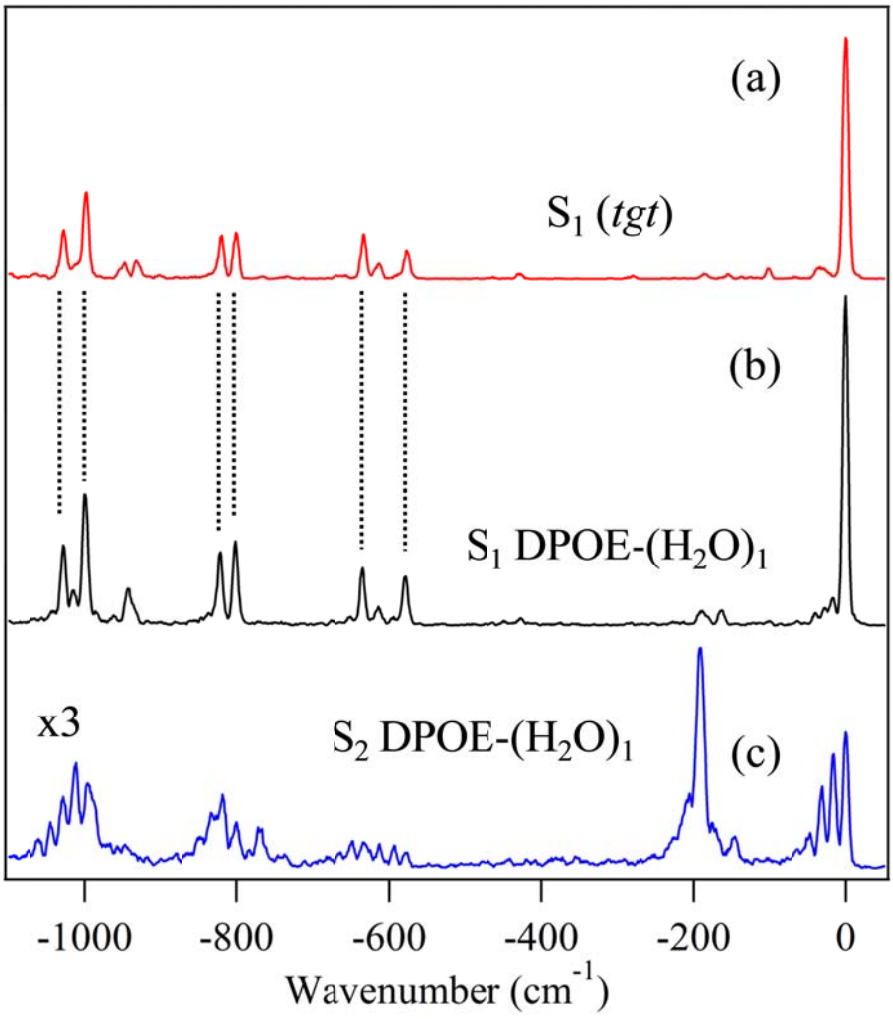

Figure 7.3 Comparison of the DFL scans of the S_1 origins of (a) *tgt* conformer of the DPOE monomer and (b) the DPOE-$(H_2O)_1$ complex. (c) DFL spectrum of the S_2 origin of DPOE-$(H_2O)_1$.

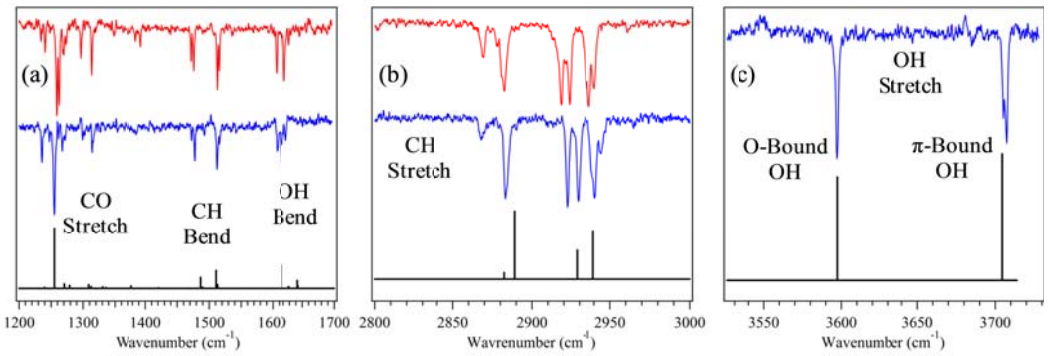

Figure 7.4 Single-conformation infrared spectra of DPOE(*tgt*) (red traces) and DPOE-$(H_2O)_1$ (blue traces) in the (a) mid-IR, (b) alkyl CH stretch region, and (c) OH stretch region.

The RIDIR spectrum of the DPOE-$(H_2O)_1$ complex in the OH stretch region (figure 7.4C) shows two OH stretch fundamentals, with the lower frequency band at 3597 cm^{-1}, and its higher-frequency counterpart a closely-spaced doublet at 3705/3707 cm^{-1}. The spectrum reflects the presence of a single H_2O molecule in the complex engaged in asymmetric binding to DPOE. The 3597 cm^{-1} transition can be ascribed to an OH···O H-bond to one of the phenoxy oxygens, while the 3707 cm^{-1} band is shifted somewhat below a typical free OH stretch (~3720 cm^{-1}), consistent with a weak interaction of the second OH group.[15-16]

The calculated vibrational frequencies and infrared intensities of the structure shown as an inset in figure 7.1c**)** account for all aspects of the infrared spectroscopy. This structure is the global minimum, 4.4 kJ/mol more stable than any other structure. DPOE-$(H_2O)_1$ is nominally built off of monomer structure *tgt*, with only slight differences in the backbone dihedrals between the two. The water molecule forms a double donor H-bonded bridge between the oxygen atom of one phenoxy group and the

π-cloud on the other ring. The calculations predict OH stretch modes that are about 75% localized on a single OH group.[17] In the mid-IR (figure 7.4c), the OH bend in DPOE-$(H_2O)_1$ appears amidst the C=C bends of the aromatic rings at 1614 cm^{-1}, 19 cm^{-1} higher in frequency than the free water bend (1599 cm^{-1}), consistent with the OH group(s) involvement in H-bond(s).

The calculated structure for DPOE-$(H_2O)_1$ (figure 7.1e) places the water molecule 3.27 Å from the center of the phenyl π-cloud and 2.01 Å from the oxygen atom to which it is H-bonded. At the DFT M05-2X/6-31+G(d) level of theory, the binding energy of DPOE-$(H_2O)_1$ was determined to be 30.3 kJ/mol after a correction for basis set superposition error (BSSE) using the counterpoise correction method.[18-19] As a comparison, the binding energies of benzene-$(H_2O)_1$ and anisole-$(H_2O)_1$ at the same level of theory are 14.9 and 21.2 kJ/mol, respectively. Thus, the calculated binding energy of DPOE-$(H_2O)_1$ is close to the sum of the binding energies of the two related complexes. The photodissociation spectrum presented in figure 7.5 shows gains in both the *tgt* and *ttt* monomer conformations. Although no experimental determination of the binding energy was obtained, a single IR photon used (2929 cm^{-1}) was enough energy to dissociate the cluster. The fact that both *tgt* and *ttt* conformations are observed in the spectrum suggests that isomerization of the water cluster occurs prior to dissociation of the water, leading to both monomer conformations.

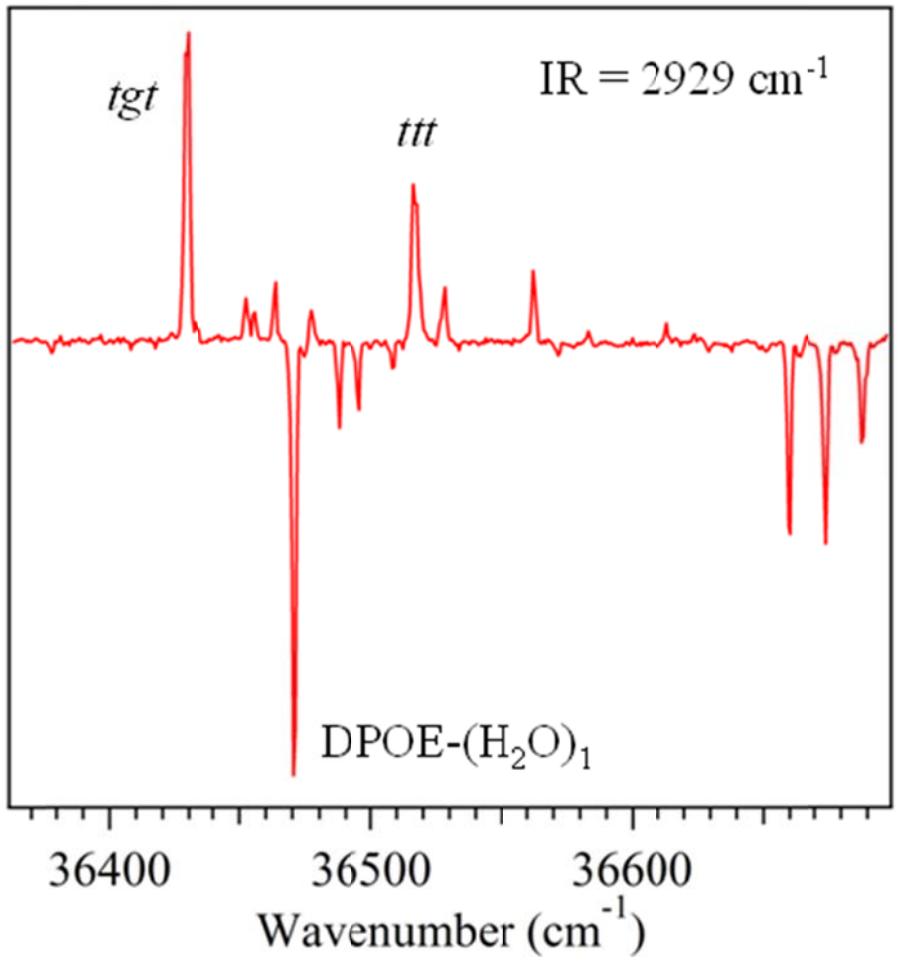

Figure 7.5 Photodissociation spectra obtained by fixing the IR laser to 2929 cm^{-1} showing the gains in both *tgt* and *ttt* monomer conformations.

Having established the structure for the DPOE-$(H_2O)_1$ complex in the ground state, we are now in a position to probe in more detail the consequences of this binding for the close-lying excited states of *tgt* conformer. The UVHB spectrum of figure 7.1d) shows little low-frequency Franck-Condon activity, suggesting that electronic excitation in the S_1 state produces little change in the geometry of the DPOE or in the position of binding of the H_2O molecule to it. However, the set of bands built off the transition at 36,660 cm^{-1} forms a Franck-Condon progression in a 14 cm^{-1} mode. The intensity

patterns in the excitation spectrum (figure 7.1d) and in the DFL from these levels (figure 7.6) can be fit as a Franck-Condon progression in a low-frequency vibration that involves motion of the water molecule in re-adjusting its bridge position in response to electronic excitation. That this Franck-Condon activity begins with the S_1 +189 cm^{-1} transition suggests a change in electronic character beginning there.

Figure 7.6 presents the first 300 cm^{-1} of the DFL spectra of the transitions +189, +203, and +217 cm^{-1} above the S_1 origin of the *tgt* conformer of DPOE-H_2O complex. All three spectra are comprised of two parts assignable to the S_2 and $S_1(v)$ contributions to the excited state level. The three transitions are assigned to the S_0-S_2 0^0_0 and a short progression in the lowest frequency vibration of the complex involving a rocking of the H_2O molecule/DPOE framework, mode 93. The DFL spectra in Figure S1 show how this Franck-Condon activity involving ν_{93} were fit using an Excel spreadsheet based Franck-Condon fitting program using the recursion formulae in Henderson et al.[1] Stick diagrams in Figure S1 show the best-fit result for a displacement parameter of D=1.39.

The remaining emission is S1(v) emission come from the portion of each excited state wave function due to S1(v) "background" levels that carry no oscillator strength in absorption, and therefore are "dark" states that are mixed with the S2 000, 931, and 932 bright states carrying the oscillator strength in absorption from the ground state zero-point level. These $S_1(v)$ levels undergo $\Delta v=0$ emission back to corresponding levels in the ground state, appearing with shifts from resonance fluorescence that are within a few cm^{-1} of their energy in excess of the S_1 origin in excitation. This emission is analogous to the "clump emission" observed and characterized in diphenylmethane.[3, 20]

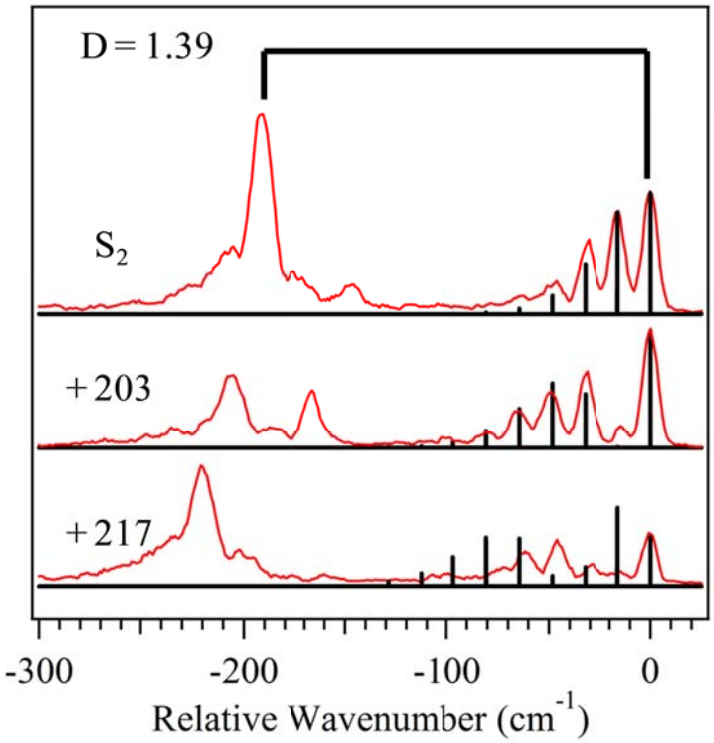

Figure 7.6 The displacement parameter (D) for the normal coordinate in the ground and excited state was determined to be 1.39. Harmonic Franck-Condon integrals were calculated using the recursion relations outlined by Henderson et al.[21] The clump emission at +189 cm^{-1} from the resonance fluorescence is due to vibronic levels in the S_1 manifold.

Indeed, all evidence points to the transition at S_1 +189 cm^{-1} as the S_2 electronic origin. Since the excitonic splitting in the *tgt* monomer is known to be 1.02 cm^{-1},[8] this splitting is induced almost entirely by the asymmetric binding of the H_2O molecule to the two electronic chromophores, as is the case in the bridge structure shown in figure 7.1d). We anticipate then, that the S_1 state involves localized excitation of one ring, and the S_2 state the other. The electronic frequency shifts point to which is which. The S_1 origin of

DPOE-$(H_2O)_1$ is +40 cm^{-1} to the blue of the *tgt* monomer origin, similar to the +55 cm^{-1} shift present in the $OH\cdots\pi$ bound benzene-$(H_2O)_1$ complex.[10, 12] By contrast, the anisole-$(H_2O)_1$ complex, in which H_2O binds to the phenoxy oxygen, produces a blue shift of 119 cm^{-1} relative to anisole monomer,[15] suggesting that the S_2 state in DPOE-$(H_2O)_1$, which appears at +189 cm^{-1}, involves excitation of the aromatic ring to which the H_2O molecule is bound by donating a H-bond to the phenoxy oxygen. Thus, the single H_2O molecule has played an active role in perturbing the excited states of the *tgt* isomer, localizing the electronic excitation on one or the other ring, and splitting the two excited states by 189 cm^{-1}.

In order to probe how the H_2O molecule responds to electronic excitation on either ring, excited state RIDIR spectra were recorded. To that end, figure 7.7 presents OH stretch RIDIR spectra following excitation of the S_1 origin (figure 7.7b) and S_2 origin (figure 7.7c), respectively, contrasting them with the ground state spectrum (figure 7.7a). The spectrum out of the S_1 zero-point level shows that the O-bound OH stretch is unchanged in frequency (3598 cm^{-1}) relative to its ground state value (3597 cm^{-1}). However, the π-bound OH group shifts -16 cm^{-1} to lower frequency, consistent with a small enhancement to the strength of the π H-bond upon electronic excitation of that ring.

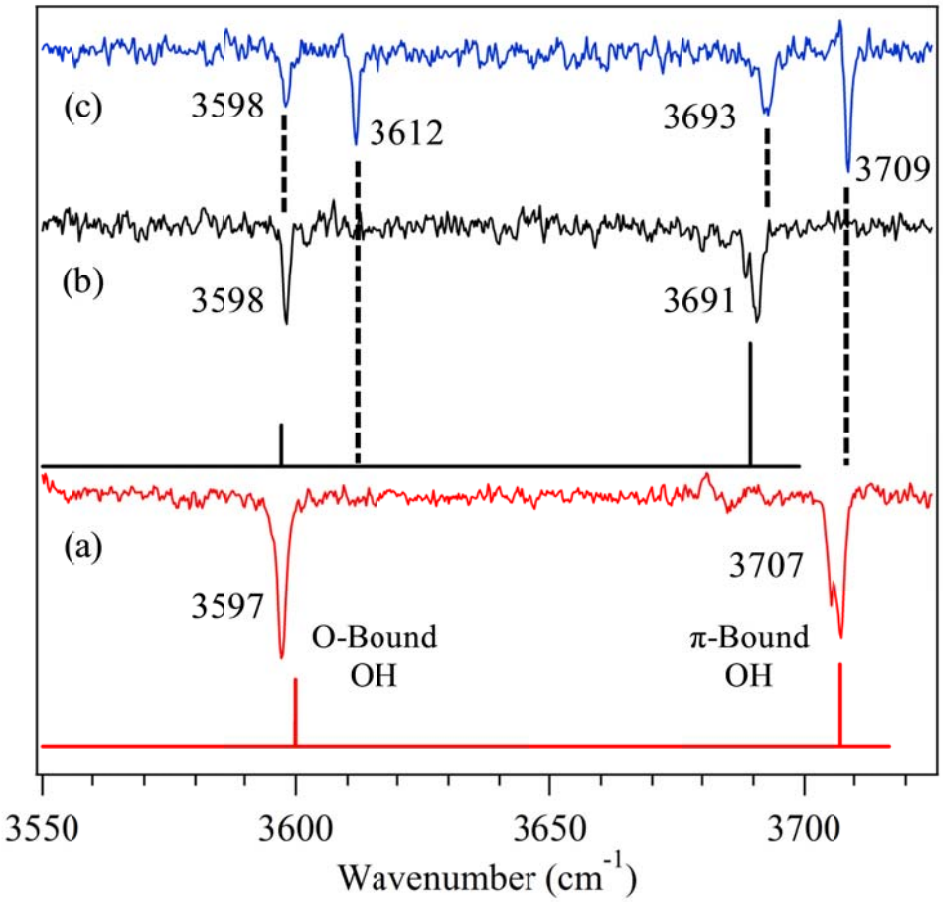

Figure 7.7 Resonant ion-dip infrared spectra of the DPOE-$(H_2O)_1$ complex out of the zero-point levels of the (a) ground electronic state, (b) S_1 state, and (c) S_2 state.

The OH stretch spectrum out of the S_2 zero-point level (figure 7.7c) is even more intriguing. There we see, not two, but four OH stretch transitions, coming in two pairs. The transitions at 3598 and 3693 cm^{-1} are very close to those in the S_1 state spectrum below it, while two new transitions appear at 3612 and 3709 cm^{-1}. The latter frequency is within two cm^{-1} of the ground state π–bound frequency (3707 cm^{-1}). The fact that the new transition in the O-bound OH stretch region is at higher frequency (3612 cm^{-1}) than its S_1 or S_0 counterparts suggests a weakening of this H-bond. Indeed, this is consistent

with the blue-shift in the electronic origin of the S_2 state, which can be interpreted as the difference in binding energy of the DPOE-$(H_2O)_1$ complex between S_0 and S_2 states, with S_2 state smaller by 189 cm^{-1}. If this interpretation of the S_2 RIDIR spectrum is correct, it indicates that the transition assigned to the S_2 origin is actually a mixed S_1/S_2 state, gaining most of its oscillator strength in excitation from the S_2 zero-point level, but showing its mixed character in the doubling of the OH stretch IR fundamentals.

As a check on this interpretation, the mixed excited state character should also be evident in the DFL spectrum of the S_2 origin, which is shown in Figure 7.3c). Indeed, while the emission near the resonance peak (relative wavenumber '0') displays a Franck-Condon progression in a 16 cm^{-1} mode characteristic of emission from the S_2 state, the large band at -192 cm^{-1} shows little such Franck-Condon activity, and is much more like the S_1 state in this respect. Furthermore, its wavenumber position (-192 cm^{-1}) accesses levels in the S_0 state that are within a few cm^{-1} of the energy excited above the S_1 origin (189 cm^{-1}). This emission is characteristic of $S_1(v)$ character in the mixed vibronic state where the density of states is about 6 states per cm^{-1}, displaying $\Delta v=0$ Franck-Condon factors in its emission back down to the ground state. More generally, the DFL spectrum of Figure 7.3c) can be understood as a sum of spectra from an electronically mixed upper state, with partial $S_2(0^0)$ and partial $S_1(v)$ character. This spectroscopic signature of mixed electronic character has been identified in previous studies of flexible bichromophores, and has been studied in some detail in diphenylmethane,[3] bis-(2-hydroxyphenyl)methane,[4] and bis-(4-hydroxyphenyl)methane.[5, 22] Even the relative integrated intensities of the S_1- and S_2-components of the emission (59%:41%, S_1:S_2) are

in keeping with the relative intensities of the OH stretch depletions ascribed to S_1 and S_2 character in the infrared (53%:47%, S_1:S_2).

It is evident, then, that this single water molecule plays an extraordinary role as a solvent molecule, binding as a hydrogen-bonded double-donor bridge between the two chromophores in an asymmetric configuration, interacting principally with the π cloud of one ring and the phenoxy O-atom of the other. In so doing, it localizes the electronic excitation of this weakly coupled bichromophore and produces local site energies for the two electronic chromophores that differ by almost 200 cm^{-1}. Each OH group of the solvent H_2O then responds to the chromophore to which it is principally bound, reporting on the strength of its H-bonds and on their changes in strength with electronic excitation. Finally, the S_2-state OH stretch spectrum shows clear evidence for the mixed excited state character of the level, with frequencies and intensities that reflect the S_1 and S_2 components of the mixing. In this sense, the water molecule also provides a means by which, via proper choice of wavelength, the initial excitation can be directed to one or the other chromophore. Furthermore, in a time-domain experiment on the DPOE-$(H_2O)_1$ complex with a suitably short UV excitation pulse, initial absorption to the S_2 state would localize excitation on the chromophore to which water is O-bound, with electronic energy transfer occurring to the π-bound chromophore. We anticipate the presence of quantum beats in the emission when monitoring the S_2 or $S_1(v)$ emission. These quantum beats may have a similar physical origin to those observed in photosynthetic chromophore arrays in solution.[1-2] The extent to which the water molecule also mediates electronic energy transfer and/or coherent wave packet evolution is a subject worthy of further investigation from both theory and experiment.

7.3 Conclusions

Size and conformation-specific ultraviolet and infrared spectra are used to probe the effects of binding a single water molecule on the close-lying excited states present in a model flexible bichromophore, 1,2-diphenoxyethane (DPOE). The water molecule binds to DPOE asymmetrically, thereby localizing the two electronically excited states on one or the other ring, producing a S1/S2 splitting of 190 cm-1. Electronic localization is reflected clearly in the OH stretch transitions in the excited states. Since the S2 origin is imbedded in vibronic levels of the S1 manifold, its OH stretch spectrum reflects the vibronic coupling between these levels, producing four OH stretch transitions that are a sum of contributions from S2-localized and S1-localized excited states. The single solvent water molecule thus plays multiple roles, localizing the electronic excitation in the bichromophore, inducing electronic energy transfer between the two rings, and reporting on the state mixing via its OH stretch absorptions.

7.4 References

1. Engel, G. S.; Calhoun, T. R.; Read, E. L.; Ahn, T. K.; Mancal, T.; Cheng, Y. C.; Blankenship, R. E.; Fleming, G. R. Evidence for Wavelike Energy Transfer through Quantum Coherence in Photosynthetic Systems. *Nature* **2007,** *446,* 782-786.

2. Lee, H.; Cheng, Y. C.; Fleming, G. R. Coherence Dynamics in Photosynthesis: Protein Protection of Excitonic Coherence. *Science* **2007,** *316,* 1462-1465.

3. Pillsbury, N. R.; Stearns, J. A.; Muller, C. W.; Plusquellic, D. F.; Zwier, T. S. State-Specific Studies of Internal Mixing in a Prototypical Flexible Bichromophore: Diphenylmethane. *J. Chem. Phys.* **2008,** *129,* 114301.

4. Pillsbury, N. R.; Muller, C. W.; Meerts, W. L.; Plusquellic, D. F.; Zwier, T. S. Conformational Effects on Excitonic Interactions in a Prototypical H-Bonded Bichromophore: Bis(2-Hydroxyphenyl)Methane. *J. Phys. Chem. A* **2009,** *113,* 5000-5012.

5. Rodrigo, C. P.; Mueller, C. W.; Pillsbury, N. R.; James, W. H., III; Plusquellic, D. F.; Zwier, T. S. Conformer-Specific Vibronic Spectroscopy and Vibronic Coupling in a Flexible Bichromophore: Bis-(4-Hydroxyphenyl)Methane. *J. Chem. Phys.* **2011,** *134*.

6. Kopec, S.; Ottiger, P.; Leutwyler, S.; Koppel, H. Vibrational Quenching of Excitonic Splittings in H-Bonded Molecular Dimers: Adiabatic Description and Effective Mode Approximation. *J. Chem. Phys.* **2012,** *137,* 184312.

7. Ottiger, P.; Leutwyler, S. Excitonic Splittings in Jet-Cooled Molecular Dimers. *Chimia* **2011,** *65,* 228-230.

8. Buchanan, E. G.; Plusquellic, D. F.; Zwier, T. S. Excitonic Splitting and Vibronic Coupling in 1,2-Diphenoxyethane: Conformation-Specific Effects in the Weak Coupling Limit. *J. Chem. Phys.* **2013,** 138, 204313.

9. Buchanan, E. G.; Sibert, E. L.; Zwier, T. S. Ground State Conformational Preferences and Ch Stretch–Bend Coupling in a Model Alkoxy Chain: 1,2-Diphenoxyethane. *The Journal of Physical Chemistry A* **2013,** *117,* 2800-2811.

10. Gotch, A. J.; Zwier, T. S. Multiphoton Ionization Studies of Clusters of Immiscible Liquids .1. C_6H_6-$(H_2O)_N$, N=1,2. *J. Chem. Phys.* **1992,** *96,* 3388-3401.

11. Pribble, R. N.; Zwier, T. S. Size-Specific Infrared-Spectra of Benzene-$(H_2O)_N$ Clusters (N=1 through 7) - Evidence for Noncyclic $(H_2O)_N$ Structures. *Science* **1994,** *265,* 75-79.

12. Pribble, R. N.; Garrett, A. W.; Haber, K.; Zwier, T. S.Resonant Ion-Dip Infrared-Spectroscopy of Benzene-H2o and Benzene-HOD. *J. Chem. Phys.* **1995,** *103,* 531-544.

13. Walsh, P. S.; Buchanan, E. G.; Gord, J. R.; Zwier, T. S. Molecular-Scale Insight to Kasha's Rule: Internal Conversion in DPOE-$(H_2O)_N$ Clusters, N=1-4. **(to be published)**.

14. Zwier, T. S. Laser Spectroscopy of Jet-Cooled Biomolecules and Their Water-Containing Clusters: Water Bridges and Molecular Conformation. *J. Phys. Chem. A* **2001,** *105,* 8827-8839.

15. Reimann, B.; Buchhold, K.; Barth, H. D.; Brutschy, B.; Tarakeshwar, P.; Kim, K. S. Anisole-$(H_2O)_N$ (N=1-3) Complexes: An Experimental and Theoretical Investigation of the Modulation of Optimal Structures, Binding Energies, and Vibrational Spectra in Both the Ground and First Excited States. *J. Chem. Phys.* **2002,** *117,* 8805-8822.

16. Huang, Z. S.; Miller, R. E. High-Resolution near-Infrared Spectroscopy of Water Dimer. *J. Chem. Phys.* **1989,** *91,* 6613-31.

17. Jamroz, M. H. *Vibrational Energy Distribution Analysis: Veda 4 Program*, Warsaw, 2004.

18. Boys, S. F.; Bernardi, F. Calculation of Small Molecular Interactions by Differences of Separate Total Energies - Some Procedures with Reduced Errors. *Mol. Phys.* **1970,** *19,* 553.

19. Vanduijneveldt, F. B.; Vanduijneveldtvanderijdt, J.; Vanlenthe, J. H. State-of-the-Art in Counterpoise Theory. *Chem. Rev.* **1994,** *94,* 1873-1885.

20. Stearns, J. A.; Pillsbury, N. R.; Douglass, K. O.; Muller, C. W.; Zwier, T. S.; Plusquellic, D. F. Rotationally Resolved Studies of S-0 and the Exciton Coupled S-1/S-2 Origin Regions of Diphenylmethane and the D(12) Isotopologue. *J. Chem. Phys.* **2008,** *129,* 224305.

21. Henderson, J. R.; Muramoto, M.; Willett, R. A. Harmonic Franck-Condon Overlap Integrals Including Displacement of Normal Coordinates. *J. Chem. Phys.* **1964,** *41,* 580-581.

22. Chou, S. G.; Rodrigo, C. P.; Mueller, C. W.; Douglass, K. O.; Zwier, T. S.; Plusquellic, D. F. Rotationally Resolved C(2) Symmetric Conformers of Bis-(4-Hydroxyphenyl)Methane: Prototypical Examples of Excitonic Coupling in the S(1) and S(2) Electronic States. *J. Phys. Chem. A* **2011,** *115,* 9643-9652.

CHAPTER 8 BINDING WATER CLUSTERS TO AN AROMATIC-RICH HYDROPHOBIC POCKET: [2.2.2]PARACYCLOPHANE-$(H_2O)_N$, N=1-5

8.1 Introduction

[2.2.2]paracyclophane is a prototypical macrocycle with fascinating properties both as a multichromophore and as an aromatic-rich binding pocket for various ligands. More commonly known as tricyclophane (TCP), it incorporates three phenyl rings into the macrocycle, with ethano bridges substituted at *para* positions on the rings acting as linker groups between the rings, which can reorient to some degree to accommodate various binding partners. In the absence of a ligand binding partner, the three phenyl rings adopt a face-to-face orientation much like [2.2]paracyclophane,[1-4] but with an increased distanced and increased dihedral between ring planes.

TCP is predicted by calculations to have two low-lying conformational minima, one with C_3 symmetry, and the other with C_2 symmetry, depending on the configuration of the ethano bridges relative to one another. As Figure 8.1 shows, the carbon atoms in the ethano bridges are labeled as 'u' or 'd' to denote whether they are up or down relative to the plane that intersects the centers of the three rings. In a previous study of the single-conformation spectroscopy of TCP in the gas phase, a single conformer of TCP was observed following cooling in a supersonic expansion, and assigned based on evidence both in the infrared and ultraviolet spectrum to the C_2 symmetry conformer.[5]

Presumably, population originally in the C_3 conformer was funneled into the C_2 structure upon cooling in the expansion. Interestingly, density functional theory (DFT) calculations that employed the dispersion-corrected M05-2X functional did not predict the C_2 structure to be a stable minimum, but both conformers were successfully optimized using the ωB97X-D functional with a 6-311+g(d,p) basis, although the C_2 isomer was predicted to be 2.5 kJ/mol higher in energy than its C_3 counterpart, at odds with experiment. A key part of the experimental assignment process was the successful modeling of the effects of stretch/bend Fermi resonance on the alkyl CH stretch region, first modeling the alkyl CH stretch region of 1,2-diphenylethane (DPE) to establish and refine the relative coupling elements between the fundamentals and overtones, especially for the gauche or *tgt* isomer of DPE.

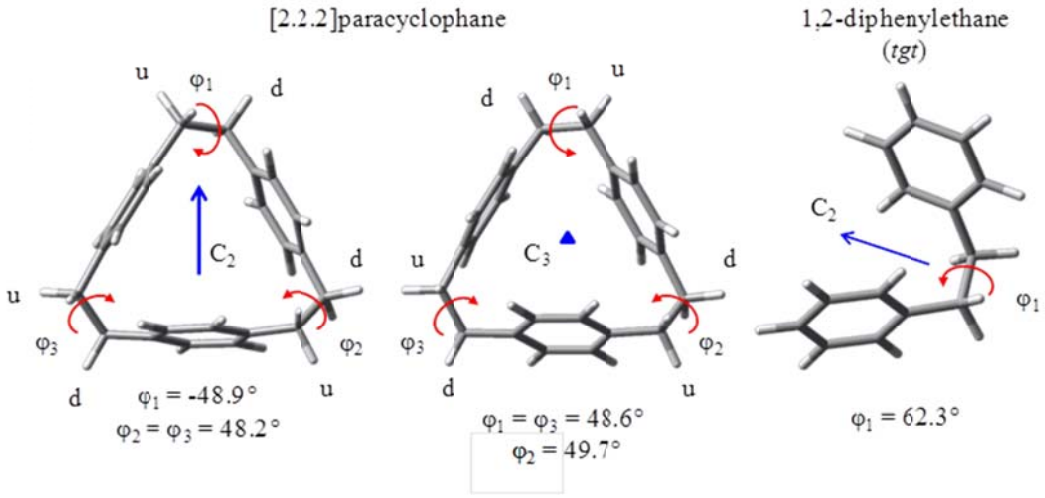

Figure 8.1 Comparison between the C_2 and C_3 structural isomers of [2.2.2]paracyclophane and the gauche (*tgt*) isomer of 1,2-diphenoxyethane.

One of the motivations for studying the spectroscopy of TCP is its status as a model trichromophore, with three chemically equivalent ultraviolet chromophores built into the macrocycle. Thus, we anticipate that the ultraviolet spectrum will reflect the presence of the three excited states in close proximity. When more than one ultraviolet chromophore is present, the vibronic spectroscopy itself is fascinating due to these close-lying excited states. Here the size of the excitonic splitting and the degree of localization or delocalization of the electronic excitation depends intimately on the relative distance, orientation, and symmetry of the three chromophores.[6] Earlier studies have focused attention on similar issues in bichromophores and molecular dimers, leading to state-to-state understanding of the vibronic coupling between the two intermingled excited states. Among the recent subjects of study are diphenylmethane,[7-8] bis(2-hydroxylphenyl)methane,[9] bis(4-hydroxylphenyl)methane,[10] 1,2-diphenoxyethane,[11] benzoic acid dimer,[12] 2-aminopyridine dimer,[13] and others. Significant new insights have come from the quantitative multi-mode theoretical modeling by Köppel, Leutwyler and co-workers[14] and Nebgen and Slipchenko.[15] TCP, a trichromophore, is a natural extension to these studies with three close lying excited states. However, here, the flexibility of TCP is limited by the formation of the macrocycle, placing the three ultraviolet chromophores in well-defined orientations, a subject more thoroughly investigated in [2.2]paracyclophane and its derivatives.[1, 4, 16-18]

While the present work will necessarily touch on the vibronic spectroscopy of TCP, a detailed consideration of TCP and TCP-$(H_2O)_n$ clusters as trichromophores is left for a future study that incorporates theoretical modeling which can help guide the interpretation of the complicated vibronic spectroscopy. Instead, the primary objective of

the present work is to probe how well-defined numbers of H_2O molecules bind to the TCP binding pocket. Our focus will be on TCP-$(H_2O)_n$ clusters with n=1-5.

In one sense, the study of TCP-$(H_2O)_n$ clusters is thus of the same genre as previous work directed towards the study of the conformational preferences and ligand binding of other prototypical macrocycles such as crown ethers and calixarenes. The general objective is to determine where and how the ligand binds to the host molecule, especially when a large geometry change is observed for the host to accommodate its guest. In several of these studies, multiple ultraviolet chromophores have been incorporated into the host guest complex, with interesting binding properties and photophysics resulting from the proximity and stiffness of the aromatic substituents. In the case of the crown ethers, the chromophores are incorporated into a macrocycle that does not require the presence of the chromophore itself, while the calixarenes have the ultraviolet chomophores built directly into the macrocycle itself. Both crown ethers and calixarenes have ether or OH groups which are natural hydrogen bond acceptor sites for H_2O molecules. For the crown ether-$(H_2O)_{1,2}$ complexes, the first water molecule has generally been observed donating both hydrogen atoms to the oxygen rich macrocycle, with the second water binding to either the opposite side of the mactrocycle or to the first water molecule.[19-24] However, the recent study by Kusaka et al. proved that the calyx[4]arene-$(H_2O)_1$ complex preferentially binds the water molecule to the interior of the cavity through water OH$\cdots\pi$ interactions with the four aromatic rings.[25-27] In so doing, the water molecule did not perturb the four intramolecular OH$\cdots$OH hydrogen bonds that cap the calix[4]arene.

The spectroscopy of TCP-$(H_2O)_n$ clusters also bears a natural and important connection with other aromatic-$(H_2O)_n$ clusters, principally with the prototypical aromatic benzene.[28-29] Benzene-$(H_2O)_n$ clusters with n=1-9 have been studying using resonant two-photon ionization (R2PI) spectroscopy and resonant ion-dip infrared (RIDIR) spectroscopy, two of the primary tools used in the present work. In the cases where definitive structures have been assigned, all benzene-$(H_2O)_n$ clusters incorporate the lowest-energy structure for the pure $(H_2O)_n$ clusters, with benzene sitting of the "surface" of the cluster and bound to it by a π H-bond involving one of the otherwise free OH groups on the water cluster.

Since benzene offers its open face to binding a single water molecule, this π-bound H_2O molecule can undergo large-amplitude tumbling about the benzene π cloud, showing evidence of this tumbling through which can tumble about the single aromatic ring, showing evidence thereof through strong combination bands involving the low frequency H_2O librations built off the anti-symmetric stretch fundamental.[30] Larger $(H_2O)_n$ clusters interact in a less symmetric fashion with the benzene π cloud, but the presence of benzene is readily apparent in the infrared spectrum, producing a π-bound OH stretch fundamental near 3650 cm^{-1}, and redistributing the intensities and shifting the frequencies of the H-bonded OH stretch fundamentals of the $(H_2O)_n$ clusters.

By contrast, in TCP-$(H_2O)_n$ clusters, the binding pocket is more complicated, with three aromatic rings facing each other along the nominally triangular walls of the macrocycle. A first question we seek to address is whether the H_2O molecule(s) bind to the interior or exterior of the pocket. This question is intriguing in part because the interior has a radius of ~5 Å, similar to that of a single-walled carbon nanotube.[31] The

binding of H_2O molecules to carbon nanotubes is an on-going subject of intense investigation, as is the transport of single water and water chains along its tubular axis. Furthermore, TCP mimics the sub-nanometer diameter transmemebrane aquaporins, where the efficient transport of water through the cell membrane occurs.[32] TCP bears a structural resemblance to a single ring of a carbon nanotube or aquaporin, especially with regards to the diameter and hydrophobicity,[32] and studies of the spectroscopy of water confined by TCP may shed some light on how water binds and moves in these nanotubes.

As we shall see, the R2PI and OH stretch infrared spectra of TCP-$(H_2O)_n$, n=1-5 reflect structures in which the water molecule(s) take up a principal binding site on the interior of the macrocycle. The first water binds sitting atop TCP, pointing both hydrogen atoms into the aromatic rich pocket, while the second water engages in a H-bond as donor to the first. The n=3-5 structures are all cyclic water clusters, with one free OH pointing into the TCP interior. The H-bonded OH stretch regions of these clusters are remarkably similar to their benzene-$(H_2O)_n$ counterparts. With increasing size the cycles begin to spill out of, and wrap around the walls of the macrocycle. In n=5, there is spectroscopic evidence for formation of a second □□H-bond, probably to the exterior in n=5. We also study the effects of electronic excitation of TCP on the OH stretch infrared spectrum of TCP-$(H_2O)_n$, n=1-3, which show selective shifts of the OH group(s) involved in □□H-bonding with the TCP pocket interior.

8.2 Results

8.2.1 R2PI and IR-UV Hole-Burning Spectra

Previously, we reported on the conformational preferences of TCP monomer, developing a reduced dimension Hamiltonian with off-diagonal cubic couplings to model the alkyl CH bend/stretch Fermi resonance couplings present in the alkyl CH stretch region.[5] The first-principles model was able to distinguish between the two predicted isomers calculated to have C_2 (ud/du/du) and C_3(du/du/du) symmetry, where up (u) and down (d) designate the position of the ethyl group carbons connecting the phenyl rings relative to the plane formed by the centers of the three phenyl rings.[5] UV holeburning spectroscopy was used to prove that a single conformer is responsible for all observed vibronic transitions (figure 8.2), apart from a weak transition +8 cm^{-1} above the S_1 origin of the main conformer, tentatively assigned to a second conformer with minor population. Based on the vibronic spectroscopy and infrared spectrum of the main conformer, it was assigned to the C_2 symmetry structure presented in figure 8.1.

As a trichromophore, the vibronic spectroscopy of the TCP monomer is fascinating in its own right due to the presence of three close-lying, coupled excited states. Evidence for the presence of more than one excited state is most readily apparent in the set of strong transitions approximately 100 cm^{-1} above the S_0-S_1 origin (figure 8.2). However, the excitonic splittings and vibronic coupling in TCP and its water containing clusters is outside the scope of the present paper, and will be addressed elsewhere.

Here, we focus attention on the spectroscopy of TCP-$(H_2O)_n$ clusters with n=1-5, having as our primary goal establishing how the water molecules bind to each other and

to the TCP pocket as a function of cluster size. Figure 8.3 provides an overview of the TCP-$(H_2O)_n$ (n=0-5) R2PI spectra obtained with water vapor seeded into the expansion. The assignments of transitions shown in the figure are based on the spectroscopy that follows. For our purposes here, it important first to note the changing fragmentation patterns with cluster size that accompanies photoionization. Table 8.1 lists the cluster size dependence of the percent fragmentation by loss of a single water molecule in one-color R2PI through the S_0-S_1 origin.

$$TCP\text{-}(H_2O)_n + h\nu_1 \rightarrow TCP(S_1)\text{-}(H_2O)_n + h\nu_1 \rightarrow TCP^+\text{-}(H_2O)_n \rightarrow TCP^+\text{-}(H_2O)_{n-1} + H_2O$$

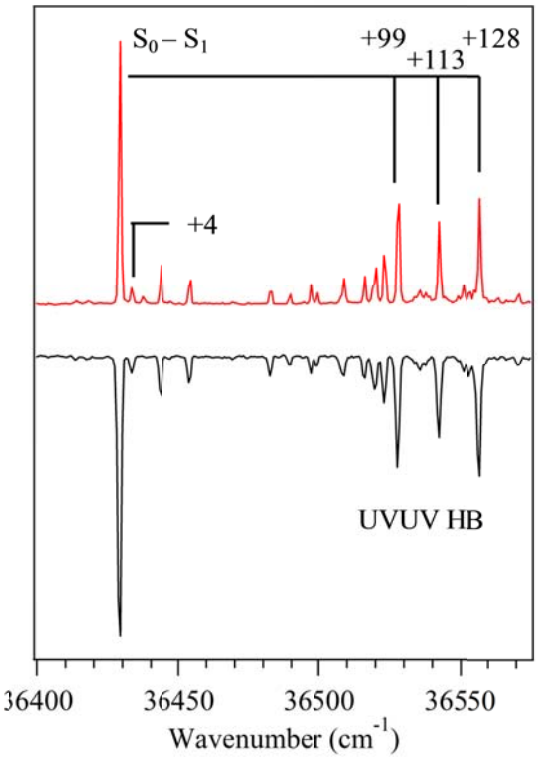

Figure 8.2 The R2PI and UVUV hole-burning spectra of TCP proving the existence of a single conformer present in the supersonic jet expansion.

Table 8.1 A comparison between the experimental S_0-S_1 origin shifts for TCP-$(H_2O)_n$ and Benzene-$(H_2O)_n$. †Shifts relative to the TCP monomer are listed in parentheses. ‡Benzene-$(H_2O)_n$ shifts are relative to the 6^0_1 transition due to the dipole forbidden origin of benzene monomer. The percent fragmentation for the TCP-$(H_2O)_n$ clusters is also listed.

	TCP-$(H_2O)_n$		Benzene-$(H_2O)_n$	
Cluster Size (n)	Exp. S_0 - S_1 (cm^{-1})†	Percent Fragmentation	Cluster Size (n)	Exp. S_0 - S_1 (cm^{-1})‡
n = 1	36365 (-64)	> 90 %	n = 1	+49
n = 2	36313 (-116)	~ 50 %	n = 2	+75
n = 3	36397/36402 (-32/-27)	< 1 %	n = 3	+98
n = 4	36348 (-81)	< 1 %	n = 4	+100
n = 5	36347 (-82)	<1 %	n = 5	+97

Notably, TCP-$(H_2O)_1$ and TCP-$(H_2O)_2$ undergo efficient fragmentation following photo-ionization, while n=3-5 hardly fragment at all. This behavior is most clearly observed in the set of R2PI spectra reported in Figure 3, where contributions attributable to the dissociation of the n=3-5 clusters into the n=0-2 R2PI spectra are negligible. As has been described in detail elsewhere,[40] efficient fragmentation following photoionization results from a large change in the preferred geometry of the H_2O molecule(s) that accompanies photoionization of TCP. The nature of this geometry change will be better evaluated once the structures of the netural TCP-$(H_2O)_n$ clusters have been established. However, one anticipates, based on previous experience with π–bound solvents to benzene (e.g., benzene-H_2O[39] or benzene-HCl[40]), that TCP-H_2O and TCP-$(H_2O)_2$ engage H_2O in a π H-bond with the positive end of its dipole nearest the

TCP pocket. Upon photoionization, the positive charge on TCP would preferably bind H_2O with its O-end towards the π cloud. Vertical photoionization then places the cation cluster well above its adiabatic ionization threshold, where fragmentation by loss of H_2O can occur. The fact that this fragmentation is much reduced with n=3-5 suggests a significant change in the nature of the interaction of the water cluster beginning with the water trimer.

Another striking feature of the R2PI spectra are the observed electronic frequency shifts for the S_0-S_1 transitions of the TCP-$(H_2O)_n$ clusters relative to the TCP monomer. As figure 8.2 and table 8.1 show, the S_0-S_1 origins of TCP-$(H_2O)_n$ are consistently red-shifted from TCP monomer, a direction opposite to that found in the benzene-$(H_2O)_n$, which were consistently blue-shifted.[41] Furthermore, the magnitude of the shift is not monotonic, with shifts of -65, -116, -30, -81, and -82 cm^{-1} for n=1-5, respectively. Once again, the largest and smallest shifts occur for n=2 and n=3, suggesting again a major structural rearrangement. The interpretation of this electronic frequency shift is complicated by the presence of the three UV chromophores, whose uncoupled excited states could in principle shift independently, and even in opposite directions, from one another, depending on the nature of each ring's interaction with the H_2O molecule(s). This, in turn, could change the degree of localization/delocalization of the electronic excitation.

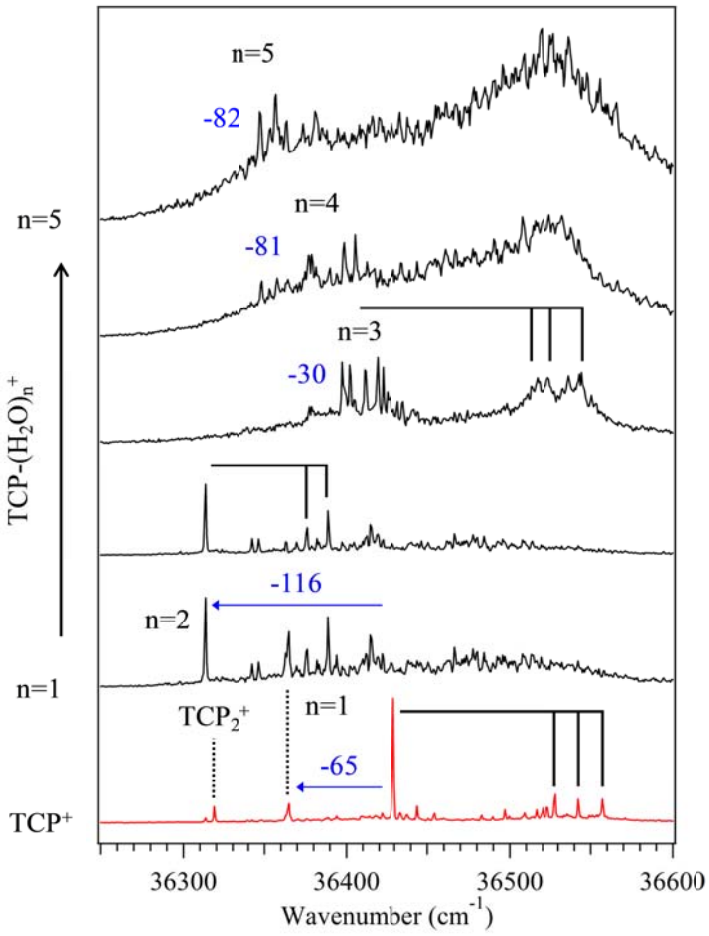

Figure 8.3 An overview of the excitation spectra of TCP and TCP-$(H_2O)_n$ (n=1-5). The bottom red trace was obtained in the TCP^+ mass channel with water vapor seeded into the expansion. The black traces were obtained in the TCP-$(H_2O)_n^+$ mass channels, with n=1-5 increasing from the bottom-up.

Hole-burning methods were required to record the UV spectrum of TCP-$(H_2O)_1$. Given the efficient fragmentation of the complex into the monomer mass channel, the transitions above the S_0-S_1 origin due to TCP-$(H_2O)_1$ were hard to observe amidst the much stronger transitions due to TCP monomer. As a result, IR-UV hole-burning was carried out in the TCP-$(H_2O)_1^+$ mass channel, where the primary interference was due to TCP-$(H_2O)_2$. The results are shown as the red trace in figure 8.4. As already mentioned,

the TCP-$(H_2O)_1$ S_0-S_1 origin occurring at 36364 cm^{-1} is red shifted by -65 cm^{-1} from the monomer origin at 36429 cm^{-1}, opposite in direction to the shift observed in benzene-$(H_2O)_1$, which is blue shifted by +55 cm^{-1} from benzene monomer.[41] Presumably, if the water molecule was bound to the outside of the TCP macrocycle, a similar blue shift of the electronic origin would be observed. Furthermore, compared to the TCP monomer, the low frequency modes associated with the in-phase and out-of-phase ring torsions are shifted to higher frequency in TCP-$(H_2O)_1$. Stiffening these low frequency vibrations is consistent with an intimate involvement of the H_2O with the three phenyl rings.

Hole-burning methods were required to record the UV spectrum of TCP-$(H_2O)_1$. Given the efficient fragmentation of the complex into the monomer mass channel, the transitions above the S_0-S_1 origin due to TCP-$(H_2O)_1$ were hard to observe amidst the much stronger transitions due to TCP monomer. As a result, IR-UV hole-burning was carried out in the TCP-$(H_2O)_1^+$ mass channel, where the primary interference was due to TCP-$(H_2O)_2$. The results are shown as the red trace in figure 4. As already mentioned, the TCP-$(H_2O)_1$ S_0-S_1 origin occurring at 36364 cm^{-1} is red shifted by -65 cm^{-1} from the monomer origin at 36429 cm^{-1}, opposite in direction to the shift observed in benzene-$(H_2O)_1$, which is blue shifted by +55 $cm^{-1}$from benzene monomer.[41] Presumably, if the water molecule was bound to the outside of the TCP macrocycle, a similar blue shift of the electronic origin would be observed. Furthermore, compared to the TCP monomer, the low frequency modes associated with the in-phase and out-of-phase ring torsions are shifted to higher frequency in TCP-$(H_2O)_1$. Stiffening these low frequency vibrations is consistent with an intimate involvement of the H_2O with the three phenyl rings.

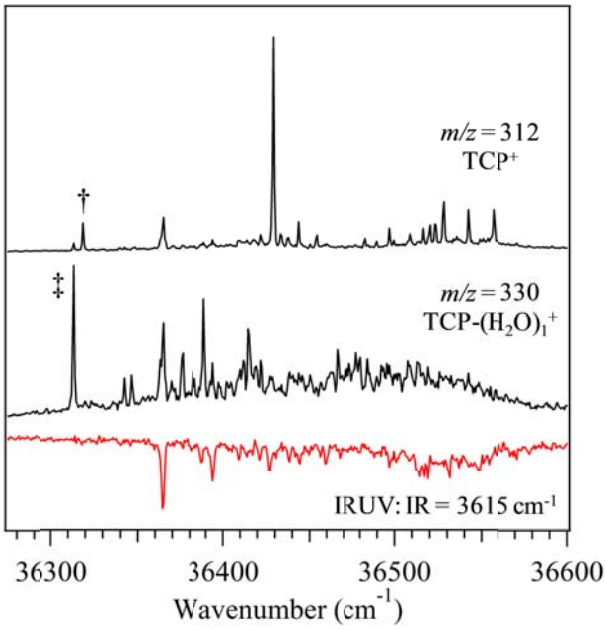

Figure 8.4 R2PI spectra obtained in the TCP^+ and TCP-$(H_2O)_1^+$ mass channels, and the IRUV hole-burning spectrum of TCP-$(H_2O)_1$ obtained in the TCP-$(H_2O)_1^+$ mass channel to avoid interference with the TCP monomer transitions. Transitions marked with a dagger and double dagger are due to TCP dimer and TCP-$(H_2O)_2$ respectively.

Figure 8.5a compares the R2PI spectra obtained in the TCP-$(H_2O)_1^+$ and TCP-$(H_2O)_2^+$ mass channels alongside the IR-UV hole-burning spectrum with the IR fixed at 3580 cm^{-1}, an IR transition unique to TCP-$(H_2O)_2$. The origin of the TCP-$(H_2O)_2$ cluster is shifted further to the red of the TCP-$(H_2O)_1$ complex by -52 cm^{-1}, corresponding to -116 cm^{-1} from TCP monomer, which is consistent with an even stronger interaction of the H_2O molecules with the TCP structure.

The IR-UV hole-burning spectra of TCP-$(H_2O)_3$ (Figure 8.5b) uncover the presence of two isomers with nearly identical UV spectra, with S_0-S_1 origins that have much smaller red shifts (-32, -27 cm^{-1}) from the monomer. These spectra were recorded at IR hole-burning frequencies of 3557 and 3550 cm^{-1}, respectively. In the absence of a

TCP, the water trimer forms a H-bonded cycle with a diameter approaching the inner diameter of TCP. The two isomers have remarkably similar UV excitation spectra, indicating that the two isomers differ in only subtle ways from one another.

The UV spectra of TCP-$(H_2O)_{4,5}$ are very congested, and in fact the position of the electronic origin is much less certain than in the smaller clusters. The tentatively assigned S_0-S_1 origin transitions appear with frequency shifts of -81 and -82 cm^{-1}. Based on the background observed in the R2PI spectrum, the lack of selectivity in IRUV hole-burning, and the two observed isomers of TCP-$(H_2O)_3$, the possible presence of multiple conformations of TCP-$(H_2O)_{4,5}$ seems likely, a point to which we return shortly. It is also worth noting the increasingly prominent bands in the 36500-36550 cm^{-1} region for the n=3-5 clusters, suggesting the presence of the S_2 and S_3 excited states in this region.

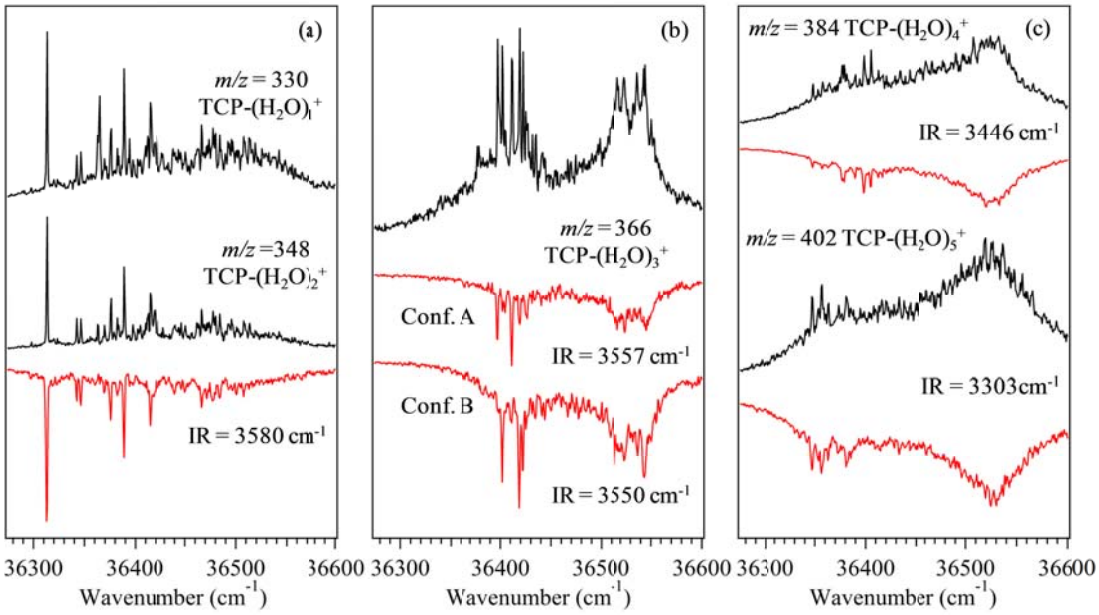

Figure 8.5 The R2PI and IRUV hole-burning spectra of the TCP-$(H_2O)_2$, TCP-$(H_2O)_3$, and TCP-$(H_2O)_{4,5}$ clusters are presented in (a), (b), and (c) respectively.

To gain a better insight to the binding motifs and H-bonded networks present in TCP-$(H_2O)_n$ clusters, ground and excited state infrared spectra in the OH stretch region were obtained for the TCP-$(H_2O)_n$ clusters. The RIDIR spectra are compared to vibrational frequency calculations at the DFT ωB97X-D/6-311+g(d,p) level of theory, the same level of theory that was required to account for the observed conformations of TCP monomer.[5] Based upon the similarity between the experimental alkyl CH stretch spectra of the TCP monomer and TCP-$(H_2O)_{1,2}$ clusters, the TCP monomer was observed to maintain its C_2 symmetry structure when binding the first two water molecules. While we have no direct proof that this still holds in n=3-5, we carried out structure optimizations and vibrational frequency calculations only on structures that incorporate TCP in its C_2 structure, with ud/du/du geometry.

8.2.2 RIDIR Spectra in the OH Stretch Region

Figure 8.6a presents the ground and excited RIDIR spectra of TCP-(H2O)1 in the OH stretch region while monitoring the ion signal with UV laser fixed on the R2PI transition at 36355 cm^{-1}. For comparison, the OH stretch RIDIR spectrum of benzene-$(H_2O)_1$ is shown as the top trace, while the predictions for the IR spectra of TCP-H_2O based on the □B97X-D calculations are shown as stick spectra. The experimental ground state spectrum is consistent with the water molecule acting as a double-donor into the pocket, forming π-hydrogen bonds with both its OH groups to the interior of the C_2 symmetry conformer of TCP monomer. Both interior and exterior binding motifs are shown in figure 8.6b, with the latter more stable by 5.73 kJ/mol. The splitting between the symmetric and antisymmetric OH stretch fundamentals in the experimental spectrum

is 69 cm^{-1} in the ground state. The calculated splitting for the interior (67 cm^{-1}) and exterior minima (78 cm^{-1}), also point to the interior structure as that observed experimentally.

In both the ground state and excited state spectra, the antisymmetric stretch region has several transitions, reminiscent of the spectrum of benzene-$(H_2O)_1$ shown above it. In the case of benzene-$(H_2O)_1$ these extra transitions were ascribed to the nearly free internal rotation and torsional tumbling motion of the H_2O on the surface of the benzene ring. For TCP-$(H_2O)_1$, the splitting between the these transition is significantly less, with the smallest splitting in the ground state spectrum being 4 cm^{-1}. Possible sources of these extra transitions are considered further in the Discussion section.

The observed ground state splitting changes in the excited state to approximately 9 cm^{-1}. In the excited spectrum, the symmetric and antisymmetric stretch vibrations are red shifted by -15 and -23 cm^{-1} respectively. The shifts of the OH stretch fundamentals to lower frequency upon electronic excitation, coupled with the red-shifted S_0-S_1 origin of TCP-$(H_2O)_1$, support a higher binding energy of water to the electronically excited state of TCP.

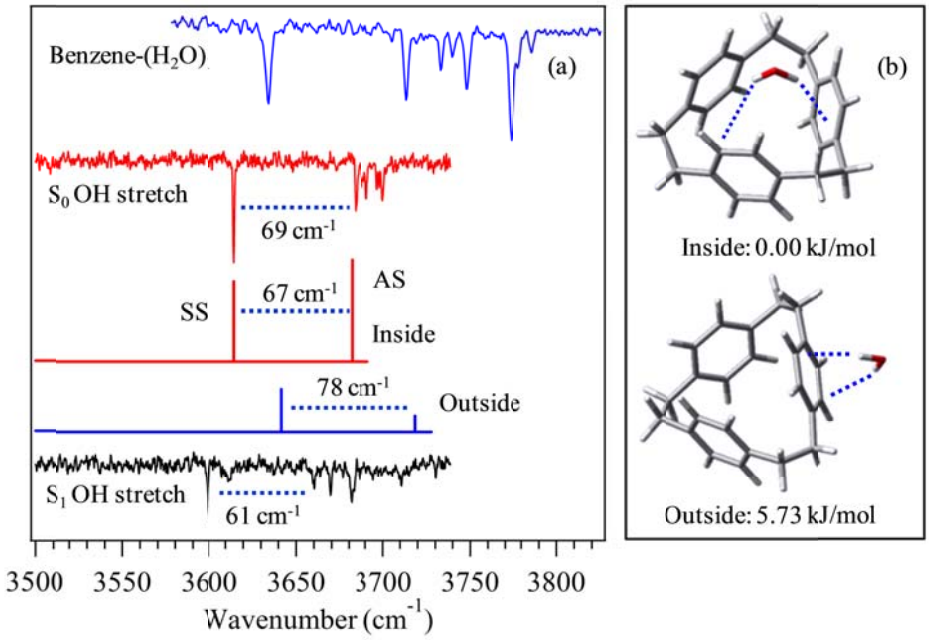

Figure 8.6 (a) The experimental ground and excited state OH stretch spectra for TCP-$(H_2O)_1$ and (b) the two calculated structures with the water bound to the interior and the exterior of TCP.

The experimental S_0 and S_1 OH stretch spectra for the TCP-$(H_2O)_2$ cluster are presented in figure 8.7a. Four OH stretch fundamentals are observed, as anticipated for the n=2 cluster. The lowest frequency of these occurs at 3475 cm^{-1}, a frequency low enough that it can only be accounted for as a H_2O-H_2O H-bond. On this basis alone, certain TCP-$(H_2O)_2$ structures, such as those with one water interior and one exterior to the binding pocket, or with two water molecules approaching the two sides of the TCP binding pocket, can be excluded. Two different interior-binding water dimer structures are shown in figure 8.7b. These structures differ in the way which the second water molecule binds to TCP-$(H_2O)_1$, either acting as a hydrogen bond acceptor or as a donor to the first water molecule. The structure where the second water molecule acts as a donor

was determined to be the global minimum, with the acceptor structure predicted to be 15.6 kJ/mol less stable. In what follows, we employ a nomenclature in which each water molecule is labeled by the H-bonds in which it is involved, with a capital letter (D or A) indicating donor or acceptor to another water molecule, and small letter (d) for a π H-bond to TCP. Thus, the global minimum structure is Add/D, while the 15.6 kJ/mol structure is Dd/A.

In the experimental spectrum, the two center-frequency transitions are due to two π hydrogen bonds to the TCP pocket, separated by 70 cm^{-1}, similar to that in TCP-$(H_2O)_1$, but shifted down in frequency by approximately 32 cm^{-1}. There is a single free OH stretch transition occurring at 3712 cm^{-1} and a cooperatively strengthened hydrogen bonded OH stretch at 3475 cm^{-1}. Comparison of the two calculated spectra with experiment point clearly to the D/Add structure as that observed.

Comparison of the excited state OH stretch spectrum with its ground state counterpart shows clearly how the water molecules respond to electronic excitation of the TCP binding pocket. Note that both π hydrogen bonded OH stretch fundamentals are shifted down in frequency by -23 cm^{-1}. This confirms our assignment of the middle two transitions in the ground state TCP-$(H_2O)_2$ OH stretch spectrum to the TCP-bound water. Interestingly, the magnitude of shift (-23 cm^{-1} compared to -15 cm^{-1} in TCP-H_2O) indicates that the water molecule that is bound to the TCP pocket in TCP-$(H_2O)_2$ interacts more strongly with TCP than in TCP-$(H_2O)_1$.

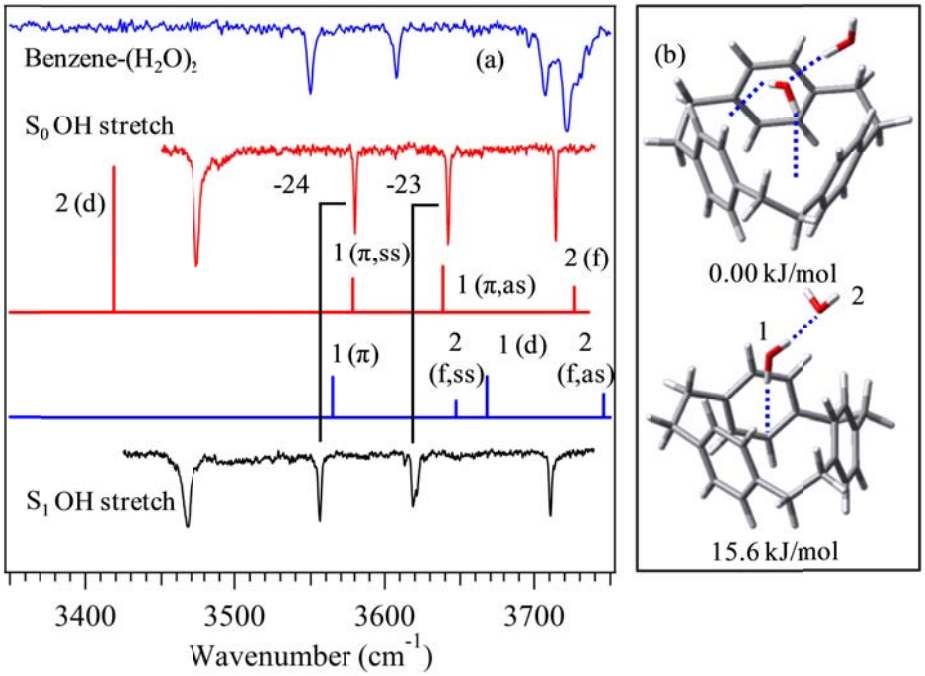

Figure 8.7 (a) The ground and excited state infrared spectrum compared to benzene-$(H_2O)_2$ and calculated vibrational frequencies presented as stick spectra.

The RIDIR spectra for the two conformations of TCP-$(H2O)_3$ are shown as red traces in Figure 8a. The two spectra are very similar, as anticipated based on their near-identical IRUV spectra (figure 8.5b). Both conformations have a single π hydrogen bond at approximately 3634 cm^{-1}, reminiscent of the benzene-$(H2O)_3$ spectrum shown as the top trace (in blue) in Figure 8a. Figure 8b shows three low-energy structures of TCP-$(H2O)_3$, two of which incorporate a cyclic water trimer, with H-bonds in clockwise (CW) and counter clockwise (CCW) directions when viewed from above. The third structure contains a chain of water molecules that extends the motif in TCP-$(H2O)_{1,2}$ by addition of a third water on the chain. The stick spectra (chain top) and cycles (below) are to be compared with experiment. Interestingly, the calculated spectra of cycle and chain are

similar in appearance to one another, and one must look to more subtle features to distinguish between them. First, the experimental spectra of TCP-$(H2O)_3$ are very similar in appearance to that of benzene-$(H2O)_3$, which is due to a H-bonded cycle. Second, the splitting between the transitions at 3641 and 3557cm^{-1} (84 cm^{-1}) is too large to be assigned to a double-donor H2O like that in the chain structure, which has splittings of 69 and 62 cm^{-1} in TCP-$(H2O)_{1,2}$. Third, the presence of two nearly isoenergetic isomers is most easily accounted for via the CW and CCW cycles. Finally, the fragmentation and electronic frequency shifts in the UV spectra of TCP-$(H2O)_3$ point to a structural rearrangement to the cycle that begins at n=3.

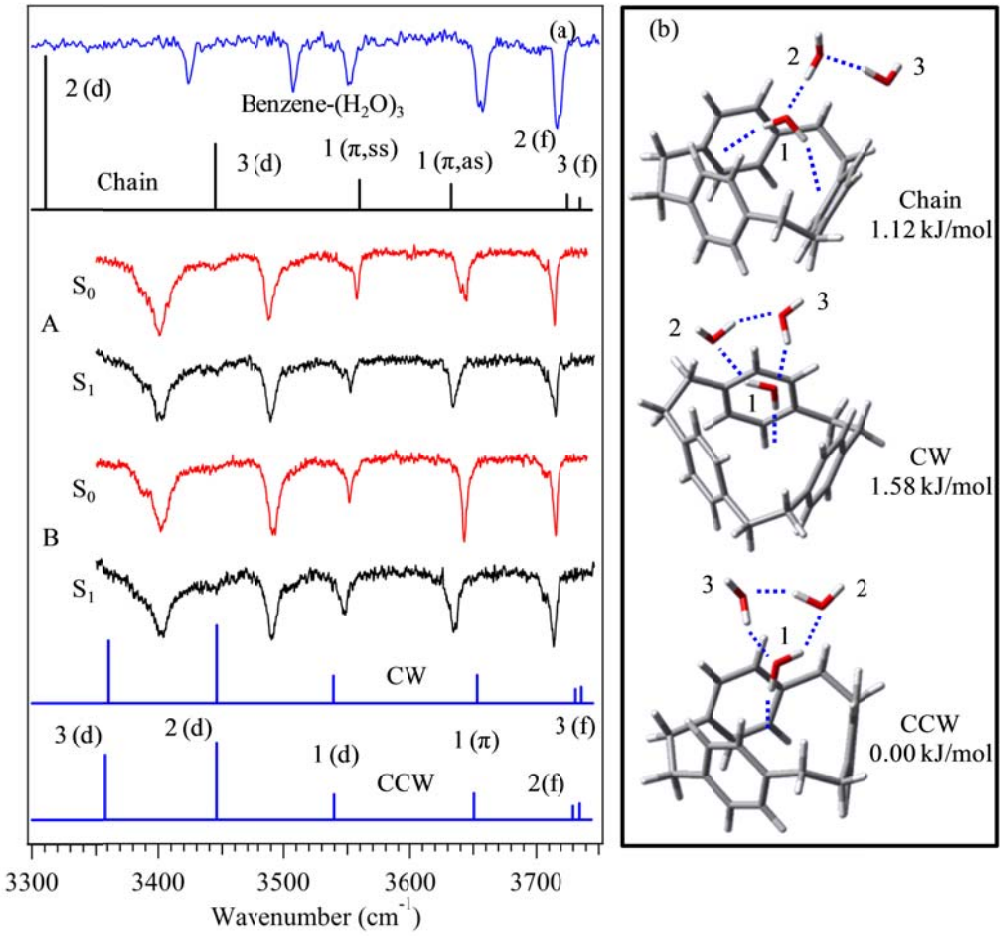

Figure 8.8 (a) Experimental S_0 and S_1 infrared spectra in the OH stretch region of the spectrum of TCP-$(H_2O)_3$ and (b) the structures associated with a chain and cycle water networks.

Figures 8.9 and 8.10 present the OH stretch spectra and best-fit structures for the TCP-$(H_2O)_4$ and TCP-$(H_2O)_5$ clusters, respectively. These clusters incorporate tetramer or pentamer H-bonded water cycles, respectively, with H-bonded OH stretch transitions that mirror those in benzene-$(H_2O)_{4,5}$ in significant detail. Figure 8.9b contains four predicted structures for TCP-$(H_2O)_4$, two CW and two CCW water cycle structures. In both CW and CCW structures, water #3 (see the figure for numbering) is interacting

principally with a single phenyl ring, and points its free OH group either up or down with respect to the phenyl ring. Although we are unable to definitively assign the TCP-$(H_2O)_4$ spectrum to a particular CW or CCW structure, evidence supports a structure pointing the hydrogen atom associated with water molecule #3 (see the numbering in the figure) away from the phenyl ring, nominally 'up'. In so doing, the water network increases its interaction with TCP, gaining CH···O interactions from all three water molecules (#2/#4) not engaged in the principle □ H-bond with the interior, thereby increasing the over-all strength of binding of the water tetramer cycle to TCP. This increased binding may contribute to the lack of fragmentation of TCP-$(H_2O)_4$ following photoionization.

The TCP-$(H_2O)_5$ spectrum shown in figure 8.10 is perhaps the most interesting of the water cycle structures. While its H-bonded OH stretch region is remarkably similar to the benzene-$(H_2O)_5$ OH stretch spectrum, its spectrum in the free/π-bound region is significantly more complicated. Much like benzene-$(H_2O)_5$ there is a π hydrogen bond to the center of TCP, with its OH stretch fundamental at 3639cm^{-1}, a value close to that in TCP-$(H_2O)_{3,4}$ and in benzene-$(H_2O)_{3\text{-}5}$. The free OH stretch transitions appear as a closely-spaced doublet with a 2:1 intensity ratio, consistent with the presence of three free OH stretches in two different local environments (#2/#4 and #3). Most intriguing, the OH stretch fundamental at 3676 cm^{-1} is two low in frequency to be a free OH stretch, serving as a signature that the water pentamer cycle is able to wrap around the TCP cage and interact a second free OH with the outside of one of the phenyl rings. In this sense, the pentamer cycle is "spilling out" of the TCP binding pocket, and is thereby capable of forming one weak and one strong π H-bond with the two faces of the same phenyl ring, as the structures in figure 8.10b show.

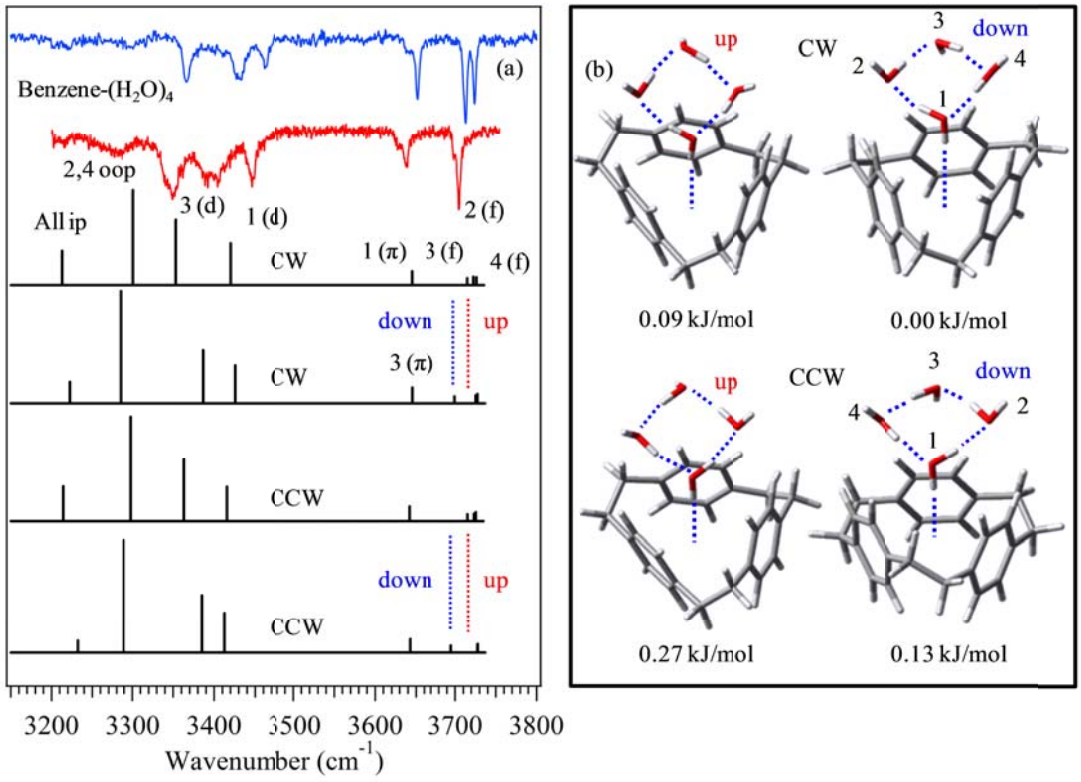

Figure 8.9 (a) Experimental S0 and S1 infrared spectra in the OH stretch region of the spectrum of TCP-(H2O)5 and (b) the structures associated with a chain and cycle water networks. The notation, ip and oop denote in-phase and out-of-phase stretch combinations.

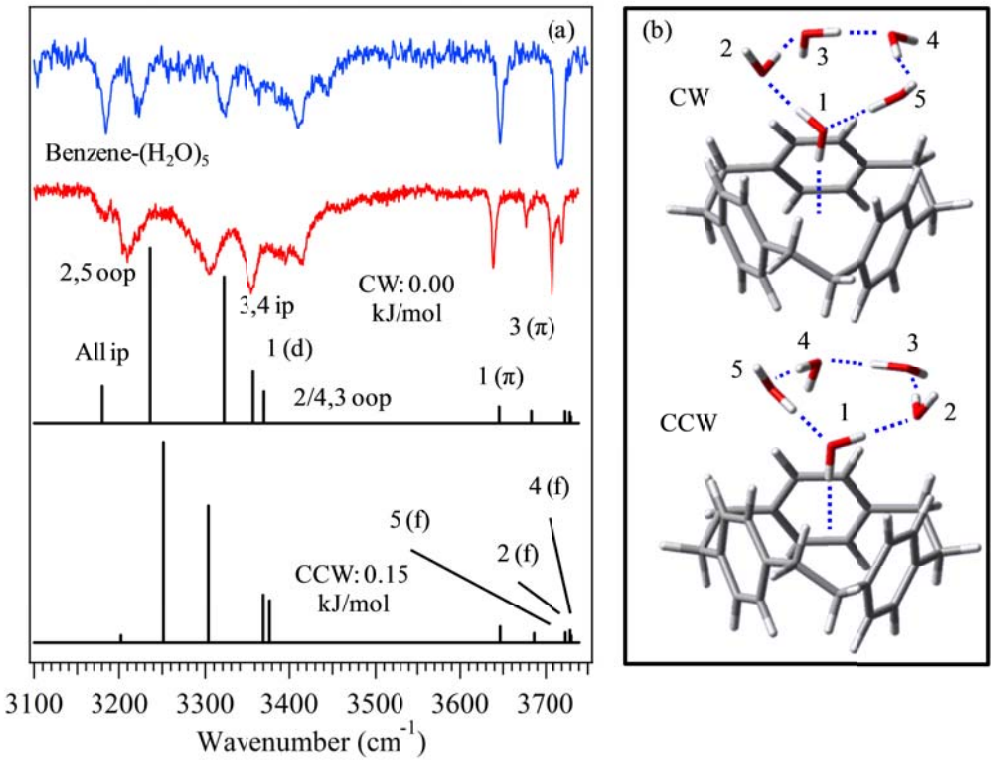

Figure 8.10 (a) Experimental S0 and S1 infrared spectra in the OH stretch region of the spectrum of TCP-(H2O)5 and (b) the structures associated with a chain and cycle water networks

8.3 Discussion

8.3.1 Binding the First H_2O Molecule to the TCP Pocket

One of primary motivations of the present study is to understand how H_2O binds to the electron-rich, hydrophobic pocket of TCP. The first most important binding is by a single H_2O molecule. As figure 8.6(b) shows, the H_2O molecule sits near the pseudo 3-fold symmetry axis of TCP, atop the pocket, with its O-atom 2.93 Å above the center-of-mass of the TCP monomer, donating both its OH groups to the interior of the pocket.

The interior of the TCP pocket must be a bit too small and/or too electron rich to accommodate the H_2O molecule taking up residence completely inside the pocket. The calculated binding energy for TCP-(H_2O) is 20.6 kJ/mol at the ωB97XD/6-311+g(d,p) level of theory, after correction for basis-set superposition error BSSE. This is 8.8 kJ/mol greater than the benzene-H_2O binding calculated at the same level of theory.

The side-on approach of the H_2O molecule to the entire TCP binding pocket means that its interaction with any one of the three phenyl rings is quite different from that in benzene-H_2O, in which the water molecule's vibrationally-averaged position is on the six-fold axis of benzene, with the two hydrogens pointing (nominally) towards the phenyl ring in forming π H-bonds. It is worth noting that the atop site is reminiscent of what is anticipated for the best way for H_2O to interact with the interior of carbon nanotubes, in which H_2O is thought to prefer a position near the nanotube axis, with its hydrogens pointing toward the nanotube walls.

As Pribble et al. described in some detail,[30] one of the most striking aspects of the structure of benzene-H_2O is the large-amplitude motion the H_2O molecule even at its zero-point level. As the top trace of figure8. 6(a) shows, this "tumbling" of the H_2O molecule on the π cloud of benzene produces an OH stretch infrared spectrum with transitions that reflect this tumbling in dramatic fashion. The H_2O molecule undergoes nearly free internal rotation about the six-fold axis of benzene (angle ϕ), with m=0 (Σ) and m= ±1 (Π) levels that correlate with para and ortho modifications of H_2O. The different nuclear spin statistics prevents cooling between these levels, thereby producing an OH stretch infrared spectrum that reflects transitions out of both Σ and Π internal rotor levels. In addition, the water molecule undergoes LAM in the plane of the H_2O

molecule, along its torsional angle ρ in a double-minimum potential well that exchanges which H is pointing towards the π cloud. In so doing, the ρ dependence of the dipole moment, produces combination bands involving the OH stretch/torsion that are nearly as intense as the OH stretch fundamentals themselves. Analysis of the observed infrared transitions provided the shape of the ρ-dependent potential.

The OH stretch region of TCP-H_2O reflects the preference for double over single donation into the binding pocket in the frequencies of the (nominally) symmetric and antisymmetric stretch fundamentals (3615 cm^{-1} and 3684 cm^{-1}, respectively). As figure 8.6 shows, the symmetric stretch is shifted down by -16 cm^{-1} from its value in benzene-H_2O, and -42 cm^{-1} relative to the free H_2O monomer. The 69 cm^{-1} splitting between SS and AS is 30% less than that in H_2O monomer (3657 / 3756 cm^{-1}). This reduction in splitting is observed in other circumstances in which the H_2O molecule engages both its OH groups in H-bonds (e.g., crown ethers, carboxylate anion). This reduction in splitting is typically associated with a reduction in the bond angle for H_2O, which leads to smaller inter-bond coupling as the angle approaches perpendicular. According to the ωB97X-D calculations, TCP-H_2O has a bond angle of 102.5°, compared to 105.2° for the H_2O monomer.

What is perhaps most striking about the OH stretch spectrum of TCP-H_2O is the presence of a set of five transitions in the (nominally) AS region, with frequencies of 3614.6, 3683.8, 3687.8, 3690.8, 3696.7, and 3700.0 cm^{-1}. In many ways, this set of transitions looks like a compressed version of the set of transitions observed in benzene-H_2O, suggesting that large-amplitude motion and tumbling of the H_2O molecule in the TCP pocket may be responsible for them.

Two limiting-case scenarios need to be considered. First, the extra transitions in the AS region may result from the presence of unresolved isomers. According to the calculations, the H_2O molecule prefers to line up along the C_2 symmetry axis of the ud/ud/du conformer of TCP (figure 1a). In this orientation, one OH group points toward the center of the 'base' phenyl ring, while the other OH points mid-way between the two 'side' phenyl rings. There should be two other nearly degenerate orientations for the H_2O molecule, placed $\pm 120^o$ from this position. If the potential energy surface supports minima at each of these orientations, with barriers separating them that prevent cooling between them on the time-scale of the expansion, then the R2PI spectrum could contain contributions from all three. If the electronic frequency shifts between them are small, the R2PI wavelength used for recording the RIDIR spectrum would contain contributions from all three. If the AS fundamentals of each isomer are slightly different, they would give rise to the observed structure.

In order to test this possibility, we carried out IR-UV holeburning scans sitting with the IR holeburn laser on different members of the set of transitions in the AS region. No clear shifts in the R2PI spectrum were observed. Furthermore, the presence and stability of minima at the other orientations in the binding pocket is hard to establish clearly, varying with the level of theory used.

In the opposite limit of free internal rotation in the pocket, the spectrum of TCP-H_2O should be qualitatively similar to that of benzene-H_2O, with transitions spread over a much wider range of frequencies than observed experimentally.

The actual potential energy surface in which the water molecule moves is likely to be somewhere between these high barrier and free limits It is likely, then, that the

corrugation and asymmetry in the potential energy surface for large-amplitude motion of the H_2O molecule in the TCP binding pocket is more restricted than that in benzene-H_2O. Nevertheless, if the H_2O molecule can undergo internal rotation and tumbling motion that leads to ortho/para H_2O levels between which cooling cannot occur, this would still be reflected in the presence of a series of OH stretch/torsion combination bands. The question is whether the frequency spread, splittings, and intensity patterns can be accounted for with potentials that are reasonable.

We take here a first step towards providing such a model. The anti-symmetric OH stretch region of TCP-$(H_2O)_1$ was simulated by confining the water molecule to a 1-D torsional potential in both the ground and excited vibrational states and solving the hindered rotor Schrödinger equation

$$H\psi_v = \left[-\beta \frac{\partial^2}{\partial \phi^2} + V(\phi) \right] \psi_v = E\psi_v \qquad (1)$$

The rotation of the water molecule is assumed to be nearly coaxial with TCP in a nominally six-fold barrier, with the internal rotation constant taken as the 'b' inertial axis of free H_2O, β=16 cm^{-1}.[30] The torsional potential was therefore approximated as a symmetric periodic potential with a truncated Fourier series containing elements from ($V_{n = 2, 4, 6}$) to account for the two-fold and nearly three-fold symmetry of H_2O and TCP, respectively.

$$V(\phi) = \frac{1}{2} \sum_{n}^{6} V_n (1 - \cos\, n\phi) \qquad (2)$$

The eigenvalues and eigenvectors were determined variationally by diagonalizing the Hamiltonian for internal rotation with a basis of 50 expanded cosine/sine free rotor wavefunctions as outlined by Laane.[42]

$$\Psi_v = \sum_{m=1}^{N} c_{vm}\psi_m \tag{3}$$

Intensities were determined by calculating the integral

$$I_{v,v'} = \left|\langle \psi_v(\phi)|\cos\phi|\psi_{v'}(\phi)\rangle\right|^2 + \left|\langle \psi_v(\phi)|\sin\phi|\psi_{v'}(\phi)\rangle\right|^2 \tag{4}$$

assuming the electric field vector is parallel to the z-axis of the TCP-$(H_2O)_1$ complex.

Given the lack of collisional cooling between the lowest *ortho* and *para* nuclear spin states of H_2O, the calculated intensities were weighted by the nuclear spin statistical weights for transition originating from the *ortho* (m = 1, I_H = 3) and *para* (m = 0, I_H = 1) levels in the ground vibrational state. Figure 8.11 provides a theoretical prediction that matches experiment reasonably well in terms of the over-all number and approximate spacing of the transitions. No attempt was made to fit the periodic potential via minimizing the least-squares between the relative experimental frequencies and the calculated eigenvalues, since the goal was to see whether such a simple model could qualitatively account for experiment.

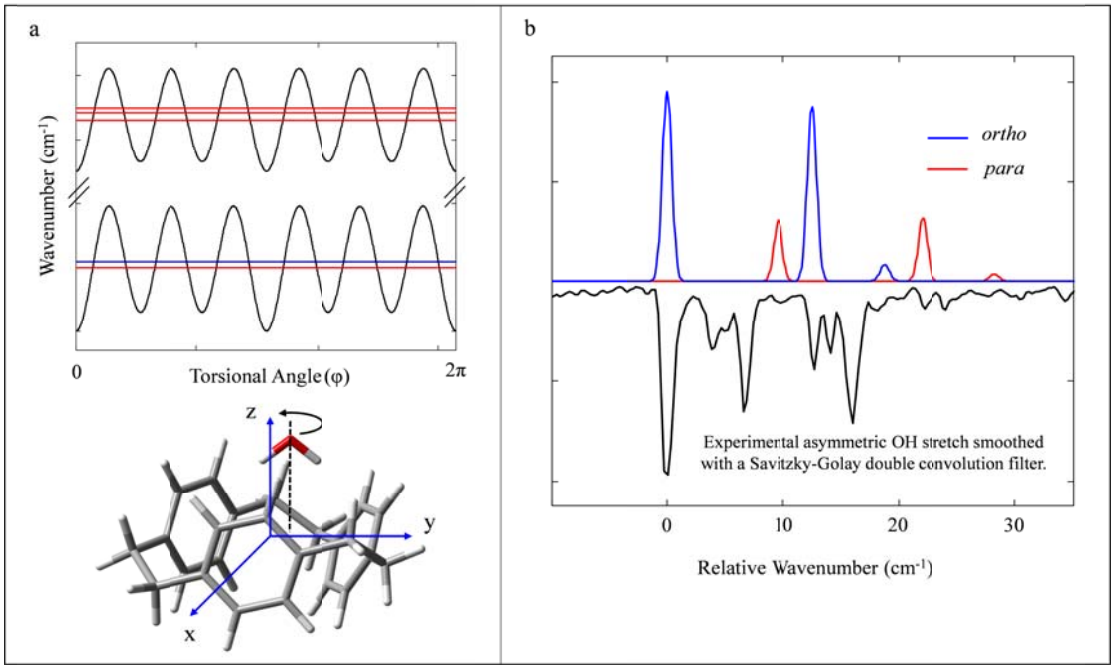

Figure 8.11 (a) The torsional potential for the vibrational ground and v=1 excited state and the structure of TCP-$(H_2O)_1$ defining the coordinate axis. The barriers to rotation in the potential were produced with $V_2 = 20$, $V_4 = 20$, $V_6 = 175$ for the ground state and $V_2 = 10$, $V_4 = 10$, and $V_6 = 150$ in the v=1 excited state. All units are in cm^{-1}. (b) The simulated spectrum originating from the *ortho* (blue) and *para* (red) states compared to the experimental spectrum in the anti-symmetric OH stretch region smoothed by a four point, double convolution Savitzky-Golay filter.

Figure 8.11a presents the torsional potentials used to provide the predictions in figure 8.11b, with $V_2 = 20/10$, $V_4 = 20/10$, and $V_6 = 175/150$ cm^{-1} for the ground/excited vibrational states. The six-fold barrier to rotation reflects the overall symmetry to hindered rotation of the water molecule inside the aromatic rich TCP pocket. The structure presented in figure 8.11a depicts this symmetry, with the z-axis containing a near three-fold rotation axis for TCP and a two-fold axis of rotation for water. It is worth noting that, in this simple model, the center-of-mass of the complex is set at the origin, and the oxygen atom of H_2O is also placed along this axis, so that internal rotation

involves only motion of the hydrogens of H_2O. The y-axis contains the C_2 symmetry axis of the TCP monomer, giving rise to the V_2 and V_4 terms and the two degenerate minima on the potential energy surface. Despite the magnitude of the V_6 terms in the potentials, the barriers to rotation are only a small fraction (<10%) of the calculated BSSE corrected binding energy for the cluster, which is calculated to be 2057 cm^{-1} (20.6 kJ/mol). Overall, the model reproduces the six transitions observed experimentally with only minor discrepancies in the relative frequencies. The intensities are not as well reproduced, probably pointing to the need for further refinement of the model, which is, after all, only a one-dimensional model. For instance, it is likely that the actual hindered rotor pathway incorporates some heavy atom motion as well, since the global minimum structure for TCP-H_2O predicts that the O-atom is off the (near) 3-fold axis of TCP.

There is a substantial opportunity for further theoretical effort in seeking a quantitatively accurate potential energy surface for H_2O molecule's motion in the TCP pocket, and then modeling the OH stretch spectrum that would arise. From an experimental stand-point, analogous studies of TCP-HOD and TCP-D_2O would be helpful in providing further constraints on the potential energy surface.

8.3.2 Perturbations Imposed on Water Clusters by TCP

Having established the mode of binding of the first H_2O molecule to TCP, we consider here in more detail the structures and mode of binding of water clusters containing 2-5 water molecules in order to better understand the development with cluster size of the interaction with TCP. Figure 8.11 presents an overview of the ground state RIDIR spectra for the entire set of clusters, comparing them with that of liquid H_2O at

room temperature. A major deduction of the present work is that water clusters varying from dimer to pentamer all take up H-bonding architectures that are the same ones preferred by pure water clusters in the absence of the TCP solute. It is noteworthy and intriguing that the frequency range subtended by the TCP-$(H_2O)_n$ spectra approach the full range present in liquid H_2O already with n=5. Since there is a strong correlation between OH stretch frequency and H-bond distance and strength,[43] one can anticipate on this basis that the H-bonded networks present in these small water clusters have H-bond strengths that are similar to the best environments present in the liquid.

In TCP-$(H_2O)_2$ (Figure 8.5b), the water molecule bound to TCP acts as the acceptor H_2O in the water dimer, while the second water acts as single-donor to the first. This is not surprising in the sense that one anticipates water-water binding to be stronger than the interaction of a second water molecule with another site on the TCP (presumably exterior to the pocket).

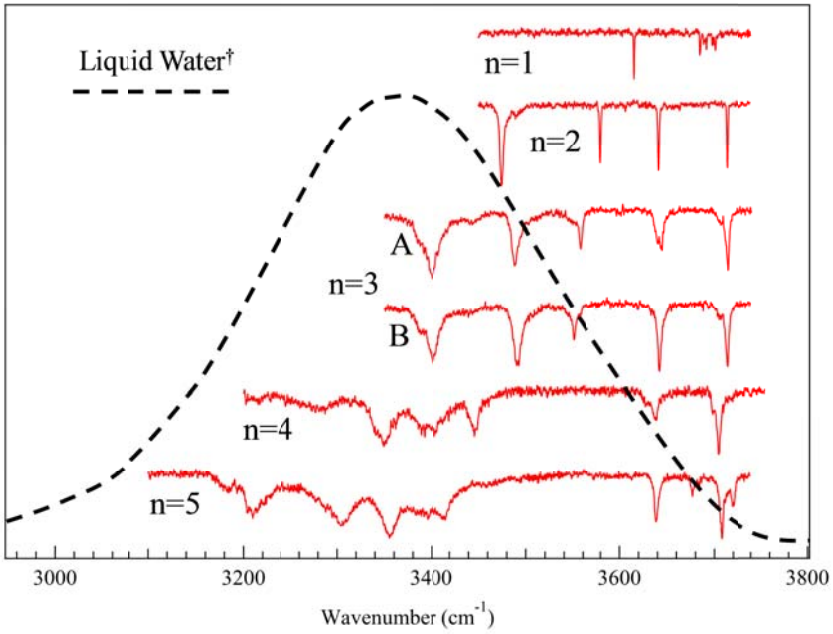

Figure 8.12 Comparison of the OH stretch infrared spectrum of TCP-$(H_2O)_n$, n=1-5 with the spectrum of liquid water at room temperature, adapted from reference 43.[44]

The comparison of the OH stretch spectrum of TCP-$(H_2O)_2$ with that of benzene-$(H_2O)_2$ shown in figure 8.5a is also instructive in establishing the changes in the water dimer induced by the aromatic-rich pocket of TCP. While the pattern of IR transitions is similar in benzene-$(H_2O)_2$ and TCP-$(H_2O)_2$, the OH stretch fundamentals associated with the TCP-bound dimer are shifted systematically to lower frequency, both for the OH···O H-bond (3550 cm^{-1}→3475 cm^{-1}) and for the aromatic-bound OH's (3608/3708 → 3580/3641). Similar frequency shifts are observed in the TCP-bound water fundamentals relative to TCP-H_2O (3615/3684). These frequency shifts reflect a cooperative strengthening of the water-water and TCP-water H-bonds in each other's presence.

In TCP-$(H_2O)_n$, n=3-5, the water clusters take up cyclic structures (figures 8.7-8.9), necessitating a re-orientation of the principal TCP-bound water from double

donation to TCP to single donation as the other OH is incorporated into the H-bonded water cycle. That this should occur in TCP-$(H_2O)_3$ is not obvious, given the weak H-bonds present in the trimer cycle. In fact, calculations predict that the TCP-$(H_2O)_3$ chain is nearly isoenergetic with the cycle (figure 8.6b). Given this fact, the exclusive presence of the cycle in TCP-$(H_2O)_3$ could point to a cluster formation mechanism in which the water trimer cycle is formed first and binds to TCP as a final step.

In many ways, the perturbations imposed on the water cycles by TCP are similar to those present in benzene-$(H_2O)_{3\text{-}5}$. The spectra of the free water cycles have just two types: free (F) and H-bonded. The H-bonded OH stretch transitions decrease in frequency as the cycle increases in size from n=3-5, leading to a widening gap between the free and H-bonded OH stretch fundamentals. In benzene-$(H_2O)_n$ and TCP-$(H_2O)_n$, one of the free OH stretch transitions is engaged in a π H-bond, which in TCP is really an interaction with the interior of all three phenyl rings. The frequency of this π OH is near 3640 cm^{-1} in n=3-5, about 10 cm^{-1} below the π OH to benzene.

Given the n-fold symmetry of $(H_2O)_n$ cycles, the H-bonded OH stretch transitions spread over a range dictated by the strength of coupling between them. Depending on the relative phases of oscillation of the OH groups, some of the H-bonded OH stretch fundamentals are dipole-forbidden. In the presence of TCP, this symmetry is broken, with the π-bound water now engaged in two H-bonds as a double donor, which weakens its $OH^{\cdots}O$ H-bond relative to that in the free water clusters. This structural distortion partially localizes the H-bonded OH stretch transitions, turning on intensity in the full set of IR fundamentals, and increasing the range of frequencies subtended. According to the calculations, the highest frequency H-bonded OH stretch fundamental is due to the π-

bound H_2O. The shortest H-bond and lowest frequency OH stretch is that due to the OH donating to the π-bound water.

The comparison between the spectra of benzene-$(H_2O)_{3-5}$ and TCP-$(H_2O)_{3-5}$ in Figures 8.7-8.9 show a remarkably close resemblance in the H-bonded OH stretch region. Indeed, one can surmise on this basis that neither the difference in strength of the π H-bond nor the structural differences between the two binding sites produce a significant change in the H-bonded OH stretch modes.

Secondary interactions of the water cycles with TCP occur through the other water molecules not involved in the interior π bond. In the n=3 and 4 clusters, these other water molecules in the cycle orient their O-atoms so that they can gain additional stabilization from interactions with the CH groups on one of the phenyl rings in the TCP 'wall', thus beginning to spill out of the pocket interior. The pentamer cycle is large enough that, when it binds to TCP, the cycle can reshape so as to fold over the top of one phenyl ring, maintaining the strong interior π bond, but also accommodating a weaker second π bond between the free OH group on W3 and the exterior of one of the rings. This secondary π interaction is clearly observed as a weak band at 3677 cm^{-1}. Even the free OH groups now split into two resolved groups with a ~2:1 intensity ratio, suggesting that the more intense transition is an unresolved pair of bands. Thus, TCP presents an aromatic-rich template around which the water pentamer can distort to maximize its interaction with the π clouds of the phenyl rings.

8.3.3 Effect of Electronic Excitation on the TCP-$(H_2O)_n$ Interactions

The present data set also affords a look at the effects of electronic excitation of this model aromatic-rich pocket on the binding of water molecule(s) to it. The electronic frequency shifts of the S_0-S_1 origins of TCP-$(H_2O)_n$ relative to the TCP monomer are first to the red (-65 cm^{-1} for n=1, -113 cm^{-1} for n=2) and then back towards the monomer origin for n=3 (-30cm^{-1}) and n=4,5 (approximately -80cm^{-1}). The clear break in trend between n=2 and n=3 clearly reflects the shift from double donation to single-donation to the interior of the TCP pocket. At the same time, it is important to note that these red-shifts are opposite in direction to those observed in benzene-$(H_2O)_n$ clusters. The interpretation of these shifts is complicated by the presence of three excited states in close proximity. The uncoupled excited state energies of the three phenyl rings and the degree of localization/delocalization of the electronic excitation among them can change with the strength and asymmetry of the interaction of the water molecule(s) with the three rings. Theoretical modeling of the excited states and vibronic coupling in TCP is still needed in order to guide our understanding of the vibronic spectroscopy, and may open the way for a more thorough understanding of the effects of the water clusters on TCP excited states.

The response of the water molecule(s) to electronic excitation is clearly observed in the comparison of ground state and excited state RIDIR spectra in the OH stretch region for n=1-3 (figures 8.4, 8.6, 8.7). Several deductions can be drawn from these spectra. First, as we have already observed in Sec. III, the OH group(s) bound to the pocket of TCP shift to lower frequency when TCP is electronically excited, indicating a strengthening of the OH group's π H-bonds upon electronic excitation. Second, for n=1

and 2, both SS and AS of the π-bound H_2O shift to lower frequency by similar amounts in the excited state, confirming that the π-bound H_2O uses both its OH groups in binding to the TCP pocket, and that this binding is larger in the excited state than ground state. Third, the magnitude of these shifts is mode-selective. In TCP-$(H_2O)_2$, the Add H_2O has SS and AS fundamentals that shift by -24 and -23 cm^{-1} reflecting their direct binding to the pocket, while the free and H-bonded OH stretch transitions of W2 are -8 and -4 cm^{-1}, consistent with their shifts being a secondary response to the π-bond water. In TCP-$(H_2O)_3$, only the transitions ascribable to the π–bound water shift measurably, with the other two water molecules in the trimer cycle largely unaffected. Finally, electronic excitation has a surprisingly large effect on the complex set of transitions that appears in the AS region of the TCP-(H_2O) complex (figure 8.4). Besides a shift to lower frequency, the set of five or six transitions that appear in this region in the ground state now resolve into a more widely-spaced triplet of transitions. The possible reasons for these changes are discussed further in supplementary material.

Having seen these effects in TCP-$(H_2O)_n$ clusters, it is worth speculating on their potential relationship to analogous processes in water's interactions with carbon nanotubes. If a single water molecule or water chain were to undergo a similar response to electronic excitation in a carbon nanotube, it would suggest that photoexcitation could be used to draw H_2O from the opening of the tube into the tube interior.

8.4 Conclusions

TCP-$(H_2O)_n$ clusters with n=1-5 have provided new molecular-scale insight to the way in which water binds to a model aromatic-rich binding pocket, and how this binding evolves with water cluster size. Not surprisingly, the principle mode of interaction is with a single water molecule, either double-donating (in n=1,2) or singly donating (n=3-5) into the pocket, but sitting atop the pocket rather than fully inserted within it. The water clusters retain the same H-bonded networks as are preferred in the absence of TCP, but the presence of TCP changes the strengths and perturbs the symmetry of the clusters, as reflected in intimate detail by the OH stretch region of the infrared. Notably, in the largest water cluster studied, the water pentamer, clear evidence is presented that the pentamer spills out of the interior of the pocket, wrapping its way around one of the phenyl rings and forming a second π H-bond with its exterior.

As so often occurs in modern spectroscopy, a full understanding of the electronic and infrared spectra will require moving beyond a static picture of these structures to consider a number of interesting dynamical issues. The vibrational dynamics of water's motion in this aromatic-rich pocket appear in the complex set of transitions observed in the TCP-H_2O infrared spectrum, which change dramatically with electronic excitation. Vibronic coupling involving the three close-lying excited states of TCP awaits theoretical modeling, as does the perturbations imposed on these states by water molecule(s) bound to it. Finally, it would be interesting to extend studies of this type to aromatic scaffolds that mimic in an even more direct way the shape and electronic structure of a carbon nanotube.

8.5 References

1. Shen, T. L.; Jackson, J. E.; Yeh, J. H.; Nocera, D. G.; Leroi, G. E. Flourescence Excitation Spectroscopy of [2,2]Paracyclophane in Supersonic Jets. *Chem. Phys. Lett.* **1992,** *191* (1-2), 149-156.

2. Lyssenko, K. A.; Antipin, M. Y.; Antonov, D. Y. The transannular interaction in [2.2]paracyclophane: Repulsive or attractive? *ChemPhysChem* **2003,** *4* (8), 817-823.

3. Henseler, D.; Hohlneicher, G. Theoretical study on the molecular distortions in [2.2]paracyclophane and cyclobutane. *J. Phys. Chem. A* **1998,** *102* (52), 10828-10833.

4. Caramori, G. F.; Galembeck, S. E. Computational study about through-bond and through-space interactions in [2.2]cyclophanes. *J. Phys. Chem. A* **2007,** *111* (9), 1705-1712.

5. Buchanan, E. G.; Dean, J. C.; Zwier, T. S.; Sibert, E. L., III. Towards a first-principles model of Fermi resonance in the alkyl CH stretch region: Application to 1,2-diphenylethane and 2,2,2-paracyclophane. *Journal of Chemical Physics* **2013,** *138* (6).

6. Scholes, G. D. Long-range resonance energy transfer in molecular systems. *Annual Review of Physical Chemistry* **2003,** *54*, 57-87.

7. Stearns, J. A.; Pillsbury, N. R.; Douglass, K. O.; Mueller, C. W.; Zwier, T. S.; Plusquellic, D. F. Rotationally resolved studies of S-0 and the exciton coupled S-1/S-2 origin regions of diphenylmethane and the d(12) isotopologue. *Journal of Chemical Physics* **2008,** *129* (22).

8. Pillsbury, N. R.; Stearns, J. A.; Muller, C. W.; Plusquellic, D. F.; Zwier, T. S. State-specific studies of internal mixing in a prototypical flexible bichromophore: Diphenylmethane. *Journal of Chemical Physics* **2008,** *129* (11), 114301.

9. Pillsbury, N. R.; Muller, C. W.; Meerts, W. L.; Plusquellic, D. F.; Zwier, T. S. Conformational Effects on Excitonic Interactions in a Prototypical H-Bonded Bichromophore: Bis(2-hydroxyphenyl)methane. *J. Phys. Chem. A* **2009,** *113* (17), 5000-5012.

10. Rodrigo, C. P.; Mueller, C. W.; Pillsbury, N. R.; James, W. H., III; Plusquellic, D. F.; Zwier, T. S. Conformer-specific vibronic spectroscopy and vibronic coupling in a flexible bichromophore: Bis-(4-hydroxyphenyl)methane. *Journal of Chemical Physics* **2011,** *134* (16).

11. Buchanan, E. G.; Walsh, P. S.; Plusquellic, D. F.; Zwier, T. S. Excitonic splitting and vibronic coupling in 1,2-diphenoxyethane: Conformation-specific effects in the weak coupling limit. *Journal of Chemical Physics* **2013,** *138* (20).

12. Ottiger, P.; Leutwyler, S. Excitonic splitting and coherent electronic energy transfer in the gas-phase benzoic acid dimer. *Journal of Chemical Physics* **2012,** *137* (20).

13. Ottiger, P.; Leutwyler, S.; Koppel, H. S-1/S-2 excitonic splittings and vibronic coupling in the excited state of the jet-cooled 2-aminopyridine dimer. *Journal of Chemical Physics* **2009,** *131* (20).

14. Kopec, S.; Ottiger, P.; Leutwyler, S.; Koeppel, H. Vibrational quenching of excitonic splittings in H-bonded molecular dimers: Adiabatic description and effective mode approximation. *Journal of Chemical Physics* **2012,** *137* (18).

15. Nebgen, B.; Emmert, F. L., III; Slipchenko, L. V. Vibronic coupling in asymmetric bichromophores: Theory and application to diphenylmethane. *Journal of Chemical Physics* **2012,** *137* (8).

16. Schon, C.; Roth, W.; Fischer, I.; Pfister, J.; Kaiser, C.; Fink, R. F.; Engels, B. Paracyclophanes as model compounds for strongly interacting pi-systems. Part 1. Pseudo-ortho-dihydroxy 2.2 paracyclophane. *Phys. Chem. Chem. Phys.* **2010,** *12* (32), 9339-9346.

17. Schon, C.; Roth, W.; Fischer, I.; Pfister, J.; Fink, R. F.; Engels, B. Paracyclophanes as model compounds for strongly interacting pi-systems. Part 2: mono-hydroxy 2.2 paracyclophane. *Phys. Chem. Chem. Phys.* **2011,** *13* (23), 11076-11082.

18. Pfister, J.; Schon, C.; Roth, W.; Kaiser, C.; Lambert, C.; Gruss, K.; Braunschweig, H.; Fischer, I.; Fink, R. F.; Engels, B. Paracyclophanes as Model Compounds for Strongly Interacting pi-Systems, Part 3: Influence of the Substitution Pattern on Photoabsorption Properties. *J. Phys. Chem. A* **2011,** *115* (15), 3583-3591.

19. Shubert, V. A.; Muller, C. W.; Zwier, T. S. Water's Role in Reshaping a Macrocycle's Binding Pocket: Infrared and Ultraviolet Spectroscopy of Benzo-15-crown-5-(H2O)(n) and 4 '-aminobenzo-15-crown-5-(H2O)(n), n=1, 2. *J. Phys. Chem. A* **2009,** *113* (28), 8067-8079.

20. Shubert, V. A.; James, W. H., III; Zwier, T. S. Jet-Cooled Electronic and Vibrational Spectroscopy of Crown Ethers: Benzo-15-Crown-5 Ether and 4 '-Amino-Benzo-15-Crown-5 Ether. *J. Phys. Chem. A* **2009,** *113* (28), 8055-8066.

21. Kusaka, R.; Inokuchi, Y.; Ebata, T. Water-mediated conformer optimization in benzo-18-crown-6-ether/water system. *Phys. Chem. Chem. Phys.* **2009,** *11* (40), 9132-9140.

22. Kusaka, R.; Inokuchi, Y.; Ebata, T. Structure of hydrated clusters of dibenzo-18-crown-6-ether in a supersonic jet-encapsulation of water molecules in the crown cavity. *Phys. Chem. Chem. Phys.* **2008,** *10* (41), 6238-6244.

23. Kusaka, R.; Inokuchi, Y.; Ebata, T. Laser spectroscopic study on the conformations and the hydrated structures of benzo-18-crown-6-ether and dibenzo-18-crown-6-ether in supersonic jets. *Phys. Chem. Chem. Phys.* **2007,** *9* (32), 4452-4459.

24. Kokubu, S.; Kusaka, R.; Inokuchi, Y.; Haino, T.; Ebata, T. Laser spectroscopic study on (dibenzo-24-crown-8-ether)-water and -methanol complexes in supersonic jets. *Phys. Chem. Chem. Phys.* **2010,** *12* (14), 3559-3565.

25. Kusaka, R.; Inokuchi, Y.; Xantheas, S. S.; Ebata, T. Structures and Encapsulation Motifs of Functional Molecules Probed by Laser Spectroscopic and Theoretical Methods. *Sensors* **2010,** *10* (4), 3519-3548.

26. Hontama, N.; Inokuchi, Y.; Ebata, T.; Dedonder-Lardeux, C.; Jouvet, C.; Xantheas, S. S. Structure of the Calix 4 arene-(H(2)O) Cluster: The World's Smallest Cup of Water. *J. Phys. Chem. A* **2010,** *114* (9), 2967-2972.

27. Ebata, T.; Hodono, Y.; Ito, T.; Inokuchi, Y. Electronic spectra of jet-cooled calix[4]arene and its van der Waals clusters: Encapsulation of a neutral atom in a molecular bowl. *Journal of Chemical Physics* **2007,** *126* (14).

28. Pribble, R. N.; Zwier, T. S. SIZE-SPECIFIC INFRARED-SPECTRA OF BENZENE-(H2O)(N) CLUSTERS (N=1 THROUGH 7) - EVIDENCE FOR NONCYCLIC (H2O)(N) STRUCTURES. *Science* **1994,** *265* (5168), 75-79.

29. Gruenloh, C. J.; Carney, J. R.; Arrington, C. A.; Zwier, T. S.; Fredericks, S. Y.; Jordan, K. D. Infrared spectrum of a molecular ice cube: The S-4 and D-2d water octamers in benzene-(water)(8). *Science* **1997,** *276* (5319), 1678-1681.

30. Pribble, R. N.; Garrett, A. W.; Haber, K.; Zwier, T. S. Resonant Ion-Dip Infrared-Spectroscopy of Benzene-H2O and Benzene-HOD. *Journal of Chemical Physics* **1995,** *103* (2), 531-544.

31. Iijima, S.; Ichihashi, T. SINGLE-SHELL CARBON NANOTUBES OF 1-NM DIAMETER. *Nature* **1993,** *363* (6430), 603-605.

32. Park, H. G.; Jung, Y. Carbon nanofluidics of rapid water transport for energy applications. *Chem. Soc. Rev.* **2014,** *43* (2), 565-576.

33. Zwier, T. S. Laser probes of conformational isomerization in flexible molecules and complexes. *J. Phys. Chem. A* **2006,** *110* (12), 4133-4150.

34. Zwier, T. S. Laser spectroscopy of jet-cooled biomolecules and their water-containing clusters: Water bridges and molecular conformation. *J. Phys. Chem. A* **2001,** *105* (39), 8827-8839.

35. Mohamadi, F.; Richards, N. G. J.; Guida, W. C.; Liskamp, R.; Lipton, M.; Caufield, C.; Chang, G.; Hendrickson, T.; Still, W. C. Macromodel - an Integrated Software System for Modeling Organic and Bioorganic Molecules Using Molecular Mechanics. *Journal of Computational Chemistry* **1990,** *11* (4), 440-467.

36. Chai, J. D.; Head-Gordon, M. Long-range corrected hybrid density functionals with damped atom-atom dispersion corrections. *Phys. Chem. Chem. Phys.* **2008,** *10* (44), 6615-6620.

37. Gaussian 09, R. A., Frisch, M. J.; Trucks, G. W.; Schlegel, H. B.; Scuseria, G. E.; Robb, M. A.; Cheeseman, J. R.; Scalmani, G.; Barone, V.; Mennucci, B.; Petersson, G. A.; Nakatsuji, H.; Caricato, M.; Li, X.; Hratchian, H. P.; Izmaylov, A. F.; Bloino, J.; Zheng, G.; Sonnenberg, J. L.; Hada, M.; Ehara, M.; Toyota, K.; Fukuda, R.; Hasegawa, J.; Ishida, M.; Nakajima, T.; Honda, Y.; Kitao, O.; Nakai, H.; Vreven, T.; Montgomery, Jr., J. A.; Peralta, J. E.; Ogliaro, F.; Bearpark, M.; Heyd, J. J.; Brothers, E.; Kudin, K. N.; Staroverov, V.N.; Kobayashi, R.; Normand, J.; Raghavachari, K.; Rendell, A.; Burant, J. C.; Iyengar, S. S.; Tomasi, J.; Cossi, M.; Rega, N.; Millam, N. J.; Klene, M.; Knox, J. E.; Cross, J. B.; Bakken, V.; Adamo, C.; Jaramillo, J.; Gomperts, R.; Stratmann, R. E.; Yazyev, O.; Austin, A.J.; Cammi, R.; Pomelli, C.; Ochterski, J. W.; Martin, R. L.; Morokuma, K.; Zakrzewski, V. G.; Voth, G. A.; Salvador, P.; Dannenberg, J. J.; Dapprich, S.; Daniels, A. D.; Farkas, Ö.; Foresman, J. B.; Ortiz, J.V.; Cioslowski, J.; Fox, D. J. Gaussian, Inc., Wallingford CT, 2009.

38. Zhao, Y.; Schultz, N. E.; Truhlar, D. G. Design of density functionals by combining the method of constraint satisfaction with parametrization for thermochemistry, thermochemical kinetics, and noncovalent interactions. *Journal of Chemical Theory and Computation* **2006,** *2* (2), 364-382.

39. Gotch, A. J.; Zwier, T. S. MULTIPHOTON IONIZATION STUDIES OF CLUSTERS OF IMMISCIBLE LIQUIDS .1. C6H6-(H2O)N, N=1,2. *Journal of Chemical Physics* **1992,** *96* (5), 3388-3401.

40. Gord, J. R.; Garrett, A. W.; Bandy, R. E.; Zwier, T. S. REMPI fragmentation as a probe of hydrogen bonding in aromatic-X clusters. *Chem. Phys. Lett.* **1990,** *171* (5-6), 443-450.

41. Gotch, A. J.; Garrett, A. W.; Severance, D. L.; Zwier, T. S. The structure and photophysics of clusters of immiscible liquids: C_6H_6-$(H_2O)_n$. *Chem. Phys. Lett.* **1991,** *178* (1), 121-129.

42. Lewis, J. D.; Malloy, T. B.; Chao, T. H.; Laane, J. PERIODIC POTENTIAL FUNCTIONS FOR PSEUDOROTATION AND INTERNAL-ROTATION. *Journal of Molecular Structure* **1972,** *12* (3), 427-&.

43. Zwier, T. S. The spectroscopy of solvation in hydrogen-bonded aromatic clusters. *Annual Review of Physical Chemistry* **1996,** *47*, 205-241.

44. Yang, M.; Skinner, J. L. Signatures of coherent vibrational energy transfer in IR and Raman line shapes for liquid water. *Phys. Chem. Chem. Phys.* **2010,** *12* (4), 982-991.

APPENDIX

APPENDIX

To extract local amide I frequencies as well as nearest-neighbor and next-nearest-neighbor amide I/I coupling constants from our DFT M05-2X/6-31+G(d) calculations, we used the original Hessian reconstruction scheme developed by Cho and coworkers (S. Ham, S. Cha, J. H. Choi, and M. Cho, J. Chem. Phys. 119 (3), 1451 (2003)). The matrix elements U_{aj} of the eigenvector matrix U were determined according to

$$U_{\alpha j} = N_j \left(r_{\alpha j} - r_\alpha^0 \right) \quad (1)$$

where r_a^0 denotes the C=O equilibrium bond lengths of each of the a C=O bonds, r_{aj} is the change in bond length caused by the j^{th} amide I normal mode in the a^{th} C=O bond, and N_j are factors normalizing separately each of the columns of the eigenvector matrix **U**. The C=O equilibrium bond lengths r_a^0 and C=O bond length displacements r_{aj} were directly determined from the equilibrium structures and normal mode displacements in Cartesian coordinates, respectively, calculated at the DFT M05-2X/6-31+G(d) level of theory. The columnwise normalized **U** matrices obtained above were orthonormalized according to a procedure that has the advantage of being a generalization of the original scheme of Cho and co-workers to peptides with more than three amide groups. Our procedure exploits the idea that a general and

straightforward way to represent an orthonormal matrix **U**(p) in a parameterized way is through the successive application of k=n(n−1)/2 Givens rotations

$$U^{(p)} = G(2,1,\theta_1)\cdot G(3,1,\theta_2)\cdot G(3,2,\theta_3)\cdot \ldots \cdot G(n,n-1,\theta_k) \quad (2)$$

where n is the number of amide groups present in the peptide, q_1 through q_k are the parameters, and the first two Givens matrices for a model peptide containing three amide groups are

$$G(2,1,\theta_1) = \begin{pmatrix} \cos\theta_1 & -\sin\theta_1 & 0 \\ \sin\theta_1 & \cos\theta_1 & 0 \\ 0 & 0 & 1 \end{pmatrix} \quad (3)$$

and

$$G(3,1,\theta_2) = \begin{pmatrix} \cos\theta_2 & 0 & -\sin\theta_2 \\ 0 & 1 & 0 \\ \sin\theta_2 & 0 & \cos\theta_2 \end{pmatrix} \quad (4)$$

Orthonormalized matrices **U**(p) (see Table S5) were thereby determined which best represented our original **U** matrices in a least-squares fit procedure that minimized the least-squares objective function

$$F = \sum_{\alpha,j=1}^{n} \left[U_{\alpha j} - U_{\alpha j}^{(p)} \right]^2 \quad (5)$$

through variation of the fit parameters q_1 through q_k. In the amide I region, the mean absolute error between the matrix elements U_{aj} and Uaj $^{(p)}$ is $2.34\cdot10^{-3}$, the percentage error relative to the mean of the absolute values $|U_{aj}^{p}|$ is 0.5%. This small deviation of the orthonormalized matrices $\mathbf{U}^{(p)}$ from the original matrices **U** indicates that amide I

normal modes can be well described as linear combinations of mainly C=O stretch local modes. Each orthonormal matrix $\mathbf{U}^{(p)}$ was used to reconstruct the non-diagonal Hessian matrix **H** associated with each of the model di- and triamides. This was achieved through unitary transformation of the corresponding diagonal matrix **L** containing the DFT M05-2X/6-31+G(d) amide I normal mode frequencies of the model di- or triamide on its diagonal, yielding in the triamide cases, e.g., local amide I frequencies (w_1, w_2, w_3), nearest-neighbor coupling constants ($J_{12}=J_{21}$, $J_{23}=J_{32}$) and next-nearest-neighbor coupling constants $J_{13}=J_{31}$.

$$H = \begin{pmatrix} \omega_1 & J_{12} & J_{13} \\ J_{21} & \omega_2 & J_{23} \\ J_{31} & J_{32} & \omega_3 \end{pmatrix} = U^{(p)} \Lambda \left[U^{(p)}\right]^{-1} \quad (6)$$

The eigenvector matrices $\mathbf{U}^{(p)}$ in the amide I region and $\mathbf{U}^{PED(p)}$ in the amide II region were also used to calculate normal mode intensities, $I_j^{(I)}$ and $I_j^{(II)}$ (in km/mol), according to

$$I_j^{(I)} = 42.2547 \left| \sum_{\alpha=1}^{n} U_{\alpha j}^{(p)} \left(\frac{\partial \mu^{(I)}}{\partial Q_\alpha} \right) \right|^2 \quad (7)$$

and

$$I_j^{(II)} = 42.2547 \left| \sum_{\alpha=1}^{n} U_{\alpha j}^{PED(p)} \left(\frac{\partial \mu^{(II)}}{\partial Q_\alpha} \right) \right|^2 \quad (8)$$

The derivatives of the local amide I and amide II transition dipole moment vectors, $\partial\mu^{(I)}/\partial Q_a$ and $\partial\mu^{(II)}/\partial Q_a$ (in $D \cdot Å^{-1} \cdot amu^{-1/2}$), were determined from the M05-2X/6 31+G(d) calculations on the $^{13}C=^{18}O$ and N–D isotopologues, respectively.

VITA

VITA

Evan Gardner Buchanan was born on December 4, 1984 to Robert and Lynn Buchanan. Evan graduated from Forest Hills Central High School in 2003 and obtained a B.S. in chemistry and a minor in mathematics from Denison University in 2007. Evan joined the research group of Timothy S. Zwier at Purdue University in 2007, obtaining his Ph.D in physical chemistry in 2014. After Purdue, Evan will be a postdoctoral research associate working with David F. Plusquellic at the National Institute of Standards and Technology in Boulder, Colorado.

PUBLICATION

THE JOURNAL OF CHEMICAL PHYSICS **138**, 204313 (2013)

Excitonic splitting and vibronic coupling in 1,2-diphenoxyethane: Conformation-specific effects in the weak coupling limit

Evan G. Buchanan,[1] Patrick S. Walsh,[1] David F. Plusquellic,[2,a)] and Timothy S. Zwier[1,a)]
[1]*Department of Chemistry, Purdue University, West Lafayette, Indiana 47907-2084 USA*
[2]*Quantum Electronics and Photonics Division, Physical Measurement Laboratory, National Institute of Standards and Technology, Boulder, Colorado 80305-3328, USA*

(Received 19 March 2013; accepted 2 May 2013; published online 30 May 2013)

Vibrationally and rotationally resolved electronic spectra of 1,2-diphenoxyethane (C_6H_5–O–CH_2–CH_2–O–C_6H_5, DPOE) are reported for the isolated molecule under jet-cooled conditions. The spectra demonstrate that the two excited surfaces are within a few cm^{-1} of one another over significant regions of the torsional potential energy surfaces that modulate the position and orientation of the two aromatic rings with respect to one another. Two-color resonant two-photon ionization (2C-R2PI) and laser-induced fluorescence excitation spectra were recorded in the near-ultraviolet in the region of the close-lying S_0–S_1 and S_0–S_2 states (36 400–36 750 cm^{-1}). In previous work, double resonance spectroscopy in the ultraviolet and alkyl CH stretch regions of the infrared was used to identify and assign transitions to two conformational isomers differing primarily in the central C–C dihedral angle, a *tgt* conformation with C_2 symmetry and a *ttt* conformation with C_{2h} symmetry [E. G. Buchanan, E. L. Sibert, and T. S. Zwier, J. Phys. Chem. A **117**, 2800 (2013)]. Comparison of 2C-R2PI spectra recorded in the *m/z* 214 (all ^{12}C) and *m/z* 215 (one ^{13}C) mass channels demonstrate the close proximity of the S_1 and S_2 excited states for both conformations, with an upper bound of 4 cm^{-1} between them. High resolution spectra of the origin band of the *tgt* conformer reveal it to consist of two transitions at 36 422.91 and 36 423.93 cm^{-1}, with transition dipole moments perpendicular to one another. These are assigned to the S_0–S_1 and S_0–S_2 origin transitions with excited states of A and B symmetry, respectively, and an excitonic splitting of only 1.02 cm^{-1}. The excited state rotational constants and transition dipole coupling model directions prove that the electronic excitation is delocalized over the two rings. The *ttt* conformer has only one dipole-allowed electronic transition ($A_g \rightarrow B_u$) giving rise to a pure b-type band at 36 508.77 cm^{-1}. Here, the asymmetry induced by a single ^{13}C atom in one of the rings is sufficient to localize the electronic excitation in one or the other ring. Dispersed fluorescence (DFL) spectra are used to provide assignments for all vibronic structure in the first 200 cm^{-1} of both conformers. In the *tgt* conformer, both "a" and "b" symmetry fundamentals are observed, consistent with extensive vibronic coupling between the two dipole-allowed, nearly degenerate excited states. In the *ttt* conformer, the lowest frequency vibronic transition located 46 cm^{-1} above the B_u origin is assigned to a b_u fundamental (labeled $\bar{R}$) built off the dipole-forbidden A_g state origin. The DFL spectrum of the $A_g(\bar{R}^1)$ level contains strong transitions to $v''(\bar{R}) = 0$, 1, and 2, seemingly at odds with vibronic coupling models. Studies of the DFL spectrum of this band as a function of distance from the nozzle reveal that much of the intensity in $v'' = 1$ arises from collisions of DPOE while in the excited state $A_g(v_b' = 1)$ level with He, producing $B_u(\bar{R} = 1)$ levels with large collision cross section. The remaining intensity in the fundamental at large x/D is ascribed to emission from the ^{13}C isotopomer, for which this emission is dipole-allowed.
 [http://dx.doi.org/10.1063/1.4807300]

I. INTRODUCTION

Excitonic and vibronic coupling between electronic chromophores plays an essential role in the absorption/emission properties and excited state dynamics of molecular samples with important applications, including light-harvesting complexes,[1–4] chromophore arrays (e.g., J- and H-aggregates),[5,6] conjugated polymers,[7–9] and fluorescence resonance energy transfer (FRET).[10] This interest is fueled in part by new experimental methods such as 2D-electronic spectroscopy,[11,12] which are providing new insight to the femtosecond dynamics of electronic energy transfer. Among the issues under active investigation is the possible role played by electronic coherence in directing electronic energy transfer through an array of chromophores, and the extent to which vibrational motions are involved.[13,14]

Regardless of the circumstance, the structural and dynamical consequences of electronic near-degeneracy provide a particular challenge to modern theories seeking to understand them. While many of these applications involve multiple chromophores in a complex environment at room

a)Authors to whom correspondence should be addressed. Electronic addresses: david.plusquellic@nist.gov and Zwier@purdue.edu

temperature, one useful strategy is to seek to control or remove many of the complicating factors in order to focus attention on the fundamental aspects of interchromophore coupling. To that end, laser spectroscopy of the gas-phase bichromophore cooled in a supersonic jet provides exquisite details of the vibronic coupling on a single-vibronic level basis free from the interference from solvent.[15–22] When the two chromophores are incorporated into separate molecules, the supersonic expansion serves as a means for synthesizing the molecular dimer and collapsing its population entirely into the ground state vibrational zero-point level.[15–23]

The other circumstance in which multiple chromophores exist in close proximity is when they are incorporated as part of the same molecule. Model bichromophores can either be held rigidly in a framework which defines the interchromophore separation and orientation,[24,25] or as part of a flexible linker along which the interchromophore distance and orientation may vary.[26–38] Flexible linkages offer the tantalizing prospect of studying interchromophore vibronic coupling on a conformation-specific basis under jet-cooled conditions in which population is collisionally cooled into more than one conformational zero-point level. The uncoupled excited state energies and interchromophore electronic coupling will be modulated from one conformer to the next by changes in the distance and relative orientation of the chromophores, and the nature of the vibrational motions involved.

Model flexible bichromophores can either incorporate two identical monomers,[28–35] or consist of chemically distinct donor and acceptor sub-units.[39,40] In a few cases, conformation-specific data have shed light on the way in which the ground state conformation of the molecule dictates the excited state spectroscopy and dynamics, producing conformation-selective broadening in the excitation spectrum, redshifted emission, or differing energy thresholds to exciplex formation.[29,30,39]

Recent experiments and theory are shedding qualitative new light on the spectroscopic consequences of interchromophore coupling.[16,18,19,41] Much of this work compares experiment with the predictions of a diabatic model of the vibronic coupling based on Förster theory,[42] as developed by Fulton and Gouterman (FG)[43,44] for the specific case of a bichromophore coupled by a single vibrational mode. Extension of this model to multiple vibrational modes[34,41] and to asymmetric bichromophores[41] have contributed to the growing ability to quantitatively account for the observed vibronic coupling patterns.

Recently, Leutwyler, Koppel, and co-workers[16,45] have developed an adiabatic vibronic coupling model and used it to obtain a quantitatively accurate account of the observed excitonic splitting in 2-aminopyridine, *o*-cyanophenol, 2-pyridone, and benzoic acid dimers, all of which are in the weak coupling limit. The theory reproduces the experimental excitonic splitting determined by the diabatic model, but provides a more intuitive picture of the excitonic splitting in the weak coupling limit. Here, the electronic energy transfer occurs through a barrier on the adiabatic surface, with the excitonic splitting modeled as a tunneling splitting in which both nuclear distortions and interchromophore electronic energy transfer contribute to the tunneling rate.

In experiments to date on jet-cooled bichromophores, there are relatively few examples in which both the S_0–S_1 and S_0–S_2 transitions have been spectroscopically characterized. When the two chromophores are sufficiently different, fast electronic energy transfer between the two chromophores inhibits the identification of the lifetime broadened S_2 state. Furthermore, in cases where the two chromophores are identical and conformational symmetry exists, only one of the S_0–S_1 or S_0–S_2 transitions is often dipole-allowed.[17] In several aromatic dimers, Leutwyler and co-workers[18,19,16] have cleverly addressed this by breaking the symmetry through recording the spectrum of the singly ^{13}C substituted isotopomer in natural abundance using resonant two-photon ionization (R2PI) coupled with time-of-flight mass analysis.

Previous work from our group has focused attention on a series of prototypical flexible bichromophores that possess a single conformational isomer for diphenylmethane (DPM),[33,35] and two isomers of both bis-(2-hydroxyphenyl)methane (2HDPM)[32] and bis-(4-hydroxyphenyl)methane (b4HPM).[34] In these molecules, the spectroscopic consequences of internal mixing between the two excited electronic states have been characterized in some detail. In DPM, the excitonic splitting was determined to be 123 cm^{-1}, leading to a dual emission from the (nominal) S_2 origin that reported on its mixing with nearby vibrational levels built off the S_1 origin. This has stimulated theoretical developments that employ a multi-mode asymmetric vibronic coupling model as an extension of the theoretical framework developed by Fulton and Gouterman[43,46] for symmetric bichromophores.[41]

A previous study reporting on the ground state conformational preferences of 1,2-diphenoxyethane (C_6H_5–O–CH_2–CH_2–O–C_6H_5, DPOE) provides the foundation for the present work,[47] which we briefly summarize here. A conformational search of the torsional potential energy surface for DPOE located 26 conformational minima. Two of the conformational isomers possessed an inversion center, while the remaining 12 structures are composed of pairs of non-superimposable mirror images with dihedral angles of opposite sign but identical magnitude. Experimentally, two conformational isomers were observed in the supersonic jet expansion and assigned based on infrared and vibronic data to the two lowest energy conformers of DPOE, with C_2 (*tgt*) and C_{2h} (*ttt*) symmetry, as shown in Figure 1. Here, the central three dihedral angles are labeled as *trans* (*t*) or *gauche* (*g*). To establish the conformational assignments, calculated harmonic vibrational frequency were compared to the experimental alkyl CH stretch, CH bend, and CO stretch spectra. Using a reduced-dimension model, the Fermi resonances present in the alkyl CH stretch infrared spectrum were successfully modeled, confirming and strengthening the assignments based on the vibronic spectroscopy.

In the current paper, we provide a detailed spectroscopic characterization of the vibronic and rovibronic spectroscopy of DPOE in the region of the close-lying S_1 and S_2 state origins. High resolution ultraviolet spectra prove that the two dipole-allowed S_0–S_1 and S_0–S_2 origins of the *tgt* isomer are separated by 1.02 cm^{-1}. Although the S_0–S_1 origin of the *ttt* conformer is dipole-forbidden, 2C-R2PI spectra of the M+1

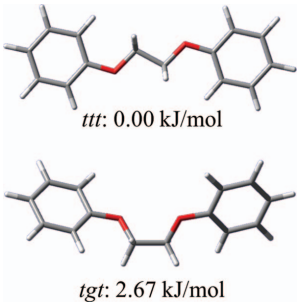

FIG. 1. Optimized structures for the two observed conformers of DPOE, with their relative energies calculated at the DFT M05-2X/6-31+G(d) level of theory.

mass channel for monomers possessing a single ^{13}C atom show a spectrum for the *ttt* conformer that possesses two dipole-allowed origins arising from near-complete localization of the electronic excitation in one or the other ring, with splitting of $\sim$4 cm^{-1}. Thus, despite the seeming close proximity of the two chromophores, interchromophore coupling in DPOE is in the extreme limit of weak coupling. The results for DPOE thus provide a window on the spectroscopic consequences of vibronic coupling in this weak coupling limit in which the two electronic states are no more than a few cm^{-1} from one another over much of the torsional potential energy surface, with electronic excitation localized or delocalized by minute asymmetries in the local environment.

II. EXPERIMENTAL METHODS

Single and double-resonance techniques used to obtain the single-conformation ultraviolet and infrared spectra have been reported previously.[48] Details specific to the current work are briefly provided here. 1,2-diphenoxyethane (Aldrich) was heated to 90 °C inside a stainless steel reservoir to obtain a sufficient vapor pressure. DPOE was seeded into a helium or neon buffer gas with a backing pressure of $\sim$3 bars and passed through a pulsed valve with a 500 μm orifice (Parker General Valve Series 9) to form the supersonic jet expansion.

Two-color resonant two-photon ionization (2C-R2PI) was employed to record the total electronic spectrum of all species present in the expansion. In 2C-R2PI, a 20 Hz UV laser resonantly excited DPOE to an excited state with a second lower-frequency, non-resonant 20 Hz UV laser used to ionize the molecules for detection with a multichannel plate.[49] Dispersed fluorescence (DFL) spectra were obtained in a fluorescence chamber described previously.[50] A $\frac{3}{4}$-m monochromator with 50 μm entrance slit provided DFL spectra with $\sim$9 cm^{-1} resolution. The dispersed emission was imaged onto the face of an ICCD camera (Andor).

Ultraviolet hole-burning (UVHB) was employed to obtain the conformation specific electronic spectra of the individual conformers. UVHB is a double resonance technique, requiring the spatially overlapped output of two ultraviolet lasers, temporally separated by 200 ns. The 10 Hz hole-burn laser is fixed on a transition due to a single conformer and preceded the 20 Hz probe, which is tuned through the region of interest. A difference spectrum is obtained by passing the integrated signal through a gated integrator operating in active baseline subtraction mode. Whenever the two lasers share the same ground state energy level, a depletion is observed.

Stimulated-emission pumping (SEP) ion-dip spectroscopy[51] was performed in a molecular beam time-of-flight mass spectrometer and used to record the ^{12}C and ^{13}C ground state spectra between 800 and 900 cm^{-1} above the zero-point level of the *ttt* origin.[52] Here, a 20 Hz UV pump laser was fixed on a UV transition due to a single conformation with a typical laser power of 0.1 mJ/pulse. The power was sufficient to excite the molecule to an electronic excited state, but produces a minimal amount of ion signal from resonant two-photon ionization. The second 20 Hz UV laser serves a dual purpose both as the second photon in 2C-R2PI and as the dump laser for SEP. The wavelength of this laser was tuned red of the origin with a laser power of 1.0 mJ/pulse to stimulate the emission back to the ground state in competition with ionization. Whenever the dump laser was resonant with a transition back to the ground state, a depletion in the total ion signal is observed. The technique provides analogous information to DFL, however, with a resolution predetermined by the laser linewidth. With mass selectivity, the technique is able to distinguish the spectra from ^{12}C and ^{13}C isotopomers even in the presence of spectral overlap.

Finally, the rotationally resolved electronic spectra were obtained at NIST by heating the sample to 135 °C in a quartz nozzle with a 125 μm diameter orifice. Details to the specific experimental apparatus have been reported previously.[50,53] The molecules were entrained in an argon backing gas with a backing pressure of 0.2 bar. About 250 mW from an Ar^+-pumped cw ring dye laser using C521 laser dye was frequency doubled in barium borate (BBO) in an external resonant cavity and the output mildly focused on a skimmed molecular beam 18 cm downstream of the source. The fluorescence was collected by two spherical mirrors and detected by a photomultiplier tube and photon counting system. Typical laser powers of 1–2 mW were used to record the rotationally resolved electronic spectra with a resolution of $\sim$21 MHz.

III. COMPUTATIONAL METHODS

Excited state structural optimizations and vibrational frequency calculations for the *ttt* and *tgt* conformers of DPOE were performed using time-dependent density functional theory (TDDFT) at the M05-2X/6-31+G(d) level of theory. Rotationally resolved spectra were fit to an asymmetric rotor Hamiltonian using the genetic algorithm as implemented in the JB95 spectral fitting program.[54] The two optimized structures, *ttt* and *tgt*, were used as input for fitting the rotational spectra.

To better understand the excitonic splitting, the transition dipole coupling model (TDM) and the FG model have been employed.[43,46] TDM is a simple electrostatic model in which the excitonic splitting is approximated utilizing the coulombic

interaction between the two electronic transition moments on the individual phenyl rings A and B. The interchromophore coupling is given by

$$V_{AB} = \frac{\mu_A \mu_B}{4\pi\varepsilon R^3}(2\cos\theta_A \cos\theta_B - \sin\theta_A \sin\theta_B \cos\varphi), \quad (1)$$

where μ is the magnitude of the electronic transition moment, R is the distance between the two transition moment vectors, θ is the angle between the two transition moment vectors along R, and φ is the dihedral between the two vectors.

The FG model for vibronic coupling uses a diabatic approach to model the vibronic structure observed in absorption and dispersed fluorescence.[18,19] In earlier work,[34] we implemented a version of this model to explain the multi-mode vibronic coupling observed in bis-(4-hydroxyphenyl)methane. We use this same program to compare the model predictions with experiment in DPOE. Details of the model are given elsewhere.[34,41]

IV. RESULTS

A. R2PI and dispersed fluorescence spectra

Figure 2 shows the 2C-R2PI spectrum (top trace) and the ultraviolet hole-burning spectra (bottom traces) of the two monomer conformations present in the supersonic jet expansion. 2C-R2PI was employed to avoid saturating the excitation spectrum. The small excursion from zero marked with an asterisk in the figure is present due to incomplete subtraction through the gated integrator when tuning through the *tgt* S_0–S_1 origin. As discussed in the previous study reporting on the ground state preferences of DPOE,[47] the two isomers adopt geometries with C_2 and C_{2h} symmetry, differing exclusively by the central OCCO dihedral angle, *gauche* or *trans*. For this reason, the C_2 symmetric conformer has been labeled *tgt* and the C_{2h} isomer as *ttt* representing the *gauche* and *trans* isomers, respectively. The *tgt* origin occurs at 36 423 cm^{-1} and the *ttt* origin at 36 509 cm^{-1}. The calculations predict an in-plane geometry of both Ph–O–C groups in both conformers, as is observed in alkoxy-benzenes such as 1,2-diethoxybenzene.[55]

Given the C_2 symmetry of the *tgt* conformer A, calculations predict that transitions from S_0 to both the S_1(A) and S_2(B) electronic excited states will be dipole-allowed. The UVHB spectrum of the *tgt* conformer has several low-frequency vibronic transitions, including transitions +24, +26, +35, +99, +155, and +185 cm^{-1} from the origin (Figure 2). Of these, the transitions at +24, +35, +99, and +155 cm^{-1} are totally symmetric fundamentals with frequencies virtually unchanged from their values in the ground electronic state, as summarized in Table I. As an example, the DFL spectrum of the +24 cm^{-1} band is shown in Figure 3(a). The spectrum is dominated by a false origin at −25 cm^{-1}, with vibronic structure built off this false origin closely similar to that of the electronic origin. The DFL spectra from the other totally symmetric fundamentals are similar, with false origins associated with $X^1{}_1$ transitions dominating the spectrum. These spectra are included in supplementary material.[59] The two remaining transitions at +26 cm^{-1} and +185 cm^{-1} are b symmetry fundamentals. Their DFL spectra are shown in Figure 3(a). These bands also display strong false origins in emission that confirm their assignments to "b" fundamentals with ground state frequencies of 30 and 186 cm^{-1}. Table I compares the observed ground and excited state frequencies of the *tgt* conformer with those predicted by calculation. The close correspondence confirms the assignments given. The "b" symmetry fundamentals appear in excitation as

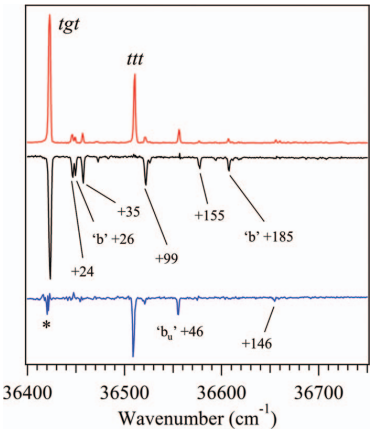

FIG. 2. 2C-R2PI and UVHB spectra of the two isomers present in the supersonic expansion. The asterisk marks an artifact due to incomplete subtraction through the gated integrator. Both UVHB spectra show vibronically induced fundamentals.

TABLE I. A comparison of the calculated ground state vibrational frequencies to the experimental ground and excited state vibrational frequencies (in cm^{-1}) is presented. The Mulliken labeling scheme has been used for the normal modes.

C_2 (*tgt*)					C_{2h} (*ttt*)				
Mode #	Calc. frequency	Exp. S_0 freq	Exp. S_1 freq	Symmetry (mode)	Mode #	Calc. frequency	Exp. S_0 freq	Exp. S_1 freq	Symmetry (mode)
40	158	157	154	a	28 (R)	149	147	146	a_g
41	104	103	98	a	41	166			b_g
42	36	36	34	a	55	141			a_u
43	25	25	24	a	56	38			a_u
82	194	186	185	b	57	22			a_u
84	30	30	26	b	84 ($\bar{R}$)	51	46	46	b_u

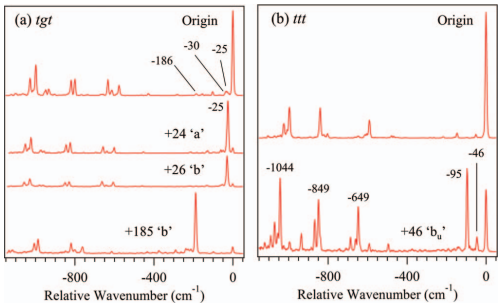

FIG. 3. Dispersed fluorescence spectra of the origin and key vibronic bands of (a) the *tgt* conformer and (b) the *ttt* conformer of DPOE.

a result of vibronic coupling between the S_1 and S_2 states. It is striking that all vibronic transitions are assigned to vibronic bands built off the single observed origin at 36 423 cm^{-1}. Thus, the location of the strong dipole-allowed S_0–S_2 origin requires further investigation in what follows.

The C_{2h} symmetry *ttt* conformation has $S_1(A_g)$ and $S_2(B_u)$ electronic excited states with transitions from the ground electronic state $S_0(A_g)$ that are dipole forbidden and dipole-allowed, respectively. The UVHB spectrum of the *ttt* conformer is shown in the bottom trace of Figure 2. According to the calculations, the lowest frequency totally symmetric mode ($\nu_{28}(a_g)$, labeled R) in the C_{2h} *ttt* conformer is at 149 cm^{-1}, in reasonable agreement with the weak transition at +146 cm^{-1} in the UVHB spectrum of the *ttt* isomer. The band 46 cm^{-1} above the B_u origin is assigned to a vibronically induced transition involving the lowest frequency b_u symmetry fundamental (ν_{84}, labeled $\bar{R}$ here) with calculated ground state frequency of 46 cm^{-1} (Table I). Figure 4 presents the form of the R and $\bar{R}$ vibrational modes, which involve symmetric and asymmetric in-plane bends of the two phenyl rings. It would appear built off the dipole-forbidden A_g symmetry excited state (A_gX b_u), gaining its oscillator strength completely through vibronic coupling. Its frequency position (+46 cm^{-1}) suggests that the dipole-forbidden origin must be near to the allowed A_g–B_u origin at 36 509 cm^{-1}.

The DFL spectra of the B_u electronic origin and $A_g(\bar{R}_0^1)$ transitions are presented for the *ttt* conformer in Figure 3(b). The origin emission spectrum has contributions only from a_g fundamentals, consistent with originating from a B_u excited electronic state. The $A_g(\bar{R}_0^1)$ band, however, has unusual vibronic activity, most notably in the triad of peaks observed at 0, −46, and −95 cm^{-1}. The 0 and −95 cm^{-1} transitions

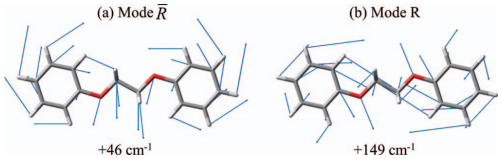

FIG. 4. Form of the normal modes of the *ttt* conformer of DPOE for the (a) b_u symmetry $\bar{R}$ vibration (46 cm^{-1}) and (b) its a_g counterpart R (149 cm^{-1}).

are attributed to vibronic coupling, producing $\Delta v_{84} = \pm 1$ Herzberg-Teller selection rules. What is puzzling is the band at −46 cm^{-1}, which should only appear from an A_g symmetry vibronic level ($B_u x b_u$) in the excited state, since its ground state vibronic symmetry is $A_g x b_u = B_u$. Its DFL spectrum also shows increased intensity in several ring modes relative to the B_u 0^0_0 spectrum above it. The enhancement of ring mode intensity in emission was previously observed in the spectrum of the S_2 origin of bis-(4-hydroxyphenyl)methane[34] and attributed to vibronic coupling effects. In that case, the FG model was able to give a quantitative account of these intensity changes. We will present further analysis of this band using the FG model in Sec. V.

B. High resolution UV spectra

One intriguing possibility for the location of the S_0–S_2 origin in the *tgt* conformer is that the electronic splitting is so small that it is unresolved from the S_0–S_1 origin. Motivated by this notion, we recorded a high resolution UV spectrum (∼21 MHz resolution) of the band at 36 423 cm^{-1} assigned to the S_0–S_1 origin. The resulting spectrum is presented in Figure 5(a) with the experimental spectrum as the top trace and the best fit produced by genetic algorithms as implemented in the JB95 spectral fitting program.[54] As hypothesized, the band is indeed composed of two transitions with band centers separated by 1.02 cm^{-1}. The two transitions are assigned to the S_0–S_1 (36 422.91 cm^{-1}) and S_0–S_2 (36 423.93) origins. The ground and excited state rotational constants and TDM directions are summarized in Table II. Note that the S_0–S_1 transition is a 23:77 a:c-type band while the S_0–S_2 origin is a pure b-type transition, with TDM directions that are perpendicular to one another. Furthermore, the excited state rotational constants of the two overlapped origin bands are remarkably similar to one another. Both these facts point to the electronic excitation being delocalized over the two rings, leading to geometry changes upon electronic excitation that are shared between the two rings, consistent with the C_2 geometry for the *tgt* conformer.

Figure 5(b) presents the high resolution spectrum of the S_0–S_1 origin of the *ttt* conformer. Once again, the fit is shown

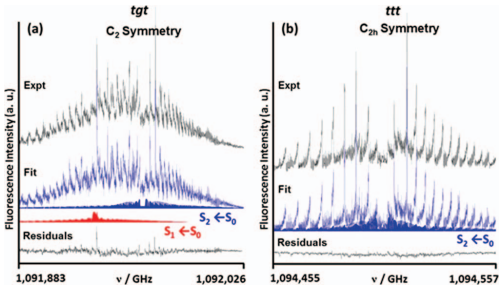

FIG. 5. High resolution LIF excitation spectrum of the electronic origin bands associated with the (a) *tgt* conformer and (b) *ttt* conformers. The fit to the experimental spectrum is shown in the bottom trace alongside the residuals to the fit.

TABLE II. The rotational constants for the two isomers of DPOE. The S_0–S_1 origin of the *ttt* conformer is dipole-forbidden and therefore not observed. Rotational constants have been rounded for clarity (see Table S1 of the supplementary material[59] for a complete listing of fitted parameters including uncertainties).

			C_2 (*tgt*)	
	S_0 state (MHz)		S_1 state (MHz)	S_2 state (MHz)
A	1873.8	ΔA	−66.4	−66.2
B	177.9	ΔB	0.9	0.8
C	171.1	ΔC	0.6	0.6
			24:76% a:c-type	100% b-type
			C_{2h} (*ttt*)	
A	2508.9	ΔA	…	−61.0
B	157.9	ΔB	…	−0.3
C	148.9	ΔC	…	−0.5
				100% b-type

below for comparison, with best fit parameters shown in Table II. In this case, a single band is able to account for all observed rovibronic structure. The band is a b-type band, consistent with its assignment to the A_g–B_u transition of the C_{2h} *ttt* conformer. A high resolution scan of the +46 cm^{-1} transition of the *ttt* conformer is included in the supplementary material.[59] This transition is also of b-type, as anticipated based on the assignment of this transition to the b_u symmetry $\bar{R}$ fundamental built off the A_g excited state. Given the close proximity of two electronic origins in the *ttt* conformer, and the position of the +46 cm^{-1} transition relative to its calculated frequency, it seems likely that the splitting between the A_g and B_u excited states should also be small. Proof for this conjecture comes in Sec. IV C.

C. ^{13}C-substituted R2PI spectroscopy

Following the lead of Leutwyler and co-workers,[18,19,16] we recorded R2PI spectra of DPOE while monitoring the M+1 mass channel associated with incorporation of a single ^{13}C atom in the molecule, which contains 14 carbon atoms. Since 12 of the 14 carbons are in the two aromatic rings that typically give rise to similar electronic frequency shifts, the M+1 R2PI spectrum reflects primarily the effects of symmetry breaking on the electronic spectroscopy. These effects are anticipated to be particularly striking in the *ttt* conformer, since breaking the symmetry of the two rings can turn on intensity in the dipole-forbidden A_g–A_g electronic transition.

Figure 6 compares R2PI spectra recorded in the *m/z* 214 mass channel (all ^{12}C DPOE, top trace) to that in the M+1 mass channel, recorded under unsaturated (red, middle) and partially saturated (blue, bottom) conditions. The ^{13}C substitution in the ring produces a doublet at the *tgt* origin, split by 4.7 cm^{-1}, which is now resolved even under low resolution. The magnitude of this splitting is more than four times the excitonic splitting (1.02 cm^{-1}), indicating that most of the splitting in the ^{13}C spectrum is site splitting due to the fact that one ring contains a ^{13}C atom, while the other does not. On that basis, we surmise that the observed doublet should be

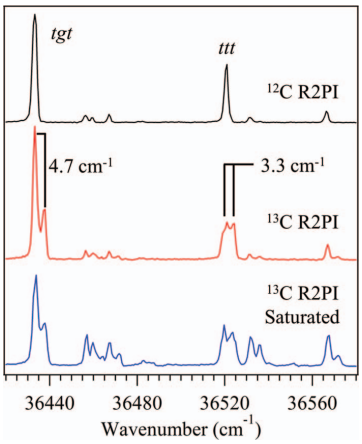

FIG. 6. R2PI spectra in the S_0–S_1/S_2 origin regions of the *tgt* and *ttt* conformers of DPOE monitoring (a) the all ^{12}C parent mass channel, (b) the M+1 mass channel associated with incorporation of one ^{13}C into the molecule under (b) unsaturated and (c) partially saturated conditions. The observed splittings of 4.7 cm^{-1} and 3.3 cm^{-1} for the *tgt* and *ttt* conformations place upper bounds on the excitonic splittings of the two conformers. See text for further discussion.

interpreted as arising from electronic excitation largely localized on the all ^{12}C or singly ^{13}C substituted rings of DPOE.

Similar arguments hold for the R2PI spectrum of the ^{13}C *ttt* conformer. Here, we see a partially resolved and somewhat broadened doublet with a splitting of 3.3 cm^{-1}. Strikingly, the two transitions are nearly equal in intensity, as would occur if electronic excitation were completely localized on one or the other ring. This is consistent with a splitting of 3.3 cm^{-1}, which is 30% less than the splitting in the *tgt* conformer. We surmise on this basis that the splitting of the electronic origins in the all ^{12}C isotopomer is significantly smaller than 1 cm^{-1} for the *ttt* conformer. The partially saturated spectra show that the band splittings present at the origins carry forward to other vibronic bands in the spectrum.

D. Collisional studies

One important benefit of the ^{13}C R2PI spectrum is that it provides the electronic frequency positions of these transitions relative to the all-^{12}C spectrum. In particular, the +4 cm^{-1} transition of the *ttt* conformer is directly overlapped with the main band of the ^{12}C spectrum, and would therefore be excited simultaneously under conditions for dispersed fluorescence. This raises the possibility that the −46 cm^{-1} transition in the *ttt* +46 cm^{-1} DFL spectrum (Figure 3(b)) could arise from the ^{13}C isotopomer, which would have an allowed transition with $\Delta v = 0$ Franck-Condon factors to the b_u fundamental in the ground electronic state. Indeed, its intensity relative to the $\Delta v = \pm 1$ transitions on either side of it, are approximately correct for ascribing the −46 cm^{-1} transition to ^{13}C DPOE.

It is noteworthy that the +46 cm^{-1} DFL spectrum shown in Figure 3(b) was recorded at x/D = 38, far downstream

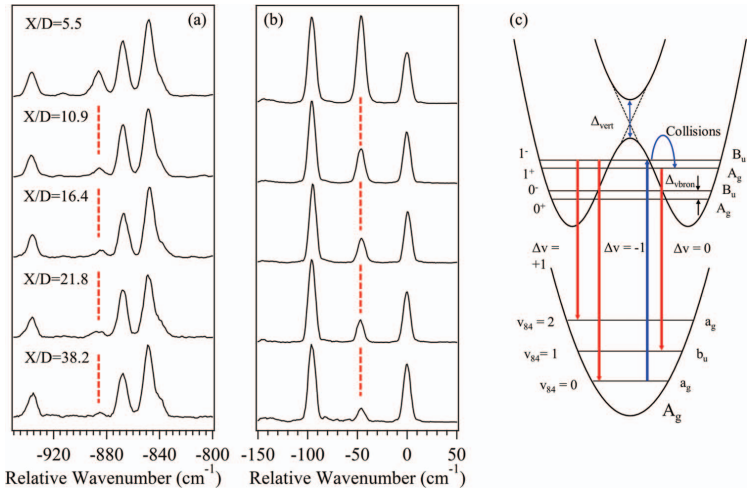

FIG. 7. Close-up views of the (a) −800 to −950 cm^{-1} and (b) +50 to −150 cm^{-1} regions of the *ttt* +46 cm^{-1} DFL spectrum taken with laser excitation occurring at different distances (x/D, D = nozzle diameter) from the nozzle in the expansion. Transitions marked with a dotted line grow in intensity at small x/D due to collisions with the backing gas. (c) Energy level diagram depicting the excitation, emission, and collisional energy transfer processes responsible for the collision free ("0," −95 cm^{-1}) and collision-induced (−46 cm^{-1}) emission.

relative to conditions often used for recording DFL spectra. Under most circumstances, the effects of collisions on DFL spectra are minimal, since the collision frequency in the jet is typically slow relative to the excited state fluorescence lifetime (∼30 ns in this case). However, the emission from the +46 cm^{-1} transition of *ttt* DPOE is a notable exception.

Figures 7(a) and 7(b) present a series of DFL spectra from the +46 cm^{-1} transition of *ttt* taken as a function of distances from the nozzle orifice (with diameter D), ranging from x/D = 5.5 to 38. A close-up of two regions of the DFL spectra are shown that highlight bands at −46 cm^{-1} and −889 cm^{-1} whose intensity is sensitive to the x/D position. Clearly, both bands grow in intensity by more than a factor of five as excitation occurs closer to the nozzle where collisions with buffer gas are more frequent.

Figure 7(c) displays an energy level diagram that summarizes the collisional mechanism responsible for the growth in this −46 cm^{-1} emission. The two excited states are drawn in an adiabatic representation in which the geometry changes accompanying electronic excitation of one or the other ring lead to displacements producing two equivalent, displaced wells in the excited state. The 1.02 cm^{-1} splitting between S_0–S_1 and S_0–S_2 origins is, in this adiabatic picture, a tunneling splitting associated with a process in which both electronic excitation and nuclear change accompany the tunneling. The +46 cm^{-1} transition in the excitation spectrum is to a B_u vibronic state that is (nominally) the b_u in-plane bending fundamental ($\bar{R}$) built off the A_g electronic origin ($A_g(\bar{R}_0^1)$). This state gains its oscillator strength by vibronic coupling with the B_u electronic state, and produces $\Delta v(\bar{R}) = \pm 1$ Herzberg-Teller selection rules in emission to produce transitions at "0" (resonance fluorescence) and −95 cm^{-1} (ending in v = 2 in the ground state). There is no dipole-allowed or vibronically induced method of producing the Δv = 0 emission from this level to the corresponding v = 1 level (at −46 cm^{-1}) in the ground state. However, if collisions with buffer gas occur during the excited state lifetime (Figure 7(c)), they can produce the other member of the v = 1 tunneling doublet, which is less than 1 cm^{-1} away. This level is of $B_u x b_u = A_g$ vibronic symmetry, and has a dipole-allowed transition to the v = 1 level in the ground state, with emission frequency −46 cm^{-1} from resonance fluorescence, as observed.

Interestingly, even at x/D = 38, some intensity remains in the −46 and −896 cm^{-1} bands. Although the remaining intensity could be attributed to collisions with an extremely large cross section for the collisional energy transfer process, it seemed more likely to us that this residual intensity arises from overlap with the ^{13}C 0^0_0+46 cm^{-1} transition (Sec. III C). As a final test of this conjecture, we recorded SEP ion-dip spectra from the *ttt* +46 cm^{-1} intermediate state while monitoring the ^{13}C and all ^{12}C mass channels. The results are shown in Figure 8.

Unfortunately, since the SEP "dump" laser frequency at −46 cm^{-1} was near resonances in absorption for the *tgt* conformer, the SEP ion-dip spectrum could not be recorded in the region of Figure 7(b) where the −46 cm^{-1} transition occurs. Instead, the corresponding collision-induced band at −889 cm^{-1} (Figure 7(a)) was free from such interference. As Figure 8 shows, the transition at −889 cm^{-1} is clearly observed in the ^{13}C spectrum, but is completely absent in the ^{12}C spectrum, confirming that the ^{13}C isotopomer is the likely source of the remaining −46 cm^{-1} intensity in Figures 3(b) and 7(b). This transition is dipole-allowed in the ^{13}C spectrum due to localization of the electronic excitation induced by one ring possessing a ^{13}C atom.

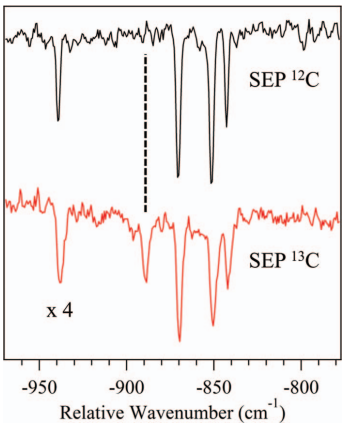

FIG. 8. The ^{12}C and ^{13}C stimulated emission pumping spectra indicating the 889 cm^{-1} transition is due to the ^{13}C spectrum.

V. DISCUSSION

A. The weak vibronic coupling limit

The primary goal of the present study has been to map out in some detail the conformational dependence of the excited state surfaces present in the model flexible bichromophore DPOE. In earlier work, LIF excitation, UV-hole burning, and resonant ion-dip infrared spectra were used to observe and assign transitions due to two conformations, the *ttt* conformer of C_{2h} symmetry, and the *tgt* conformer, with C_2 symmetry. In this paper, we have determined the magnitude of the excitonic splitting between the S_1 and S_2 states for both conformers, and determined and analyzed the spectroscopic signatures of vibronic coupling between the S_1 and S_2 states in the two conformations.

Perhaps the most striking result of this work is the extraordinarily small excitonic splittings present in the two conformers, with the *tgt* conformer possessing a splitting of 1.02 cm^{-1}, and its *ttt* counterpart even smaller based on the spectrum of its isotopomer containing a single ^{13}C atom in one of the rings. This is to be compared with an electronic transition from S_0 of more than 34 000 cm^{-1}. Thus, DPOE is in the extreme limit of weak vibronic coupling, with an excitonic splitting similar in size to the recently studied benzoic acid dimer (0.94 cm^{-1}).[45]

The splittings of the exciton coupled S_1 and S_2 origins reported in previous jet-cooled studies of the C_2 symmetric bichromophores, bis-(4-hydroxyphenyl)methane,[34] and diphenylmethane[33] were in excess of 100 cm^{-1} because of the close proximity of the two chromophores. In these cases, both exciton states are orbitally allowed and the vibronic spectra built off of each origin are readily resolved. The close proximity of the two rings rotates the direction of each ring's TDM and induced an out-of-ring-plane TDM component, significantly increasing the excitonic coupling relative to a monomer point-dipole model.[35] In contrast, the chromophores of DPOE are more weakly coupled because of the larger inter-ring separations that minimize direct interactions between the rings.

The weak coupling in DPOE is evident from predictions for the exciton splitting based on the transition dipole coupling of Förster theory,[10] and from vertical splittings calculated at the TDDFT M05-2X/6-31+G(d) level of theory. These are summarized in Table III for DPOE. The TDDFT vertical splittings (9 cm^{-1} for *tgt*, 25 cm^{-1} for *ttt*) and transition dipole coupling estimates (17 cm^{-1} for *tgt*, 43 cm^{-1} for *ttt*) are generally consistent with one another, and are quite small compared to those in DPM and b4HPM. For the *ttt* isomer of DPOE, the distance between the center-of-masses of the two aromatic rings is 8.6 Å, while in *tgt* this distance is 8.0 Å. Yet, these estimates are still more than 10-fold too large compared to the experimental splittings between the S_0–S_1 and S_0–S_2 origins (1 cm^{-1} or less).

Within the diabatic model typically used for analysis of excitonic splitting, the vertical splitting (Δ_{elec}) is vibrationally "quenched" by a Franck-Condon factor that accounts for the shift in excited state geometry relative to the ground state minimum.[16] This leads in the weak vibronic coupling limit to a "quenched" vibronic splitting Δ_{vibron} that is more than

TABLE III. Calculated vertical frequencies, S_1/S_2 splittings and oscillator strengths at the TDDFT M05-2X/6-31+G(d) level of theory. Comparison with experimental splittings and the excitonic splittings predicted with the transition dipole coupling model (TDM).

		Conformer: *tgt*		
	Vertical splitting (cm^{-1})	Scaled vertical splitting (cm^{-1})	Exp. freq (cm^{-1})	Calc. osc. strength
S_0–S_1	43 617	36 422.91	36 422.91	0.0277
S_0–S_2	43 628	36 432.09	36 423.93	0.0440
	TDDFT splitting	9 cm^{-1}	Exp. splitting	
	TDM splitting	17 cm^{-1}	1.02 cm^{-1}	
		Conformer: *ttt*		
	Vertical splitting (cm^{-1})	Scaled vertical splitting (cm^{-1})	Exp. freq (cm^{-1})	Calc. osc. strength
S_0–S_1	43 737	36 523.12	...	0.0000
S_0–S_2	43 767	36 548.17	36 508.77	0.0683
	TDDFT splitting	25 cm^{-1}	Exp. splitting	
	TDM splitting	43 cm^{-1}	~1.0 cm^{-1}	

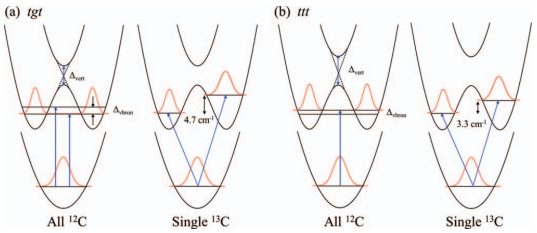

FIG. 9. Schematic adiabatic potential energy curves for the (a) *tgt* and (b) *ttt* conformers of DPOE showing (left) electronic delocalization of the symmetric all ^{12}C structures with tunneling splittings of $\Delta_{vibron} = 1.02$ and $\sim 1\ cm^{-1}$, respectively, and (right) the electronic localization associated with incorporation of a single ^{13}C atom into one of the rings, with S_1/S_2 splittings of 4.7 and 3.3 cm^{-1}, respectively.

10-fold smaller, with experimental splittings of 1.02 cm^{-1} (*tgt*) or less (*ttt*).

In this circumstance, the observed splitting is understood most intuitively in an adiabatic model in which the observed splitting is considered as a nonadiabatic tunneling splitting on the lower double-minimum potential energy surface. This is shown schematically for the two conformers of DPOE in Figure 9. As Kopec *et al.*[16] have laid out in some detail, this tunneling splitting cannot be calculated from the shape of the lower double minimum surface alone, since the tunneling is influenced by nonadiabatic interactions with the upper electronic state.

At the same time, the rotational constants and TDM orientations extracted from the rotationally resolved spectra provide unequivocal evidence that the electronic excitation is completely delocalized over the two aromatic rings, with TDM directions consistent with excited states which are equal contributions from local excitations of anisole ($C_6H_5OCH_3$). In the end, this is a requirement of the symmetric configurations for the two conformers, in which the two aromatic chromophores are placed in equivalent configurations.

On this basis, one would anticipate that most other geometries that are away from these highly symmetric points on the excited state potential energy surfaces will be characterized by nearly localized electronic excitation of the two rings with even modest shifts of a few cm^{-1} in the site frequencies sufficient to cause electronic localization, since the nonadiabatic tunneling splittings at C_2 and C_{2h} geometries are 1 cm^{-1} or less. This fact was brought home in dramatic fashion by the R2PI spectra of the singly ^{13}C-substituted isotopomer of DPOE, where shifts in the zero-point energies of the two excited states of 3–4 cm^{-1} led to substantial localization of the electronic excitation, as Figure 9 illustrates. In the *ttt* conformer, this turned a pair of electronic transitions in which one is dipole-allowed and the other dipole-forbidden into a pair of transitions that have nearly equal oscillator strengths, with excitation localized either on the ^{13}C-substituted ring or the non-substituted one, with a splitting of 3.3 cm^{-1}. One could imagine that, in the condensed phase, small asymmetries or fluctuations in the solvent surroundings will be sufficient to localize electronic excitation there too. The effects of asymmetric solvation are seen already in the DPOE–H_2O complex involving the asymmetry induced by a single H_2O molecule.[56]

B. Spectroscopic signatures of vibronic coupling involving near-degenerate excited states

We have just proven that in both the *tgt* and *ttt* conformers of DPOE, the first two levels on the adiabatic double-minimum potential energy surface, associated with electronic character

$$\psi_1 = \frac{1}{\sqrt{2}}(|A^*B\rangle + |AB^*\rangle),$$
$$\psi_2 = \frac{1}{\sqrt{2}}(|A^*B\rangle - |AB^*\rangle), \quad (2)$$

are separated in energy by no more than 1 cm^{-1} at the C_2 and C_{2h} geometries associated with the *tgt* and *ttt* conformers, respectively. This splitting is small compared to all vibrational frequencies in the *tgt* and *ttt* conformers. As a result, each vibrational level is split by nonadiabatic effects into a pair of levels. We focus in this section on the spectroscopic signatures of this near-degeneracy in the vibronic spectroscopy of the two conformers.

In the C_2 *tgt* conformer, both members of the tunneling doublet associated with each vibronic level carry oscillator strength from S_0. As a result, every vibronic transition in the *tgt* spectrum in Figure 2 is in fact an unresolved doublet, as was shown in Figure 5 to be the case at the electronic origin by high resolution spectroscopy. Furthermore, the strong intensities observed in the non-totally symmetric fundamentals result from vibronic coupling between the two states, with the S_1 state borrowing intensity from S_2 and vice versa. Since the emission from both members of the pair is dipole-allowed, a strong $\Delta v = 0$ false origin appears in the DFL spectra of both totally symmetric and non-totally symmetric fundamentals (Figure 3(a)).

By contrast, the C_{2h} *ttt* conformer has only one dipole-allowed electronic transition (A_g–B_u), but ^{13}C R2PI spectra located the dipole-forbidden A_g–A_g origin split by only 3.3 cm^{-1}. Based on a comparison with the *tgt*, where a 4.7 cm^{-1} ^{13}C splitting arose from a 1.02 cm^{-1} non-adiabatic tunneling splitting, the two states are placed within 1 cm^{-1} of one another. As a result, once again, each vibronic band is split into a pair of transitions, but in this case only one member of each pair carries intensity. Vibronic coupling nevertheless plays an important role in the spectrum, with the band 46 cm^{-1} above the A_g–B_u origin assigned to b_u symmetry $\bar{R}$ fundamental built off the A_g electronic state, gaining its intensity purely through vibronic coupling.

It is worth noting that the smaller splitting ascribed to the *ttt* conformer is opposite to the ordering of the splittings predicted by TDM model or TDDFT calculations (Table III). One possible reason for this smaller splitting would be that the *ttt* conformer has a larger Franck-Condon quenching than *tgt*. However, comparison of the DFL spectra of the S_1 origins of *ttt* (Figure 3(b)) and *tgt* conformers (Figure 3(a)) show little difference between the two in the intensities of the ring modes that dominate this quenching factor. In the end, the

only experimentally measured quantity we report here for the *ttt* conformer is the 3.3 cm^{-1} splitting in the ^{13}C R2PI spectrum, which is the composite of the quenched excitonic and zero-point energy effects that include contributions from the different sets of inter-ring modes for each conformer given in Table I. A direct measure of the splitting in the ^{12}C isotopomer would require comparison of the one-photon and two-photon allowed transitions, a task left for future work.

The adiabatic model developed by Kopec *et al.*[16] projects non-adiabatic coupling onto a single effective vibrational coordinate, leading to accurate predictions for the nonadiabatic tunneling splitting at the electronic origin in model homodimers. By contrast, a multi-mode version of the diabatic Fulton-Gouterman model has recently been developed, providing a means for modeling the observed vibronic intensities in DPOE. The *tgt* conformer was not modeled due to the unresolved overlap of contributions from the two excited states in the excitation and dispersed fluorescence spectra. In the *ttt* conformer, the model is able to account for the vibronic intensities in the R/$\bar{R}$ pair of interchromophore bends both in excitation and in dispersed fluorescence from the dipole-allowed B_u origin (Fig. S1 of the supplementary material[59]). Similar modeling of the intensities in the origin emission into the ring mode pairs 6a, 1, and 12 (in Varsanyi notation)[57] at −590/−610, −802/−840, and −996/−1005 cm^{-1} are similarly successful (Figs. S2–S4 of the supplementary material[59]). Similar modeling of the $A_g(\bar{R}^1)$ emission (the +46 cm^{-1} band) accounts for the vibronically induced emission to $v'' = 0, 2$. However, the strong emission bands from the $A_g(\bar{R}^1)$ level to transitions at −649, −849, and −1044 cm^{-1} are not accounted for in the FG model, pointing to the need for further refinement of intermode coupling in the theory.

C. Collision-induced electronic energy transfer

One of the more striking results of the present study is the unusual sensitivity of the DFL spectrum of the *ttt* +46 cm^{-1} band to collisions, as shown in Figures 7(a) and 7(b). As discussed in some detail in Sec. IV D and shown pictorially in Figure 7(c), we have shown that the bands that grow in can be ascribed to the lower member of the non-adiabatic tunneling doublet associated with the $R^1{}_0$ fundamental. This state is dipole forbidden from the S_0 zero-point level, but its close proximity (within 1 cm^{-1}) to the other member of the tunneling doublet initially populated by the laser provides a pathway for collisional energy transfer that is extremely facile, and competes with fluorescence even under conditions under which one would typically have thought were collision-free.

Table IV presents estimates of the number of collisions experienced by DPOE during the lifetime of the excited state (30 ns), assuming a gas-kinetic cross section for transfer between members of the tunneling doublet ($\sigma_{coll} = 75$ Å^2). Under conditions closest to the nozzle, there are multiple collisions during the excited state lifetime, suggesting that the two tunneling states could have their populations equilibrated. On the other hand, at x/D = 38, where only 1% of the excited state molecules undergo a gas-kinetic collision, the remaining intensity is likely to be mostly or entirely due to the ^{13}C isotopomer. Invoking these assumptions, the intensity ratio on the right of the table is the collision-induced intensity in the −46 cm^{-1} band relative to the sum of the "0" and −95 cm^{-1} transitions. This ratio falls off at a rate in keeping with the fall off in number of collisions. While these data are not sufficient to quantify the magnitude of the collision cross section as a function of position in the expansion, it seems likely to us that very large cross sections for electronic energy transfer across this small tunneling doublet are at play, with glancing collisions with cross sections significantly exceeding gas kinetic are possible.

TABLE IV. Fractional collision-induced intensity in the $\Delta v_{84} = 0$ transition of the *ttt* conformer of DPOE relative to that in the $\Delta v_{84} = \pm 1$ transitions as a function of distance from the nozzle in nozzle diameters, x/D. The number of gas-kinetic collisions experienced by DPOE in its excited state lifetime is given for comparison.

x/D	No. of collisions[a]	Fractional collision induced intensity
5	2.15	0.56
11	0.32	0.17
16	0.11	0.08
22	0.05	0.05
38	0.01	0.00[b]

[a]Assuming a gas-kinetic collision cross section of 75 Å^2. Calculated using the equations of Ref. 49.[58]
[b]By assumption. See text for further discussion.

It is interesting to consider how these studies under jet-cooled conditions in the gas phase transfer into condensed phase environments in which collisions are likely to provide an efficient means of interchromophore electronic energy transfer in chromophore arrays, multichromophore polymers, and the like.

VI. CONCLUSIONS

We have presented detailed spectroscopic data on the close-lying S_1/S_2 states of DPOE that prove that the molecule is in the extreme limit of weak vibronic coupling. At the C_2 and C_{2h} geometries, the electronic excitation is delocalized over the two rings (by symmetry), but the splitting between the two states is 1 cm^{-1} or less. Given this weak coupling, it is likely that the two potential energy surfaces lie within a few cm^{-1} of one another over large regions of the torsional potential energy surface. In this weak vibronic coupling limit, the excitonic splitting is best thought of as a nonadiabatic tunneling splitting on the lower double-minimum potential energy surfaces associated with electronic excitation on one or the other aromatic ring. This splitting is more than a factor of 10 smaller than vertical splittings calculated via standard methods. In light of this weak vibronic coupling, the smallest of perturbations to one of the rings is sufficient to localize the electronic excitation on one or the other ring. This was illustrated in dramatic fashion in the spectra recorded for the ^{13}C isotopomer that contains a single ^{13}C atom somewhere in one or the two aromatic rings. This zero-point asymmetry was enough to split the electronic origins by 4.7 cm^{-1} (*tgt*) and 3.3 cm^{-1} (*ttt*), and nearly completely localize the electronic

excitation. One would anticipate similar effects by asymmetric solvation in the condensed phase. We will show elsewhere the interesting effects associated with binding a single H_2O molecule to DPOE.[56]

ACKNOWLEDGMENTS

E.G.B., P.S.W., and T.S.Z. gratefully acknowledge support from the (U.S.) Department of Energy (DOE) Basic Energy Sciences, Division of Chemical Sciences under Grant No. DE-FG02-96ER14656.

[1] G. Panitchayangkoon, D. V. Voronine, D. Abramavicius, J. R. Caram, N. H. C. Lewis, S. Mukamel, and G. S. Engel, Proc. Natl. Acad. Sci. U.S.A. **108**, 20908 (2011).
[2] K. M. Pelzer, G. B. Griffin, S. K. Gray, and G. S. Engel, J. Chem. Phys. **136**, 164508 (2012).
[3] G. S. Engel, T. R. Calhoun, E. L. Read, T. K. Ahn, T. Mancal, Y. C. Cheng, R. E. Blankenship, and G. R. Fleming, Nature (London) **446**, 782 (2007).
[4] H. Lee, Y. C. Cheng, and G. R. Fleming, Science **316**, 1462 (2007).
[5] S. Polyutov, O. Kuhn, and T. Pullerits, Chem. Phys. **394**, 21 (2012).
[6] R. Tempelaar, A. Stradomska, J. Knoester, and F. C. Spano, J. Phys. Chem. B **117**, 457 (2013).
[7] S. Habuchi, H. Fujita, T. Michinobu, and M. Vacha, J. Phys. Chem. B **115**, 14404 (2011).
[8] O. R. Tozer and W. Barford, J. Phys. Chem. A **116**, 10310 (2012).
[9] M. Maus, R. De, M. Lor, T. Weil, S. Mitra, U. M. Wiesler, A. Herrmann, J. Hofkens, T. Vosch, K. Mullen, and F. C. De Schryver, J. Am. Chem. Soc. **123**, 7668 (2001).
[10] G. D. Scholes, Annu. Rev. Phys. Chem. **54**, 57 (2003).
[11] J. D. Hybl, A. A. Ferro, and D. M. Jonas, J. Chem. Phys. **115**, 6606 (2001).
[12] D. M. Jonas, Annu. Rev. Phys. Chem. **54**, 425 (2003).
[13] F. Fassioli, A. Olaya-Castro, and G. D. Scholes, J. Phys. Chem. Lett. **3**, 3136 (2012).
[14] H. Hossein-Nejad, A. Olaya-Castro, and G. D. Scholes, J. Chem. Phys. **136**, 024112 (2012).
[15] D. R. Borst, J. R. Roscioli, D. W. Pratt, G. M. Florio, T. S. Zwier, A. Muller, and S. Leutwyler, Chem. Phys. **283**, 341 (2002).
[16] S. Kopec, P. Ottiger, S. Leutwyler, and H. Koppel, J. Chem. Phys. **137**, 184312 (2012).
[17] A. Muller, F. Talbot, and S. Leutwyler, J. Chem. Phys. **116**, 2836 (2002).
[18] P. Ottiger, S. Leutwyler, and H. Koppel, J. Chem. Phys. **131**, 204308 (2009).
[19] P. Ottiger, S. Leutwyler, and H. Koppel, J. Chem. Phys. **136**, 174308 (2012).
[20] K. Le Barbu-Debus, M. Broquier, F. Lahmani, and A. Zehnacker-Rentien, Mol. Phys. **103**, 1655 (2005).
[21] N. Seurre, K. Le Barbu-Debus, F. Lahmani, A. Zehnacker-Rentien, and J. Sepiol, Chem. Phys. **295**, 21 (2003).
[22] C. A. Southern, D. H. Levy, J. A. Stearns, G. M. Florio, A. Longarte, and T. S. Zwier, J. Phys. Chem. A **108**, 4599 (2004).
[23] C. G. Heid, P. Ottiger, R. Leist, and S. Leutwyler, J. Chem. Phys. **135**, 154311 (2011).
[24] M. Chattoraj, B. Paulson, Y. Shi, G. L. Closs, and D. H. Levy, J. Phys. Chem. **97**, 13046 (1993).
[25] W. T. Yip, D. H. Levy, R. Kobetic, and P. Piotrowiak, J. Phys. Chem. A **103**, 10 (1999).
[26] N. A. van Dantzig, D. H. Levy, C. Vigo, and P. Piotrowiak, J. Chem. Phys. **103**, 4894 (1995).
[27] X. Wang, D. H. Levy, M. B. Rubin, and S. Speiser, J. Phys. Chem. A **104**, 6558 (2000).
[28] A. Zehnacker, F. Lahmani, E. Breheret, J. P. Desvergne, H. BouasLaurent, A. Germain, V. Brenner, and P. Millie, Chem. Phys. **208**, 243 (1996).
[29] A. Zehnacker, F. Lahmani, J. P. Desvergne, and H. Bouas-Laurent, Chem. Phys. Lett. **293**, 357 (1998).
[30] A. L. L. East, P. Cid-Aguero, H. S. Liu, R. H. Judge, and E. C. Lim, J. Phys. Chem. A **104**, 1456 (2000).
[31] J. K. Lee, R. H. Judge, B. H. Boo, and E. C. Lim, J. Chem. Phys. **116**, 8809 (2002).
[32] N. R. Pillsbury, C. W. Muller, W. L. Meerts, D. F. Plusquellic, and T. S. Zwier, J. Phys. Chem. A **113**, 5000 (2009).
[33] N. R. Pillsbury, J. A. Stearns, C. W. Muller, D. F. Plusquellic, and T. S. Zwier, J. Chem. Phys. **129**, 114301 (2008).
[34] C. P. Rodrigo, C. W. Mueller, N. R. Pillsbury, W. H. James III, D. F. Plusquellic, and T. S. Zwier, J. Chem. Phys. **134**, 164312 (2011).
[35] J. A. Stearns, N. R. Pillsbury, K. O. Douglass, C. W. Muller, T. S. Zwier, and D. F. Plusquellic, J. Chem. Phys. **129**, 224305 (2008).
[36] Y. Inokuchi, O. V. Boyarkin, R. Kusaka, T. Haino, T. Ebata, and T. R. Rizzo, J. Am. Chem. Soc. **133**, 12256 (2011).
[37] S. Kokubu, R. Kusaka, Y. Inokuchi, T. Haino, and T. Ebata, Phys. Chem. Chem. Phys. **12**, 3559 (2010).
[38] R. Kusaka, Y. Inokuchi, and T. Ebata, Phys. Chem. Chem. Phys. **10**, 6238 (2008).
[39] N. A. van Dantzig, H. S. Shou, J. C. Alfano, N. C. C. Yang, and D. H. Levy, J. Chem. Phys. **100**, 7068 (1994).
[40] E. E. Baquero, W. H. James III, T. H. Choi, K. D. Jordan, and T. S. Zwier, J. Phys. Chem. A **112**, 11115 (2008).
[41] B. Nebgen, F. L. Emmert, and L. V. Slipchenko, J. Chem. Phys. **137**, 084112 (2012).
[42] T. Forster, in *Modern Quantum Chemistry*, edited by O. Sinanoglu (Academic, New York, 1965), p. 93.
[43] R. L. Fulton and M. Gouterman, J. Chem. Phys. **35**, 1059 (1961).
[44] R. L. Fulton and M. Gouterman, J. Chem. Phys. **41**, 2280 (1964).
[45] P. Ottiger and S. Leutwyler, J. Chem. Phys. **137**, 204303 (2012).
[46] R. L. Fulton and M. Gouterman, Spectrochim. Acta **17**, 1093 (1961).
[47] E. G. Buchanan, E. L. Sibert, and T. S. Zwier, J. Phys. Chem. A **117**, 2800 (2013).
[48] T. S. Zwier, J. Phys. Chem. A **105**, 8827 (2001).
[49] T. S. Zwier, J. Phys. Chem. A **110**, 4133 (2006).
[50] W. Majewski and W. L. Meerts, J. Mol. Spectrosc. **104**, 271 (1984).
[51] R. J. Stanley and A. W. Castleman, J. Chem. Phys. **94**, 7744 (1991).
[52] J. R. Clarkson, E. Baquero, V. A. Shubert, E. M. Myshakin, K. D. Jordan, and T. S. Zwier, Science **307**, 1443 (2005).
[53] D. F. Plusquellic, S. R. Davis, and F. Jahanmir, J. Chem. Phys. **115**, 225 (2001).
[54] D. F. Plusquellic, jb95 - spectral fitting program, NIST, Gaithersburg, MD, 2009, see http://physics.nist.gov/jb95.
[55] V. A. Shubert, W. H. James, and T. S. Zwier, J. Phys. Chem. A **113**, 8055 (2009).
[56] E. G. Buchanan, J. R. Gord, and T. S. Zwier, J. Phys. Chem. Lett. **4**, 1644 (2013).
[57] G. Varsanyi, *Assignments for Vibrational Spectra of 700 Benzene Derivatives* (Wiley, New York, 1974).
[58] D. M. Lubman, C. T. Rettner, and R. N. Zare, J. Phys. Chem. **86**, 1129 (1982).
[59] See supplementary material at http://dx.doi.org/10.1063/1.4807300 for dispersed fluorescence spectra of the totally symmetric fundamentals for the *tgt* conformer, details, and results specific to using the multi-mode Fulton-Gouterman model of vibronic coupling on the *ttt* isomer, the principal axis orientation of both conformers, and a table listing the parameters and uncertainties from the genetic algorithm and linear least-squares fits of the origin bands of DPOE are provided for clarity.